ISSN 0915-6348

NATIONAL INSTITUTE FOR FUSION SCIENCE

Physics and Applications of Micro and Fast Z-Pinch Plasmas

(Dec. 5-6, 2002, NIFS)

Ed. by K. Masugata

(Received - July 4, 2003)

NIFS-PROC-54 July 2003

RESEARCH REPORT
NIFS-PROC Series

TOKI, JAPAN

Physics and Applications of Micro and Fast Z-Pinch Plasmas

Edited by Katsumi Masugata

December 5-6, 2002
National Institute for Fusion Science
Toki, Gifu, Japan

Abstract

This is the proceedings of symposium on "Physics and Application of Micro and Fast z-Pinch Plasma" held at National Institute for Fusion Science. Recent progress of experimental and theoretical works on high energy density plasmas produced by pulsed power is presented.

Keywords: high energy density plasma, z-pinch, pulsed power, soft x-ray, high power particle beam, pulsed discharge, high power microwave

PREFACE

The collaborative research symposium entitled "Physics and Applications of Micro and Fast Z-Pinch Plasmas" was held at National Institute for Fusion Science (NIFS), Toki, from 5 to 6 December 2002. During the 2 days symposium 36 scientists attended from universities and institutes. Totally 22 papers were presented on the physics and applications of Z-pinch plasmas, high power particle beams, pulsed discharges and pulsed power technologies. The proceedings contain most of the papers presented at the symposium. Great achievements were obtained by this symposium through fruitful discussions. I would like to express my sincere thanks to all of the authors, participants, and National Institute of Fusion Science.

Katsumi Masugata
Faculty of Engineering
Toyama University

CONTENTS

List of participants

K. Takaki (Iwate University)
S. Kawata (Utsunomiya University)
Q. Kong, (Utsunomiya University)
S. Miyazaki (Utsunomiya University)
M. Sato (Gunma University)
S. Furuya, (Nagaoka University of Technology)
K. Takasugi (Nihon University)
T. Chiba (Nihon University)
F. Kobayashi (Nihon University)
K. Minagawa (Nihon University)
M. Shirota (Nihon University)
T. Miyamoto (Atomic Research Institute)
T. Yokoyama (Tokyo Institute of Technology)
E. Hotta (Tokyo Institute of Technology)
M. Watanabe (Tokyo Institute of Technology)
Y. Hayashi (Tokyo Institute of Technology)
T. Kasao (Tokyo Institute of Technology)
K. Horioka (Tokyo Institute of Technology)
M. Masnavi (Tokyo Institute of Technology)
N. Sakamoto (Tokyo Institute of Technology)
T. Mizoguchi (Tokyo Institute of Technology)
H. Matsuzawa (University of Yamanashi)
K. Masugata (Toyama University)
T. Honda (Toyama University)
Y. Fujioka (Toyama University)
R. Tejima (Toyama University)
K. Kamada (Kanazawa University)
M. Kamada (Kanazawa University)
K. Kurihara (Kanazawa University)
H. Shirasaka (Kanazawa University)
M. Yatsuzuka (Himeji Institute of Technology)
H. Akiyama (Kumamoto University)
S. Katsuki (Kumamoto University)
T. Namihira (Kumamoto University)
D. Hemmert (Kumamoto University)
T. Tazima (National Institute for Fusion Science)

EXPERIMENTS ON DENSE PLASMA USING PULSE POWER DEVICE

Takashi Mizoguchi, Takashi Kikuchi, Mitsuo Nakajima and Kazuhiko Horioka

Department of Energy Sciences, Tokyo Institute of Technology, Nagatsuta 4259, Midori-ku, Yokohama, 226-8502, Japan

ABSTRACT

Among a number of methods to make a strongly coupled plasma, the method to use wire dicharge in water is selected in this study. Using a small pulse power device, a dense and cold plasma with coupling parameter of $\Gamma \sim 1.0$ is successfully produced. This paper discusses the advantages of this method, and briefly describes the subject of future study with preliminary experimental results.

1 Introduction

In the target of inertial confinement fusion, the plasma is compressed to a strongly coupled state. However, the behavior of the plasma is not yet understood well. Although there are several methods to change the plasma into the strongly coupled state, we are planning to use wire electric discharge.

For an index of the strongly coupled plasma, we use the coupling parameter Γ expressed by the next equation [1],[2].

$$\Gamma = \frac{(Ze)^2/a}{k_b T} = \frac{Potential\ Energy}{Kinetic\ Energy} = 2.69 \times \left[\frac{n}{10^{12} cm^{-3}}\right]^{\frac{1}{3}} \left[\frac{T}{10^6 K}\right]^{-1}$$
$$a \equiv \left(\frac{3}{4\pi n}\right)^{\frac{1}{3}} \qquad (1)$$

Here a is called the ion-sphere radius, Z is effective charge, and T is the plasma temperature. As shown in Eq.1, the value of Γ is a function of plasma density, plasma temperature, and average charge. It also shows that if we need a plasma with $\Gamma > 1$, we have to make a dense and low temperature state. For example, typical values of Γ are;

(a) Tokamak plasma; $\sim 10^{-5}$

(b) Gas discharge plasma in usual experimental condition; $\sim 10^{-3}$

(c) Laser ablation plasma; $\sim 10^{-3}$

(d) Z-pinch plasma; $10^{-3} \sim 10^{-2}$

(e) Radiation converter of inertial fusion plasma; $1 \sim 10$.

2 Advantages of pulse power plasma

In order to investigate the behavior of strongly coupled plasma, it is necessary to precisely evaluate the plasma temperature, the density, and the average electric charge. In this section, procedures for the estimation of those parameters in pulse power devices are described briefly.

2.1 Estimation of plasma temperature

In a pulse power device, the energy inputted into the load E can be estimated by using the next relation.

$$E = \int_0^t VIdt \tag{2}$$

Here, V is the load voltage and I is the current. However, Eq.2 should be carefully used. Because the E is composed of the energy of the space (in this case, energy stored in a magnetic field), the kinetic energy of moving plasma, and internal energy of the plasma. When the circuit inductance is negligibly small, we can estimate the internal energy directory from the waveform of current I and voltage V; thus the plasma temperature. In the following sections, we show the details of the calculation method of this input energy.

2.2 Calculation of density

When the initial radius and density (solid density) of a wire are assumed to be r_0 and n_0 and all wires become plasma by the input energy, the plasma ion density n_i at some instance can be simply estimated from the plasma radius n as,

$$\frac{n_0}{n_i} = \left(\frac{r_0}{r_i}\right)^2. \tag{3}$$

2.3 Evaluation of pressure

When pressure rises rapidly in a medium, a cylindrical shock wave is generated from the exploding plasma. The relation between the shock speed and the pressure jump is exactly described by the Rankine-Hugoniot equation in cylindrical geometry. If shock wave speed and sound velocity are denoted by V_s and a respectively, V_s and ΔP can be correlated as;

$$V_s = M_s a = f(\Delta p/p). \tag{4}$$

Here M_s is the shock Mach number, $\Delta p = p - p_0$, and p_0 is the initial pressure of medium. Based on the above equation, we can estimate Δp by carrying out the observation of shock wave trace [3].

Then the pressure history of the plasma can be evaluated by observing the generated shock wave behavior. We can estimate the plasma pressure from the observation of temporal evolution of the plasma column.

2.4 Advantages of pulsed discharges in water

Based on the above consideration, our group took pulsed wire-discharge in water as a method of the dense plasma formation. The advantages of this method are;

(a) It can locally input the electric energy to a wire by carrying out pulsed electric discharge.

(b) We can accurately measure the input energy E, just from the $V-I$ characteristics of wire discharges.

(c) The generated plasma is confined by tamping effect of the water.

(d) We can measure pressure history from the shock wave trace observed by schlieren method.

3 Experimental Setup

The experimental arrangement of wire discharge in water is shown in Fig.1. A Rogowski belt surrounds the wire to measure the time evolution of the current, and a high voltage probe monitors the load voltage. Copper or Aluminum wire with each diameter of 100 μm was inserted into water in a chamber. The current was driven from eight capacitors connected in parallel, totaling 3.2 μF, and generally charged to 10 kV. The total stored energy was calculated to be 160 J. Due to rapid rise current from capacitor bank, the wire was heated, vaporized, and made into wire plasma.

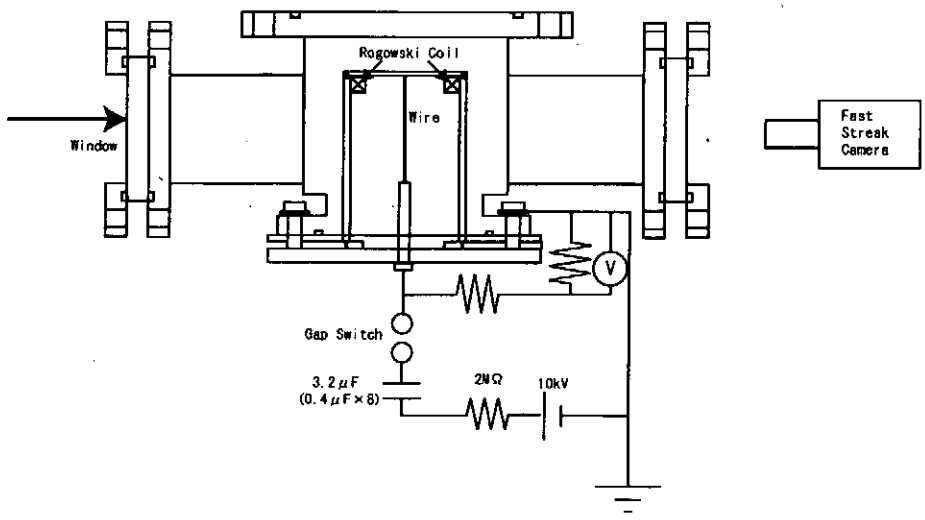

Figure 1: Experimental setup for wire discharge experiments

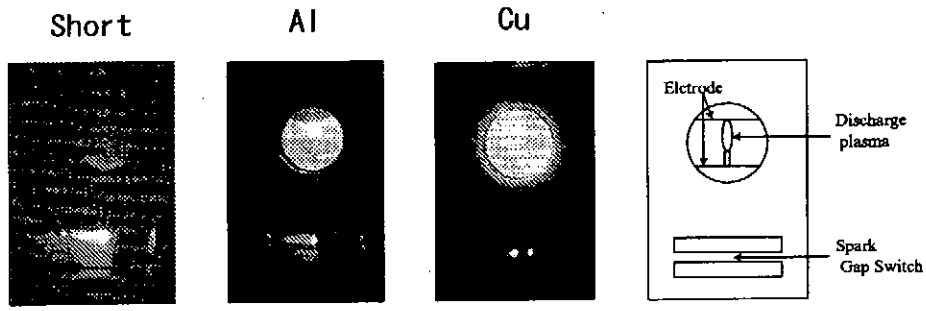

Figure 2: Typical time integrated pictures of discharging wire

4 Inductive correction and resistive voltage

When we discuss the voltage of the electrode gap, we have to pay attention to the effect of circuit (stray) inductance. The observed voltage $V_{oscillo}$ generally consists of resistive and inductive components as shown;

$$V_{oscillo} = IR + L_{circuit}\frac{dI}{dt} + I\frac{dL_{circuit}}{dt}. \tag{5}$$

If the electrode's gap is shorted by a metal rod with sufficient radius, we can neglect the first and the third term as the following equation, because resistance of the wire is negligible $R \simeq 0$, and wire inductance doesn ' t change $dL_{circuit}/dt \simeq 0$.

$$V_{short} \simeq L_{circuit}\frac{dI}{dt} \tag{6}$$

By using Eq.6, we can calculate the circuit inductance $L_{circuit}$. When $L_{circuit}$ doesn't change in time, this gives the resistive voltage of the wire as follows.

$$V_{wire} = V_{oscillo} - L_{circuit}\frac{dI}{dt} = IR \tag{7}$$

As Eq.7 can lead to V_{wire}/I, we can calculate the electrical conductivity of wire plasma together with the information of plasma radius.

5 Experimental Results

5.1 Evaluation of circuit inductance

Fig.3 shows the current and the voltage waveforms when the electrode gap was short-circuited. From this waveforms, circuit inductance $L_{circuit}$ of our device is estimated to be about 40 nH.

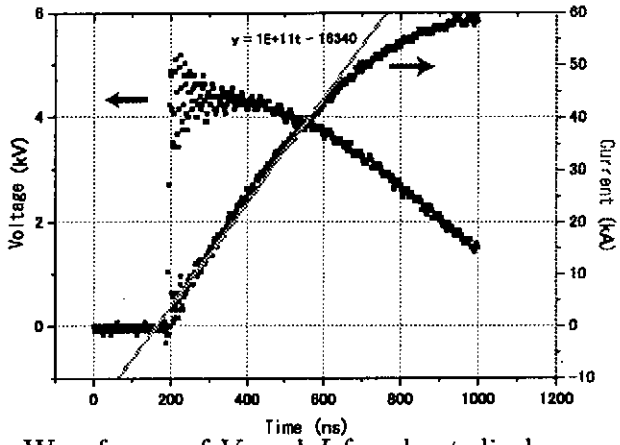

Figure 3: Waveforms of V and I for short discharge condition

5.2 Characteristics of Al wire discharge

Fig.4 $\sim$ 7 show the time evolutions of current and voltage, input energy E, corrected voltage V_{wire} and wire plasma resistance for Al wire discharge. The discharging time was estimated to be 200 ns $\sim$ 600 ns by current and voltage values shown in Fig.4. As shown in Fig.5, the input energy in load is estimated to be 15 J at 500 ns (300 ns from the the discharge onset).

5.3 Characteristics of Cu wire discharge

Fig.8 $\sim$ 11 denote the typical evolutions of the current and voltage, input energy, corrected voltage, and plasma resistance for Cu wire discharge. In case of Cu wire discharge, the discharging time was also estimated to be 200 ns $\sim$ 600 ns by current and voltage waveforms shown in Fig.8. As shown in Fig.9, the input energy in load is estimated to be about 26 J at 500 ns for discharging the Cu wire.

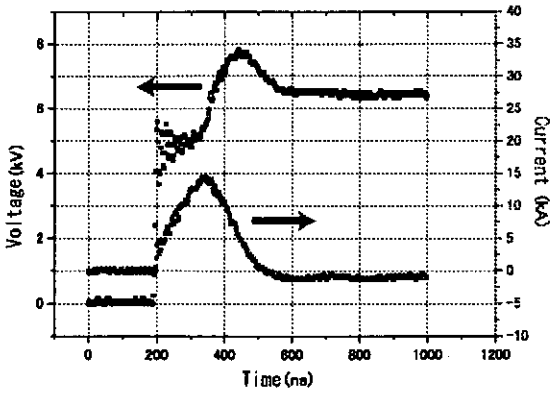

Figure 4: Current and voltage waveforms for Al-wire discharge

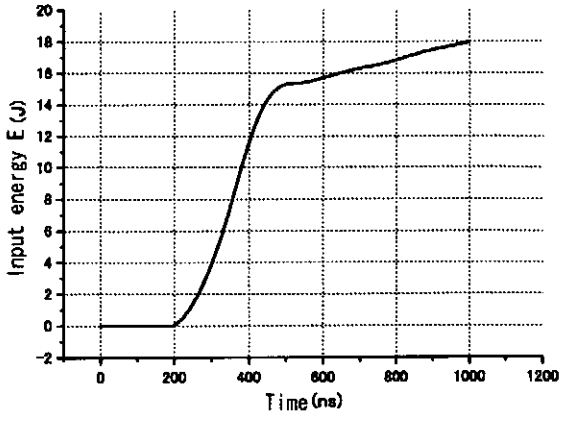

Figure 5: Temporal behavior of input energy for Al-wire discharge

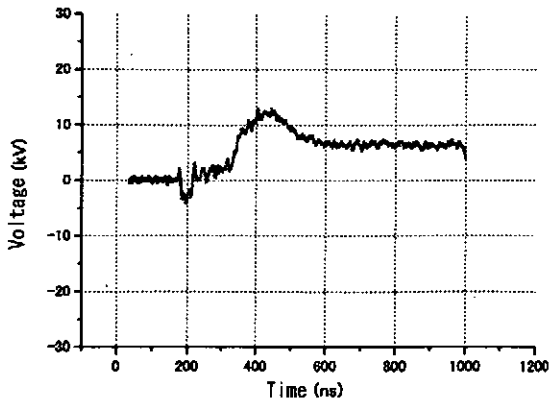

Figure 6: Corrected voltage for *Al*-wire discharge

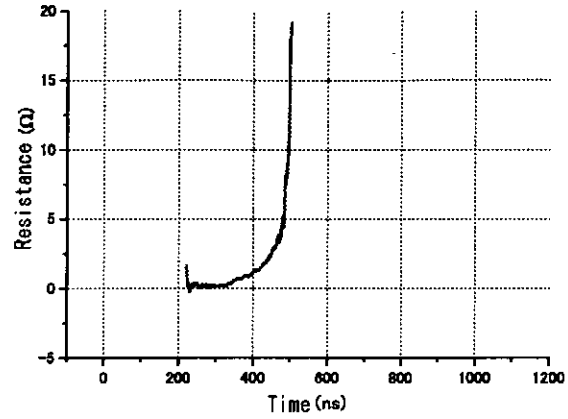

Figure 7: Wire resistance for *Al*-wire discharge

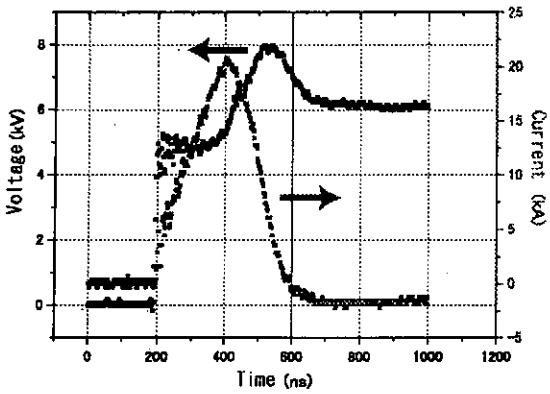

Figure 8: Current and voltage waveforms for *Cu*-wire discharge

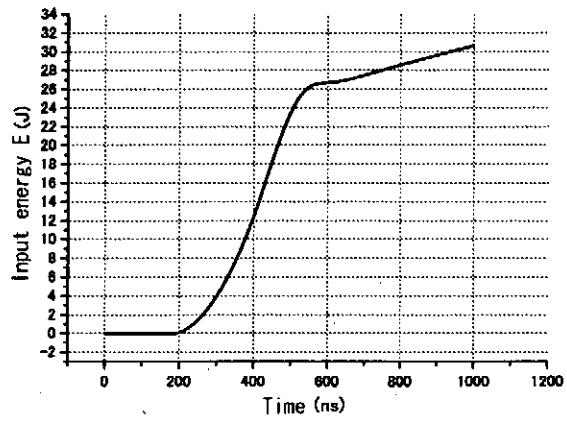

Figure 9: Temproal behavior of input energy for *Cu*-wire discharge

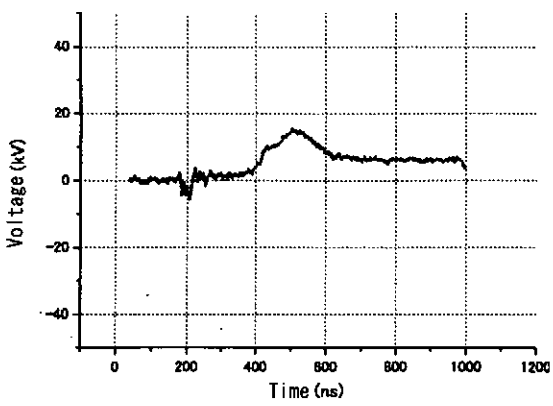

Figure 10: Corrected voltage for *Cu*-wire discharge

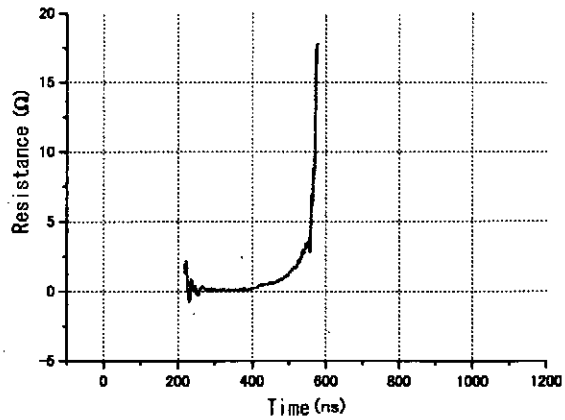

Figure 11: Wire resistance for *Cu*-wire discharge

6 Concluding remarks and discussion

As shown in section 5, although the pulse power device was operated under the same condition, the input energy into Cu wire was lager than that of Al. The brightness of time-integrated photos shown in Fig.2 reflect this difference. From these experimental results, plasma temperature is approximately estimated using the next equation [4].

$$T = \left(\frac{E_i}{6.34 \times 3.6}\right)^{-1.2} \quad [eV] \quad (with\ Al) \tag{8}$$

Using the temperature derived from Eq.8, and assuming that the density of generated plasma from the wire exploding is initial density of the wire, and that the average charge Z_{eff} is 1, the coupling parameter Γ can be estimated. Fig.12 shows the typical behavior of the coupling parameter Γ for Al-wire discharge. As shown in Fig.12, it is shown that

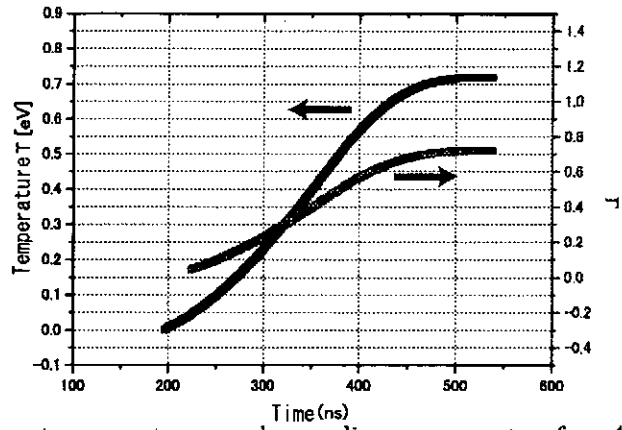

Figure 12: Plasma temperature and coupling parameter for Al-wire discharge

coupling parameter Γ rises with discharge time and reaches to about 0.7, and that plasma temperature rises to about 0.7 eV at 500 ns. Because of the lack of EOS data, in the case of the copper wire, Γ value can not be estimated. However from the preliminary experimental results, we can conclude that the wire explosion in water is a convenient method to make a dense plasma.

Total input energy can be assumed to be consisting of vaporization energy, excitation and ionization energy, and kinetic energy of the plasma. The table shown below

Wire	Length [cm]	Mass [mg]	Vaporization [joules]
Cu	7.1	326	2028

Table 1: Vaporization energy obtained by explosion of constant-mass sample using 56.8 μF capacitor at 10 kV

is experimentally obtained vaporization energy of Cu wire [5]. When we apply the vaporization data to our parameter (wire radius: 50 μm, wire length: about 3 cm, wire

density: 8.93 $g \cdot cm^{-3}$), vaporization energy is estimated to be 13 J. On the contrary, as shown in Fig.9, the total input energy to the wire load is much lager than the vaporization energy. Although the coupling parameter can not be estimated for Cu wire case, this estimation implies that input energy is sufficient to make the plasma state from Cu-wire.

7 Future directions

We are planning to make clear the characteristics of strongly coupled plasmas, such as the conductivity, EOS data (Equation of State) and the energy deposition process of beams in the dense plasma, over a wide range of plasma conditions. In this report, the preliminary consideration and preparatory experimental results for the study plan are shown. Issues of our future study are;

- To find out the plasma behavior over a wide range of input energy and power level of the discharge
- To examine plasma pressure history, especially at the initial phase, with fast streak camera
- To estimate the plasma temperature T, ion density n_i, and average ionization Z_{eff} with sufficient accuracy; thus the exact coupling values of parameter Γ
- To estimate the electrical conductivity as a function of the coupling parameter for various materials

References

[1] A. W. DeSiva and J. D. Katsouros, "Electrical conductivity of dense copper and aluminum plasma," *Phys. Rev E*, vol. 57, pp. 5945–5951, 1998.

[2] A. W. DeSiva and J. D. Katsouros, "Experimental study of the electrical conductivity of strongly coupled copper plasmas," *Phys. Rev E*, vol. 49, pp. 4448–4454, 1994.

[3] Myron N. Plooster, "Shock Wave from Line Sources. Numerical Solutions and Experimental Measurements" *The physics of fluids*, vol.13, pp.2665–2674, 1970.

[4] M. Murakaki, J.Meyer-Ter-Vehn, and R. Ramis "Thermal X-Ray Emission from ion-Beam-Heated Matter" *Journal of X-Ray Science And Technology*, vol.2, pp.127–148, 1990.

[5] William G. Chance and Howard K. Moore "Exploding wires volume 2," (plenum press, New York,1962) pp. 5-13, 1962.

CHARACTERISTICS OF TIME-DEPENDENT IONIZATION PROCESS IN HIGH ENERGY-DENSITY ARGON PLASMA

Majid MASNAVI, Mitsuo NAKAJIMA and Kazuhiko HORIOKA

Department of Energy Sciences, Tokyo Institute of Technology, 4259 Nagatsuta, Midori-ku, Yokohama 226-8502, Japan

ABSTRACT

Low-Z neon (Ne)-like collisionally pumped X-ray lasers exhibit maximum gain at electron density ranging $\approx 10^{17} \leq n_e \leq 10^{21}(\mathrm{cm}^{-3})$, a density regime at which neither the Coronal nor LTE (local thermodynamic equilibrium) conditions can be expected to apply. This paper presents some calculation results for optically thin argon plasma based on reduced time-dependent non-LTE ionization model. The relaxation time for different ionization states and effective ionic charge are found as a function of the electron temperature and plasma density, in particular, for conditions which are relevant to collisionally pumped Ne-like argon (ArIX) XUV laser. The gain coefficient on the J=0 $\rightarrow$ 1 transition ($\lambda = 46.9$nm) of ArIX XUV laser is also presented.

1. Introduction

The ionization state distribution of plasma is a fundamental quantity that is required for the determination such as; equation of state, thermal and electrical conductivities, radiative transfer and gain in X-ray lasers.[1)] Various ionization models, namely, local thermodynamic equilibrium (LTE), Corona equilibrium (CE) and Collisional-radiative model (CR) have been investigated by several workers in the time-dependent[1-3)] and steady-state conditions.[4,5)] In LTE approximation, the distribution of state densities both in the ground or excited states are given by Saha-Boltzman equation. The LTE is satisfied mainly for very dense plasmas where collisions dominate all state changing processes. On the other hand, if the plasma is very tenuous then partially charged ions will be excited from their ground-states mainly by electron collisions, and will rapidly decay back to their ground-states by radiative transitions. This is Coronal equilibrium. For example, such a condition for argon plasma with an electron temperature of about 70 eV (according to

McWhirter relation[4]), requires electron densities larger than $n_e \geq 5 \times 10^{20}(\mathrm{cm}^{-3})$ for LTE to happen, and for Corona region using Cooper relation,[4] electron density must be lower than $n_e \leq 10^{17}(\mathrm{cm}^{-3})$. The Collisional-radiative model describes the intermediate density region which is typical of fusion and X-ray laser plasmas. The CR model is a generalized model taking into account all the recombination processes. In this article, we follow the suggested idea[2] of describing a non-LTE plasma by a few dominant ion states, and will present calculation results using the reduced time-dependent Collisional-radiative model for transient argon plasma.

2. Ionization Model and Rate Coefficients

Considering only collisional ionization from the ground-state of ion and recombination from the continuum into the ground-state, then the reduced time-dependent Collisional-radiative model for the relative populations; $n_j = N_j/N_T$ (where N_T being the total number density), reads as:[2]

$$\frac{dn_{j-1}}{dt} = n_e T_j n_j - n_e S_{j-1} n_{j-1} \tag{2.1}$$

$$\frac{dn_j}{dt} = n_e S_{j-1} n_{j-1} + n_e T_{j+1} n_{j+1} - n_e (S_j + T_j) n_j, \tag{2.2}$$

where $T_m = \alpha_m + n_e \beta_m + D_m$ is the total recombination term. Here, S_Z is the collisional ionization rate coefficient corresponding to the ionic charge state Z, and α_{Z+1},β_{Z+1} and D_{Z+1} are respectively, radiative, three-body and dielectronic recombination rate coefficients corresponding to the ionic charge state $Z+1$. The closure equation is given by: $\sum_{j=1}^{Z} n_j = 1$. In this article, the ionization rate coefficients are calculated using McWhirter formula,[4] and a simple practical fit relation[6] including autoionization as follows:

$$S_Z = 2.43 \times 10^{-6} \xi_Z k T_e^{-3/2} \left(\exp(-u)/u^{7/4}\right) (\mathrm{cm}^3 \mathrm{sec}^{-1}), \tag{2.3}$$

and

$$Sfit_Z = A \frac{(1 + P \times \sqrt{U})}{X + U} U^K \exp(-U) (\mathrm{cm}^3 \mathrm{sec}^{-1}), \tag{2.4}$$

where $u = \chi_Z / kT_e$, that χ_Z is ionization potential and ξ_Z number of electrons in outermost layer of ion Z. The ionization potentials are calculated from More's screening constant and formula.[7] Also, $U = dE/kT_e$, where dE, A, P, X and K are fit parameters.[6] The

radiative and three-body recombination rate coefficients are calculated using Kolb and McWhirter expressions:[4)]

$$\alpha_{Z+1} = 5.2 \times 10^{-14}(Z+1)(\chi_Z/kT_e)^{1/2}(0.429+ \\ 0.5\ln(\chi_Z/kT_e) + 0.469(\chi_Z/kT_e)^{-1/2})(\mathrm{cm}^3\,\mathrm{sec}^{-1}), \tag{2.5}$$

and

$$\beta_{Z+1} = \frac{2.97 \times 10^{-27}\xi_z}{kT_e\chi_Z(4.88 + (kT_e/\chi_Z))}(\mathrm{cm}^6\,\mathrm{sec}^{-1}). \tag{2.6}$$

The dielectronic rate coefficients are calculated using Burgess and Merts formula at so-called zero-density approximation with data (C_{mj}, E_{mj}) taken from Ref. (8), as follows:

$$D_{DR} = \frac{1}{(kT_e)^{3/2}} \sum_{j=2}^{Z-1} \sum_{m=1}^{4} C_{mj} \exp(-E_{mj}/kT_e)(\mathrm{cm}^3\,\mathrm{sec}^{-1}). \tag{2.7}$$

Relaxation time is given by:[2)]

$$\tau_R = \psi^{-1} \left(\frac{N_T}{n_e}\right) Z_{eff}, \tag{2.8}$$

where

$$\psi = \frac{N_T\left[(j+1)S_jS_{j-1} + jT_{j+1}S_{j-1} + (j-1)T_jT_{j+1}\right]}{T_{j+1} + T_j + S_j + S_{j-1}}, \tag{2.9}$$

and effective ionic charge reads:

$$Z_{eff} \equiv \frac{n_e}{N_T} = \left(\frac{\sum_{j=1}^{Z} jn_j}{\sum_{j=1}^{Z} n_j}\right). \tag{2.10}$$

3. Numerical Results and Discussion

We have considered argon ions and examined their behaviors with two approaches; (1) the sequence of events followed in our calculations is one which the ion is introduced as a neutral (or partially ionized) to a region of steady electron temperature, i.e., a constant temperature is reached in a time much shorter than that required for the ions to reach steady-state, and also electron density is changed according to Eq. (10).[9)] In second approach, we have calculated ionization model at fixed plasma density when the temperature

changes, instantaneously (although these assumptions are unphysical, but that gives a beneficial insight into a number of issues[10]). The main assumption is that the initial ionization state distribution is similar to those found at somewhat lower temperatures. In our calculations, the ionization state distributions at initial time for a given temperature and ion density of plasma have calculated using the steady-state CR ionization model. It is apparent from the ionization rate equations that the factors, which determine the evolution of the argon ions are the initial ionization state distribution, the electron temperature and the time integral of the electron density. Following Ref. (9), we present the latter by the quantity $n_e\tau$, which is convenient to estimate kinetic parameters such as; effective ionic charge versus time at different temperature and electron density of plasma. The $n_e\tau_R$ (which τ_R is the relaxation time) values required for the initially partial ionized argon to reach steady-state shown in Fig. (1). In order to calculate the relaxation time, we followed time evolution of ionization state distributions until that the effective ionic charge at a given density and temperature is close to its value in the steady-state CR ionization model. When an envelope is taken from the ionization state distributions at relaxation time as shown in Fig. (2), a correlation is seen between different degree of ionizations and the $n_e\tau_R$ diagram. The relatively small values of $n_e\tau_R$ required to reaching steady-state for closed shell configurations of He as well as Ne-like ions, is a result of the large difference in ionization potential between that a single electron shell state and closed shell state. The reduced ionization rate prevents the next state being heavily populated. With comparison of Fig. (1) and Fig. (2), the relaxation times for closed shell configurations can be easily scaled with electron density as follows:

$$\tau_{R_{(\mathrm{Ne})}} \approx \frac{(1-2)\times 10^{11}}{n_e(\mathrm{cm}^{-3})}(\mathrm{second}),$$

and

$$\tau_{R_{(\mathrm{He})}} \approx \frac{(2-6)\times 10^{11}}{n_e(\mathrm{cm}^{-3})}(\mathrm{second}).$$

The effective ionic charge against electron temperature is shown in Fig.(3), for different values of the $n_e\tau$. The solid line ($n_e\tau = 10^{12}(\mathrm{cm}^{-3}\mathrm{sec})$) is almost corresponding to the result of steady-state CR ionization model. An inspection of Fig. (2) and Fig. (3) indicates that two plateau regions are due to the closed shell ionization state distributions,

i.e., Ne as well as He-like degree of ionizations. In other words, as $n_e\tau$ is increased the ionization states which are first to reach their steady-state are those whose ionization distribution curves are broadly peaked at steady-state condition.

As an alternative approach, we have calculated the time evolution of different degree of ionizations, in particular, sodium (Na), Ne as well as fluorine (F)-like populations and effective ionic charge state (relevant to Ne-like argon XUV laser) at fixed electron density of plasma, when the electron temperature jumps from an initial low values to high temperature. Time evolutions of Na, Ne as well as F-like ions at three different electron densities when electron temperature jumps from 1 to 50 and 100 eV are shown in Fig. (4) and Fig. (5), respectively, using both ionization rate coefficients due to McWhirter and fit formulas. As can be seen the times required to reach steady-state for different electron densities of Na, F as well as Ne-like degree of ionizations have close agreement with the relaxation time curve shown in Fig.(1). For example, the relaxation time for Ne-like state increases from $\simeq$ 10, 100 to 1000 nsec as the electron density decreases from 10^{19}, 10^{18} to $10^{17}(\mathrm{cm}^{-3})$, respectively. At low temperature, the McWhirter ionization rate coefficient overestimates Ne-like and underestimates Na-like degree of ionizations; relatively contrast to in the case of higher temperature for Ne as well as F-like ions. Figure (6) shows time evolution of effective ionic charge using two different ionization rate coefficients. As can be seen the effective ionic charge derived by McWhirter expression has close agreement with fit formula due to Ref.(6) at this temperature. An inspection of Fig. (3) and Fig. (6) reveals that effective ionic charge calculated is close at both approaches. For example in Fig. (3), at temperature of 100 eV, line of $n_e\tau = 10^9(\mathrm{cm}^{-3}\,\mathrm{sec})$;(for $n_e = 10^{18}(\mathrm{cm}^{-3})$ and $\tau = 10^{-9}\,\mathrm{sec}$), shows almost the same value of Z_{eff} with Fig. (6) at corresponding time, temperature and plasma density.

In connection with collisionally pumped ArIX XUV laser, we have investigated gain coefficient of J=0$\rightarrow$ 1 line. The gain coefficient (G) for a Doppler-broadened spectral line on a radiative transition between an upper level u and a lower level l is expressed as [11,12]

$$G_{ul} = \frac{1}{8\pi}\left(\frac{M}{2\pi kT_i}\right)^{1/2} A_{ul}\lambda_{ul}^3 g_u\left(\frac{N_u}{g_u} - \frac{N_l}{g_l}\right) = \sigma g_u\left(\frac{N_u}{g_u} - \frac{N_l}{g_l}\right) \tag{3.1}$$

where λ_{ul} is the wavelength of the transition, A_{ul} the radiative decay rate, N_j the ion

population density in the level j having statistical weight g_j, k the Boltzmann constant, M the atomic mass of the ion, σ the stimulated emission cross section and T_i the ion temperature. In this paper, 37 levels including $2s^22p^6$, $2s^22p^53s$, $2s^22p^53p$, $2s^22p^53d$, $2s2p^63s$, $2s2p^63p$ and $2s2p^63d$ configurations in ArIX ion have been considered. Since equilibrium between the excited levels is readily established due to their short relaxation times, the quasi-steady-state approximation has been adopted for excited states in our calculations. This means that only the time evolution of the ground state is traced using ionization model on the basis of this approximation. The detailed description and opacity treatment on gain coefficient have been already given in Refs. (11-13). Figure (7) shows the time evolutions of the effective ionic charge (where Z_{eff} is divided by a factor of 2), Ne-like degree of ionization (where δ_{Ne} is multiplied by a factor of 4) and gain coefficient ($\lambda = 46.9$nm transition) in a more realistic transient case, for a linear ramp of the electron temperature ($0.01 \leq kT_e \leq 100$ eV, which kT_e is divided by a factor of 25 for a better view.), at different values of the initial electron density ($n_e(t) = Z_{eff} \times n_e(t=0)(\mathrm{cm}^{-3})$. Therefore the effective ionic charges show value of the electron density.). An inspection of Fig. (7) shows that the Ne-like degree of ionization has maximum between $\simeq 20-30$ nsec for different electron densities and temperatures ranging $\approx 4\times10^{18} \leq n_e \leq 2\times10^{19}(\mathrm{cm}^{-3})$ and $50 \leq kT_e \leq 75$eV, respectively, at almost constant Z_{eff}. As can be seen, the gain coefficients have maximum in electron density region of $\simeq 5\times10^{18} - 3\times10^{19}(\mathrm{cm}^{-3})$ at $\simeq 35$nsec for electron temperature of $\simeq 87$(eV). Figure (7) also shows that the mismatch between the electron temperature which maximizes the gain coefficient and fractional of Ne-like argon ion. This is a general problem of Ne-like x-ray lasers.[14] The mismatch arises because the excitation energy into the upper laser levels ($2s^22p^53p$) are typically 3/4 times of ionization potential of Ne-like ion (a kT_e which optimizes the gain per total ArIX ion density is $\simeq 250$ eV), and thus an electron temperature which gives large ground-state excitation rates will lead to large ionization rates if the plasma density is sufficient (It is important to note that the relaxation time for Ne-like degree of ionization is $\tau_R \approx \frac{(1-2)\times10^{11}}{n_e(\mathrm{cm}^{-3})}$(second).). The gain coefficient as a function of electron density and temperature is shown in Fig. (8), for the static plasma without opacity effect and with reabsorption calculated using the Zemansky escape probability factor for plasma with ra-

dius equal to 0.01 cm. We have taken into account opacity effect of the 3d $^1P_1 - 2p^6\ ^1S_0$, 3d $^3D_1 - 2p^6\ ^1S_0$, 3d $^3P_1 - 2p^6\ ^1S_0$, 3s $^3P_1 - 2p^6\ ^1S_0$ and 3s $^1P_1 - 2p^6\ ^1S_0$ transitions on the gain coefficient, and also we neglected its effect on the ionization state distributions. Figure (8) indicates that the gain coefficients drastically reduced with the opacity effect due to the values of static optical depths of resonance transitions and even its effect increases gain at special conditions.[11,15] However, a realistic calculation would require space and time-dependent information about the density-temperature history of the plasma. This requires a calculation where magnetohydrodynamics and atomic physics of ionization and excitation for optically thick plasmas are coupled self-consistently and advanced in time. This work is the subject of the future study.

4. Summary

The relaxation time, τ_R, that partially charged argon ions must spend in a plasma before reaching to the Collisional-radiative equilibrium has been computed and scaled with electron density. The results show that the relaxation time depends weakly on the electron temperature and increases as electron density decreases. The effective ionic charge is also calculated versus time and plasma parameters, in particular, for the interest regime of Ne-like argon XUV laser.

Acknowledgment

M. Masnavi gratefully acknowledge financial support from the Ministry of Education, Culture, Sports, Science and Technology.

References

1) A. Djaoui, " Time-Dependent Hydrogenic Ionization Model for Non-LTE Mixtures", J. Quant. Spectrosc. Radiat. Transf., **62**, 303-320 (1999).

2) S. Eliezer, R. Falquina and E. Minguez, " Stochastic Substitute for Coupled Rate Equations in the Modeling of Highly Ionized Transient Plasmas", Phys. Rev. E, **49** ,4735-4738 (1994).

3) M. Busquet, " Reduced Time-Dependent Collisional-Radiative Model", J. Quant. Spectrosc. Radiat. Transf., **58**, 519-530 (1997).

4) G. P. Gupta and B. K. Sinha, " Effect of Ionization and Recombination Coefficients

on the Charge-State Distribution of Ions in Laser-Produced Aluminum Plasmas", Phys. Rev. E, **56**, 2104-2111 (1997), and references therein.

5) Y. T. Lee, " A Model for Ionization Balance and L-Shell Spectroscopy of Non-LTE Plasmas", J. Quant. Spectrosc. Radiat. Transf., **38**, 131-145 (1987).

6) G. S. Voronov, " A Practical Fit Formula for Ionization Rate Coefficients of Atoms and Ions by Electron Impact: Z=1-28", At. Data Nucl. Data Tables, **65**, 1-35 (1997).

7) R. M. More, " Electronic Energy-Levels in Dense Plasmas", J. Quant. Spectrosc. Radiat. Transf., **27**, 345-357 (1982).

8) P. Mazzotta, G. Mazzitelli, S. Colafrancesco and N. Vittorio, " Ionization Balance for Optically Thin Plasmas: Rate Coefficients for All Atoms and Ions of the Elements H to Ni", Astron. Astrophys. Suppl. Ser., **133**, 403-409 (1998).

9) P. G. Carolan and V. A. Piotrowicz, " The Behaviour of Impurities Out of Coronal Equilibrium", Plasma Phys., **25** , 1065-1086 (1983).

10) S. B. Healy, A. Djaoui, P. B. Holden, G. J. Pert and S. J. Roses, " A Comparison of Time-Dependent Ionization Models for Laser-Produced Plasmas", J. Phys. B: At. Mol. Opt. Phys., **28**, 1381-1391 (1995).

11) M. Masnavi, T. Kikuchi, M. Nakajima and K. Horioka, " Influence of Opacity on Gain Coefficients in Static, and Fast Moving Neon-Like Krypton Plasmas", J. Appl. Phys., **92**, 3480-3486 (2002).

12) M. Masnavi, T. Kikuchi, M. Nakajima and K. Horioka, " A Study on Relative Populations and Gain Coefficients of Neon-Like Krypton for Fast Moving Plasma in Capillary Discharge", NIFS - PROC Series - 51, 55-72 (2002).

13) M. Masnavi, M. Nakajima and K. Horioka, , " Effect of Opacity on Neon-Like Argon, and Krypton Line Intensity Ratios in Static, and Cylindrically Imploding High-Density Plasmas", Jpn. J. Appl. Phys., **41**, 5392-5398 (2002).

14) P. B. Holden and G. J. Pert, " Long-Wavelength, Prepulsed Driving as a Means to Greatly Increase the Gain in Low-Z Ne-like XUV Lasers ", J. Phys. B: At. Mol. Opt. Phys., **29**, 2151-2157 (1996).

15) Dong-Eon Kim, Dae-Soung Kim and Albert L. Osterheld, " Characteristics of Populations and Gains in Neon-Like Argon (ArIX)", J. Appl. Phys., **84**, 5862-5866 (1998).

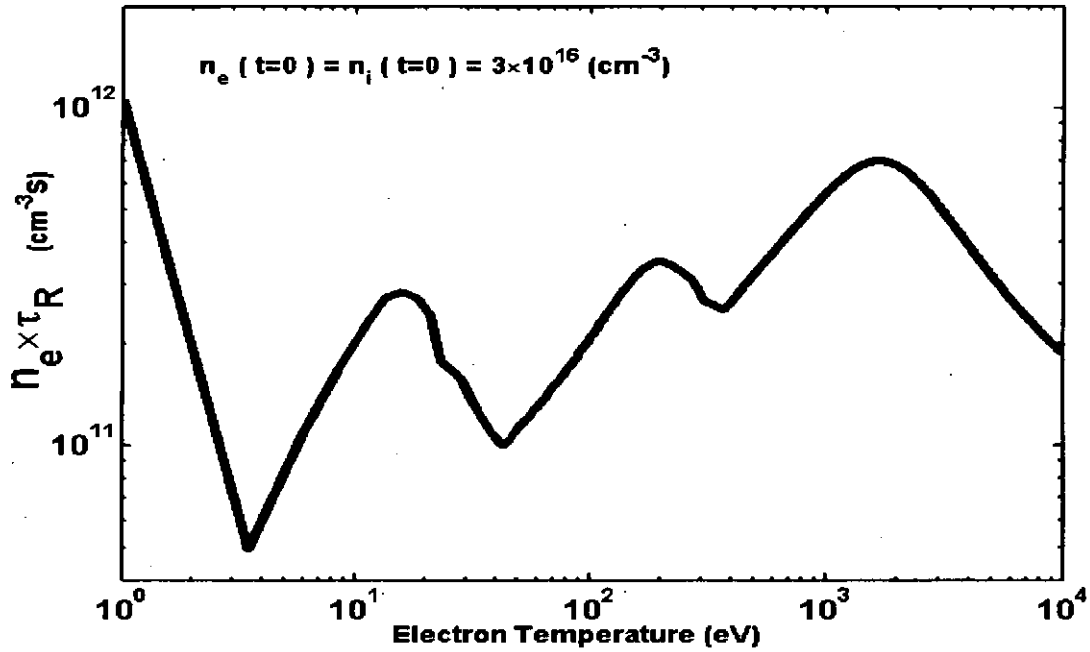

Fig.(1): Diagram of $n_e\tau_R$ value, which τ_R is the relaxation time for argon ions.

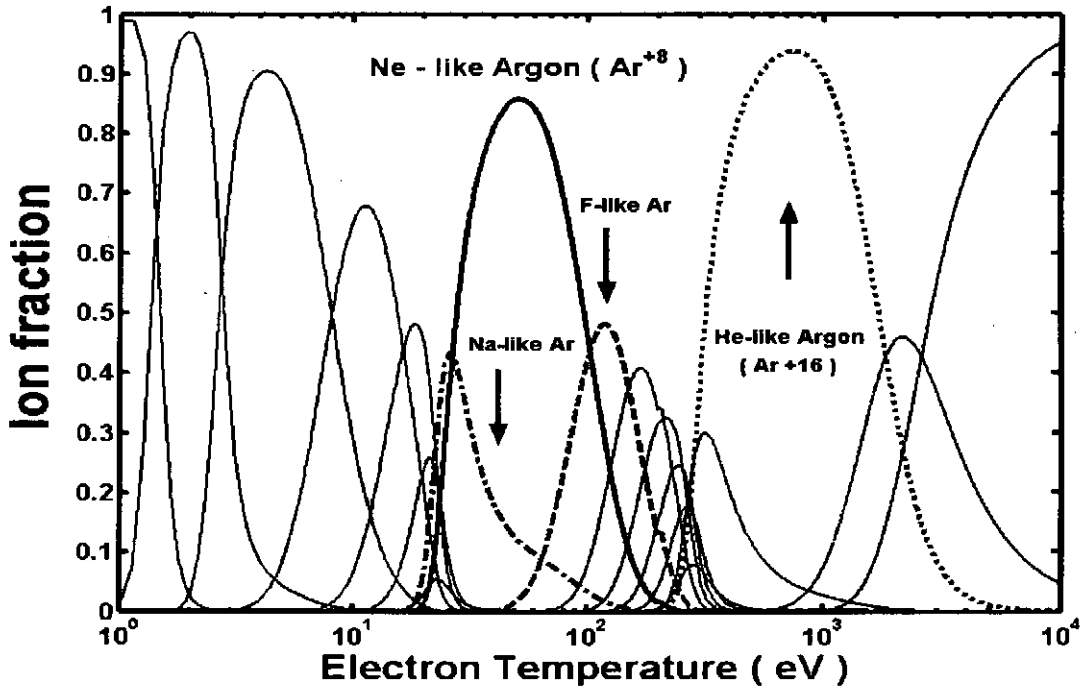

Fig.(2): The argon equilibrium ionization state distributions.

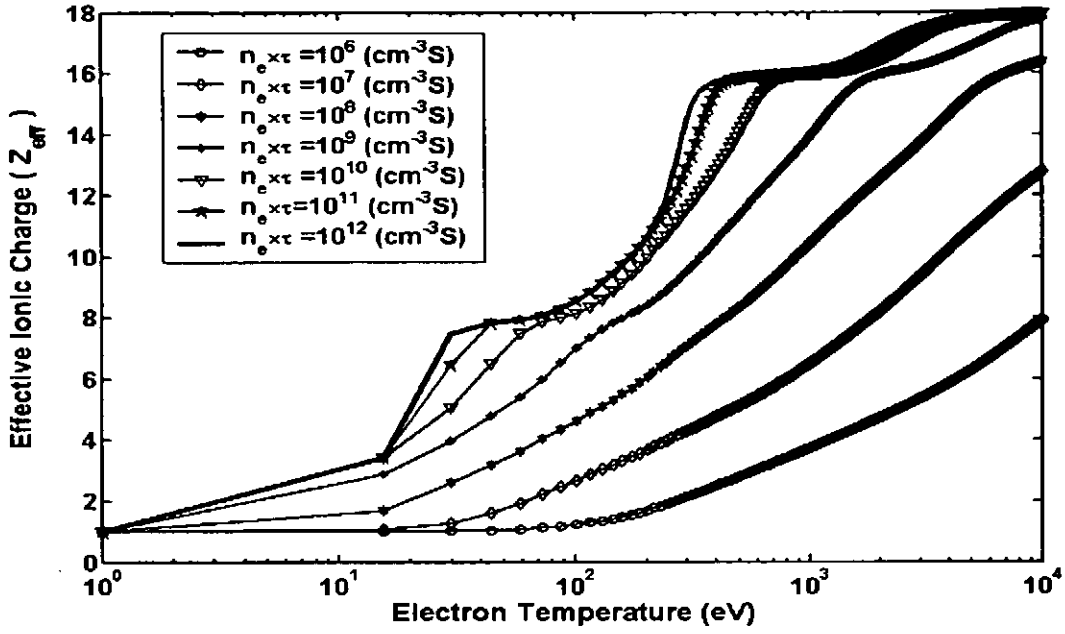

Fig.(3): The argon effective ionic charge for different values of $n_e\tau$, against electron temperature.

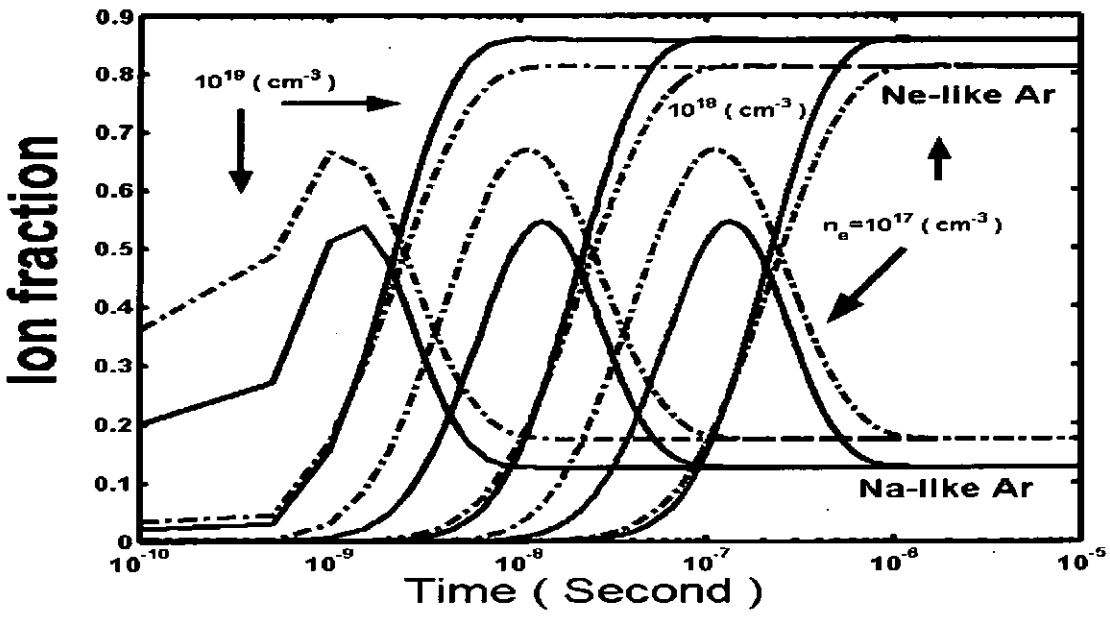

Fig.(4): The Na as well as Ne-like degree of ionizations at three different electron densities, when electron temperature jumps from 1 to 50 eV, versus time; using McWhirter ionization rate coefficients (solid line), and fit formula taken from Ref. (6) (dot-dashed line).

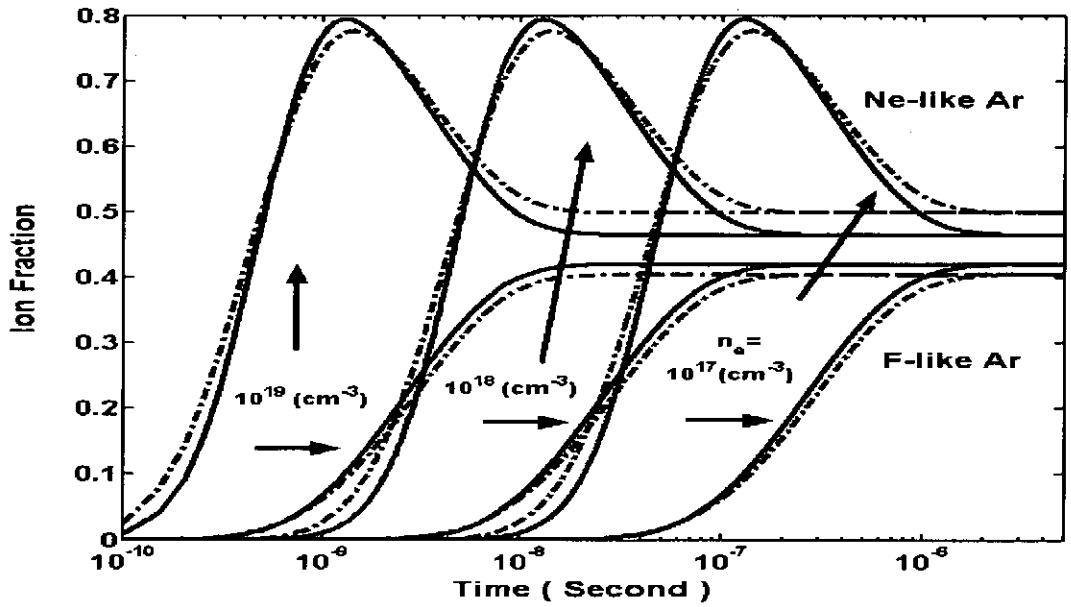

Fig.(5): The Ne as well as F-like degree of ionizations at three different electron densities, when electron temperature jumps from 1 to 100 eV, versus time; using McWhirter ionization rate coefficients (solid line), and fit formula taken from Ref. (6) (dot-dashed line).

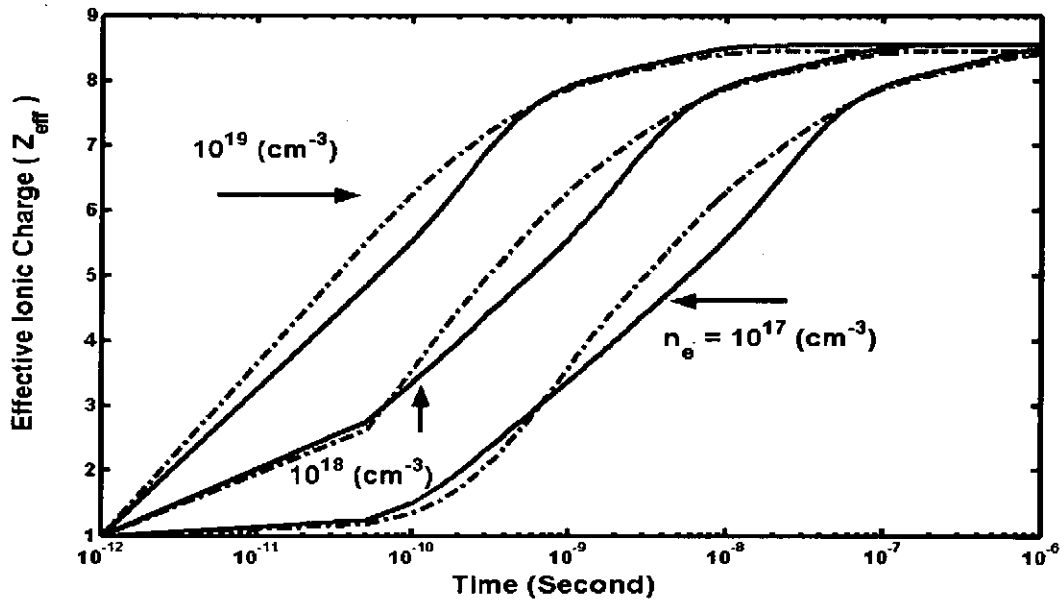

Fig.(6): The argon effective ionic charge for different electron densities against time, when electron temperature jumps from 1 to 100 eV, using McWhirter ionization rate coefficient (solid line), and fit formula taken from Ref. (6) (dot-dashed line).

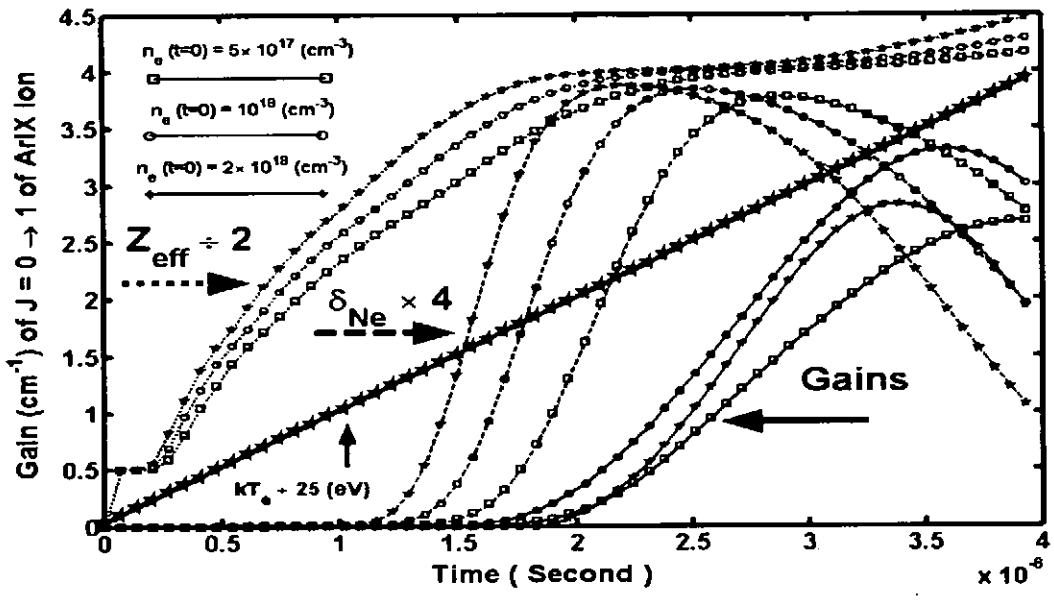

Fig.(7): Time evolution of Ne-like degree of ionization, effective ionic charge and gain coefficients of ArIX ion, for different electron densities and a linear ramp of electron temperature against time.

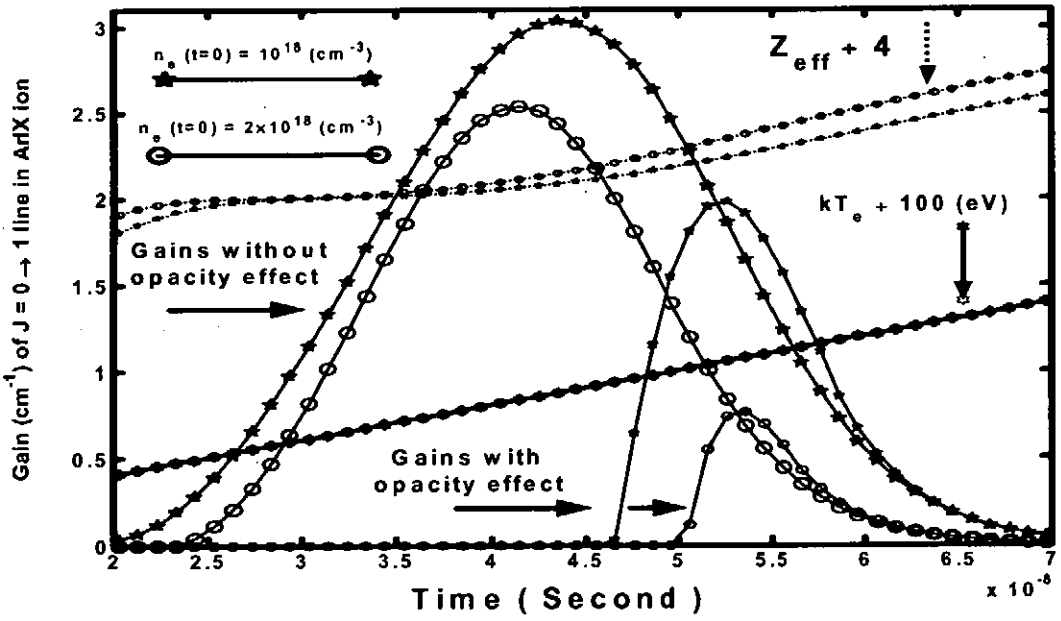

Fig.(8): Time evolution of effective ionic charge, gains with (for static plasma at radius of 0.01 cm using Zemansky escape probability) and without opacity effect for different electron densities and a linear ramp of electron temperature against time.

PLASMA CONFINEMENT WITH MELT-PROCESSED SUPERCONDUCTING BULK MAGNETS

H. Matsuzawa, K. Ohishi, K. Ishikawa, and T. Morita
Faculty of Engineering, University of Yamanashi, Kofu 400-8511, Japan

M. Yoshikawa
IMRA Material R&D Co., Ltd., Hachiken-cho, Kariya, Aichi 448-0021, Japan

H. Ikuta
CIRSE, Nagoya University, Nagoya 464-8603, Japan

U. Mizutani
Department of Crystalline Materials Science, Nagoya University, Nagoya 464-8603, Japan

ABSTRACT

This report describes the application of single-domain superconducting bulk magnets as a plasma confinement. A through-hole of 11.8 mm diameter was drilled at the center of a Sm123 bulk superconductor of 39 mm diameter and 17 mm thickness. After its field-cooling at 77 K in a 2 T field, the resulting bulk magnet trapped a magnetic field of ~0.5 T of a type similar to a magnetic mirror in the bore of the hole, and was applied to a neon plasma column. The plasma was generated in a glass tube of 10 mm outer diameter at 2 Torr and 1 mA dc discharge current. The tube was inserted through the hole, and this combination was kept in liquid nitrogen. Spatial distribution of red fluorescence of the plasma, within the tube, confirmed that the magnet confined the plasma. These results would provide a clue to applications of compact, superconducting bulk magnets of strong magnetic field.

I. Introduction

Since the discovery of the high-temperature cuprate superconductor, melt-processed bulk superconductors of single domain have actively been developed in pinning higher magnetic fields[1-7] and in enlarging sample diameters.[8, 9] Because the maximum trapped fields increase with the diameters[10] and with lowering temperatures, it is difficult to directly compare different materiales. Regardless of these characteristics, the highest trapped fields are 2.1 T for Sm123 (Refs. 1-3) and 2.6 T for Gd123 (Ref. 4) both at 77 K, and 13.3 T at 33 K for Y123 (Ref. 7). These samples were mostly cracked at the highest fields by the tensile stress due to the trapped fields. The largest samples are an Y123 disk[8] of 150 mm diameter

and a (Sm-Gd)123 trapezoidal plate[9] with a 120 mm base and 105 mm height. Melt-processed samples are able to bear ~50 — 100 times higher current densities than conventional copper wires. Therefore, the bulk magnets provide efficient devices in which the high magnetic fields required are generated in highly reduced spaces.

In contrast to the remarkable development of the magnets, their main applications thus far reported are limited as follows: noncontact bearings[11, 12] and their applications, superconducting motors,[13] Maglev trains,[14] fault current limiters,[15] magnetic separation,[16] and a magnetron sputtering film deposition apparatus.[17] In this letter, we report another application of the magnets: the magnetic confinement of dc plasma using a Sm123 bulk magnet. As a container of pulsed discharge plasma, we have already used[18, 19] Bi2223 sintered tubes (supertrons[20]).

Previously,[21] a Sm123 bulk sample was axially magnetized after a through-hole was drilled at the center. The magnetic fields that were trapped in the bore diverged with being more apart from the bulk magnet. In other words, the field lines were closest together in the bore, and formed a constricted throat of the fields. A configuration of fields of this type, a magnetic mirror, is one of the fundamental field types[22] used for plasma confinement. We show, in this report, that a Sm123 magnet with a through-hole confines a plasma as a magnetic mirror of small size but of strong field.

II. Experimental setup

Figure 1 shows the Sm123 bulk sample used. The sample had a 39 mm diameter and a 17 mm thickness with a through-hole of 11.8 mm bore diameter. Figure 2 illustrates the experimental setup. The magnetic field lines are drawn schematically as broken lines through the bore. The sample was magnetized at 77 K by applying a 2 T dc field. A glass tube for electric discharge, with an outer and inner diameter of 10 and 8 mm, respectively, was inserted through the hole. The tube and magnet were both submerged in liquid nitrogen. Neon plasma was ignited inside the tube at 2 Torr and 1 mA dc discharge current. The distribution of red, neon fluorescence longer than ~630 nm in wavelength was detected within the tube by using an imaging optical guide. The guide consisted of 12,000 elementary fibers with a total diameter of 1 mm and a viewing angle of ~95° . Neon gas

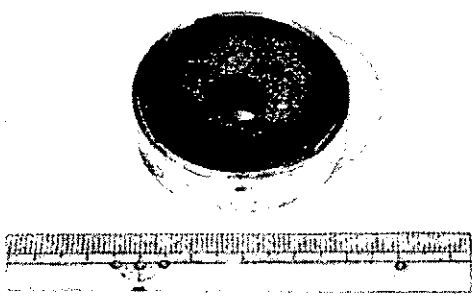

Fig. 1. Sm123 bulk sample used as a permanent magnet.

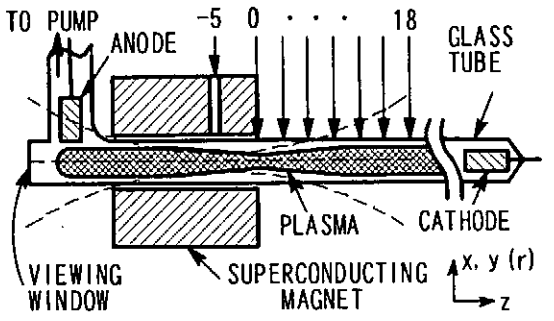

Fig. 2. Experimental setup. The broken lines schematically indicate the magnetic field lines.

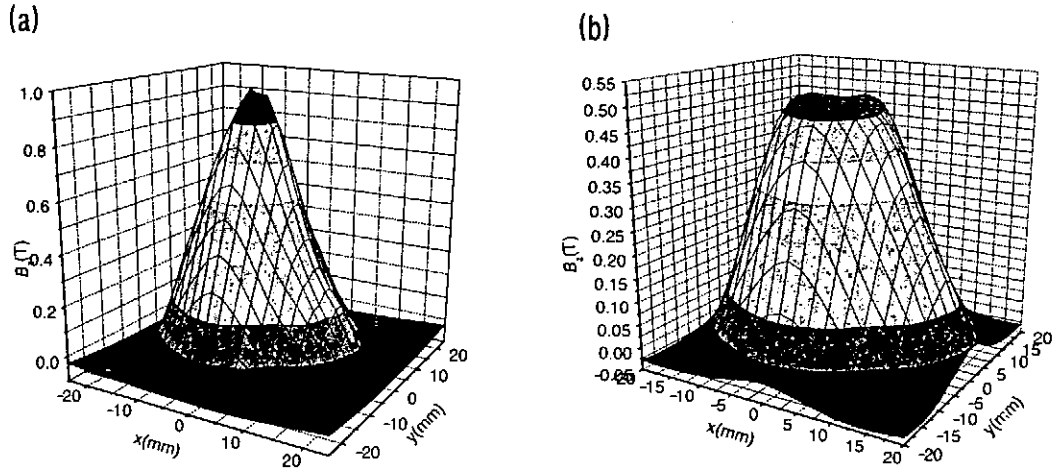

Fig. 3. Profiles of trapped magnetic fields of the Sm123 bulk magnet 1.1 mm above the surface after it had been field-cooled at 77 K in (a) a 3 T field before drilling the through -hole and in (b) a 2 T after drilling the hole.

was chosen because it has the lowest thermal conductivity among the gases that do not liquefy at liquid nitrogen temperature.

Figure 3 plots the trapped fields when the sample was field-cooled to 77 K in (a) a 3 T field before the hole drilling and in (b) a 2 T field after the drilling, being detected with a Hall sensor 1.1 mm above the sample surface. We performed the following experiments using the magnet with a remaining maximum field strength of ~0.5 T as it is shown in Fig. 3(b). Some flux creep might have occurred in the magnet during the course of the experiments, but we did not measure it.

Figure 4 shows the axial dependence of the fields trapped in the axial z direction in the bore and outside the magnet. The shaded area at the bottom indicates the axial position of the magnet. The right-end surface of the magnet was set at $z = 0$ mm. The field had a peak at $z = -5$ mm in the bore, not at the center ($z = -8.5$ mm). This asymmetric trapping arose from the fact that the sample domain was grown from the right-end surface. For $z > -5$ mm, the field decreased monotonically with z, indicating that the fields diverged with z and formed a magnetic mirror.

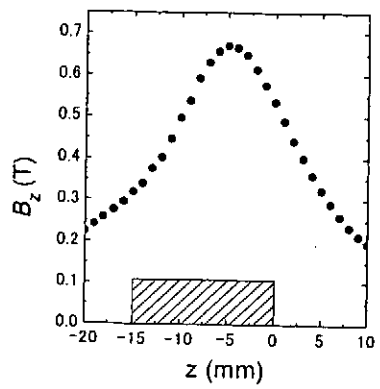

Fig. 4. Axial evolution of the z component of the trapped field for the field-cooled sample at 77 K in 2 T. The shaded area indicates the axial position of the magnet. The highest field was trapped at $z = -5$ mm in the bore.

III. Experimental results

The two-dimensional, radial and axial intensity distribution of the red fluorescence in the tube was obtained from photographs taken through the optical guide, using a CCD camera combined with a red glass filter. Figure 5 depicts the recorded signal as a function of both the radial r and axial z position for (a) a non-magnetized and (b) magnetized plasma. The red fluorescence is emitted from neutral neon atoms. Therefore, Fig. 5 represents the distribution of excited neutral atoms, and of weakly ionized plasma as well. The profiles at the throat ($z = -5$ mm) were obtained with the optical guide inserted in the radial direction of the sample through a hole of 1.5 mm diameter. The radial profiles in Fig. 5(a) are almost independent of the axial positions. In Fig. 5(b), except for the throat profile, both the peak values and full-widths at half-maximum (FWHM) of the profiles increased with z. The FWHMs are indicated with dotted lines in the respective profiles. For $z \geqq \sim 15$ mm, the profiles changed no more, probably because the tube wall prevented the plasma from following the magnetic fields.

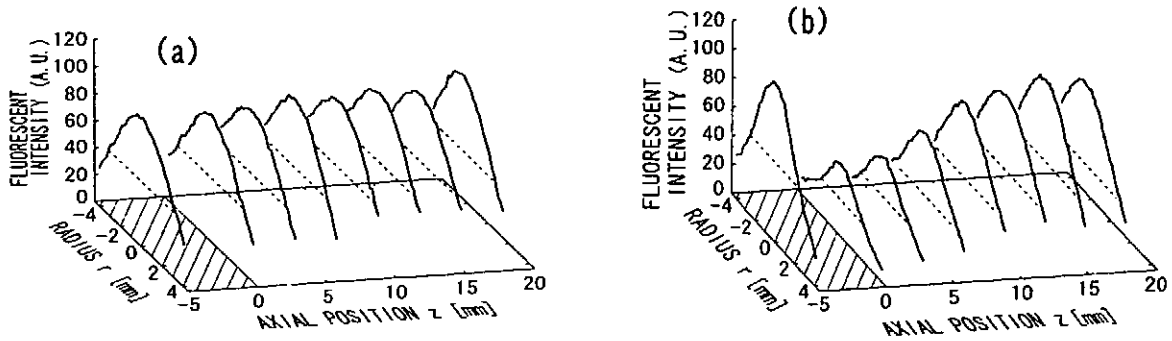

Fig. 5. Distributions of red, neon fluorescence as a function of the radial position r and axial position z for 2 Torr Ne and 1 mA dc discharge current for (a) the non-magnetized and (b) magnetized bulk magnet.

In Fig. 5(b), the throat profile is almost the highest in peak among the profiles, and the FWHM is wider than those at $z = 0$ to 3 mm. If the plasma had behaved as in ideal magnetic mirrors, the throat profile would have had the lowest peak and narrowest FWHM. This notable discrepancy is explained as follows: In most magnetic-mirror devices, plasma is generated in between the mirrors. In these cases, no electric currents flow through the throat. Contrary, in the present experiments, one of the electrodes, the anode, was placed outside the mirror. Accordingly, the electrons contributing to discharge currents were not reflected from near the throat, but were forced to propagate through the throat. At the throat, the electron currents were squeezed by the strong fields. Therefore, the electrons ionized and excited neon atoms repeatedly via collisions in the passage through the throat. The plasma thus generated expanded in the radial direction, and consequently had a large FWHM. At the wall $r = \pm 4$ mm, the fluorescence was observed to have nonzero intensity, contradicting a theoretical model[22] of positive columns, presumably because of the lens effect of the wall. The profiles in Fig. 5 are, thus, explained by the effect of the magnetic mirror, and

demonstrate that the magnet confined the plasma.

Figure 6 presents photographs of the red plasma column for (a) a non-magnetized and (b) magnetized plasma, respectively, visually showing the plasma confinement. The dark areas on the left end correspond to the magnet. The dark gray spots are ice pieces attached on to the tube wall. In Fig. 6(b), although a constant current of 1 mA flowed through the entire tube, the plasma column was dark near the magnet and was very bright in the region apart from the magnet. The long tail of the column in Fig. 6(b), gradually decreasing in luminosity toward the magnet, was caused by the discharge currents flowing through the throat, as mentioned above. If the plasma were generated in between two mirrors, then the tail would have a shorter, clearly defined profile resulting from more effective confinement of the plasma.

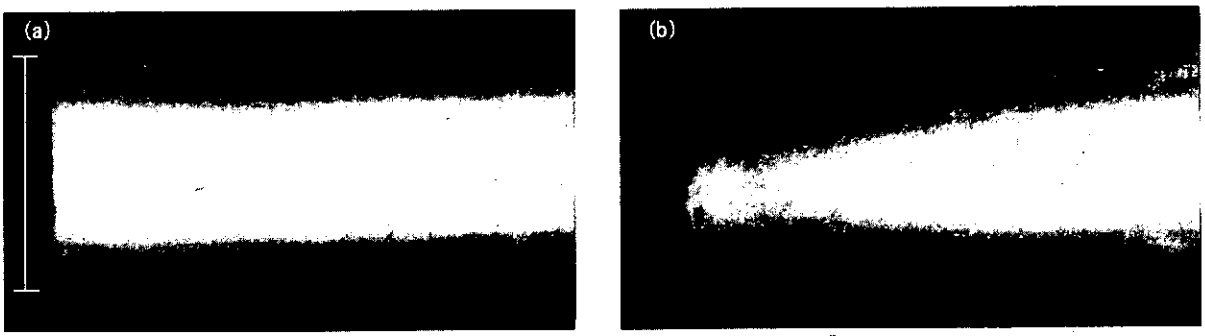

Fig. 6. Photographs of (a) the non-magnetized and (b) magnetized plasma column. The dark areas on the left end indicate the bulk magnet. The vertical line indicates the tube diameter of 10 mm.

IV. Conclusions

In summary, the Sm123 bulk magnet with a through-hole functioned as a magnetic mirror. Such bulk magnets have several merits. Despite the generation of high magnetic fields, the magnets occupy much smaller spaces than conventional solenoidal coils. Furthermore, when bulk samples are magnetized with pulse field magnetization (PFM) or IMRA,[23] the system configuration is much more simple than that with the coils. A drawback of magnets of the present type is that their central part, in which the maximum field is trapped, is removed. In this letter, a Sm123 bulk magnet was applied to only a dc plasma. We think, however, that the scheme would be applicable to pulsed and radio frequency (rf) discharge plasmas and that a variety of configurations of the magnetic fields and hence their applications can be realized when two or more magnets are combined.

References

1) H. Ikuta, A. Mase, Y. Yanagi, M. Yoshikawa, Y. Itoh, T. Oka, and U. Mizutani, Supercond. Sci. Technol., **11**, 1345 (1998).

2) U. Mizutani, A. Mase, H. Ikuta, Y. Yanagi, M. Yoshikawa, Y. Itoh, and T. Oka, Mater. Sci. Eng., **B65**, 66 (1999).

3) H. Ikuta, A. Mase, U. Mizutani, Y. Yanagi, M. Yoshikawa, Y. Itoh, and T. Oka, IEEE Trans. Appl. Supercond., **9**, 2219 (1999).
4) S. Nariki, N. Sakai, and M. Murakami, Supercond. Sci. Technol., **15**, 648 (2002).
4) S. Gruss, G. Fuchs, G. Krabbes, P. Verges, G. Stöver, K. -H. Müller, J. Fink, and L. Schulz, Appl. Phys. Lett., **79**, 3131 (2001).
6) M. Muralidhar, S. Nariki, M. Jirsa, Y. Wu, and M. Murakami, Appl. Phys. Lett., **80**, 1016 (2002).
7) R. Gonzalez-Arrabal, M. Eisterer, H. W. Weber, G. Fuchs, P. Verges, and G. Krabbes, Appl. Phys. Lett., **81**, 868 (2002).
8) Chubu Electric Power Co., Inc. (Nagoya) and Dowa Mining Co., Ltd. (Tokyo), in *Business & Technology Daily News* (Oct. 6, 1998) in Japanese.
9) Chubu Electric Power Co., Inc. (Nagoya) and Dowa Mining Co., Ltd. (Tokyo), in *Business & Technology Daily News* (June 18, 2002) in Japanese.
10) For example, C. P. Poole, Jr., H. A. Farach, and R. J. Creswick, *Superconductivity* (Academic, San Diego, 1995), Chap. 12.
11) F. C. Moon, *Superconducting Levitation* (Wiley, New York, 1994).
12) J. R. Hull, Supercond. Sci. Technol., **13**, R1 (2000).
13) Y. Itoh, Y. Yanagi, M. Yoshikawa, T. Oka, S. Harada, T. Sakakibara, Y. Yamada, and U. Mizutani, Jpn. J. Appl. Phys., **34**, 5574 (1995).
14) H. Kamijo, K. Nemoto, and H. Fujimoto, in *Advances in Superconductivity IX*, edited by S. Nakajima and M. Murakami (Springer, Tokyo, 1997), pp. 1473-1476.
15) L. Porcar, D. Bourgault, J. M. Barbut, M. Barrault, P. Germi, and R. Tournier, Physica C, **275**, 293 (1997).
16) N. Nishijima, N. Saho, K. Asano, H. Hayashi, K. Tsutsumi, and M. Murakami, IEEE Trans. Appl. Supercond., to be published.
17) U. Mizutani, T. Matsuda, Y. Yanagi, Y. Itoh, H. Ikuta, and T. Oka, J. Am. Ceram. Soc., to be published as an article from 104th Annual Meeting of the American Ceramic Society held in St. Louis, Missouri, in April 2002.
18) Y. Mizutani, J. Ishikawa, and H. Matsuzawa, in *Advances in Superconductivity VIII*, edited by H. Hayakawa and Y. Enomoto (Springer, Tokyo, 1996), pp. 1229-1232.
19) T. Yamauchi, H. Matsuzawa, K. Mikami, and J. Ishikawa, Jpn. J. Appl. Phys., **41**, 5799 (2002).
20) For a review of supertrons, see H. Matsuzawa, J. Appl. Phys., **74**, R111 (1993) [Erratum: **76**, 624 (1994)].
21) U. Mizutani, A. Mase, K. Tazoe, H. Ikuta,. T. Oka, Y. Itoh, Y. Yanagi, and M. Yoshikawa, Physica C, **335**, 92 (2000).
22) For example, F. F. Chen, *Introduction to Plasma Physics and Controlled Fusion*, 2nd ed. (Plenum, New York, 1984).
23) H. Ikuta, H. Ishihara, Y. Yanagi, Y. Itoh, and U. Mizutani, Supercond. Sci. Technol.,**15**, 606 (2002).

EVOLUTION AND LASING CONDITIONS OF FAST PINCH PLASMAS

N.Sakamoto, M.Nakajima, M.Masnavi, G.Niimi, Y.Hayashi, E.Hotta and K.Horioka

Department of Energy Sciences, Tokyo Institute of Technology, Nagatsuta 4259, Midori-ku Yokohama, Japan, 226-8502

ABSTRACT

In order to discuss the potentiality of fast capillary discharge plasma as a source of coherent X-ray, numerical investigation is made using a one-dimensional MHD simulation code. The principal parameters for the calculations are the initial gas pressure and rising rate of the load current, in the range where we have observed lasing signals experimentally. Based on the comparison between the calculated results and the experimental observation, the correlations of the Z-pinch dynamics with the process to lead the appropriate plasma parameters for lasing are discussed.

1. Introduction

With the progress of the recent technology that handles the nanometer order areas, to obtain shorter wavelength lasers with sufficient available energy and reasonable construction cost is quite meaningful for various fields like fundamental sciences, material processings, medical treatments and so on.

Since 1994, when J.J.Rocca *et al.* succeeded to get a lasing at 3p-3s transition (~469Å) of Ne-like Ar [1], the lasing by fast capillary discharges has been paid attention because Z-discharges have possibility to accomplish practical lasing sources for soft x-ray regions compared with high-power laser systems, mainly from the view point of energy efficiency and the size of devices.

The fast capillary Z-discharges utilize electron-collisional excitation scheme. Therefore, the electron temperature and electron density of plasma have to be increased up to appropriate values. Capillary Z-discharges achieve the lasing conditions by fast pinching effects. The fast compression process inevitably accompanies the energy dissipation. That is to say, the faster compression process makes the hotter and lower density plasmas. Moreover, the interaction between the shock wave and the current sheet makes an inner structure with temperature, density and velocity distribution, in the plasma column.[2] All of these parameters affect the gain distribution, refraction of stimulated emission and opacity of the resonance levels.[3] Consequently, for the realization of larger energy and shorter wavelength lasers with capillary discharges, it is very important to understand the pinching process of discharge plasmas in detail.

We have experimentally investigated the lasing conditions of Ne-like Ar, as a function of initial Ar gas pressure in the capillary; P_0, and the rising rate of driving current; dI/dt. For the discharge conditions that we could get lasing signals, we have estimated the time intervals between the shock wave; t_s and current sheet arrival times; t_p to the axis. The time evolution of the pinching process is illustrated on N_i(ion number density)-Te(electron density) diagrams using a one-dimensional MHD simulation code

called "Multi-Z". By comparing the experimental results with the calculated plasma parameters, we discuss the correlation between the plasma dynamics and the lasing conditions in fast capillary discharge plasmas.

2. Experimental set-up and results

2.1 Experimental apparatus

2.1.1 Discharge devices

We used two types of pulse-power devices for the experiments. One device called "LIMAY" is composed of a Marx generator, a pulse forming line and a transmission line.[2] The maximum output voltage is 600 kV and the characteristic impedance is 3 Ω, hence it can drive a maximum peak current of 200 kA. Another device has a step-up transformer type pulse generator and it can produce sinusoidal waveform with maximum current of 50 kA. [4,5]

2.1.2. Capillary load section and diagnostic devices

One of the structures of a capillary load part is shown in Fig.1. The capillary is made of alumina ceramic with the bore diameter of 3 mm, and the maximum capillary length is 200 mm. We can change the capillary length by inserting a molybdenum rod into the capillary. The parameter ranges we have investigated are the initial Ar gas pressure of 100~1000 mTorr and dI/dt of 10^{11}~10^{12} A/s. We detected the lasing signals by a X-ray diode (XRD) and the current values by a Rogowski coil or a pickup coil. Dividing the current value at lasing by the lasing time; t_l, we calculated the current rising rate; dI/dt. Here, we define the lasing time t_l as the interval between current starting time and the time when the lasing appears.

2.2. Experimental results

We obtained lasing signals by adjusting the conditions of capillary discharges. Fig.2 is a typical lasing waveform that we got in our experiments. The spike-like waveform in Fig.2 indicates the XRD signal of the lasing. In this figure, "current" means the load current in the capillary. We made sure that the spike-like XRD signals showed lasing by the examination of the directivity and gain of the spike-like waveform.[6,7]

We have investigated the lasing time defined above and the peak values of the spike-like XRD lasing signals as a function of P_0 and dI/dt.[8] Fig.3(A) shows the lasing time t_l as a function of P_0 with dI/dt as a parameter. On the other hand, Fig.3(B) shows t_l versus dI/dt. Fig.3 indicates that the t_l increases with the increase of P_0, and the decrease of dI/dt. Fig.4 shows the peak values of spike-like XRD signals as a function of P_0 and dI/dt. As shown in the figures, there appears the distributions that had optimum conditions of P_0 and dI/dt for lasing.

3. Comparison between the experimental and calculated results

3.1 One-dimensional MHD simulation code "Multi-Z"

To discuss the correlation between the plasma dynamics and the lasing conditions in fast capillary discharge plasmas, we estimated t_s, t_p using a one-dimensional MHD

simulation code and drew the compression process on Ni-Te diagrams. The code named "Multi-Z" was developed for Z-pinch based on MULTI7 code.[9,10] To solve the MHD equations, a finite difference method is used, and Lagrangian scheme is adopted for the hydrodynamics. Also, to make calculations faster, tabulated data of the equation of state, the charge state of the plasma ions and the radiation opacities from the SESAME library[11] are used.

3.2. Discussion

3.2.1 Relation between t_i and t_s, t_p

As mentioned above, for the realization of larger energy and shorter wavelength lasers with capillary discharges, it is essential to understand the pinch process of discharge plasmas in detail. Especially to know the evolution of Ni and Te in the pinch plasmas has crucial meaning. Fig.5 shows a schematic of the Ni-Te diagrams of the expected compression processes in the capillary discharge plasmas with fixed P_0 and dI/dt. To compare these expected compression processes with those based on the calculated Ni-Te data, it is necessary to get information of t_i, t_s and t_p. Fig.6 shows the relationship between t_i that was observed experimentally and t_s, t_p that was obtained by the numerical calculations. These graphs are based on the experimental data indicated in Fig.3. As shown in Fig.6, the lasing mostly occurs between t_s and t_p, or just before t_s in the case of our experimental range.

3.2.2. Calculated Ni-Te diagrams

Fig.7,8,9 show the calculated Ni-Te diagrams on the axis of the capillary. On each graphs, the solid line shows the Ni-Te history on the conditions that was optimum for lasing on the fixed condition. The broken and small dotted lines correspond to the pinching history on the threshold conditions we could get lasing signals. The shaded areas indicate the expected lasing parameters for Ne-like Ar [12] that is the same with the lasing parameter showed in Fig.5.

Fig.7 indicates the typical relationship between the plasma parameters at t_s and t_p with corresponding compression curves on the Ni-Te plane. As shown in Fig.7, the character of the Ni-Te curve changes at t_s due to the effect of the shock wave reflection, and t_p is indicated on the end-points of each curves. Here, t_i exists between t_s and t_p or just before t_s as seen in Fig.6.

Fig.8 and 9 are the Ni-Te diagrams for different values of parameters, P_0 and dI/dt. As shown in these figures, Ni-Te history changes depending on the discharge parameters. That is to say, Fig.8 indicates that when P_0 is low, the core plasma after t_s proceeds to the direction that increases Te values with almost constant Ni values. On the other hand, when P_0 becomes higher, the plasma proceeds to increase both Ni and Te values. Fig.9 shows the Ni-Te curves for different dI/dt. Those figures also indicate the dependence of Ni-Te curves on the discharge conditions; i.e., that Ni don't increase after t_s when P_0 is relatively low, whereas for higher P_0 both Ni and Te values increase after t_s.

Comparing these numerically calculated results with Fig.5, we can see that the gradient of the compression curves in the initial phase is extremely high compared with the adiabatic compression line. This means that the core plasma is abruptly compressed by the converging shock wave driven by the current sheet.[2] The results also show that the compression process and the evolution of plasma parameter after t_s are dominated by the shock wave interaction. These shock wave effects are expected to play dominant roles to achieve the plasma parameters for lasing. We can also see that the all of the calculated Ni-Te traces do not intersect the lasing plasma parameters, then we couldn't

make quantitative discussion with experimental results probably because of inadequate modeling for the shock wave structure. However, the evaluation of pinching history with Ni-Te curves is considered to be helpful to find out the exact way for achievement of lasing at the shorter wave length region and higher energy level.

4. Summary

Comparisons of experimental results with numerical simulations clearly show the importance of pinching dynamics close to the capillary axis for making the lasing condition of capillary lasers. It was also shown that shock wave interaction in the core plasma plays dominant roles to make the lasing condition. More detailed analysis of shock wave structure including the ionization relaxation effect and quantitative discussions of available energy and attainable wavelength are the future works of us.

Acknowledgement

We thank Prof. T.Aoki, Dr. J.Hasegawa and Dr. T.Kikuchi for valuable advice on the "Multi-Z" and the SESAME table.

References

1) J.J.Rocca, V.Shlyaptsev, F.G.Tomasel, O,D,Cortazar, D.Hartshorn and J.L.A.Chilla, Phys. Rev. Lett. **73**, 2192 (1994).
2) T.Hosokai, M.Nakajima, T.Aoki, M.Ogawa and K.Horioka, Jpn. J. Appl. Phys. **36**, 2327 (1997).
3) M.Masnavi, T.Kikuchi, M.Nakajima and K.Horioka, J.Appl. Phys., **92**, 3480(2002).
4) G.Niimi, Y.Hayashi, A.Okino, M.Watanabe and E.Hotta, J. Plasma Fusion Res. **77**, 1239 (2001).
5) G.Niimi, Y.Hayashi, M.Nakajima, M.Watanabe, A.Okino, K.Horioka and E.Hotta, J. Phys. D.: Appl. Phys. **34**, 2123 (2001)
6) N.Sakamoto, G.Niimi, M.Nakajima, E.Hotta and K.Horioka, Res. Rep. Natl. Inst. Fusion Sci. NIFS-PROC-51, 45(2001).
7) G.Niimi, Y.Hayashi, N.Sakamoto, M.Nakajima, A.Okino, M.Watanabe, K.Horioka and E.Hotta, IEEE Trans. Plasma Sci., **30**, No.2, 616(2002).
8) N.Sakamoto, G.Niimi, Y.Hayashi, M.Masnavi, M.Nakajima, E.Hotta and K.Horioka, Dense Z-pinches, Proc. High Power Particle Beams, pp169-172, (2002).
9) R.Ramis, R.Schmalz and J.Meyer-ter-Vehn: Comp. Phys. Comm. **49**, 475(1988).
10) T.Aoki, K.Horioka and M.Ogawa, Res. Rep. Natl. Inst. Fusion Sci. NIFS-PROC-23, 124(1995).
11) http://t1web.lanl.gov/
12) V.N.Shlyaptsev, A.V.Gerusov, A.V.Vinogradov, J.J.Rocca, O.D.Cortazar, F.Tomasel and B.Szapio, SPIE **2012**, Ultrashort Wavelength Lasers II 99(1993).

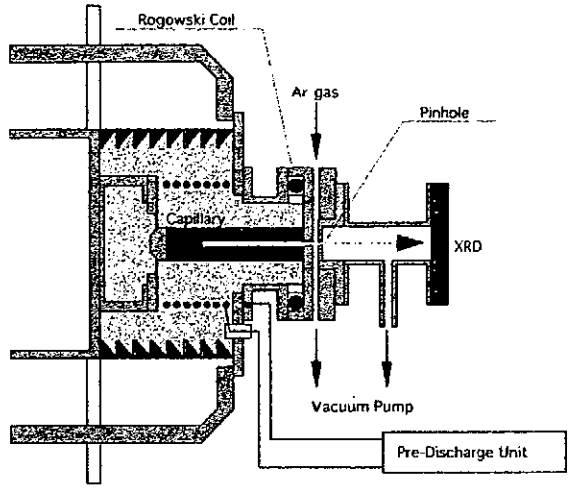

Fig.1 Typical setup of load section for capillary discharge experiments.

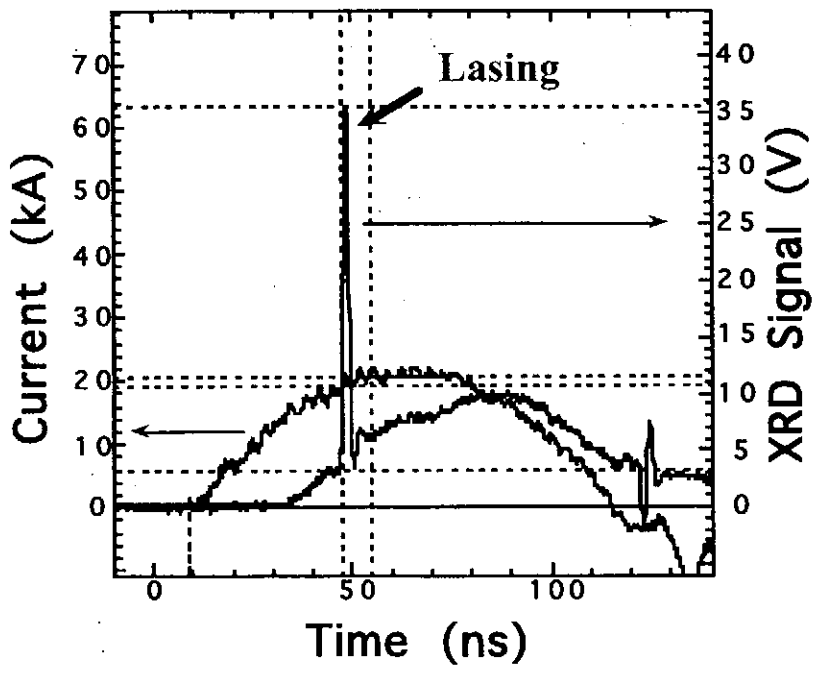

Fig.2 Typical waveforms of load current and XRD signals.

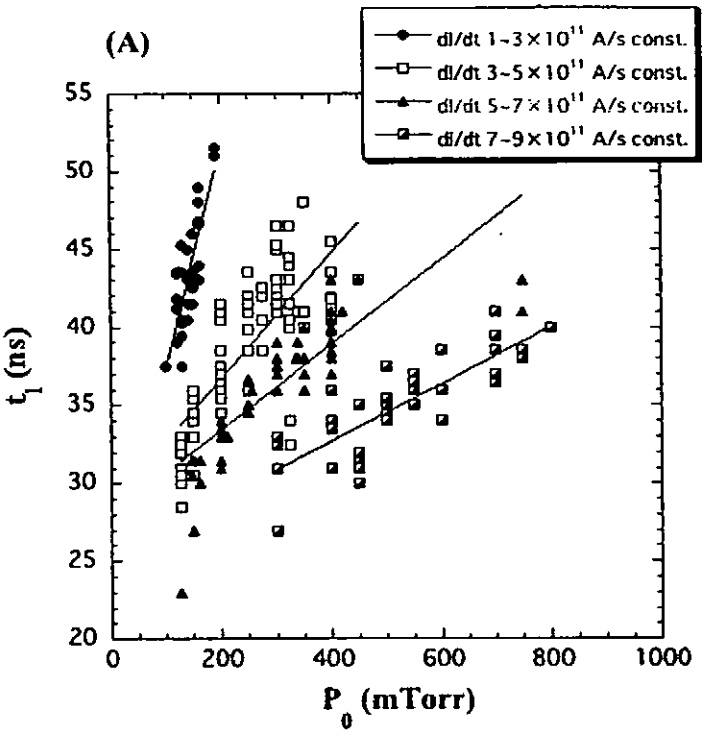

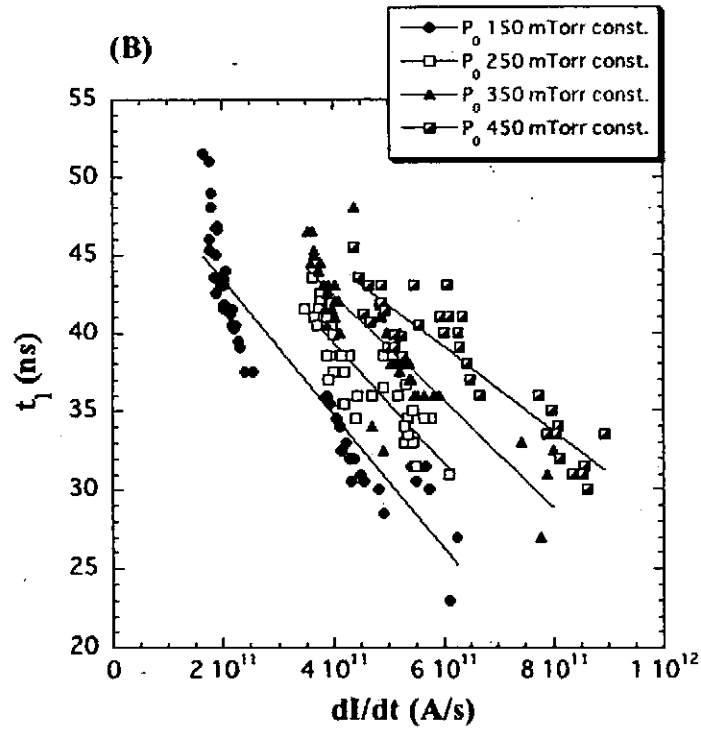

Fig.3 Lasing time t_l as a function of P_0:(A) and dI/dt:(B).

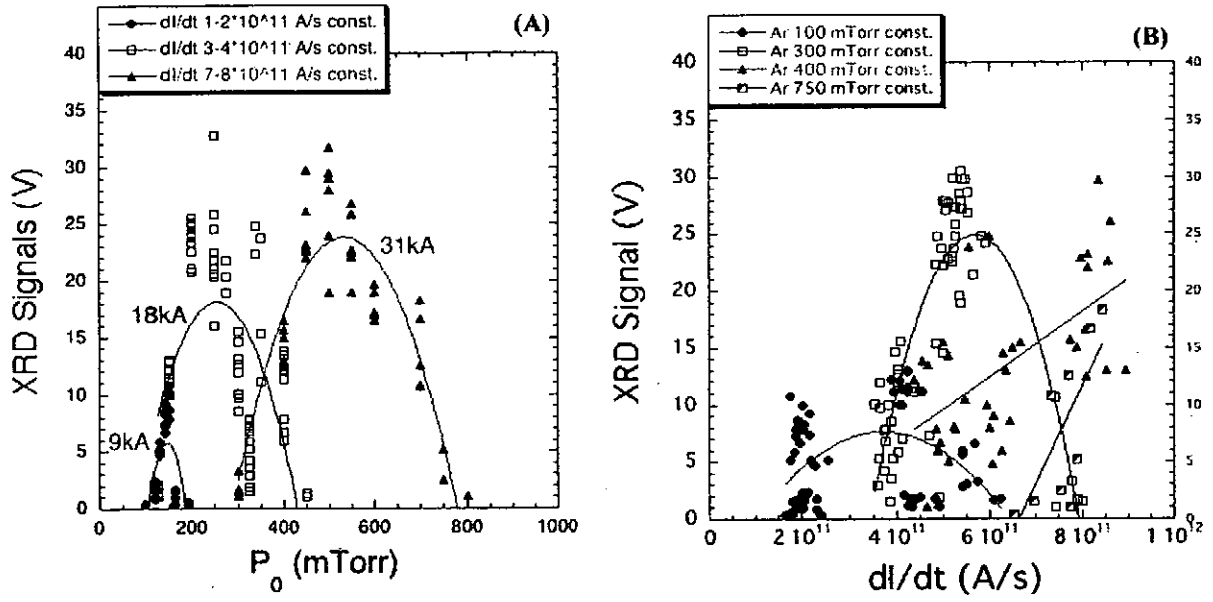

Fig.4 XRD signals as a function of P_0:(A) and dI/dt:(B).

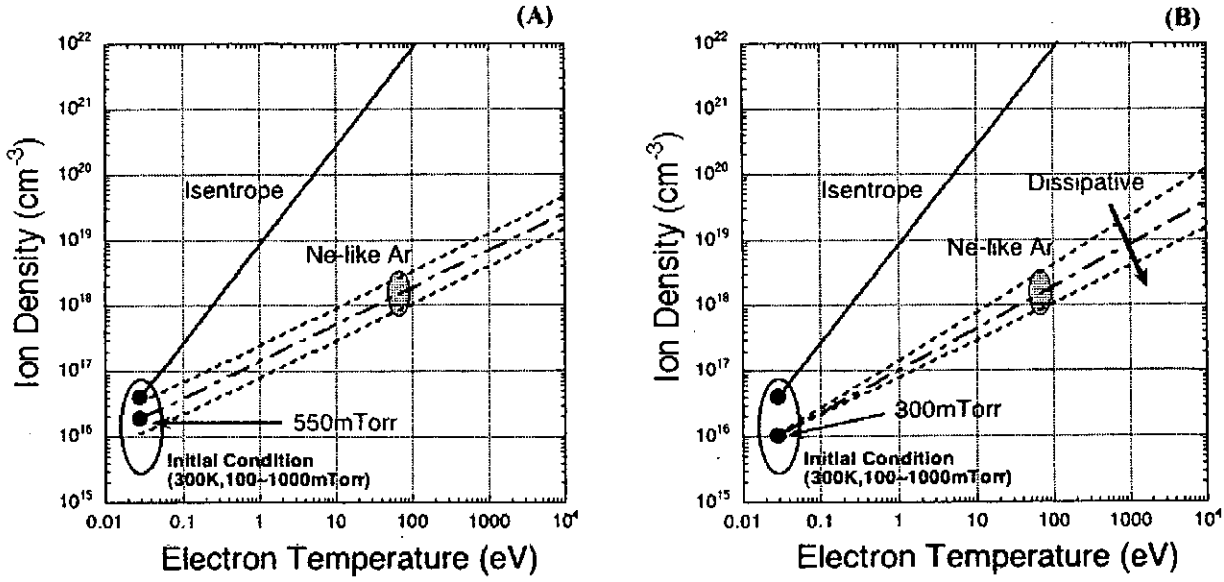

Fig.5 Schematic diagrams of the expected compression processes of capillary discharge for changes of P_0:(A) and dI/dt:(B).

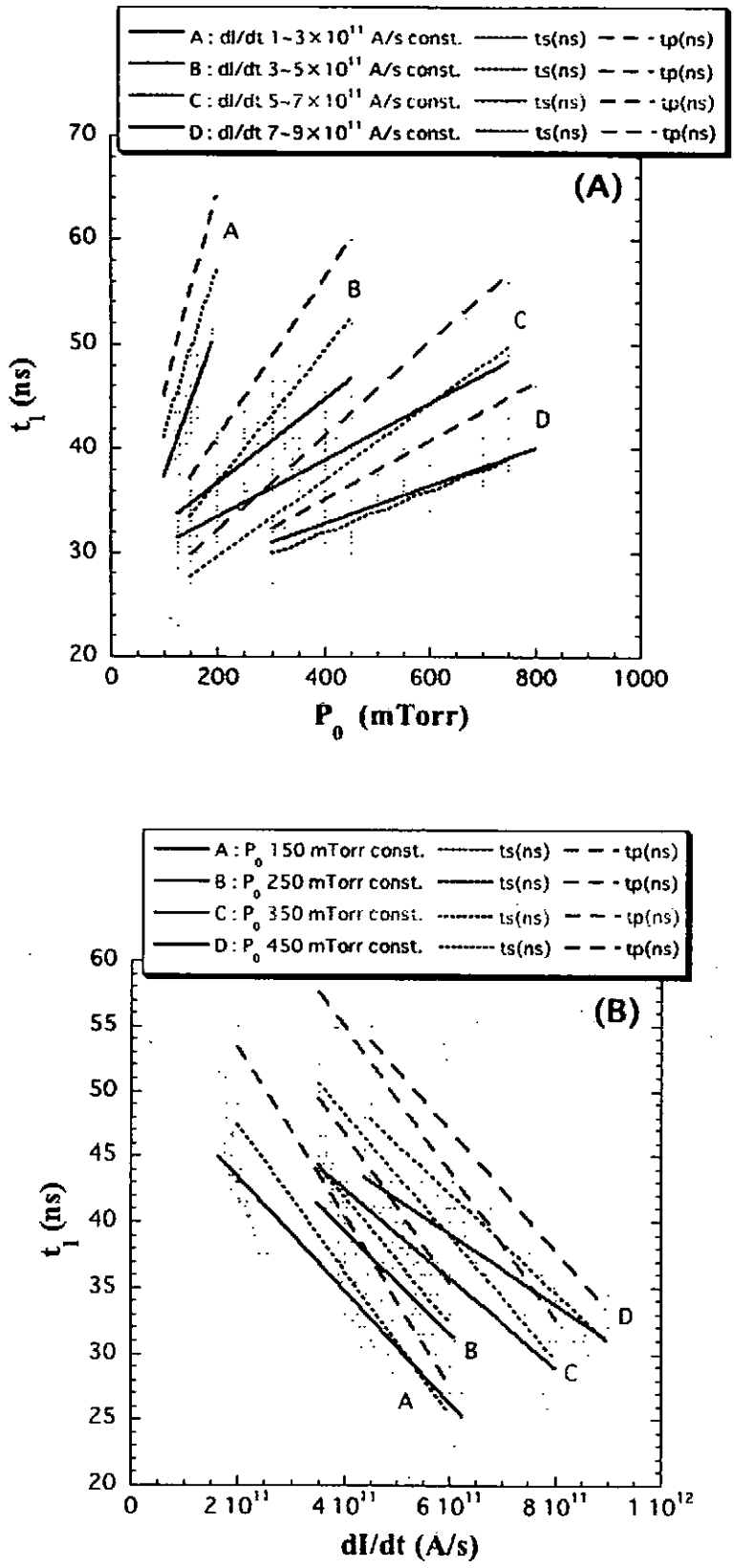

Fig.6 The relationship between Lasing time experimentally measured and t_s, t_p obtained by calculations. These graphs are shown as a function of P_0:(A) and dI/dt:(B).

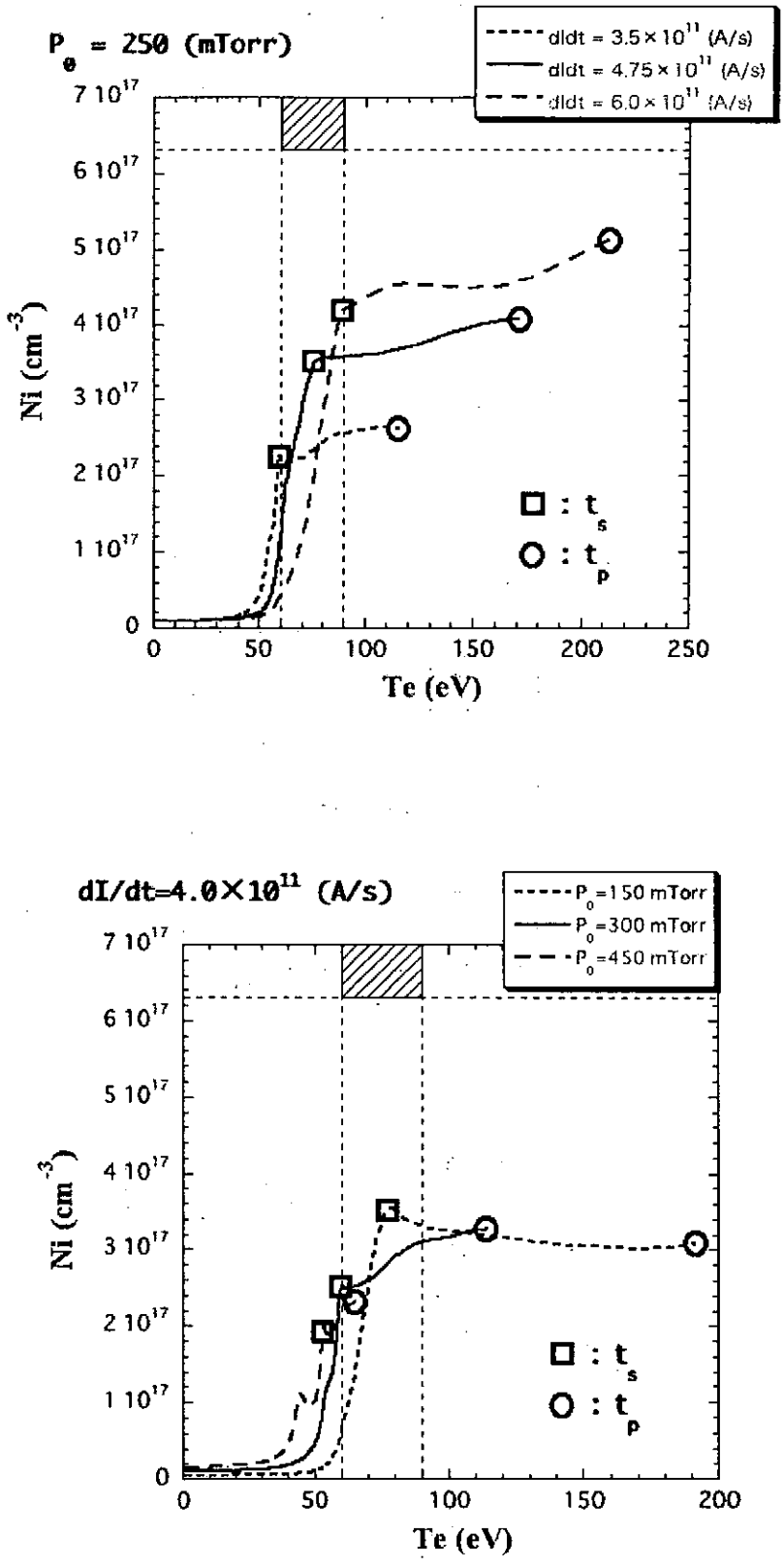

Fig.7 Evolution of plasma parameters (Ni and Te) at capillary axis.

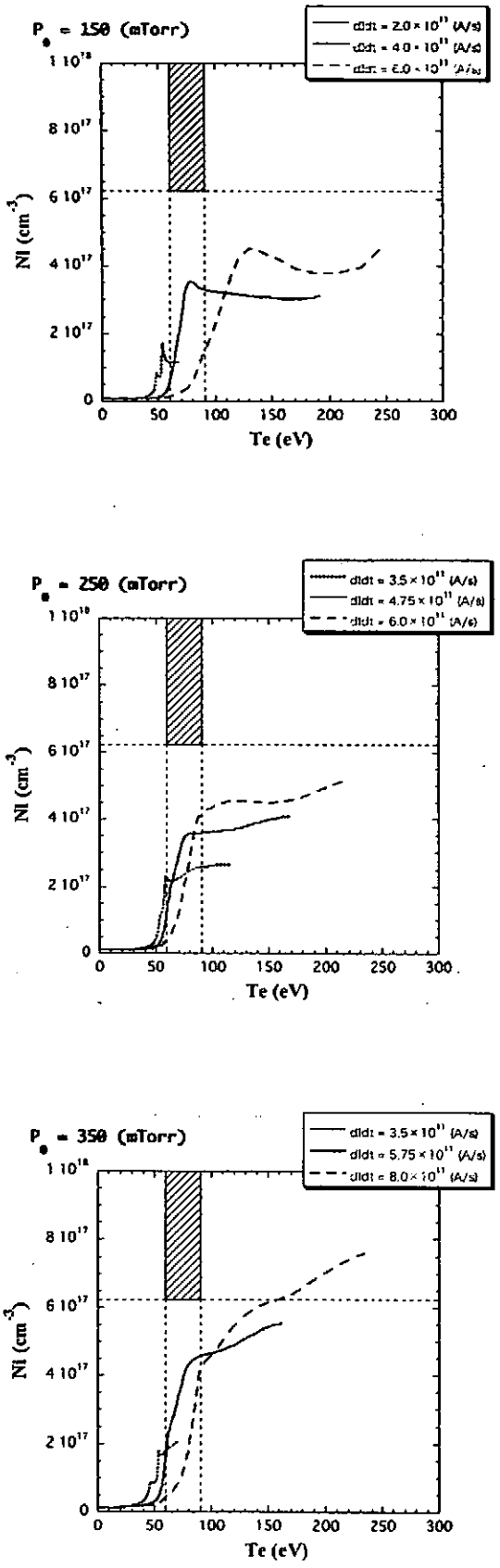

Fig.8 Numerical results of plasma evolutions at capillary axis.

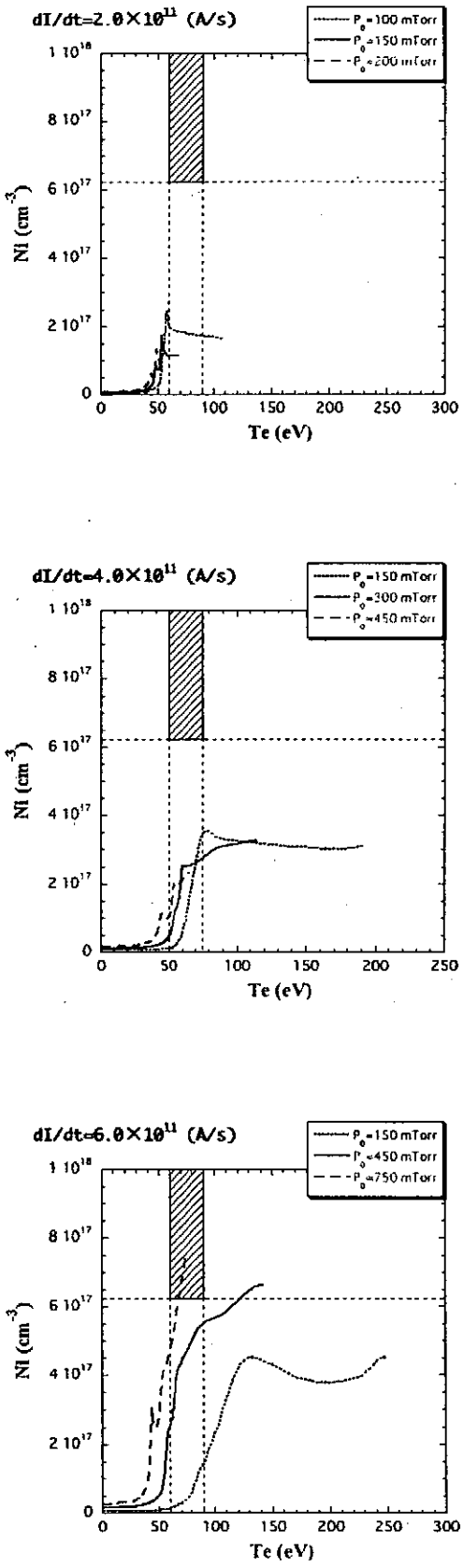

Fig.9 Numerical results of plasma evolutions at capillary axis.

DEVELOPMENT OF BIPOLAR PULSE ACCELERATOR FOR INTENSE PULSED ION BEAM ACCELERATION

Y. Fujioka, C. Mitsui, I. Kitamura, T. Takahashi, K. Masugata, H. Tanoue[a], K. Arai[a]

Faculty of Engineering, Toyama University, 3190, Gofuku, Toyama 930-8555, Japan
[a] National Institute of Advanced Industry Science and Technology, 1-1-1, Umezono, Tukuba 305-8568, Japan

ABSTRACT

To improve the purity of an intense pulsed ion beams a new type of pulsed ion beam accelerator named "bipolar pulse accelerator (BPA)" was proposed. In the accelerator purity of the beam is expected. To confirm the principle of the accelerator experimental system was developed. The system utilizes B_y type magnetically insulated acceleration gap and operated with single polar negative pulse. A coaxial gas puff plasma gun placed in the grounded anode was used as an ion source, and source plasma (nitrogen) of current density ≈ 25 A/cm^2, duration ≈ 1.5 μs was injected into the acceleration gap. The ions are successfully accelerated from the grounded anode to the drift tube by applying negative pulse of voltage 180 kV, duration 60 ns to the drift tube. Pulsed ion beam of current density ≈ 40 A/cm^2, duration ≈ 60 ns was obtained at 42 mm downstream from the anode surface.

I. Introduction

Intense pulsed ion beams (PIB) of carbon, nitrogen or aluminum, have a wide area of applications including nuclear fusion, materials science, etc. PIB can easily be generated in a conventional pulsed power ion diode using flashboard ion source. However, since many kinds of ions are produced in the same time, the purity of the beam is usually very poor. For example, in a point pinch ion diode we found that produced PIB contains protons, multiply ionized carbons, organic ions, etc[1]. Hence an application of the PIB has been limited. To improve the purity a new type of pulsed power beam accelerator named "bipolar pulse accelerator (BPA)" was proposed[2-4]. As the first step of the development of the BPA, an experimental system was constructed to confirm the principle of the acceleration. In the paper the preliminary results of the experiment are described.

II. Bipolar Pulse Accelerator

Figure 1 shows the concept of the bipolar pulse accelerator. A conventional PIB diode is also shown for comparison. As shown in Fig.1 (a), proposed ion accelerator consists of a grounded ion source, a drift tube and a grounded cathode. In the diode, bipolar pulse (V_1) is applied to the drift tube. At first the negative voltage pulse of duration τ_p is applied to the drift tube and ions on the grounded ion source are accelerated toward the drift tube. If τ_p is adjusted to the time of flight delay of the ions to pass the drift tube, the pulse is reversed and the positive voltage of duration τ_p is applied to the drift tube when top of the ion beam reaches the 2nd gap. As a result the ions are again accelerated in the 2nd gap toward the grounded cathode.

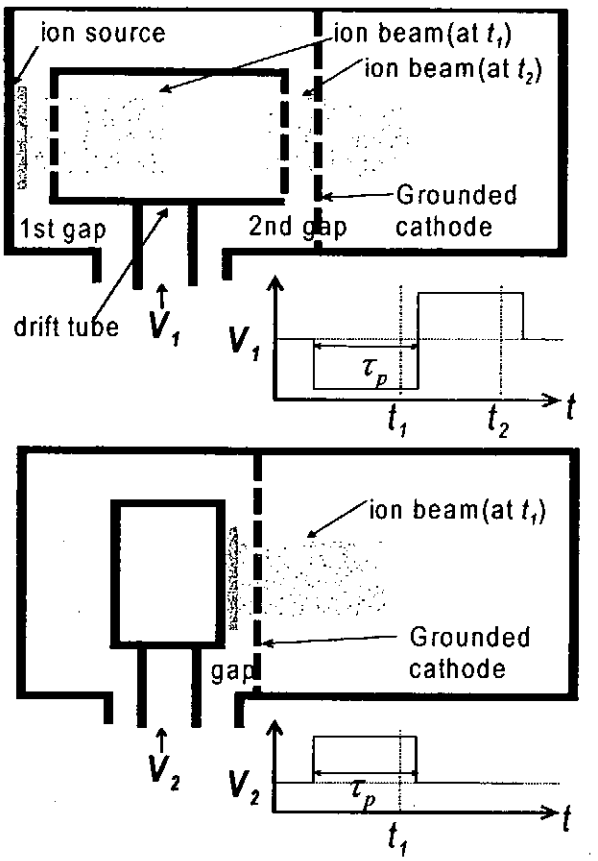

Fig. 1. Conceptual drawing of (a) bipolar pulse accelerator and (b) conventional pulsed ion beam accelerator.

As seen in Fig.1 (b), in the conventional PIB diode, ion source is placed on the anode where high voltage pulse is applied, while in the proposed ion diode, ion source is on the grounded anode. This seems to be favorable for the active ion sources where ion source is powered by an external power supply.

Here, considering the acceleration of ions in the case that ion source contains N^+ and impurity ions of H^+ in the proposed diode (see Fig. 2). In the case, ions of N^+ and H^+ are accelerated in the 1st gap toward the drift tube when negative voltage is applied. In Fig. 2, N^+ and H^+ beams are schematically described and as seen in the figure, due to the deference of the velocity the length of H^+ beam is much longer than

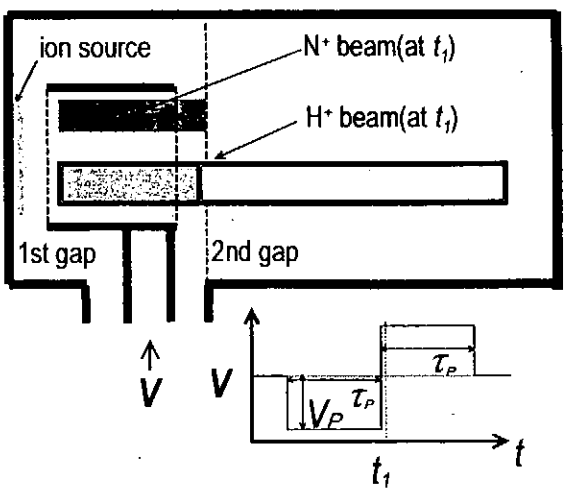

Fig. 2. Principle of the improvement of the purity of the ion beam.

that of N^+. Here assuming that the length of the drift tube is designed to be same as the beam length of N^+ of duration τ_p at acceleration voltage V_p. It is, for example calculated to be 0.19 m when V_p = 1 MV, τ_p = 50 ns. When N^+ beam of length 0.19 m is in the drift tube ($t = t_1$) the voltage is reversed and positive voltage is applied to the drift tube, which accelerate N^+ beam in the 2nd gap. In contrast, since length of H^+ beam at V_p = 1 MV, τ_p = 50 ns is 0.71 m, 73 % of the beam is out of the drift tube at t_1 and it is not accelerated in the 2nd gap. Hence 73 % of H^+ beam is removed in the accelerator.

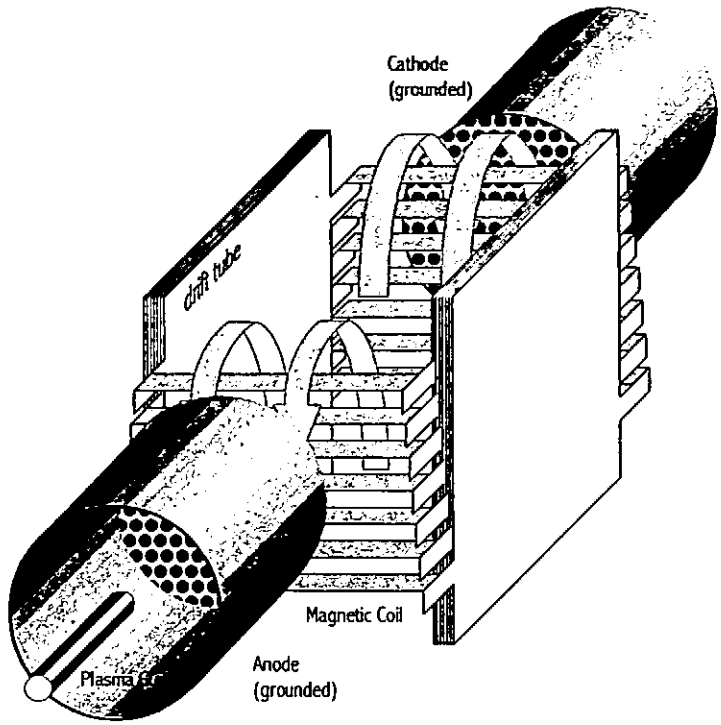

Fig. 3. Conceptual drawing of B_y type magnetically insulated gap for the BPA.

Figure 3 shows the conceptual design of the BPA. The accelerator consists of a grounded anode, drift tube and a grounded cathode. To produce insulating magnetic fields in two acceleration gaps, a magnetic field coil of grating structure is used to produce uniform magnetic field in vertical direction (y-direction).

III. Experiment

Figure 4 shows the cross-sectional view of the experimental system. The system consists of a grounded anode (copper), a drift tube (stainless steel) and a magnetically insulated acceleration gap (MIG). The drift tube is connected to a high voltage terminal of Blumlein type PFL (designed output, 300 kV, 48 kA, 60 ns). By applying negative pulse, ions on the anode are accelerated toward the drift tube. The magnetic coil of the MIG is installed on the rectangular drift tube where acceleration voltage is applied and produces magnetic field of vertical direction (y-direction). To obtain higher transmission efficiency of the ion beam, right and left sides of the coil (facing the anode or cathode) consist of 8 blades each and have a grating structure. Each of the blade (10 mm^W x 118 mm^L x 1 mm^T) are connected in series and constructs an 8-turn coil. Since high voltage pulse is applied to the drift tube, pulsed current produced in the capacitor bank (500 μF, 5 kV) is applied to the coil through an inductively isolated current feeder (IC). The IC is a helically winded coaxial cable and the

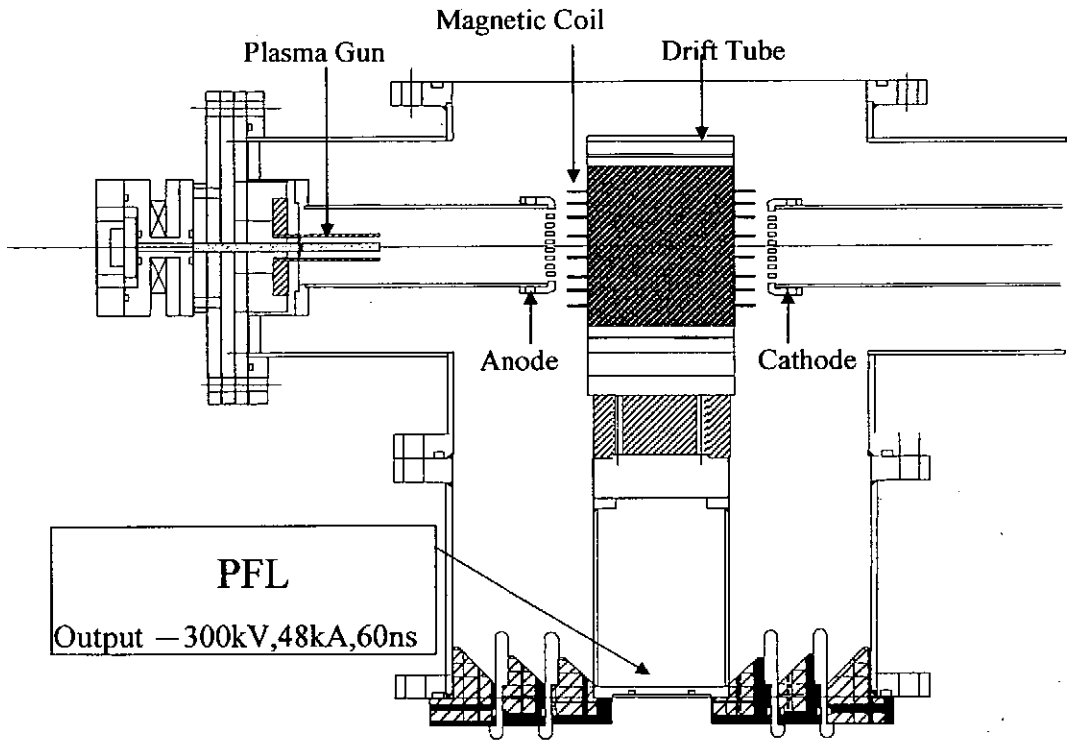

Fig. 4. Cross sectional view of the experimental system.

outer conductor of the IC is connecting the grounded vacuum chamber and the drift tube with inductance of 4.6 μH.

Anode and cathode are circuler blass electrode of diameter 78 mm, thickness 5mm. The electrodes are uniformly drilled with apertures of diameter 4 mm, giving beam transmission efficiency of 50 %. To produce anode plasma (source plasma of the ion beam) gas puff plasma gun was used, which was placed inside the anode.

Figure 5 shows the magnetic filed distribution in the gap. As seen in the figure uniform B_y field of strength 0.4-0.5 T is produced in the acceleration gap of $d_{A\text{-}K}$ = 10 mm.

Figure 6 shows the cross-sectional view of the gas puff plasma gun used in the experiment. The

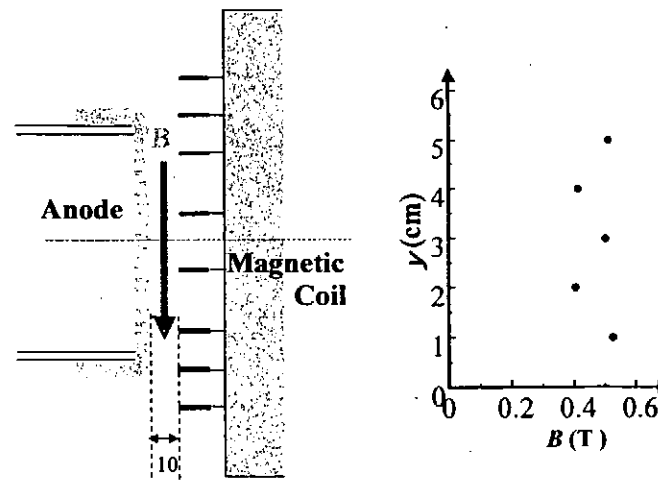

Fig. 5. Magnetic field (B_y) distribution in the acceleration gap when charging voltage of the bank is 4.0 kV.

plasma gun consists of a high-speed gas puff valve and a coaxial plasma gun. The gas puff valve consists of a nylon vessel, an aluminum valve and a drive coil and the vessel is pre-filled with N_2 gas. By applying pulse current to the coil magnetic stress presses the aluminum valve to open. The gas expands with a supersonic velocity and reaches the gas nozzles on the inner electrode of the plasma gun.

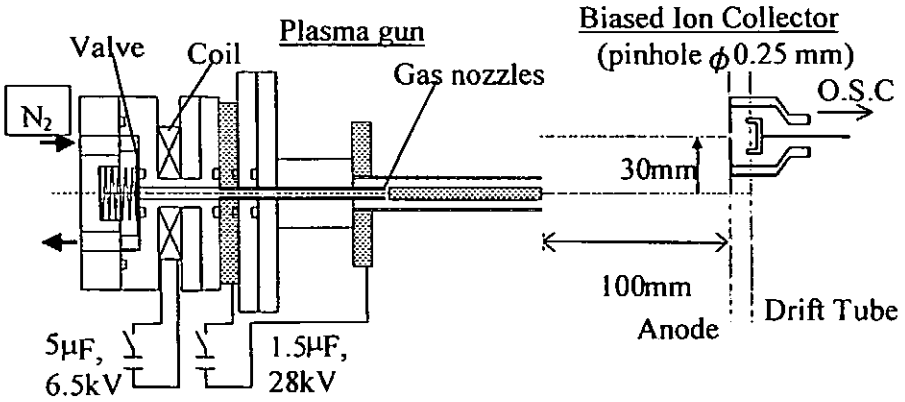

Fig. 6. Cross-sectional view of the gas puff plasma gun.

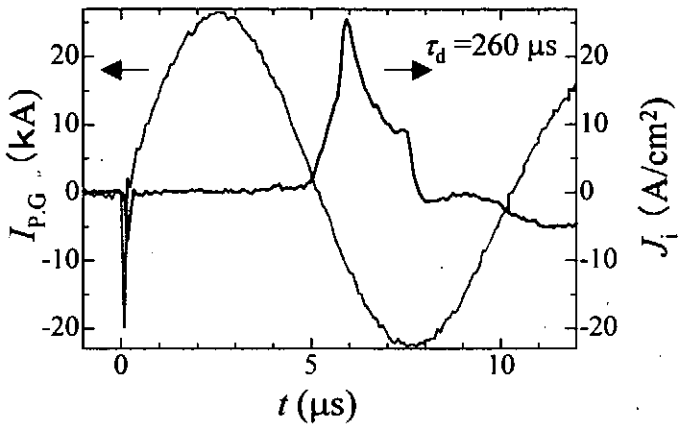

Fig. 7. Typical waveforms of $I_{P.G}$ and J_i.

The plasma gun has a pair of coaxial electrodes, i.e. an inner electrode of outer diameter 4 mm, length 100 mm, and an outer electrode of inner diameter 10 mm. Since it takes about a hundred μs to open the valve and several tens μs for N_2 gas to drift to reach the gas nozzle of the plasma gun, the capacitor bank of the plasma gun is discharged with a delay time of τ_d around 200-320. To apply pulsed current to the gas puff coil and the plasma gun capacitor banks of 5 μF and 1.5 μF were used, respectively. Both of the capacitors were usually charged to 6.5 kV, and 28 kV, respectively.

Figure 7 shows the waveforms of the discharge current of the plasma gun ($I_{P.G}$) and the ion current density (J_i) obtained by a biased ion collector

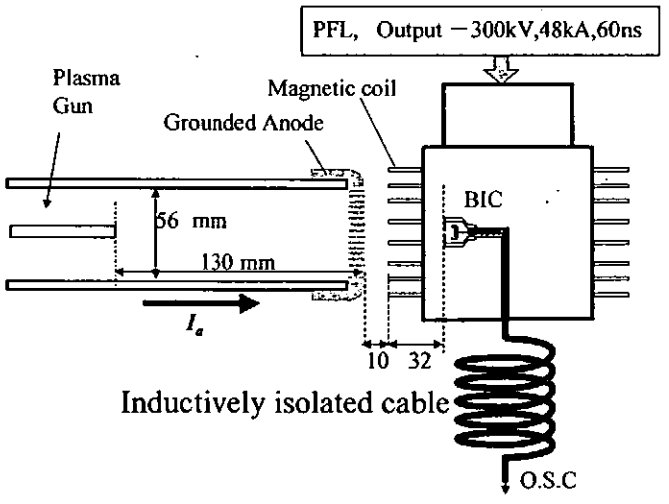

Fig. 8. Experimental setup.

(BIC) when τ_d = 260 μs. As seen in the figure $I_{P.G}$ rises in 2.5 μs and have a peak value of 27 kA. The peak value of J_i of 25 A/cm^2 was obtained at 100 mm downstream from the plasma gun at t = 5 μs after the rise of $I_{P.G}$.

The dependence of J_i on τ_d was evaluated experimentally and found that J_i rises at $\tau_d \approx$ 210 μs and have a peak around 220 μs, and after that gradually decreased. The results suggest that it takes 210 μs after the election of gas puff coil for the gas to reach the nozzles.

Figure 8 shows the experimental setup to measure the accelerated ion beam. BIC was installed inside the drift tube to observe the ion current density (J_i) in the drift tube. Since high voltage pulse is applied to the drift tube, inductively isolated cable was used to transport the BIC signal.

IV. Experimental Results

To confirm the acceleration of ions in the 1st gap negative pulse was applied to the drift tube. The test system was operated at 60 % of the full charge condition of the PFL. Insulating magnetic field of 0.3-0.4 T was applied to the acceleration gap of gap length $d_{A\text{-}K}$ = 10 mm. The plasma gun was operated at $\tau_d \approx$ 260 μs. PFL was fired to apply negative pulse tu the drift tube at and high voltage negative pulse was applied to the drift tube at $\tau_{pp} \approx$ 6.2 μs after the rise of the $I_{P.G}$.

Figure 9 shows typical waveforms of the output voltage (V_g), anode current (I_a) ion current density (J_i). I_a is equivalent to the current flowing in the 1st gap. As seen in the figure, V_g rises at t = 200 ns and peak voltage of -180 kV is obtained. I_a rises with V_g and has a peak of 9 kV. J_i rises at t = 270 ns and have a peak of 30 A/cm^2.

Figure 10 shows the dependence

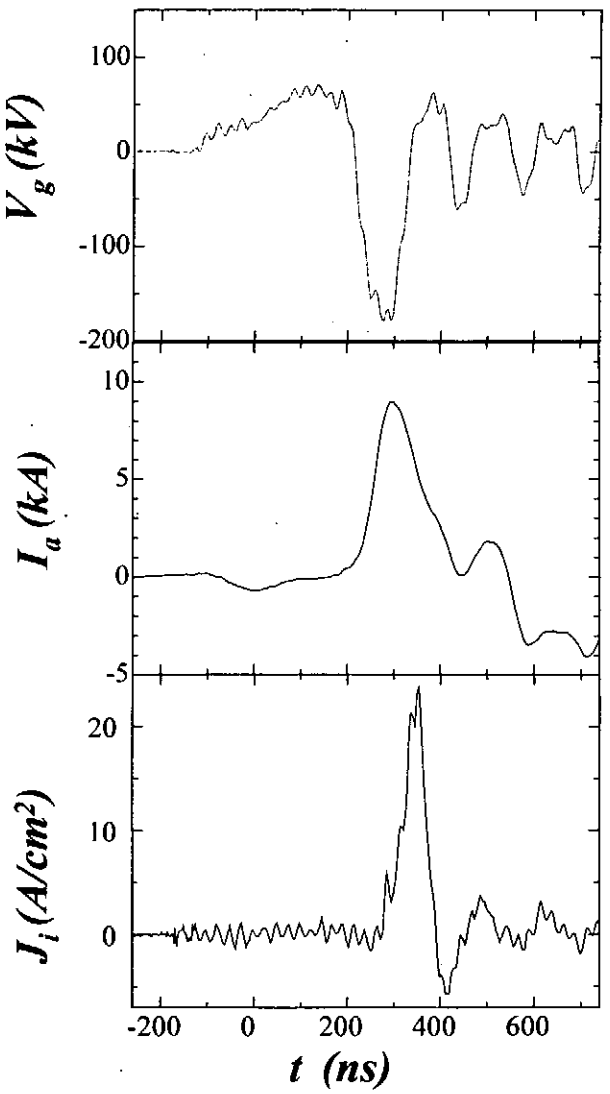

Fig. 9. Typical waveforms of V_g, I_a and J_i.

of V_g and J_i on the delay time (τ_{pp}) for the fixed condition of insulating magnetic field = 0.3-0.4 T and 60 % of full charging voltage of the PFL. As seen in the figure J_i increases monotonically with increasing τ_{pp}. This seems to be due to that quantity of the plasma on the anode or in the first gap increases with increasing τ_{pp}. Due to the increase of J_i, output current of the PFL incrases and as the results V_T decreases with increasing τ_{pp}.

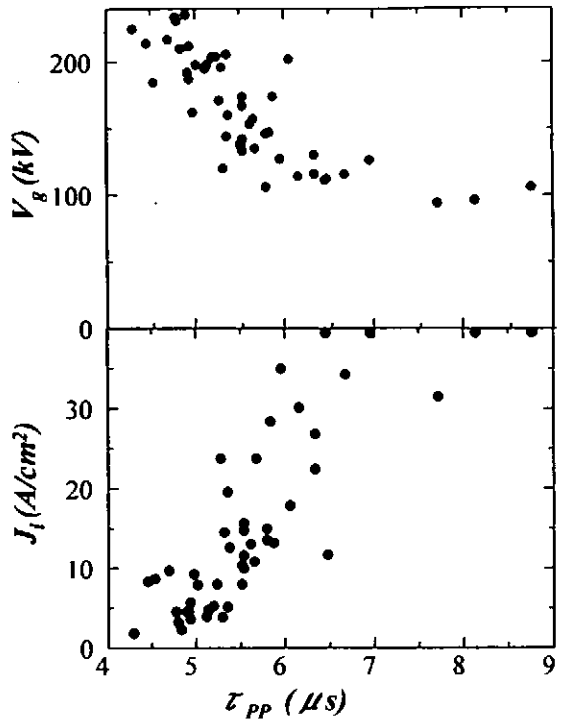

Fig. 10. Dependence of the peak values of V_g and J_i on the delay time (τ_{pp})

V. Conclusion

To confirm the principle of the BPA accelerator experimental system was developed. The system utilizes B_y type magnetically insulated acceleration gap and operated with single polar negative pulse. A coaxial gas puff plasma gun placed in the grounded anode was used as an ion source, and source plasma (nitrogen) of current density ≈ 25 A/cm^2, duration ≈ 1.5 μs was injected into the acceleration gap. The ions are successfully accelerated from the grounded anode to the drift tube by applying negative pulse of voltage 180 kV, duration 60 ns to the drift tube. Pulse Ion beam of current density ≈ 40 A/cm^2, duration ≈ 60 ns was obtained at 42 mm downstream from the anode surface.

References

1) K. Masugata, H. Okuda, K. Yatsui and T. Tazima, J. Appl. Phys. **80** pp. 4813-4818, 1996

2) K. Masugata, "High current pulsed ion beam accelerators using bi-directional pulses" Nuclear Instrum. & Methods in Phys. Res., A 411, pp.205-209, 1998

3) K. Masugata, K. Kinbara, T. Atsumura, Y. Kawahara, T. Takao, I. Kitamura, and T. Takahashi, Proc. 12th Symp. on High Current Electronics (1st Int'l Congress on Radiation Physics, High Current Electronics, and Modification of Materials, Tomsk, Russia, 24-29 September 2000), pp.111-114 (2000)

4) K. Masugata, I. Kitamura, T. Takahashi, Y. Tanaka, H. Tanoue, K. Arai, Proc. 28th IEEE Int'l Conf. on Plasma Science and 13th IEEE Int'l Pulsed Power Conf., Las Vegas, Nevada, June 17-22 2001, pp.1366-1369 (2001)

GENERATION OF INTENSE PULSED NITROGEN ION BEAM BY A B_R TYPE ION DIODE WITH GAS PUFF PLASMA GUN

R. Tejima, I. Kitamura, T. Takahasi, K. Masugata,
H. Tanoue*, and K. Arai*

Faculty of Eng., Toyama Univ., Toyama, 930-8555 Japan
National Institute of Advanced Industry Science and Technology,
1-1-4, Tsukuba, Ibaraki, 305-8568 Japan*

ABSTRACT

To apply the pulsed heavy ion beam (PHIB) to an implantation process of semiconductor, purity of the ion beam is very important. To obtain pure PHIB a new type of pulsed ion beam source has been developed. In the diode B_r type magnetically insulated ion diode is used with a nitrogen gas puff plasma gun. Ion source plasma of ion current density $\approx$ 30 A/cm^2 was produced by the plasma gun, which was injected into the acceleration gap of the diode. The ion diode was successfully operated with the plasma gun at diode voltage $\approx$ 240 kV, diode current $\approx$ 1.2 kA, pulse duration $\approx$ 250 ns and ion beam of ion current density $\approx$ 2.2 A/cm^2 was obtained at 45 mm downstream from the anode. The ion current density was found to be strongly depending on the injection timing of the source plasma.

1. Introduction

Intense pulsed heavy ion beams (PHIB) such as carbon, nitrogen, or aluminum have a wide area of applications including nuclear fusion, materials science, etc. For example, by the irradiation of PHIB on to the material, very attractive effects are expected as shown in the followings;

1) Pulsed surface heating,
2) Production of high dense ablation plasma,
3) Production of strong pressure and shock wave,
4) Deposition of atoms.

Hence it is expected to be applied to surface treatment, thin films deposition, or an implantation process. Especially for the implantation process, PHIB is expected to be used as a new type of ion implantation technology since the ion implantation and surface heat

treatment or surface annealing are completed in the same time.

Pulsed ion beam easily generated in pulsed power ion diodes with surface flashover ion sources. However, in the diodes producible ion species are limited. In addition plastics contains many kinds of atoms and those atoms are ionized and accelerated with expected ions[1]. Hence the purity of the conventional pulsed ion diodes is very poor. For example, in a point pinch ion diode experiment we found that produced ion beam contains protons, multiply ionized carbons, organic ions, etc[1]. To apply the ion beam to implantation process of semiconductor, the purity is very important, hence those ion beams are not suitable for the application.

To produce pulsed ion beam of desirable ion species with acceptable purity a new type of ion diode has been developed[2,3]. In the diode B_r type magnetically insulated diode is used with gas puff plasma gun. In the paper preliminary results of the experiment is described.

2. Ion diode experiment

In the experiment B_r–type magnetically instated diode[4] was used with gas puff plasma gun. Figure 1 shows the schematic of the system. The system consists of a high voltage pulsed power generator, a gas puff plasma gun as an ion beam source, and a B_r type magnetically insulated ion diode (acceleration gap). The anode of the diode is made of aluminum and the outer diameter, the inner diameter and the thickness are 165 mm, 120 mm, and 20 mm, respectively. The anode has two slits of width 6 mm (inner) and 6.5 mm (outer) to pass through the ion source plasma. The cathode consists of an inner cathode (outer diam. 53 mm) and an outer cathode (inner diam. 93 mm). Both cathodes have magnetic coils inside them to produce pulsed insulating magnetic field of rise-time 100 μs. The coils are powered by a capacitor bank of 250 μF. The magnetic coil is designed to produce magnetic field lines parallel to the anode surface.

The pulsed power generator consists of a fast capacitor bank and a step up transformer using

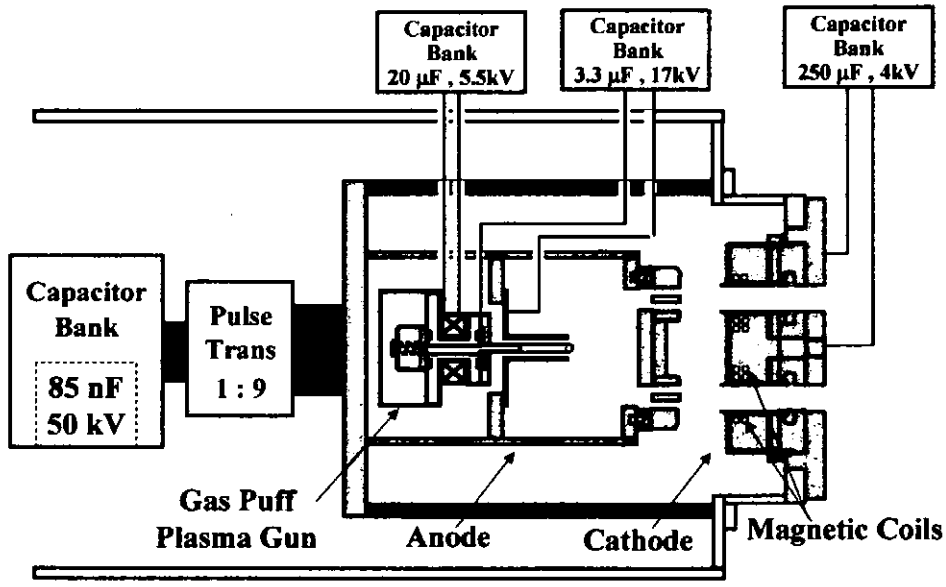

Fig.1. Schematic of the experimental system.

a magnetic core of amorphous metallic material. In the capacitor bank (maximum charging voltage of 50 kV), high power pulse of duration ≈ 150 ns (FWHM) is generated and the pulse is voltage magnified by the step up transformer of winding ratio 1:9. Since the plasma gun is placed inside the anode where high voltage pulse is applied, pulsed voltages generated by two capacitor banks are fed through inductively isolated power feeders.

Figure 2 shows the cross-sectional view of the gas puff plasma gun. The plasma gun consists of a high-speed gas puff valve and a coaxial plasma gun. The gas puff valve consists of a nylon vessel, an aluminum valve and a driver coil. The vessel is pre-filled with 2 atm of N_2 gas. By applying pulse current to the driver coil, the magnetic pressure pushes the valve and the gas expands with a supersonic velocity and reaches the gas nozzles on the inner electrode of the plasma gun.

The plasma gun has a pair of coaxial electrodes, i.e. an inner electrode of outer diameter 6 mm, length 80 mm, and an outer electrode of inner diameter 18 mm. Since it takes 150? μs to open the valve and several tens μs for N_2 gas to reach the gas nozzle of the plasma gun, the capacitor bank of the plasma gun is discharged with a delay time of τ_d = 236 μs. To apply pulsed current to the driver coil and the plasma gun capacitor banks of 20 μF and 3.3 μF are used, which were usually charged to 5.5 kV, and 17 kV, respectively. To measure the ion current density of the produced plasma, a biased ion collector (BIC), which is placed at z = 90 mm downstream from the top of the plasma gun and r = 40 mm from the axis of the plasma gun.

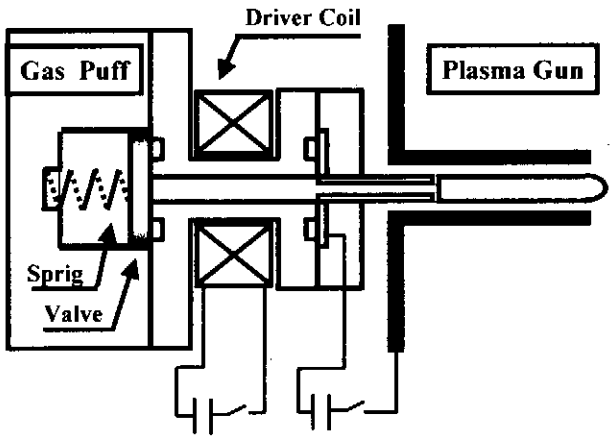

Fig. 2. Cross-sectional view of gas puff plasma gun.

Figure 3 shows the typical waveforms of discharge current (I_p) and ion current density measured by BIC (J_p) at 90 mm downstream from the top of the plasma gun. As seen in the figure I_p has a sinusoidal waveform of peak current 13 kA and 6 μs after the rise of I_p, J_{ip} has a peak of 28 A/cm^2.

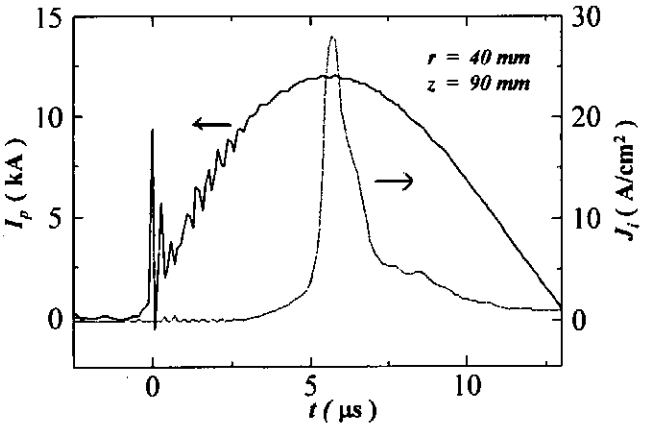

Fig. 3. Typical waveforms of discharge current (I_p) and ion current density measured by BIC (J_p).

The sequence of the diode

operation is as follows:

(1) Source plasma is generated and accelerated by the plasma gun and accelerated toward the B_r gap.

(2) When the plasma reaches the gap, high voltage main pulse is applied to the gap and the ions in the anode plasma are accelerated toward the cathode.

(3) Since the insulating magnetic field is produced in the gap prior to the main pulse, electrons in the gap are insulated and ions are efficiently accelerated in the gap.

In the experiment, the anode cathode gap was adjusted to 17 mm and insulating magnetic field on the anode surface at r = 30 mm of 0.5 T is obtained when charging voltage of the capacitor bank is 3 kV. The diode was evacuated to 5 x 10^{-3} Torr in the experiment.

3. Experimental results

Figure 4 (a) shows the typical waveforms of diode voltage (V_d), diode current (I_d). As seen in the figure, V_d rises in 150 ns and has a peak of 240 kV. On the other hand I_d rises with V_d and have a narrow peak of 1.2 kA at t = 125 ns. After that it decreases gradually. The ion current density J_i of the accelerated beam was measured by BIC placed inside the cathode at z

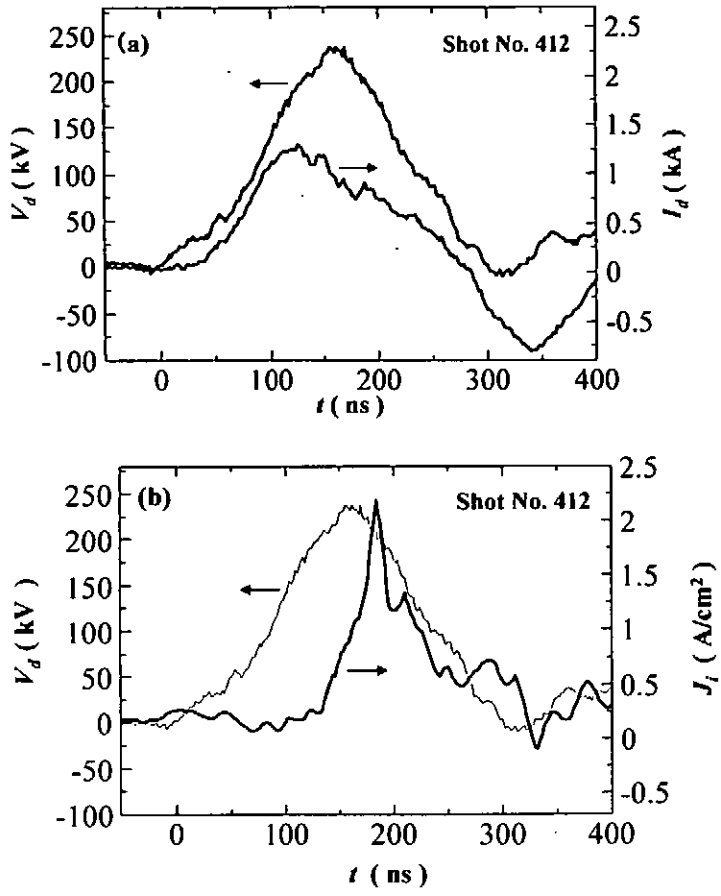

Fig.4. Typical waveforms of (a) diode voltage (V_d) and diode current (I_d) and (b) ion current density (J_i) with V_d.

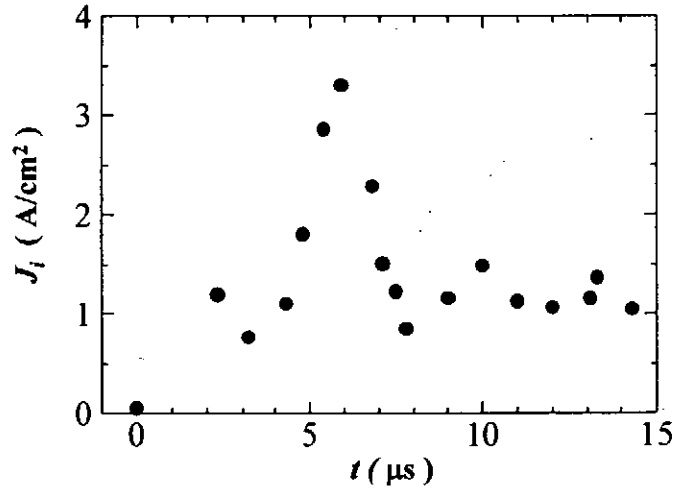

Fig. 5. Dependence of J_i on the delay time of the rise of the main pulse from the rise of the discharge current of the plasma gun (τ_{pd}).

= 42 mm downstream from the surface of the anode surface. As seen in Fig. 4 (b) J_i of 2.2 A/cm^2 was observed at t = 180 ns. Considering the time of flight delay, the ions corresponding the peak of J_i seems to be accelerated just before the peak of V_d.

Figure 5 shows the dependence of J_i on the delay time of the main pulse rise from the rise of the discharge current of the plasma gun (τ_{pd}). As seen in the figure J_i has a clear peak at τ_{pd} = 6 μs. As shown in Fig.3, J_{id} has a time of flight delay around 6 μs for ions to reach the position of the anode. Hence, maximum value of J_i is obtained when acceleration voltage is coincided with a peak of J_{id}.

Figure 6 shows an arrangement of shadow box measurement and an obtained shadow box image. As seen in the figure, the shadow box consists of a multi-pinhole plate and an ion track detecting plastic of CR-39 placed at 10 mm behind of the pinhole plate. The pinhole plate has 15 pinholes of diameter 0.2 mm each. As seen in Fig. 6 (b) 15 of pinhole images are observed, each of which correspond to each pinhole. From the size of each image the divergence angle of the beam is estimated to be consists of two large images each of which correspond to the ions accelerated from inner and outer slits of the anode. From the images the divergence angle of the beam is estimated to be ≈ 0.2 rad in r-direction and ≈ 0.3 rad in θ-direction.

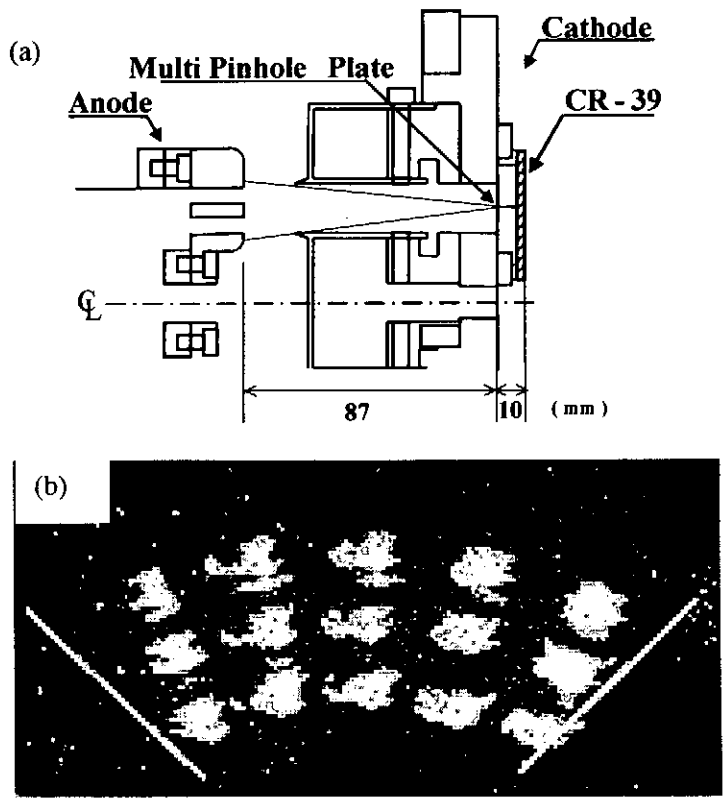

Fig. 6. A pinhole image of the ion beam on an ion track detecting plastic of CR-39 obtained with a shadow box. (a)arrangement of the measurement. (b) pinhole image.

4. Summary

A new type of pulsed ion beam source using B_r ion diode with a nitrogen gas puff plasma gun was successfully developed. In the diode, ion source plasma of ion current density ≈ 30 A/cm^2 was produced by the plasma gun, which is injected into the B_r type magnetically insulated acceleration gap of the diode. The ion diode was successfully operated with the plasma gun at diode voltage ≈ 240 kV, diode current ≈ 1.2 kA, pulse duration ≈ 250 ns and 2.2

A/cm^2 of ion current density was obtained at 42 mm downstream from the anode. The ion current density was found to be strongly depending on the injection timing of the source plasma.

References

1) K. Masugata, H. Okuda, K. Yatsui and T. Tazima, "Diagnosis of high-brightness ion beams produced in point pinch diodes", J. Appl. Phys. **80**(9) pp. 4813-4818 (1996)
2) Y. Doi, Y. Maetubo, I. Kitamura, T. Takahashi, K. Masugata, Y. Tanaka, H. Tanoue, and K. Arai, "Generation of intense pulsed ion beam By a Br type magnetically insulated ion diode with carbon plasma gun" Research Report, NIFS-PROC-50 (National Institute for Fusion Science, Nagoya, Japan, Workshop on Extremely High Energy Density Plasmas and their Diagnostics, Mar. 8-9, 2001) pp.1-6 (2001)
3) K. Masugata, K. Takao, M. Shiotani, T. Honda, R. Tejima, I. Kitamura, and T. Takahashi Application of Intense Pulsed Ion Beam to Materials Processes, Proc. Int'l Power Modulator Conf., Hollywood, CA, USA, June 30-July3, 2002, PB43 (2002)
4) E. Chishiro, A. Matsuyama, K. Masugata and K. Yatsui, "Dependence of characteristics of Br-type magnetically insulated diode on configuration of insulation magnetic field", Jpn. J. Appl. Phys., 35(4A), pp.2350-2355 (1996).

ELECTRON ACCELERATION BY INTENSE SHORT PULSE LASER IN VACUUM

S.Miyazaki, Q.Kong, S.Kawata

Department of Electrical and Electronic Engineering, Utsunomiya University, Yohtoh 7-1-2, Utsunomiya 321-8585, Japan. kwt@cc.utsunomiya-u.ac.jp

ABSTRACT

We study a generation of a high-energy electron bunch by an intense *fs* TEM(1,0) laser in vacuum. We performed three-dimensional particle simulations in which the relativistic equation of motion is solved with an analytically expressed laser field. In this paper we found that electrons are accelerated longitudinally and confined in the transverse direction by a ponderomotive force of an intense short pulse TEM(1,0) laser. By a TEM(1,0) laser of 10^{17} W/cm^2, we can suppress a divergence of electrons, and the electrons are successfully trapped in the polarized direction and accelerated to the order of tens of MeV with an acceleration gradient on ~GeV/m. The electron bunch generated has a small emittance in the transverse and longitudinal directions, and the spatial size of the electron bunch is about several hundred μm in each direction with a high electron number density. This electron acceleration mechanism may open a new engineering world toward a point radiation source, a precise measurement, applications to material sciences, and so on.

I. Introduction

In recent years, we have seen developments of intense laser and laser pulse length compression with the invention of the Chirped Pulse Amplification (CPA) technique[1]. The CPA laser can make the intensities larger than ~10^{21} W/cm^2 with short pulses. Such the laser pioneered new research areas to an electron acceleration[2-6]. Among them, we study the generation of a high-energy and high-density micro electron bunch by using a high intense short pulse TEM(1,0) laser in vacuum. The electron motion can be divided into a high frequency quiver and a drift motion. The quiver motion is a result of the laser oscillation. The drift is cased by the ponderomotive force, which is generated by a nonlinear effect. The ponderomotive force is proportional to the gradient of the laser field energy density. At the high intensity laser ($a_0 \geq$ 0.1 - 1.0) focused on the electrons, the strong ponderomotive force pushes the electrons to the opposite direction of the gradient of the laser intensity. Here a_0=

$e E_0 / m_e \omega c$ is a dimensionless parameter of the laser field intensity, e and m_e are the electron charge and rest mass, respectively, ω is the laser angular frequency, E_0 is the amplitude of electric field and c is the speed of light in vacuum. On the other hand, the focused laser has also a field gradient in the radial direction. The transverse ponderomotive force may scatter electrons in the radial direction[7-8]. The TEM(0,0) laser, which is widely used, has an intensity peak at the central axis. Therefore, the electrons receive the strong ponderomotive force to the transverse direction with the oscillating in the polarized direction. Therefore, the electrons scattered to the polarized direction strongly and the quality of the electron bunch accelerated is degraded. The main purpose of this study is to suppress the scattering in the polarized direction and to generate the high-energy and high-density micro electron bunch. We adopt a TEM(1,0) laser[9] in order to suppress the electron scattering to the polarized direction. The TEM(1,0) laser has two peaks in the polarized direction. The electrons are accelerated near the laser focal point and confined between the two intensity peaks in the polarized direction by the transverse ponderomotive force. Consequently, the high-quality electron bunch can be generated.

In Section II, we describe our simulation model and parameter set. In Section III, simulation results are presented and the quality of the accelerated electron bunch is investigated. In section IV, conclusions are described.

II. Simulation Model

Figure 1 shows the schematic view of electron acceleration by the intense short pulse TEM(1,0) laser. The width of an injected electron bunch (l_x, l_y, l_z) is ($2w_0$, $2w_0$, $8L_z$). Here w_0 and L_z are the laser minimal spot size and the pulse length, respectively. The electron bunch moves to the z direction at the speed of $0.95c$. At the initial time t_{begin}, the injected electron bunch does not interact with the laser pulse. The center of the laser pulse and the electron bunch coincides with each other at the focal point $(x, y, z) = (0, 0, 0)$ at the time $t = 0$. The laser wavelength λ is 1.053 μ m, the laser intensity 10^{17} W/cm^2 ($a_0 \sim 0.2$), the laser pulse length 10λ, the minimal spot size 35λ, and the number density of initial electron bunch is 5.48×10^{10} cm^{-3}.

We used the TEM(1,0) laser, which is linearly polarized in the x direction and propagates along the z direction. In our simulation, we give the laser field analytically and solve the relativistic motion of the electrons in the field. The paraxial approximation[10-12] is used for the analytical formula of the laser field. The expression about the laser field is shown below. The electric field component of polarized direction[9] is

$$E_x = 2\sqrt{2}\,E_0 \frac{w_0}{w(z)^2} x \exp\left(-\frac{r^2}{w(z)^2} - \frac{(z-ct)^2}{L_z^2}\right) \exp\left\{ i\left(kz - \omega t - 2\phi(z) + k\frac{r^2}{2R(z)} \right) \right\}. \quad (1)$$

The other electric and magnetic components are obtained by the paraxial approximation:

$$E_y = 0, \tag{2}$$

$$E_z = \frac{i}{k}\frac{\partial E_x}{\partial x}, \tag{3}$$

$$\mathrm{B} = -\frac{i}{\omega}\nabla \times \mathrm{E}, \tag{4}$$

where

$$r^2 = x^2 + y^2, \tag{5}$$

$$w(z) = w_0\left\{1+(z/z_R)^2\right\}^{1/2}, \tag{6}$$

$$R(z) = z\left\{1+(z_R/z)^2\right\}, \tag{7}$$

$$\phi(z) = \tan^{-1}(z/z_R). \tag{8}$$

Here $z_R = \pi w_0^2/\lambda$ is the Rayleigh length. The accuracy of this approximation is related to the minimal spot size of the laser. When $kw_0 \geq 50$, this approximation is accurate enough to describe the electron-laser interaction[12]. The motion of electron is calculated by using a relativistic equation of motion,

$$\frac{d\mathbf{P}}{dt} = -e\left(\mathbf{E}+\frac{1}{c}\mathbf{v}\times\mathbf{B}\right). \tag{9}$$

Here **v** and **P** indicate the velocity and momentum of electron, respectively.

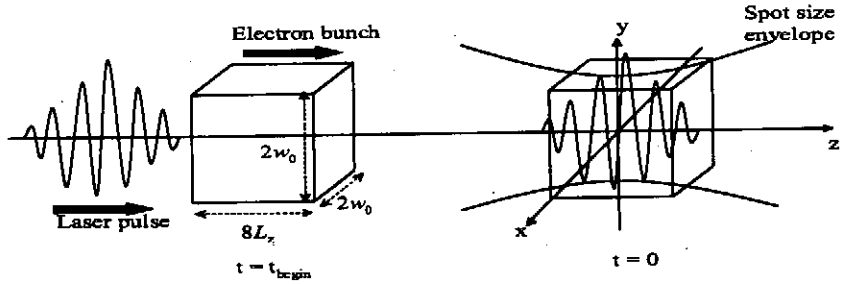

Fig. 1. Schematic view of the simulation model of the electron acceleration in vacuum by the intense short pulse TEM(1,0) laser. The laser and injected electron bunch propagate along the laser axis. Here w_0 is the minimal spot size of laser and L_z is the laser pulse length. The left side view of Fig. 1 shows the state of the laser and an electron bunch at the time t_{begin}. We set that the center of the laser and electron bunch coincides with each other at the time $t=0$.

III. Simulation Results

The incident electron bunch interacts with the laser pulse near the focal point. When the laser pulse reaches to the focal point, the electrons, which exist near the intensity peaks,

are accelerated well to the z direction according to the strong ponderomotive force in the z direction. Figures 2a) and b) represent distributions of the final electron relativistic factor γ at the t_{final} in the z-x plane and the z-y plane, respectively. Here $t_{final} = 30000\,\lambda/c$. Fig. 2a) shows that the electrons are accelerated to the z direction and the accelerated electrons are gathered around the central axis. The laser is polarized in the x direction. The electrons oscillate by the electric field in the polarized direction and the transverse ponderomotive force works in the x and y directions. The electric field E_y is zero in the TEM(1,0) laser. Therefore, the electrons are not scattered much in the y direction compared with the electrons scattering in the x direction as shown in Fig. 2b). Figure 3 shows the averaged electron number density distribution in the z-x plane at the t_{final}. The number density is averaged in the y direction. The number density peak of electrons appears around $x = 0$ and $z = 30000\ \lambda/c$. The maximum electron number density is about 2.70×10^{8} cm^{-3} and the maximum energy density is about 5.39 PeV/cm^3. Consequently, the accelerated electrons are confined between the intensity peaks in the x direction, and the high-density high-energy electron bunch is generated as shown in Figs.2 and 3.

Figure 4a) shows trajectories of most accelerated electron (Case1) and other scattered electron (Case2) in the x-z plane. Figure 4b) corresponds to the electron energy change along the laser axis for these electrons. The initial position of the Case1 electron is near the peak of laser intensity in the x direction. In the Case2 the electron is initially located slightly outside of the peak of laser intensity. The Case1 electron is accelerated well successively near the focal point and captured by the laser field along the laser axis. On the other hand, the Case2 electron receives a strong scattering by the laser pulse near the focal point and does not well absorb the laser wave energy. The ponderomotive force in the x direction for the Case1 electron near the focal point is small compared with that in the Case2. Therefore in the Case2 the strong ponderomotive force pushes the Case2 electron far from the laser axis in the x direction before the sufficient acceleration. The electron final energy E_{max} in the Case1 is about 39.9 MeV with an acceleration gradient of 5.55 GeV/m.

In order to make the acceleration mechanism clear, we compare the motion for the two electrons. We use an energy equation $d(m_e c^2 \gamma)/dt = -e\,\mathbf{v}\cdot\mathbf{E}$ and a time-averaged ponderomotive force, which is given by[13)]

$$F_{pond}(t) = -\nabla V_{pond}(x,y,z,t), \tag{10}$$

$$V_{pond}(x,y,z,t) = \left\{\left(1+a^2(x,y,z,t)\right)^{1/2} - 1\right\} m_e c^2. \tag{11}$$

Here $a^2/2$ is the normalized time-averaged laser intensity, which is written by

$$a^2(x,y,z,t) = 8a_0{}^2 \frac{w_0{}^2}{w(z)^4} x^2 \exp\left\{-\frac{2r^2}{w(z)^2} - \frac{2(z-ct)^2}{L_z{}^2}\right\}. \tag{12}$$

The work and the ponderomotive force acting on the two electrons are shown in Fig. 5. Figures 5a1) and a2) show the electron energy γ versus z. Figures 5b1), c1), b2) and c2) present the x and y components of the energy equation. Figures 6d1), e1), d2) and e2) represent the x and z components of the ponderomotive force as a function of z. As shown in Figs. 5b1), c1), d2) and c2) the longitudinal electric field E_z is much smaller than the transverse electric field E_x. Therefore, the longitudinal component of the energy equation $-ev_z E_z$ influences neither the energy variation in Case1 and Case2. Therefore the energy change of the electrons is governed mainly by the x component of the energy equation $-ev_x E_x$. In the Case1 the electron receives the laser energy in the vicinity of the focal point. On the other hand, the Case2 electron cannot absorb the wave energy. The ponderomotive force works in the opposite direction of the gradient of the laser intensity. The Case1 electron is located near the laser intensity peak in the x direction near the focal point. From Figs. 5d1) and e1), the Case1 electron has nearly no influence by the gradient of the intensity in the x direction. The Case1 electron is accelerated successively. Because of the effective acceleration in the Case1, a difference of a phase velocity between the electron and laser pulse becomes small. Therefore the Case1 electron is sitting for a long time on the front of the laser pulse. When the Case1 electron moves behind the laser pulse peak, the laser already expands, its intensity becomes weak and the ponderomotive force becomes small. In Figs. 5d2) and e2) the initial position of the Case2 electron is located just outside of the laser intensity peak, and the ponderomotive force pushes the electron quickly outward in the x direction. As a result, the Case2 electron slips out of the laser pulse and loses its energy.

Figures 6a) and b) show the enlarged electron bunch maps in the z-x and z-y planes at the t_{final}, respectively. The size of the accelerated electron bunch is 100 ~ 200λ in the x direction, 100 ~ 150λ in the y direction and 30 ~ 50λ in the z direction. The transverse and longitudinal *rms* emittances, which measure the quantity of the accelerated electron bunch, are shown by[8, 14)]

$$\varepsilon_x = \sqrt{\overline{(x-\bar{x})^2}\,\overline{(x'-\bar{x}')^2} - \left\{\overline{(x-\bar{x})(x'-\bar{x}')}\right\}^2}\,, \tag{13}$$

$$\varepsilon_z = \tilde{z}\frac{\Delta\tilde{P}_z}{P_0}. \tag{14}$$

Here $x'=dx/dz$ is the slope of the trajectory, $z=s(t)-s_0(t)$ is the difference in the direction of the beam propagation, $\Delta P_z = P_z - P_0$ is the difference in the longitudinal momentum. The $s(t)$ is the distance of travel along the direction of beam propagation. The P_z and P_0 are the longitudinal momentum and the averaged value of the longitudinal momentum, respectively. The *rms* emittances of the electron bunch accelerated in the x, y and z directions (ε_x, ε_y, ε_z) are about (0.322 mm mrad, 1.54×10^{-3} mm mrad, 5.23 mm

mrad). The averaged energy of the accelerated electron bunch is about 18.6 MeV and the averaged number density is about 0.835×10^{8} cm^{-3}.

In our simulations, the electron-electron interaction is neglected. Here the limit of the accelerated electron number, under which the interaction between the accelerated electrons is negligible, is estimated. It is given by[8)]

$$N<\frac{w(z)}{r_e}\left(\frac{P_\perp}{m_e c}\right)^2. \tag{15}$$

Here N is the limit of the accelerated electrons number, r_e is the classical electron radius, $P_\perp$ is the transverse momentum of accelerated electrons. As a result, the limit number of the accelerated electrons N is about 4.82×10^{7} and it corresponds to the number density ~ 10^{11} cm^{-3}. The maximum accelerated electrons number density in our simulations is about 2.70×10^{8} cm^{-3}, and we can ignore the electron-electron interaction. The accelerated electron also receives the acceleration and radiates the energy. The expression of the radiation effect is written by[15)]

$$E_{radiation}=\frac{2e^4}{3m_e^{\,2}c^3}\int_{-\infty}^{\infty}\gamma^2\left\{\left(\mathbf{E}+\frac{1}{c^2}\mathbf{v}\times\mathbf{H}\right)^2-\frac{1}{c^2}(\mathbf{Ev})^2\right\}dt. \tag{16}$$

The radiation energy of the most accelerated electron is about 0.201 eV. Therefore $E_{\text{radiation}}/E_{\max}$ ~ 1.99×10^{-8} and the radiation effect is also negligible.

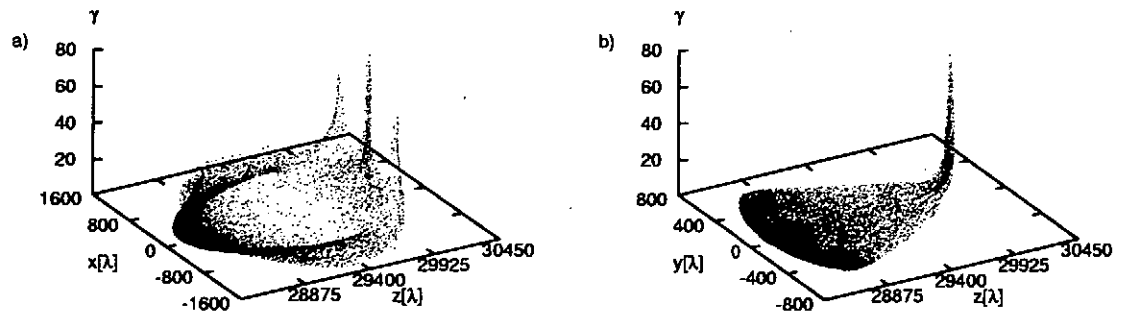

Fig. 2. The electron energy γ maps in a) the x-z plane and b) the y-z plane at the t_{final}.

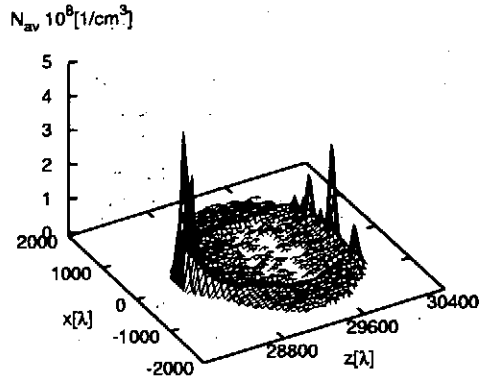

Fig. 3. The electron number density distribution in the x-z plane at the t_{final}.

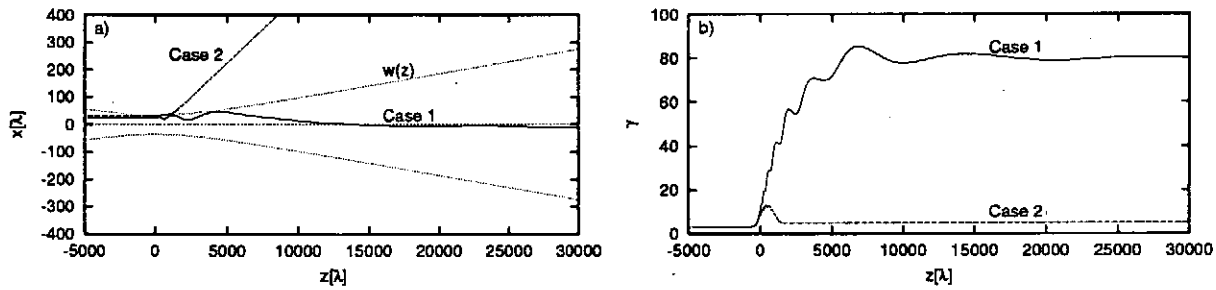

Fig. 4. a) The electron trajectories in the x-z plane. b) The electron energy γ versus z. Here $w(z)$ represents the laser spot size envelope. The Case1 shows the most accelerated electron and the Case2 shows the scattered electron.

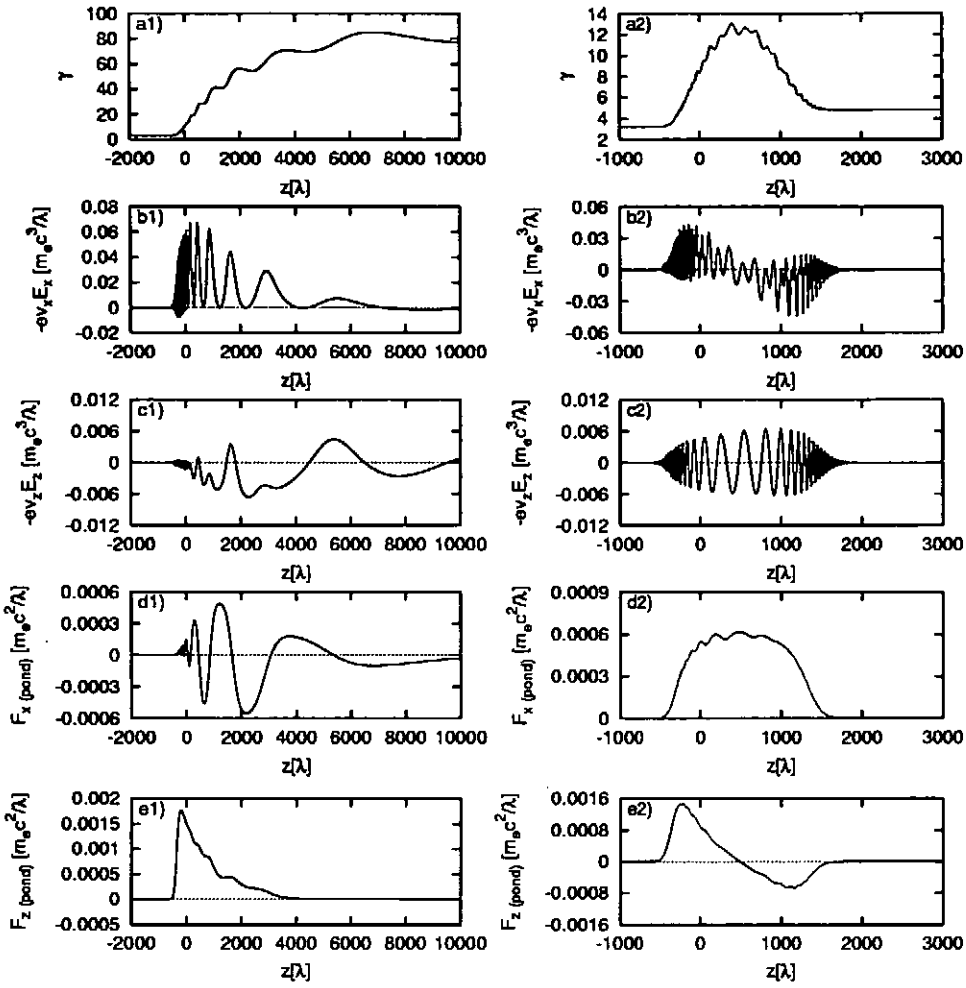

Fig. 5. The work and the ponderomotive force acting on the electrons versus z. The left side shows the well-accelerated electron (Case1) and the right presents the scattered electron (Case2). Figures a1) and a2) represent the variation of the electron energy γ near the focus, figures b1), b2), c1) and c2) show the work in the x and z directions as a function of z based on the energy equation and Figs. d1), d2), e1) and e2) represent the time-averaged ponderomotive forces in the x and z directions as the function of z.

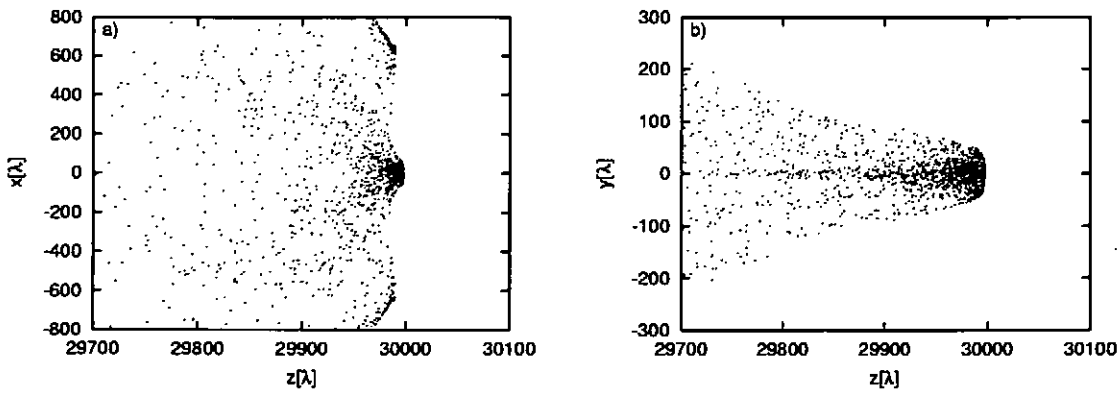

Fig. 6. The enlarged electron bunch maps in a) the x-z and b) the y-z planes.

IV. Conclusions

We study the high-energy and high-density micro electron bunch generation by using the intense short pulse TEM(1,0) laser. The electrons are accelerated by the longitudinal ponderomotive force near the focal point and captured by the laser field without the scattering to the polarized direction. During the laser-electron interaction, the electrons accelerated are focused around the central axis by the ponderomotive force in the polarized direction. The size of the electron bunch accelerated is smaller than 200λ in the transverse direction and 30 ~ 50λ in the longitudinal direction. The number density of the accelerated electron bunch is ~10^8 cm^{-3}. The *rms* emittance in the transverse and longitudinal directions are ~ mm mrad. The electron energy reaches a few tens of MeV with an acceleration gradient of ~ GeV/m. The production of such an electron bunch may open a new field for the points light source or a new EUV source or applications for nano-technologies or particle acceleration schemes[16].

References

1) G. A. Mourou and T. Tajima, *Inertial Fusion Sciences and Applications 2001*, 831 (2001).

2) M. O. Scully and M. S. Zubairy, Phys. Rev. A **44**, 2656 (1991).

3) B. Hafizi, A. Ting, E. Esarey, P. Sprangle and J. Krall, Phys. Rev. E **55**, 5924 (1997).

4) Q. Kong, Y. K. Ho, J. X. Wang, P. X. Wang, L. Feng and Z. S. Yuan, Phys. Rev. E **61**, 1981 (2000).

5) Y. Cheng and Z. Xu, Appl. Phys. Lett. **74**, 2116 (1999).

6) G. Malka, E. Lefebvre and J. L. Miquel, Phys. Rev. Lett. **78**, 3314 (1997).

7) J. L. Chaloupka and D. D. Meyerhofer, Phys. Rev. Lett. **83**, 4538 (1999).

8) G. V. Stupakov and M. S. Zolotorev, Phys. Rev. Lett. **86**, 5274 (2001).

9) Amnon Yariv, *OPTICAL ELECTRONICS*, 3rd ed. (Published simultaneously in Canada, 1985).

10) M. Lax, W. H. Louisell and W. B. McKnight, Phys. Rev. A **11**, 1365 (1975).

11) L. W. Davis, Phys. Rev. A **19**, 1199 (1979).

12) N. Cao, Y. K. Ho, Q. Kong, P. X. Wang, X. Q. Yuan, Y. Nishida, N. Yugami, H. Ito, Opt. Commun. **204, 7** (2002).

13) P. X. Wang, Y. K. Ho, X. Q. Yuan, Q. Kong, N. Cao, A. M. Sessier, E. Esarey, E. Moshkovich, Y. Nishida, N. Yugami, H. Ito, J. X. Wang and S. Scheid, Jpn. J. Appl. Phys. **91**, 856 (2002).

14) M. Reiser, *Theory and Design of Charged Particle Beams*, (A Wiley-Interscience Publication, New York, 1994).

15) L. D. Landau and E. M. Lifshitz, *Course of Theoretical Physics Vol.2:The Classical Theory of Field* 4th ed. (Pergamon Press, London, 1975).

16) T. Nakamura and S. Kawata, Phys. Rev. E, in press (2003).

Design of a 5 GHz cylindrical corrugated waveguide and formation of an energy increasing IREB

Haruki Shirasaka, Kazuteru Kurihara, Masaki Kamada, Takashi Nishiguchi, Keiichi Ishibana, Ritoku Ando and Keiichi Kamada

Department of Physics, Faculty of Science, Kanazawa University, Kanazawa 920-1192, Japan

ABSTRACT

The possibility of generation of C band microwave pulse with output power of gigawatt is demonstrated using an intense relativistic electron beam with duration of 12 nanoseconds passing through cylindrical corrugated structure. It is suggested by PIC simulation that the beam duration has optimum value for the output power of the radiated microwave. Moreover, as increase of microwave peak power can be expected by optimization of voltage and current waveforms, the waveform modifications of electron energy and current of the intense electron beam pulse are carried out using autoacceleration scheme with passive coaxial cavities.

1 Introduction

Generation of intense mili/centi-meter electromagnetic wave is studied extensively in these decades for application of nuclear fusion, particle accelerator etc. Nearly continuous power output of ~1 MW is achieved by Gyrotron. An electron beam with energy of several hundreds kV and current of several tens mA is used as an energy source for the Gyrotron. On the other hands, the microwave devices with output power near 1 GW are still in an experimental stage. An intense relativistic electron beam (IREB) with energy of 1 MV< and current of 1 kA< is used as an energy source for high power microwave generation. The device with output of more than 1 GW is suffered from breakdown in the transmission line or else. Two solutions against the breakdown are considered. One is the development of the surface of the material and another is the use of a short pulse electron beam.

Usually, microwave generation theory is considered in steady state condition even in the high-power output regime. The physics of microwave generation for steady state might be applied as long as the length of an electron beam is much longer than that of the apparatus. Actually, the typical length of the apparatus is less than 1 m and the duration of an IREB is more than 10 ns, i.e. the length is more than 3 m, so that the steady state theory could be applicable for conventional microwave devices. Here, a specific pulsive

mechanism of microwave radiation called superradiance (SR) is proposed [1,2,3] using an electron beam whose length is shorter than or comparable with interaction length. An electron beam with duration of less than one ns is requested for millimeter waveband SR. However, it is technically difficult for conventional pulse line system to generate an IREB with duration of less than 10 ns. We proposed multi-stage autoacceleration using a series of passive coaxial cavities with decreasing lengths and obtained an IREB with duration of less than 1 ns from 12 ns IREB [4,5] for millimeter waveband SR.

For observation of SR in centimeter waveband, rather long nanosecond electron beams are suitable, so that it is easier to design the beam source. Moreover, it was proposed in [6] to use an IREB with increasing energy in time to increase peak power of SR pulse. In this paper, we report two subjects of centimeter waveband SR. First, a design and experimental results of a cylindrical corrugated waveguide for 5 GHz SR are reported. Second, formation of the energy increasing IREB using coaxial cavities for more effective SR is carried out.

2 Cylindrical corrugated waveguide.

2.1 Design of a cylindrical corrugated waveguide.

The IREB with energy of 550 keV, current of 5.5 kA and duration of 12 ns is utilized as an energy source. A cylindrical corrugated waveguide structure for microwave radiation with frequency of 5 GHz is selected because it is easy to make by ourselves. The final structure is shown in Fig.1. At first, the mean radius and periodic length are decided to be 25 mm and 30 mm, respectively, by approximate dispersion relation (Fig. 2) for 4.9 GHz microwave radiation with the IREB. As the backward wave of TM_{01} mode is expected, the inner radius of the waveguide is decreased to be 22 mm to reflect the wave to the downstream side at the entrance of the corrugated part (indicated by A in Fig.1.). Therefore, the outer radius of corrugated part is set to be 28 mm. We use PIC simulation

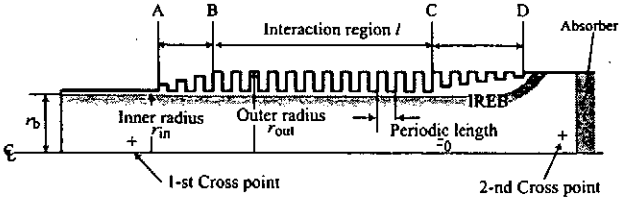

Fig. 1: Cross section of the cylindrical corrugated waveguide where $r_b = 20\text{mm}, r_{in} = 22\text{mm}, r_{out} = 28\text{mm}, z_0 = 30\text{mm}$ and $l = 300\text{mm}$. Output microwave is observed at 2-nd cross point.

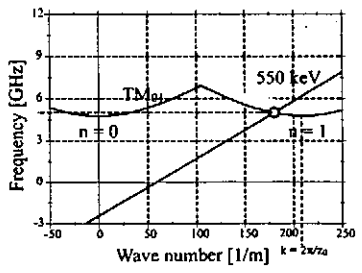

Fig. 2: Approximate dispersion relation.

code KARAT[7] to optimize the other parameters. Gradually increasing radii region is added at both sides of the interaction region to propagate an electron beam smoothly.

The optimum length of the interaction region is simulated to be 30 cm in our case (Fig.3). The output power of the radiated microwave is saturated at the length of 30 cm. The difference between the inner wall and the beam radii is also simulated and the beam radius is decided to be 20 mm.

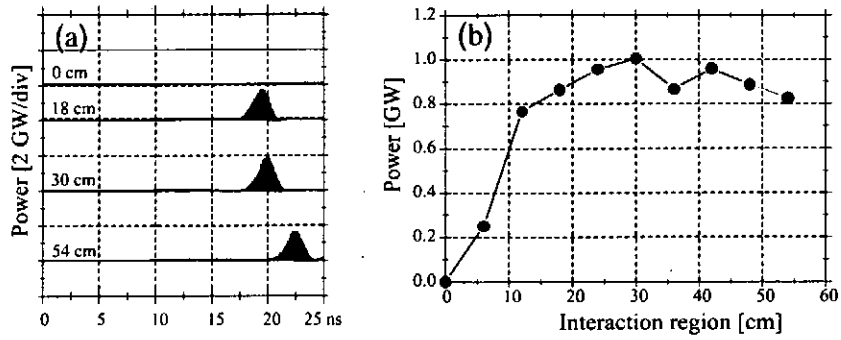

Fig. 3: The microwave outputs from different length of the interaction region.

From the simulation, the microwave radiation with frequency of 4.9 GHz, output power of 1 GW and duration of 3 ns is expected using the above designed cylindrically corrugated waveguide and the IREB with energy of 550 keV, current of 5.5 kA and duration of 12 ns (Fig.4). The efficiency is calculated to be 34 %.

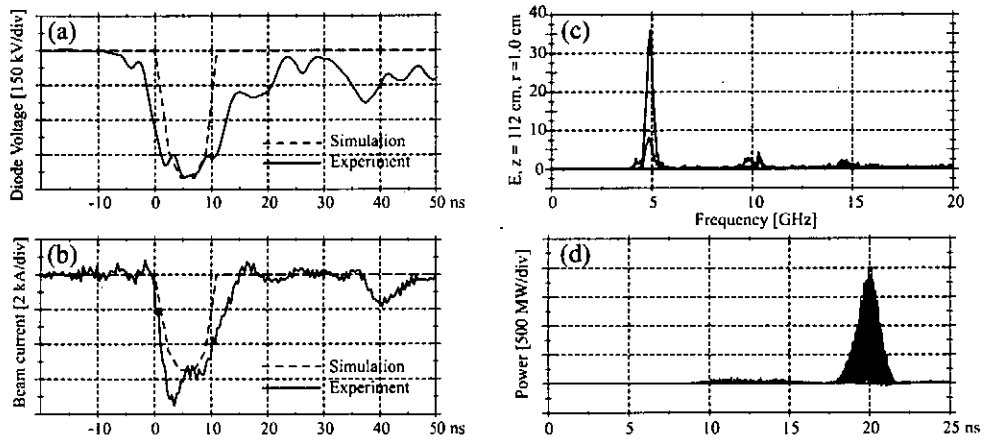

Fig. 4: The waveforms of a) the diode voltage, b) the beam current, c) simulated output frequency and simulated microwave output. Dotted lines of a) and b) are used waveforms in the simulation.

It is difficult to declare that the microwave radiation described above is identified to be SR. However, the simulation results suggested some characteristic mechanism of SR. The

simulation shows how the beam length influences on the microwave output. In Fig. 5, the simulated results of microwave outputs with different beam lengths using the cylindrical corrugated waveguide are shown. For the corrugated waveguide and the IREB described above, the microwave output shows the maximum value with the beam duration of 12 ns.

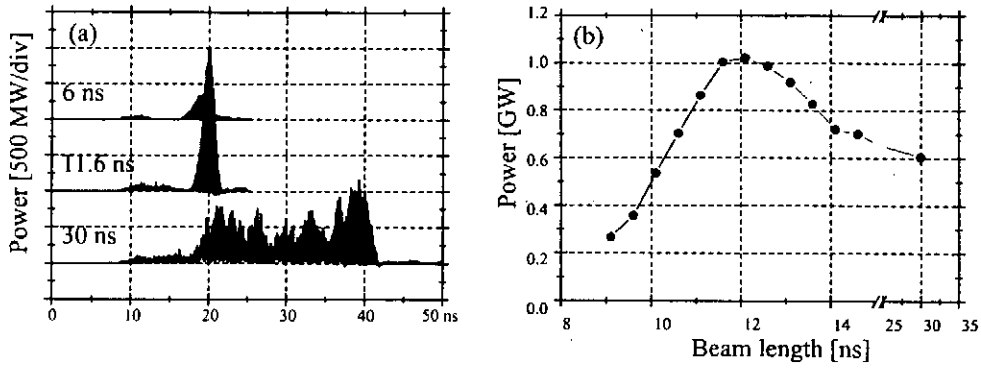

Fig. 5: Simulated microwave outputs for different beam lengths. Left: time dependence of microwave output. Right: the maximum output values are plotted against the beam lengths.

Figure 6 shows the positions of the radiated microwave and the beam electrons at the time when the front of the backward microwave is reached at the entrance of the corrugated part. When the duration of the beam is 12 ns, the tail of the beam electrons has already passed the entrance of the corrugated part (indicated by A in Fig.1). On the other hands, the beam electrons are present together with the microwave when the beam duration is 30 ns. It is supposed that the reflected microwave has a chance to be absorbed by the electrons in case of the long beam. The beam duration of 12 ns is the maximum duration that the tail of the electrons goes ahead of the head of the reflected microwave.

2.2 Preliminary experiments with the corrugated waveguide.

As the system for microwave detection has not established yet, only preliminary experiments are carried out until now. Pulserad 105A produced by Physics International is utilized to generate an IREB of 550 keV, 5.5 kA, 12 ns. Foilless diode consists of a carbon cathode with hollow knife-edge of 35 mm diameter and a carbon anode with 40 mm diameter aperture. An annular electron beam with diameter of $\sim$ 40 mm and thickness of 1 mm is injected from the diode into a conducting drift tube with inner diameter of 44 mm and following cylindrical corrugated waveguide. The system is immersed in axial magnetic field of 1 T applied by solenoid coils. The base pressure in the system is maintained below 1 x 10^{-5} Torr. The experimental setup is shown in Fig. 7.

The microwave is radiated from the horn at the end of the vacuum chamber through

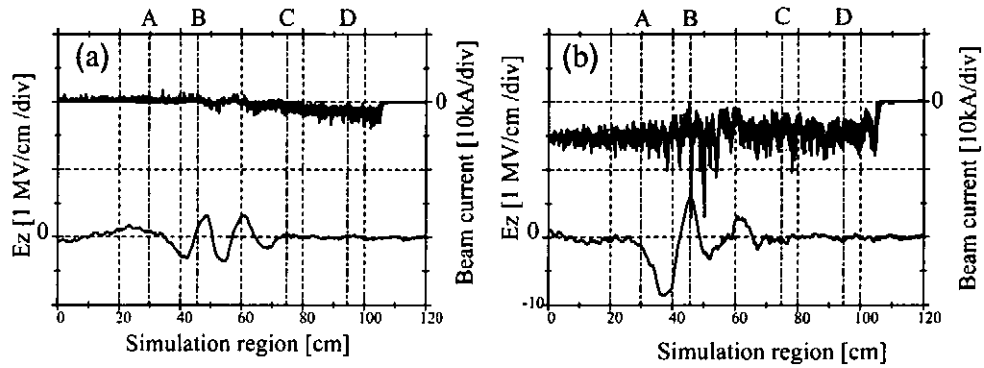

Fig. 6: Simulated results of beam current(upper) and radiated electric field (lower) at the time when the radiated microwave propagates backward to the reflection point indicated by A. Left: beam duration is 12 ns. The tail of the beam current has already passed the point A. Right: beam duration is 30 ns. The beam current is present all through the waveguide.

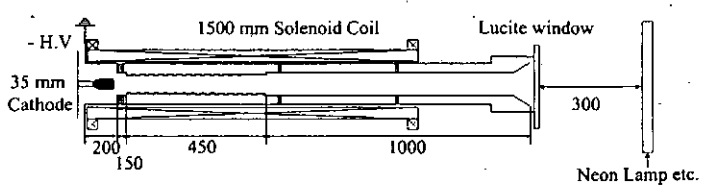

Fig. 7: Experimental setup.

Fig. 8: Neon lumps and fluorescent tubes are lit on at 30 cm.

a Lucite window to the atmosphere. Neon lumps and fluorescent tubes are set in the atmosphere to estimate the output power of the microwave. They are considered to be lit on with over 1 MW pulsive microwave. At 30 cm from the Lucite window, all lumps and tubes are lit on (Fig. 8). Moreover, at 60 and 100 cm, the neon lumps located on the center axis is not lit on but they at far around the axis are lit on. We expect that the output power of the radiated microwave is larger than 1 MW even 1 m from the Lucite window and the mode is identified to be the TM_{01}.

Now the microwave detection system is constructing and more information will be obtained.

3 Formation of energy increasing IREB

3.1 Energy increasing IREB.

In the previous theoretical works [1-3] it was assumed that the electron pulses with a flat top waveform were the most suitable for superradiance (SR) emission (similar to the case of steady state generation). It was shown in [6] that due to nonstationary nature of SR emission an accelerating voltage should change over electron pulse duration to enhance peak amplitude of electromagnetic pulse. Optimization of profile of voltage and current pulses provided possibility for increasing peak power of SR pulses. In the case of cylindrical corrugated waveguide, the simulated results showed that the increasing energy and current waveforms made the microwave output twice larger than flat top waveforms (Fig. 9).

However, it is technically difficult to control the waveforms at the diode, because a cold cathode and an anode are utilized for conventional IREB generator. The voltage between diode applied by a Marx generator and a pulse forming line is changed by the evolution of the diode impedance caused by cathode and anode plasmas. There is no way to control the plasmas. On the other hands, propagation characteristics of an IREB through drift tubes with coaxial cavities are studied intensively for autoacceleration or automodulation. The waveforms of an IREB can be reformed by a coaxial cavity located at the drift tube (Fig. 10). When the IREB reaches at the gap, electrons are decelerated because of sudden increase of the radius of the drift tube. The decelerated voltage across the gap is induced. The voltage between the inner and the outer wall propagates through the coaxial cavity and it is reflected at the shorted end of the cavity. As the polarity of the voltage becomes opposite at the shorted end, the accelerated voltage appears at the gap after the round trip time for the electromagnetic wave in the cavity. The time dependence of the gap voltage, $V_g(t)$, is expressed as the equation below by transmission line theory.

$$V_g(t) = Z \times (I(t) - 2I(t - T) + \cdots,), \quad (1)$$

where Z is the impedance of the cavity, I is the beam current and T is the round trip time for electromagnetic wave in the cavity. Using the waveform of the beam current detected in the experiment, appropriate length of the cavity for an energy increasing waveform can

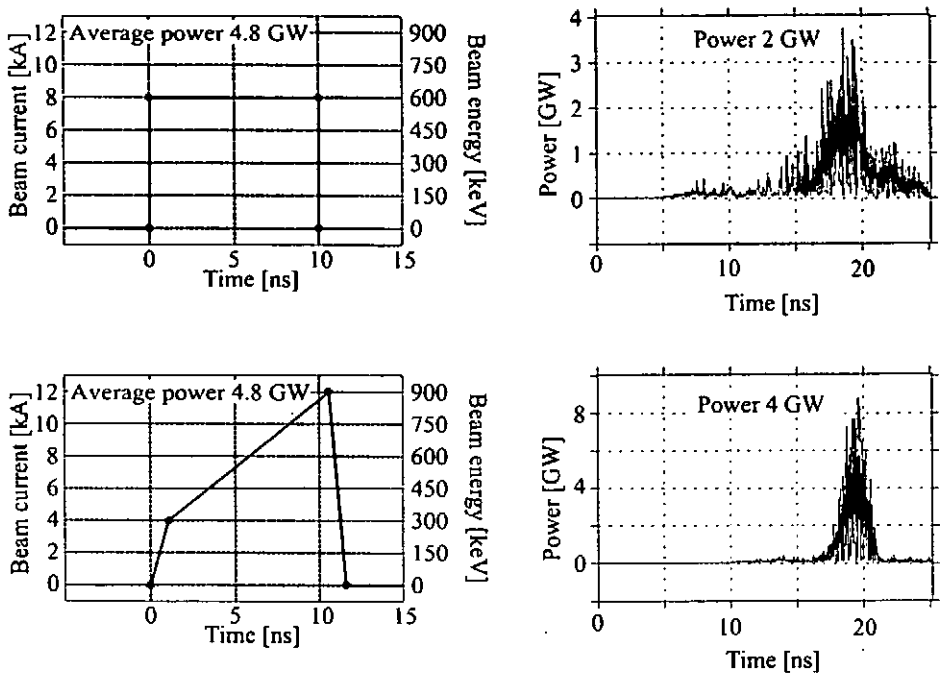

Fig. 9: Left: waveforms of beam current and energy. Right: microwave output. Upper: square shape. Lower: increasing in time.

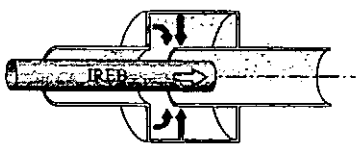

Fig. 10: A coaxial cavity is connected to a drift tube via gap. Induced gap voltage reform the time evolution of energies of beam electrons.

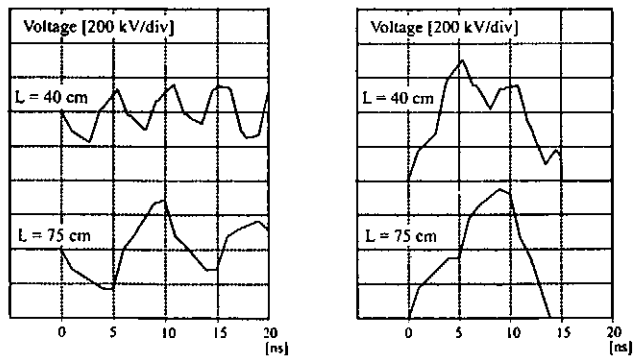

Fig. 11: Calculated gap voltage (left) and the expected time evolution of electron energy (right).

be evaluated by above equation (Fig. 11). As the time evolution of the incident beam energy is expressed by the inductively corrected diode voltage waveform, that of beam energy passed through the gap is evaluated by sum of the diode and the gap voltages. The time evolution of beam energy is reformed by a cavity as shown in Fig.11. The waveform of the beam energy can be changed by the length of the cavity. As this scheme is strongly limited by the incident waveform of the beam current, it is better to be applied together with the reconstruction of the diode structure to obtain a suitable beam current waveform.

3.2 Experiments.

Pulserad 105A is utilized to generate an IREB of 580 keV, 3 kA, 15 ns. Schematic of the experimental setup is shown in Fig. 12. The foilless diode consisted of a carbon cathode with hollow knife-edge of 15 mm diameter and a carbon anode with 30 mm diameter aperture. An annular electron beam with diameter of 17 mm and thickness of 1 mm was injected from the diode into a conducting drift tube with inner diameter of 31 mm and a coaxial cavity. The system was immersed in axial magnetic field of 1 T applied by solenoid coils. A cavity whose length is variable is located 20 cm downstream side of the anode. The gap spacing of the cavity is 3.0 cm and the impedance of any cavity is 76 Ω. The base pressure in the system was maintained below 1×10^{-5} Torr. A Faraday cup is

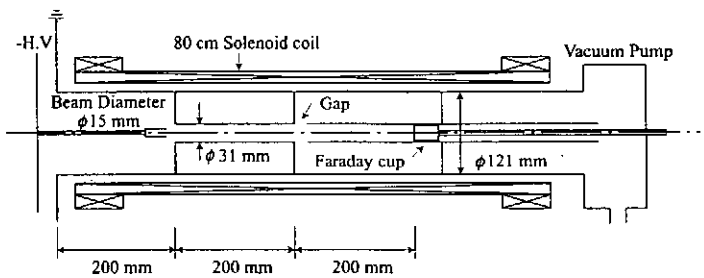

Fig. 12: Experimental setup of formation of energy increasing IREB.

used to measure the beam current at various locations along the axis in the drift tube and to estimate the kinetic energy of beam electrons. Aluminum foils of various thicknesses are placed in front of the Faraday cup and a transmitted current through aluminum foils is measured. Using the ratio of the transmitted current to the current detected without foil and the range-energy relations, the kinetic energy of beam electrons is estimated. A magnetic analyzer located at the end of the drift tube is used to check the electron kinetic energy obtained by the range-energy relations. And the measured energy is in good agreement with the estimated one. Magnetic probes are also used to measure the beam current and the current at the end of cavity. The differentiated currents detected by magnetic probes are integrated numerically.

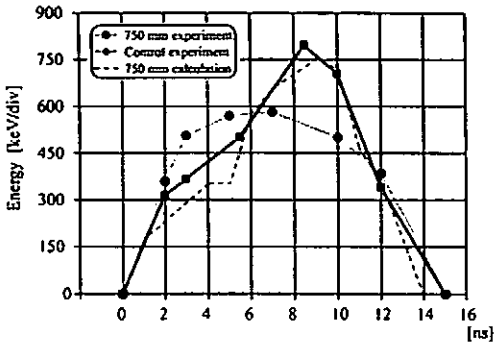

Fig. 13: Time evolution of beam electron energy with a 750 mm cavity.

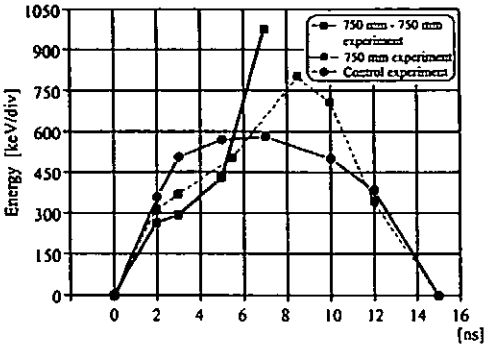

Fig. 14: Time evolution of beam electron energy with two 750 mm cavities.

The time evolution of beam electron energy measured by a Faraday cup with aluminum foils agrees with the calculated results as shown in Fig. 13. When the cavity length is set to 75 cm, the gradual increasing energy beam is obtained. The time evolution of electron energy can be changed using a single cavity within the limit of initial diode waveform. It can be estimated for different cavity lengths. Moreover, the energy increasing rate for time can be increased by using two cavities (Fig. 14). The length of the second cavity is also decided by eq. (1) using the current passed through the first gap.

Now, it becomes possible to change the time evolution of the beam energy using a coaxial cavity. However, the waveform of the beam current is not mentioned yet. We propose to use a drift tube with thicker radius behind a coaxial cavity (Fig. 15). As shown in Fig. 16, the waveform of the beam current passing through a thicker drift tube is reformed in the simulation. The appropriate radius, length and position will be examined experimentally.

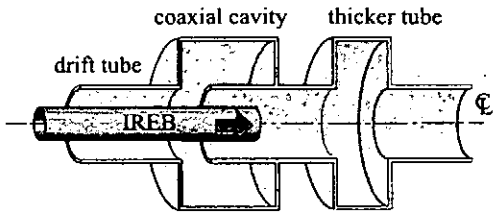

Fig. 15: A drift tube with thicker radius is located downstream side of the coaxial cavity.

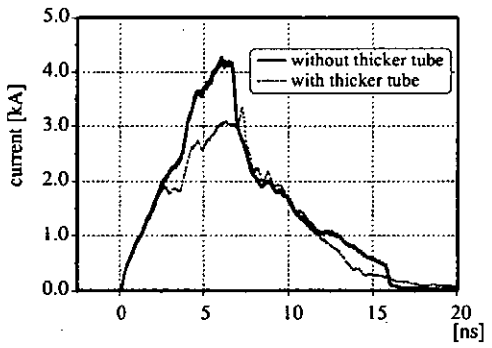

Fig. 16: Time evolution of beam currents is reformed by a thicker tube.

4 Conclusion

A cylindrical corrugated waveguide is designed to expect 5 GHz microwave with output power of 1 GW. The simulation results suggest that the mechanism of the microwave generation has a pulsive character. It is found that the length of the injected beam has an optimum value for microwave output. The formation of the energy increasing waveform is possible using a coaxial cavity for enhancement of the microwave output.

Acknowledgement

A part of this work is supported by a Grant-in-Aid for Scientific Research from Ministry of Education, Science, Sports and Culture, Japan

References

[1] N. S. Ginzburg, I. V. Zotova A. S . Sergeev I. V. Konoplev A. D. R. Phelps A. W. Cross S. J. Cooke, V. G. Shpak, M. I. Yalandin, S. A. Shunalinov, and M. R. Ulmaskulov, "Experimental observation of cyclotron superradiance under group synchronism conditions",, Phys. Rev. Lett., 78, pp. 2365-2368, (1997).

[2] M. I. Yalandin, V. G. Shpak, S. A. Shunailov, M. R. Ulmaskulov, N. S. Ginzburg, I. V. Zotova, A. S. Sergeev, A. D. R. Phelps, A. W. Cross, K. Ronald, S. M. Wiggins, "Generation of powerful subnanosecond microwave pulses in the range of 38-150 GHz", IEEE, vol. 28, pp. 1615-1618. 2000.

[3] S. M.Wiggins , D. A. Jaroszynski, B. W. J. McNeil, G. R. M. Robb, P. Aitken, A. D. R. Phelps, A. W. Cross, K. Ronald, V. G. Shpak, M. I. Yalandin, S. A. Shunailov , M. R. Ulmaskulov, N. S. Ginzburg, "Self-amplification of coherent spontaneous emission in a Cherenkov free-electron maser ", Phys. Rev. Lett., vol. 84, pp. 2393-2396. 2000.

[4]K. Kamada, D. Hasegawa, K. Shimizu, R. Andou and M. Masuzaki, "Two-stage autoacceleration using decreasing length cavities", IEEE Trans. Plasma Sci., vol. 27, pp. 1609–1610, 1999.

[5] D. Hasegawa, K. Kamada, K. Shimizu, R. Andou and M. Masuzaki, "Four-stage autoacceleration for a subnanosecond intense relativistic electron beam", IEEE Trans. Plasma Sci., vol. 28, pp. 1648–1651, 2000.

[6] N. S. Ginzburg, I. V. Zotova, R. M. Rozental, A. S. Sergeev, M. Kamada, K.Sugawara , K.Kurihara, H. Shirasaka, R. Ando, K. Kamada:, " Increasing of peak power of superradiation pulses by variation of accelerating voltage", Proc. 14th Int. Conf. High-Power Particles Beams, (Albuquerque USA, 2002), pp. 291-294, 2002.

[7] V. P. Tarakanov, "Users manual for code KARAT", vor. 7.09, 1999.

EUV SPECTROSCOPIC MEASUREMENT OF AN ARGON Z-PINCH PLASMA

F. Kobayashi and K. Takasugi

College of Science and Technology, Nihon University
1-8-14 Kanda-surugadai, Chiyoda-ku, Tokyo 101-8308, JAPAN

ABSTRACT

Spectroscopic measurements of EUV light emitted from an Ar gas-puff z-pinch plasma has been carried out. Spectra of both Ar IX and Ar X were observed, and the electron temperature of the region where these ions exist was estimated to be 50 - 80 eV. In the experiment using Al electrodes, a spectrum of Al V was observed at 13.08 nm.

I. Introduction

Gas-puff z-pinch is known as a compact, efficient and repetitive source of x-ray and EUV radiation.[1] High temperature and high density plasma called hot spot is generated by self-contraction of the z-pinch column, and it radiates strong pulsed soft x-ray. In the Ar gas-puff discharge of the SHOTGUN z-pinch, K-shell radiation of He-like Ar ion (~ 0.4 nm) is strongly radiated from the hot spots. X-ray spectroscopy shows that the electron temperature of those spots is nearly 1 keV.[2] As the strong contraction is driven by $m = 0$ mode of instability, the plasma temperature is considered to be distributed. L-shell radiations of Ar ion exist near the Water Window region (2.3 - 4.4 nm), and they are emitted from plasmas whose electron temperature is around 100 eV. As the pulse width of emission is different between soft x-ray and EUV light, the temperature is distributed both spatially and temporally.[3] The spectral region of radiation has been controlled by applying axial magnetic field.[3] K_α radiations of metal vapor of wall and electrode materials was observed, and it was confirmed that cloud structure of x-ray image was made up of them.[4, 5]

Recently, EUV light source of wavelength region 11 - 13 nm is demanded as that for the next generation semiconductor lithography. For this reason, development of the light source using Xe or Al has been undergoing. Although it is thought that Ar plasma does not emit light in this wavelength region in itself, depending on electrode material, the light is emitted in this region. In order to know the EUV spectral characteristic in wide region, EUV spectroscopy of Ar z-pinch plasma has been tried.

II. Experimental Setup

The device here used for spectroscopic measurement is the SHOTGUN z-pinch. The schematic of the device is shown in Fig. 1. The storage section consists of 24 μF fast capacitor bank which is charged up to 23 kV (6.3 kJ). Pressurized gas is puffed by a high speed gas valve through hollow nozzle mounted on the anode. The plenum pressure is 8 atm and Ar gas is used in the experiment. The cathode has many holes in order to prevent stagnation of gas. The spacing between the electrodes is 30 mm. Although the POS section for the experiment of plasma opening switch is attached on the power supply side, it is not used

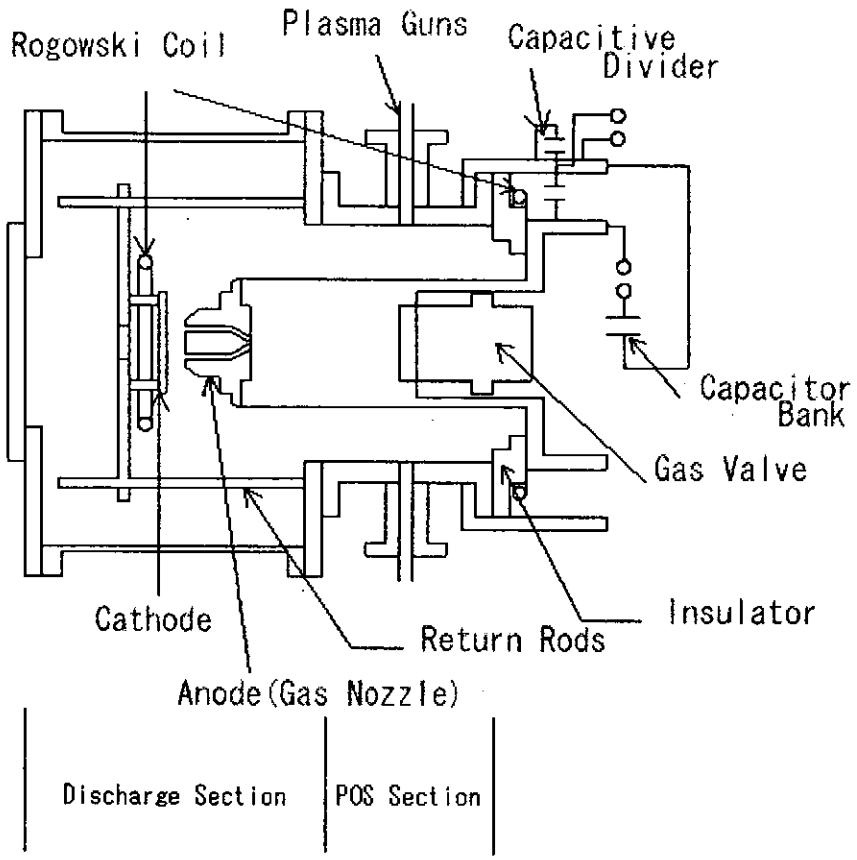

Fig. 1 Schematic view of the SHOTGUN z-pinch device.

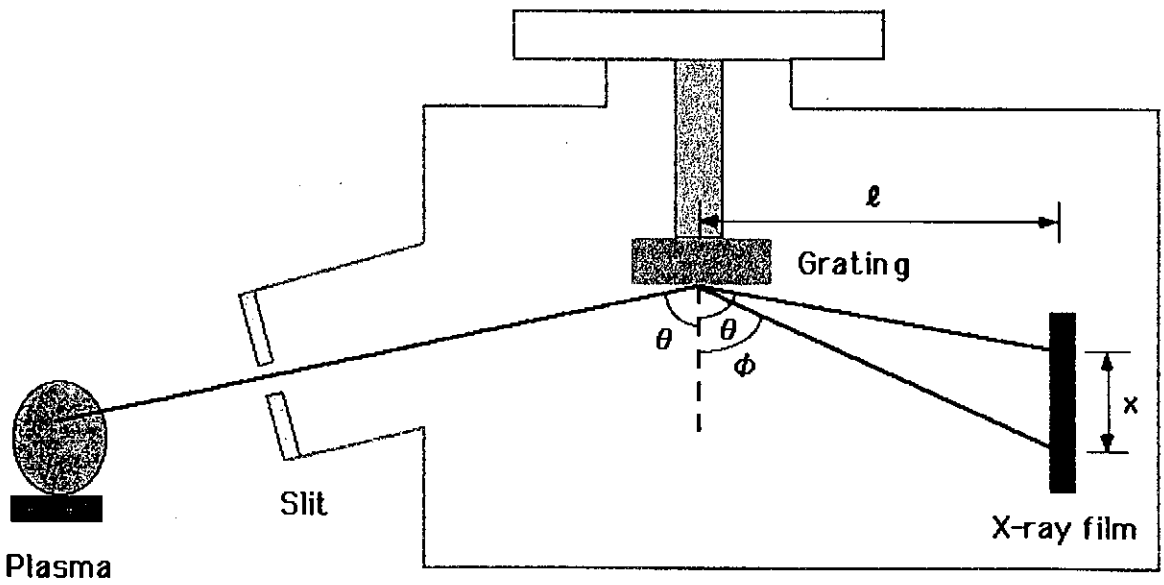

Fig. 2 The glazing incidence spectrometer for EUV light (4 – 20 nm).

here. Rogowski coils are used for the measurement of discharge currents. The anode coil measures the input current from the power supply, and the cathode coil measures the current that flows between the electrodes.

A scintillation probe was used to detect time dependent signal of soft x-ray emitted from the plasma. The sensitive energy region of the probe is restricted above 1 keV by a 10 μm Be filter. This region is about the K-shell radiation of Ar ions and K_α radiation of impurity metals coming from Hot Spots. Luminescence of plastic scintillator is introduced to the shield room using an optical fiber, and is converted to electric signal by a photomultiplier. The EUV light emitted from the plasma is detected by an x-ray diode (XRD) with Al photocathode. XRD is a detecting instrument using photoelectric effect. The sensitive range of XRD is spreading from UV to soft x-ray (1 – 100 nm). The XRD signal mainly shows L-shell radiations of Ar ions.

A glazing incidence spectrometer was used for the measurement of EUV light. Figure 2 shows the schematic of the spectrometer. The grating has the groove density 1200 lines/mm, and is coated by Au. The spectrometer is designed at the incident angle $\theta = 87°$. Kodak DEF film was used for recording EUV spectra. Since there is no filter between the plasma and the film, all light can be led to the film without loss. The distance between the grating and the film is 235 mm. The available range of EUV light in the spectrometer is 4 - 20 nm.

III. Experimental Results

The examples of the discharge current in the z-pinch operation region, the XRD signal, and the signal of the scintillation probe are shown in Fig. 3. Three set of strong contraction occurred, and dips in the current waveform and soft x-ray emission occurred in connection with them. The shape of the scintillation probe signal is sharp pulse. This is mainly from K-shell radiation of Ar ions and K_α radiation of impurity metal atoms.[5] Pulse width of XRD signal is wider than this, and this shows that the EUV radiation lasts longer than the soft x-ray radiation.

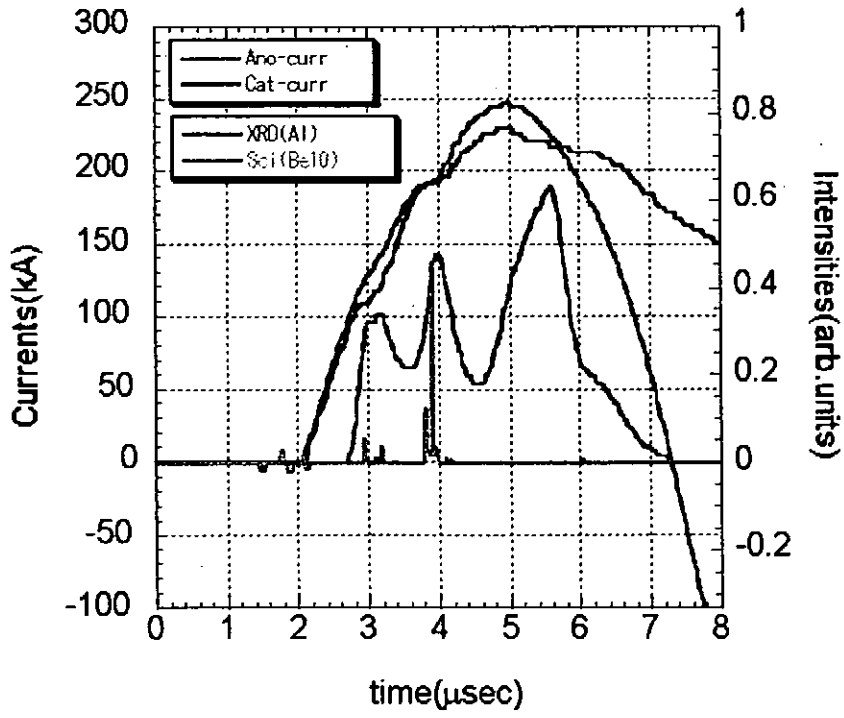

Fig. 3 Example of discharge currents, x-ray and EUV signals.

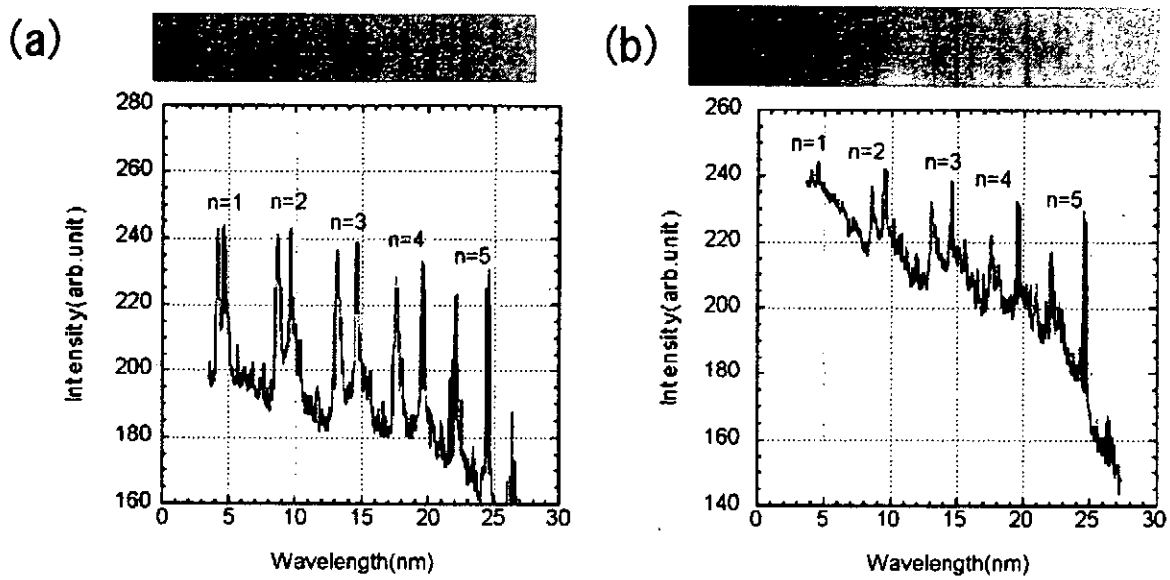

Fig. 4 EUV spectra of discharges with (a) C and (b) Al electrodes.

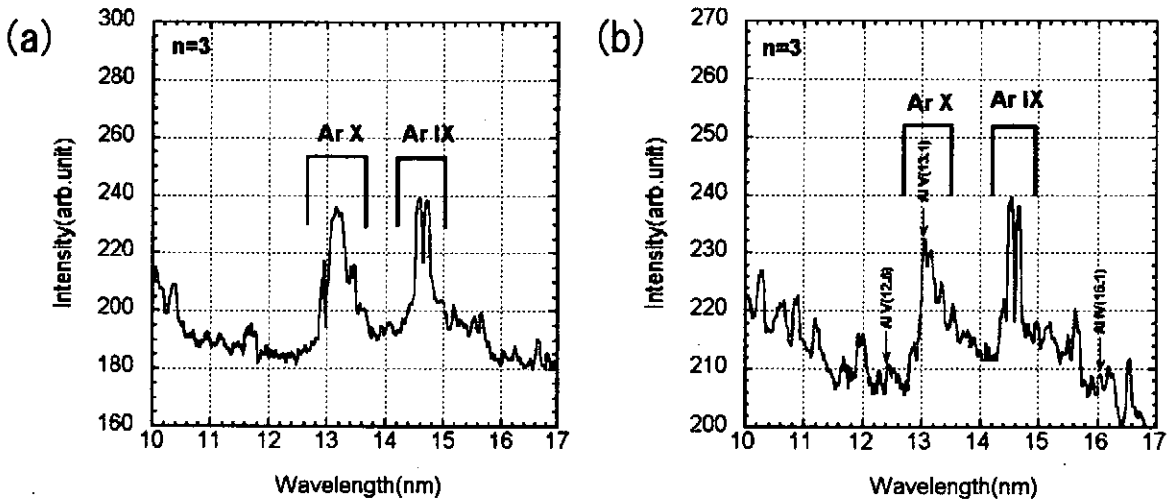

Fig. 5 EUV spectra near the third diffraction region with (a) C and (b) Al electrodes.

The results of EUV spectroscopy is shown in Fig. 4 for the case of (a) C electrode and (b) Al electrode. Both figures clearly show that periodic spectra have appeared. These are the integral multiples of wavelength of two groups. One is Ar X (4.327 to 4.503 nm), and another is Ar IX (4.873 and 4.918 nm). Figure 5 shows the spectral region near the third diffraction (n = 3). In Fig. 5 (a) only Ar spectra are observed, and no other line was found in the C electrode discharge. The lines of Ar X and Ar IX have almost equal intensity. On the other hand some characteristic lines of Al ions were observed in the Al electrode discharge (Fig. 5 (b)). The lines of Al V (12.60 and 13.08 nm) and Al IV (16.01 nm) are shown in the figure. The line of Al V (13.08 nm) is rather intense. The intensity of Ar X is a little weaker than Ar IX for this case.

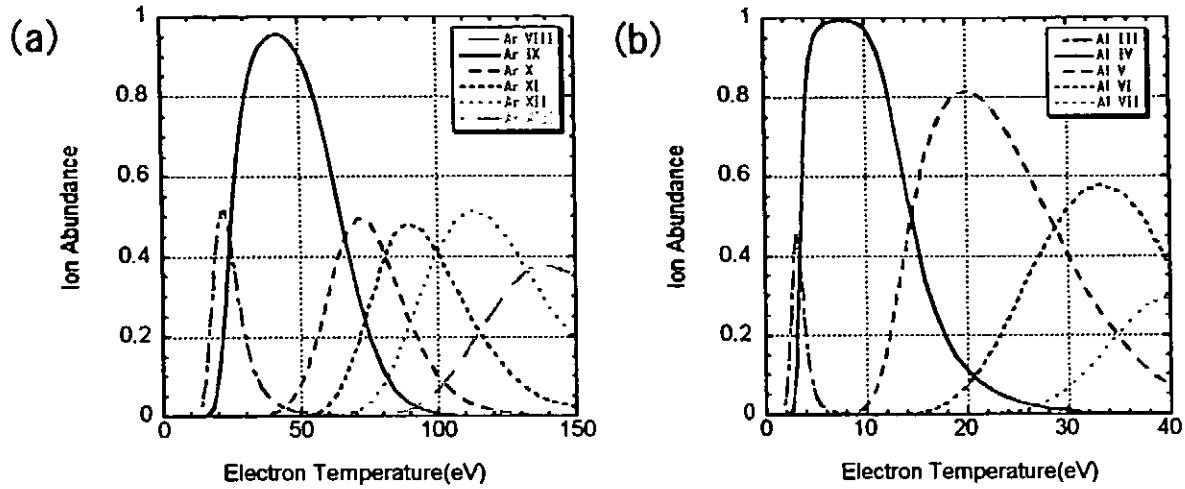

Fig. 6 Ion abundances of (a) Ar and (b) Al ions in Corona equilibrium.

IV. Summary and Discussion

The temperature of the plasma can be presumed to some extent according to the kind of existing ions. Spectroscopy shows Ar IX and Ar X always existed in the plasma. Figure 6 shows ion abundances of (a) Ar ions and (b) Al ions assuming Corona equilibrium. In the case of Ar ion, the temperature range with which Ar IX and Ar X coexist is 50 - 80 eV. The plasma which emits EUV light turns out to be lower in temperature than the hot spots. And XRD data shows that the self-sustaining time for the EUV emitting plasma is longer than that for the hot spots.

In the experiment using Al electrodes, the spectrum of Al V was observed near wavelength 13 nm. The electron temperature range for which Al V exists is 10 - 40 eV. The result that impurities exist in the region of the cloud structure which spread rather than z-pinch column is obtained from the spatially resolved measurement of x-ray spectroscopy of impurities. And the difference in temperature is thought to be the difference in the space distribution.

In comparison of C and Al electrodes, the intensity of Al X is a little weak in the Al electrode experiment. This indicates that the electron temperature for Al is a little lower than for C. The reason for this is radiative energy loss is larger for Al than C.

References

1) K. Takasugi, H. Suzuki, K. Morioka and T. Miyamoto: Jpn. J. Appl. Phys. **35**, 4051 (1996).
2) N. Akiyama and K. Takasugi: NIFS-PROC-51, 17 (2002).
3) K. Takasugi, T. Miyamoto, K. Moriyama and H. Suzuki: AIP Conf. Proc. **299**, 251 (1994).
4) S. Narisawa and K. Takasugi: NIFS-PROC-51, 11 (2002).
5) K. Takasugi, S. Narisawa and H. Akiyama: AIP Conf. Proc. **651**, 131 (2002).

STUDY OF CAPILLARY DISCHARGE LIGHT SOURCE FOR EXTREME-ULTRAVIOLET LITHOGRAPHY

T. Kasao, M. Okamoto, I-H. Song,
M. Watanabe, A. Okino, K. Horioka and E. Hotta

Department of Energy Sciences, Tokyo Institute of Technology,
Nagatsuta, Midori-ku, Yokohama, 226-8502, Japan.

ABSTRACT

Extreme-ultraviolet (EUV) lithography is most promising technology for 50 nm technology node which will be used from around the year 2007. There are many issues for realizing EUV lithography such as developing optical components and radiation sources and one of the most important challenging tasks is to develop an EUV light source. Various technical concepts for realizing high power sources for EUV lithography are under investigation worldwide. Laser produced plasmas (LPP) and discharge produced plasmas (DPP) are the most promising schemes. In general, DPP methods are of special interest, because their prospected costs for the demanded throughput is expected to be much lower than those of LPPs. However, the discharge plasmas are of high risk, because many crucial problems have to be solved before reaching the required power levels.

In this work, a high repetitive, compact and low-debris Xe-filled capillary Z-pinch discharge system has been designed and fabricated as an EUV source. We devised an electrode configuration compatible with that system and applied a magnetic switch and a static induction (SI) thyristor stack as a main switch.

1. Introduction

Extreme ultraviolet lithography (EUVL) is under discussion to be the successor of the deep ultraviolet lithography to reduce structures in semiconductor devices to below 70nm. The use of extreme ultraviolet radiation around 13nm ~ 14nm in comparison to the longer wavelength UV radiation allows to reduce the structure sizes and offers as well a sufficient large depths of focus. The usable spectral band is defined by the fact that there is a consensus to use molybdenum-silicon multilayer mirrors, which best compromise high reflectivity and usable bandwidth around 13.5nm [1]. A debris free EUV source with collectable radiation power of about 100W will be required to achieve an economical wafer throughput of up to 100 wafer/hour and up to now few sources have been developed to test bed maturity for long time operation or with repetition rates exceeding 1kHz. In principle there are many different concepts to generate laser produced and gas discharge plasmas. Common to all approaches and all concepts is that optimized conversion efficiency is of major importance because this minimizes the demand on driving power for demanded EUV power. The driving power influences directly the cost of ownership of the source with

respect to both investment costs and operational costs so that a source with lowest driving power has best chances for technical realization. For DPP, since the electrical energy is directly converted into the plasma energy, high plug-in conversion efficiency can be expected and the conversion efficiency depends on the method to generate proper discharge plasmas and parameters to operate such a system. So the chances to succeed in developing a viable source are greater than DPP. There are several types of DPP light sources, Z-pinch, capillary-discharge, dense plasma-focus and hollow-cathode triggered Z-pinch, etc. In Fig. 1, schematic drawings of typical discharge devices are shown. The comparisons of these methods are well defined in the reference [2]. With all discharge systems under investigation the driver current is generated in a fast discharge of electrically energy stored in a capacitor at a high voltage. To achieve the required plasma temperature the duration of the compression has to be on the order of sub-microsecond. Several concepts are known which differ in the geometry of the electrode system and the current pulse generator.

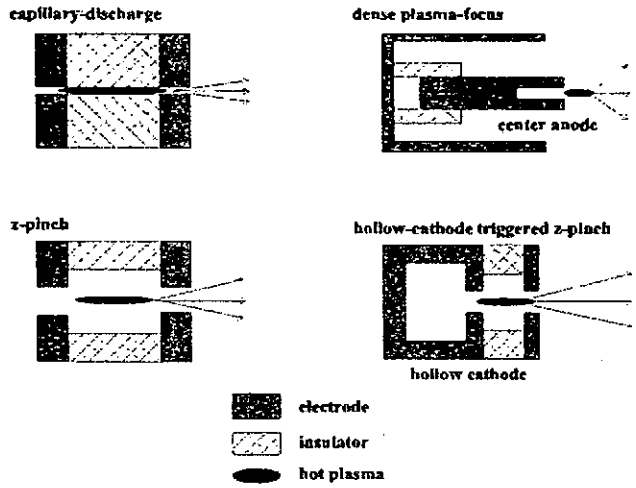

Fig. 1. Schematic drawings of typical discharge devices

We have been investigated the capillary Z-pinch discharge as a potential source for the EUV lithography. However, it has a problem of debris generation, which is due to the melting and evaporation of electrodes and a capillary caused by the excess input of heat into their surfaces and the fact that the pinching plasma interacts stronger with the insulator surface than others. In order to overcome these difficulties and to satisfy the source requirements, following means have been planned. (1) Restriction of the electric energy input to minimum for getting moderate EUV output by increasing conversion efficiency, (2) plasma confinement by magnetic field away from a capillary wall, (3) minimization of current density on electrode surface and large EUV collection angle, (4) stabilization of magnetically confined plasma column, (5) stabilization of plasma position.

At present, following parameters have been obtained elsewhere for DPP light sources: EUV output is 10~20W, the repetition frequency is 1kHz, the life of device is 10^6 pulses. By 2007, they should be increased to 80~120W, 5kHz, 10^{11} pulses, respectively. In this paper, we present the design of capillary Z-pinch discharge system and all solid-state pulse power system with magnetic switch and introduce the design concepts.

2. Experimental setup

2-1. Discharge section and Vacuum Chamber

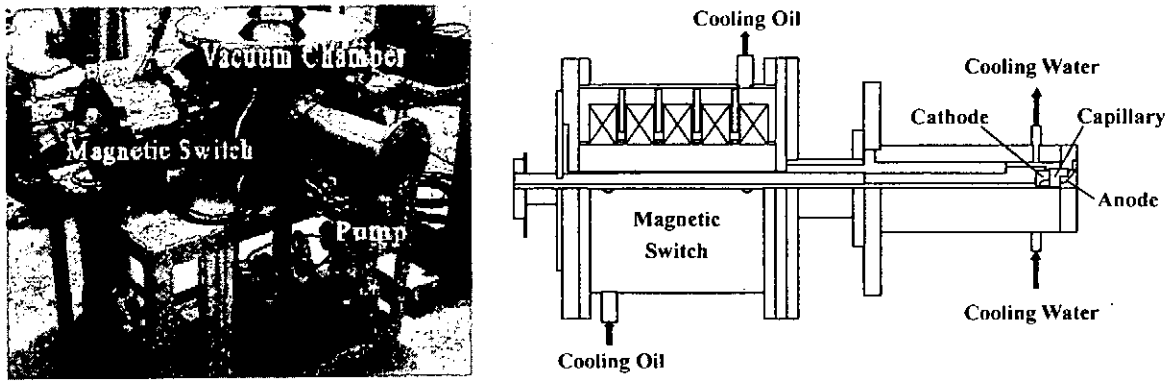

Fig. 2. Photograph and schematic drawing of magnetic switch and discharge section

In Fig. 2, a photograph of the device under construction is shown. Also, schematic drawing of a magnetic switch and discharge section is presented. The conductors are made of stainless steel and aluminum. The magnetic switch, which is set near the discharge section to decrease stray inductance, is used not only to assist a semiconductor switch but also to provide preionization current. It has been confirmed that a uniform and stable plasma can be generated by preionization [4] and details of preionization are described in the section 3. Magnetic cores used in the magnetic switch are cooled with oil.

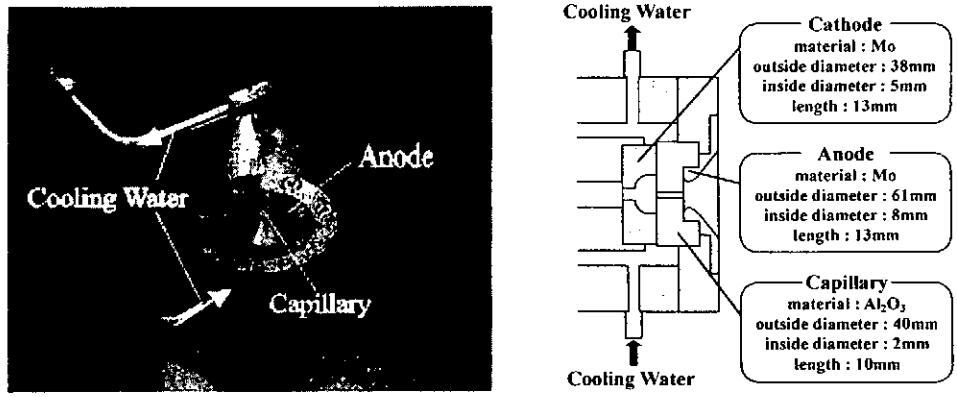

Fig. 3. Photograph and schematic drawing of discharge section

A photograph and a schematic drawing of the discharge section are shown in Fig. 3, respectively. The features of the discharge section are as follows. (1) To decrease the current density on the surfaces, the electrode structure has been made to have large surface area. (2) To get enough EUV light flux, the anode structure has been devised to have large collection angle. (3) To enable the high repetition rate operation, the electrodes and capillary can be cooled with forced water circulation. To increase the output power of gas discharge sources the electrical input power, especially the repetition rate, must be increased. This will lead to high thermal load on electrodes and insulators, which requires effective cooling. Cooling water, which cools the discharge section is fed through ports installed in the vacuum chamber.

Fig. 4 shows a schematic drawing of the whole device. Xenon gas of several hundreds Torr is fed through gas flow controller. Pressure is measured with vacuum gauges set upstream of the capillary and at

the vacuum chamber. The section encircled with an ellipse in Fig. 4 is the magnetic switch and the discharge section. This section of the device is connected to the vacuum chamber. The vacuum chamber has several ports for measurement and a lot of threaded holes inside at the bottom of the chamber in order to set up a gas curtain etc.

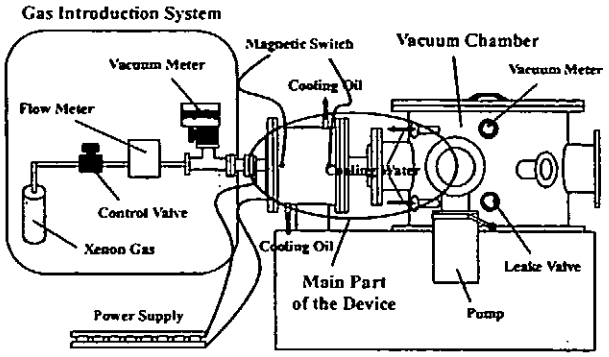

Fig. 4. Schematic drawing of whole device. Vacuum meter is vacuum gauge or pressure gauge, and gas introduction system is gas supply system

2-2. Pulsed power supply

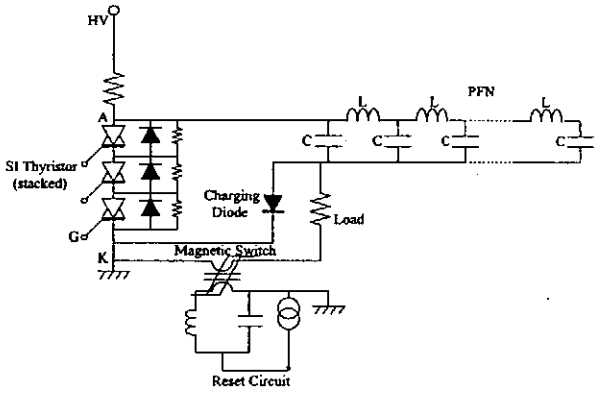

Fig. 5. Electric circuit of pulsed power supply

An electric circuit of the pulsed power supply used in this work is shown in Fig. 5. The device is mainly composed of a PFN (Pulse Forming Network), an SI (Static Induction) thyristor stack and a magnetic switch. The PFN is composed of 68 ceramic capacitors, each of which has a capacitance of 5.3nF and 20kV voltage rating. These are connected in parallel to make a 17 stage PFN. The measured total capacitance of the PFN is 360.4nF. SI thyristors are used as a main switching device. Since the SI thyristor has a high holding voltage and a high peak current, it is suitable for the pulsed power supply. The holding voltage of the used SI thyristor is 3.4 kV and surge current rating exceeds 10kA. Three SI thyristors are connected in series because the maximum charging voltage of PFN reaches 9 kV. A magnetic switch is connected in series. The magnetizing current leaking through the magnetic switch during the holding phase is used as the preionization current. The pulse power system is composed of all solid-state components, so we can increase the pulse repetition rate.

3. Results and discussions

In Fig.6, output waveforms of the pulsed power supply without the magnetic switch at charging voltage of 9kV is shown. The rise time of the current is 180 ns and the energy transfer efficiency is 90%. A good result has been obtained for the rise time of current and the efficiency. However, the output energy is 10.1J/shot and the energy loss in the thyristor stack is 0.8J/shot. The loss in the thyristor stack corresponds to about 70% of the entire loss. The loss leads to overheating of the thyristor when conducting high repetition rate operation. Therefore, it is necessary to reduce the loss in the thyristor. In Fig. 7, output waveforms obtained when a magnetic switch is connected in series is shown. Because the rise time of current depends on the performance of magnetic switch, increase of rise time should be prevented. The rise time of current measured when the magnetic switch is used is 160 ns. Therefore, the rise time of current is 20ns faster than that without the magnetic switch. The measurement of thyristor voltage and current confirms the remarkable reduction of heat loss in thyristor.

Next, the necessity of preionization will be described. In a Ne-like Ar soft X-ray laser experiment, the effect of preionization on the formation of plasma column has been confirmed. In the experiment, main currents were supplied through a capillary of 3 mm in diameter and 60 mm in length, which is filled with Ar of 150mTorr. In Fig. 8 and Fig. 9, framing photographs of the discharge plasma without and with preionization are shown. Without preionization, unstable plasma is generated. On the other hand, with preionization, plasma is stabilized and a thin stable plasma column can be obtained. Therefore, preionization is indispensable to generate stable plasma with good reproducibility.

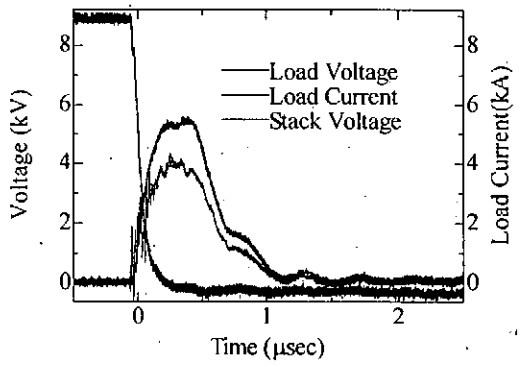

Fig. 6. The output waveforms of the pulsed power supply without the magnetic switch at 9kV

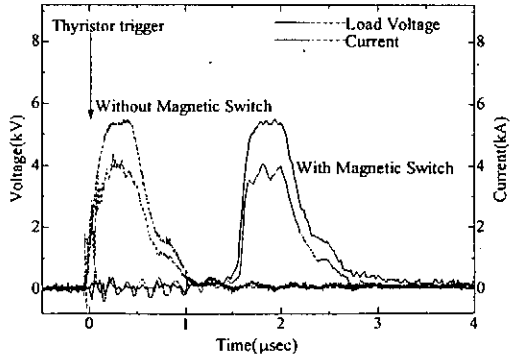

Fig. 7. The output waveforms of the pulsed power supply with and without a magnetic switch

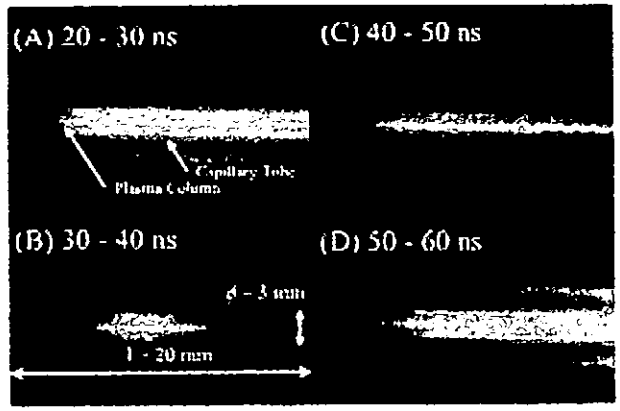

Fig. 8. Framing photographs of discharge plasma without preionization

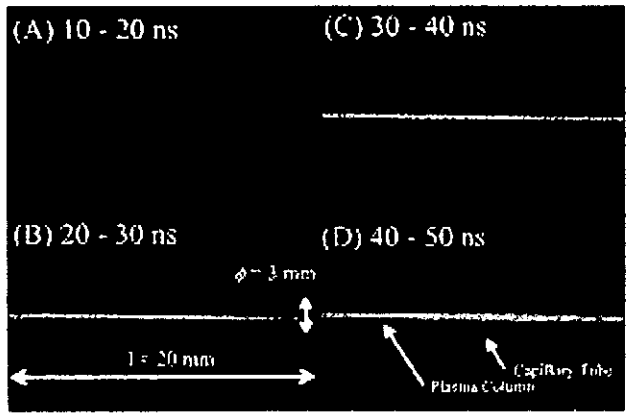

Fig. 9. Framing photographs of discharge plasma with preionization

4. Summary

The capillary z-pinch discharge light source for the EUV lithography has been studied. An experimental device was made devising the electrode structure of the discharge section and the method of cooling. For preionization, a magnetic switch was connected in series in the main electric circuit. The magnetizing current flowing during the hold-off phase is used as the preionization current. The insertion of magnetic switch improved the rise time of main current and reduced the loss in thyristors.

5. Acknowledgement

This work is partly supported by Extreme Ultraviolet Lithography System Development Association (EUVA).

References

[1] J. E. Njorkholm, Intel Technology Journal Q3'98, p.1-8

[2] W. Neff, K. Bergmann, O. Rosier, R. Lebert, L. Juschkin, Contrib. Plasma Phys., 41 (2001) 6, p. 589-597

[3] K. Yamashita, P. R. Chalise, M. Watanabe, A. Okino, E. Hotta, K-C. Ko, N. Shimizu and K. Iida: *Proc.*

European Pulsed Power Symposium, 2002, p. 17/1.

[4] G. Niimi, Y. Hayashi, N. Sakamoto, M. Nakajima, A. Okino, M. Watanabe, K. Horioka, and E. Hotta: IEEE Trans. Plasma Science, **30** (2002) 616.

SPECSTROPIC MEASUREMENT OF Ne-LIKE Ar SOFT X-RAY LASER PRODUCE BY CAPILLARY Z-PINCH DISCHARGE

Yasushi Hayashi, Hiroaki Taniguchi, Masato Watanabe, Akitoshi Okino,
Nobuhiro Sakamoto, Kazuhiko Horioka and Eiki Hotta

Department of Energy Sciences, Tokyo Institute of Technology
4259 Nagatsuta, Midori-ku, Yokohama 226-8502, Japan

ABSTRACT

We have performed observations of Ne-like Ar soft X-ray laser generated from a capillary z-pinch discharge, by varying the distance from the end of the capillary and the measuring point. Soft X-ray output measured with a XRD shows a spike signal near the pinch time, and this spike is found to have strong directivity. Spectroscopic measurements have also been performed to study the line spectra of the soft X-ray output. A strong line has been observed at λ=46.9 nm, and it is found that this line also possesse directivity. Among the line spectra, the line spectrum at 46.9 nm is the only one that shows directivity just as the spike signal observed by the XRD experiments does. Thus, it is concluded that the spike observed from the XRD output is identical to the Ne-like Ar lasing at 3p - 3s level. In a focusing experiment, the background light with an image of 10 mm in diameter is focused into a spot of 1mm by a grazing incident mirror. This is the first observation, using a Wolter type mirror, of the focusing of the soft x-ray emitted from capillary discharge.

I. Introduction

Soft X-ray lasers have been expected as a key technology by the modern scientific research and development. It exhibits not only excellent characteristic as a laser, but also some unique properties of the soft X-ray. However, the problem that exists for this kind of laser is their low energy conversion efficiency. A Z-pinch using a capillary discharge is considered as the solution of this problem, because its lasing equipment and power source can be reduced to a "Table-top" size. In 1994, Rocca has first observed this kind of laser, which appears as a spike in the XRD output. Same kind of spike signal has also been reported in our recent works [2-4]. However, in order to prove that the spike observed on the XRD output signal is identical to the Ne-like Ar lasing (J=0-1, λ=46.9 nm), it is necessary to perform a measurement of the wavelength.

Spectroscopic measurement has been performed using a grazing incidence spectrometer. The line at 46.9 nm has been observed. From the experiment conducted by changing the distance between the end of the capillary and the grating from 35 to 80 cm, it was confirmed that the line has shown strong directivity. Among the XRD outputs, the spike is the only one that shows directivity. This implies that the spike signal in the XRD output is attributed to the Ne-like Ar lasing at λ=46.9 nm. The XRD measurement has also been performed by varying the capillary length.

Focusing of the soft x-ray has also been tried by using a Wolter type mirror. It is found that

the soft x-ray beam of 10 mm in diameter can be focused into a spot of 1 mm. The detail about the experiment will be given in the next sections.

II Measurement of the soft X-ray output

The device used in the experiment is schematically shown in Fig.1. The capillary used is made of Al_2O_3 ceramics with an inner diameter of 3 mm and a length of 150 mm. In order to reduce the noise from the background and the reabsorption of laser light by the neutral argon gas between the end of capillary and the XRD, a pinhole of 1 mm in diameter is set at a distance of 15 mm from the end of the capillary and the space between them is pumped through the pinhole. The XRD is used for detection of the laser output. The distance between the pinhole and the XRD is adjustable in order to obtain a qualitative indication of the directivity of the output. The optical alignment has been performed before the system was connected to the power system.

The discharge system is driven by a pulsed power supply, which consists of a 3-stage Marx generator, a 2:30 step-up transformer and a pulse forming line (PFL) made of a water capacitor. The impedance of the PFL is 5.5 Ohm. The capillary is pre-discharged by a current of up to 20 A, which is provided by a separate circuit. The maximum output voltage of the Marx generator is 60 kV, which subsequently yields a PFL output voltage of 430 kV. With this power supply system, it is able to obtain a discharge current pulse of up to 32 kA.

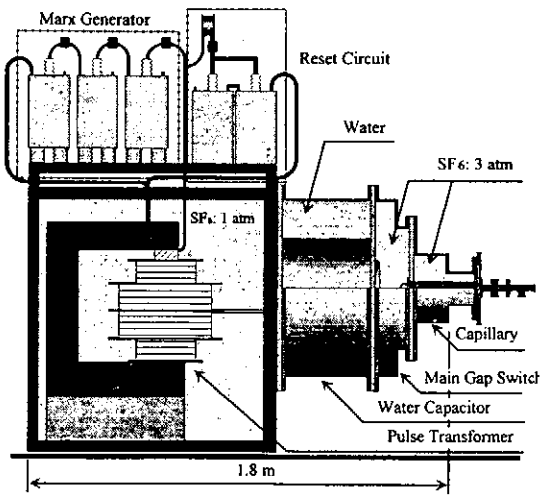

Fig.1 Schematics of experimental apparatus

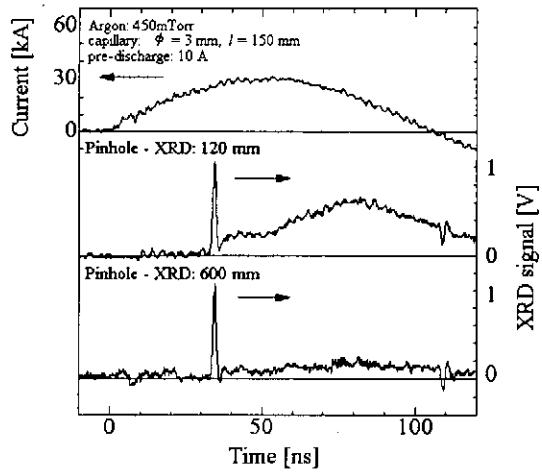

Fig.2 Soft X-ray output measured by changing the distance between the end of the capillary and XRD

Figure 2 shows the soft X-ray laser outputs measured by changing the distance between the end of the capillary and the XRD. Ar gas pressure is 450 mTorr. The discharge current has a peak value of 32 kA and a pulse width of 100 ns. Spike signal in the XRD output has been observed at about 33 ns. The amplitude of spike signal does not change while the distance between the end of capillary and the XRD detector is changed from 120 mm to 600 mm. This indicates that the spike signal has directivity. The directivity is known as a characteristic of laser. However, in order to reveal that the spike signal observed on the XRD output is identical to the Ne-like Ar lasing (J=0-1, 46.9 nm), it is necessary to perform measurement of the wavelength. In the present study, we have performed spectroscopic measurement, and its detail is given in the next section.

II Measurement of beam divergence and method of alignment

Prior to the spectroscopic measurement, some works have been done on observation of the divergence of the background light and alignment. The former measures the divergence of the background light in order to know the axial position that we should locate the spectrometer, and the latter is to know the exact position of slit in a direction perpendicular to the light axis. The alignment, particularly, is an important process in many optical experiments. However, in the case of a soft x-ray experiment, because the light is invisible, alignment is generally done using a subsidiary visible laser beam. This induces errors to the measurement because the direction of the subsidiary laser beam cannot be exactly the same as the soft x-ray beam. In the present study, we adopt a method of alignment, which uses directly the soft x-ray beam. Using this method, the deviation of the beam position can be minimized.

Figure 3 shows the experimental set up for the beam divergence measurement and the alignment experiment. The capillary and pumping system are the same with those of our previous experiments[2-4]. A phosphor screen is introduced at a variable distance from the end of the capillary, which is painted with fluorescent material only sensitive to the light in soft x-ray range. A digital camera (Olympus, Camedia E-20) is set behind the phosphor screen to record the image of the light spot.

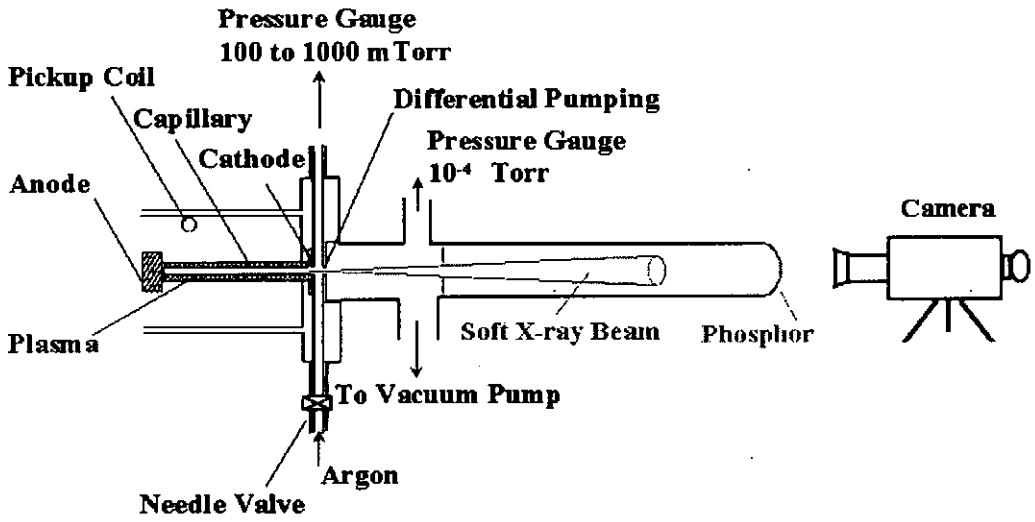

Fig.3 experimental apparatus for measurement of beam divergence and alignment

Figure 4 shows the images of the light spots taken at distances of 40, 60 and 80 cm downstream from the end of the capillary. Unfortunately, we are unable to observe the laser beam because it has a pulse width of only 3ns and may be faded out by the background light. The radius of the light spot expands in a rate of α=0.015 to the axial distance L, which approximately agrees with the result of calculation using the dimension of the pinhole. This indicates that the intensity of the background light reduces in a rate of $1/(\alpha L)^2$, which then gives us an indication on the axial distance that the spectroscopic device should be set for the observations with or without background light. These photographs are then analyzed to obtain the center of the beam spot. Alignment is performed based on the above-mentioned method to find center locations, which then used to define the optical axis. The final deviation of the beam axis is found to be lower than 1mm, which is smaller than the size of the laser beam.

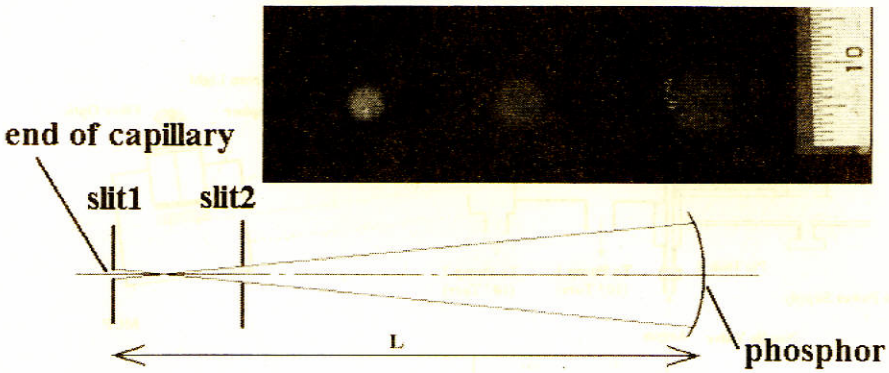

Fig.4 Beam spot measured by changing the distance between the end of capillary and the phosphor screen

III Spectroscopic measurement

Figure 5 shows a schematic drawing of the device used in the present experiment. The left part of the device is the capillary, which is the same as that we have described in our previous papers[2-4]. A grazing incidence grating (McPherson Model 248/310G) is located at a distance from the end of the capillary. The distance between the end of the capillary and the grating can be changed from 35 to 80 cm, in order to conform the directivity of the laser. In the present experiment, the incident angle is set to approximately 87 degrees. On the Rowland circle, at a distance downstream from the grating, a movable MCP is installed to receive the light. The position of the MCP is adjustable along the Rowland circle using a ball slide. A phosphor screen and a fiber plate are installed in sequence to observed the lines at each wavelength. The voltages applied between the two sides of MCP and the phosphor screen are 0.85 and 3.4 kV, respectively. The wavelength of the light is calibrated by using the He II lines at λ=25.6 and 30.4 nm obtained from the He discharge in the same capillary. With this measurement system, it is possible to measure the spectra of wavelength from 1 to 70 nm.

The lines observed when the distance between the end of the capillary and the grating from 35 to 80 cm are shown in Fig.6. When setting the grating at the distance of 35 cm from the end of the capillary, many lines have been observed, which include not only the line at λ=46.9 nm, but also the lines due to the background light. As we set the distance to 80 cm, the background lines fade out and the line at λ=46.9 nm becomes prominent. This indicates that the line observed at λ=46.9 nm possesses strong directivity. Among the line spectra, the line spectrum at 46.9 nm is the only one that shows directivity. This implies that the spike signal is attributed to the Ne-like Ar lasing at 46.9 nm.

IV Soft x-ray focusing using a Wolter type mirror

We have also performed reflecting experiment using the background soft x-ray from the capillary discharge. The purpose of the experiment is to examine if it is possible to converge the soft x-ray by using a grazing incidence Wolter type mirror, which is made of Pyrex glass. The device used in the experiment is the same as that shown in the alignment experiment, except that we have installed a Wolter type mirror in front of the phosphor screen as shown in Fig.7. The dimension and the working principle of the mirror is the same as that described in the reference 5. Before the experiment, alignment is performed using the method described in the previous section.

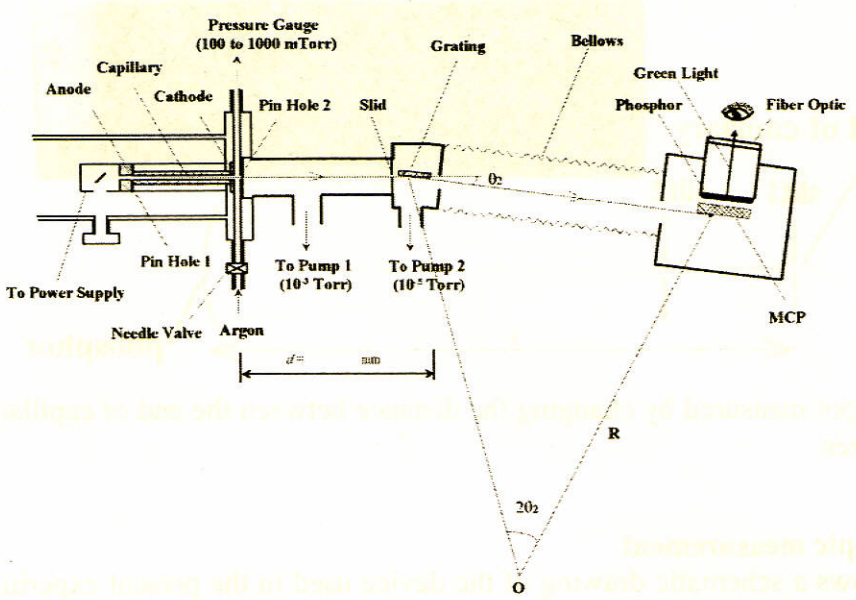

Fig.5 Device used in spectroscopic measurement

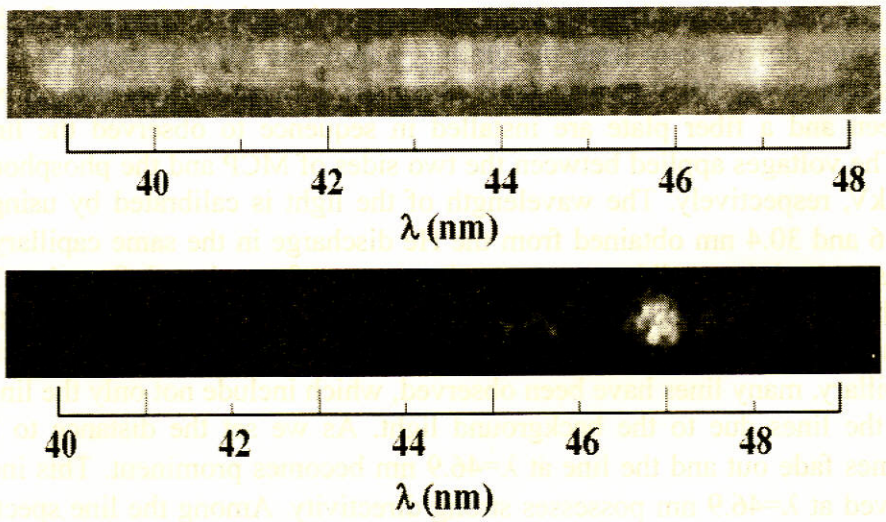

Fig.6 Line spectra observed by changing the distance between the end of the capillary and the grating

The observed images of the light spot with and without a Wolter mirror are shown in Fig.8, where the images are taken at a distance of 80 cm downstream from the end of the capillary. Without the mirror, the diameter of the spot is found to be approximately 1 cm as shown in Fig.8(a). When the Wolter mirror applies, the light is focused to a spot of approximately 1mm, as shown by the center spot in Fig.8(b). Here the outer boundary of the image is the light through the center hole of the mirror, and the other two circles are caused by the reflection at front and back edges of the mirror. Thus, by applying the Wolter mirror, it is possible to focus a light beam of diameter of 10 mm to a spot of size of 1mm. This is the first reported observation, using a Wolter type mirror, of focusing the soft x-ray emitted from a capillary

discharge. Note that a grazing incident is used in the present focusing experiment, so that the efficiency of the reflection may be much higher than that reported by using other method.[6]

V Conclusion

We have observed the soft X-ray output and its line spectra from the capillary discharge by varying the distances from the end of the capillary to the point of the observation. The XRD output shows a spike near the pinch time, and this spike signal is found to reveal strong directivity. On the other hand, strong line has been observed at λ=46.9 nm from the spectroscopic measurement. It is found that this line also shows directivity. Because the line at 46.9 nm is the only one that shows directivity among the line spectra, this gives the conclusion that the spike signal is attributed to the Ne-like Ar lasing at 46.9 nm. In a focusing experiment, the background light with an image of 10 mm in diameter is focused into a spot of 1mm by a grazing incidence mirror. This is the first observation, using a Wolter type mirror, of the focusing of the soft x-ray emitted from a capillary discharge.

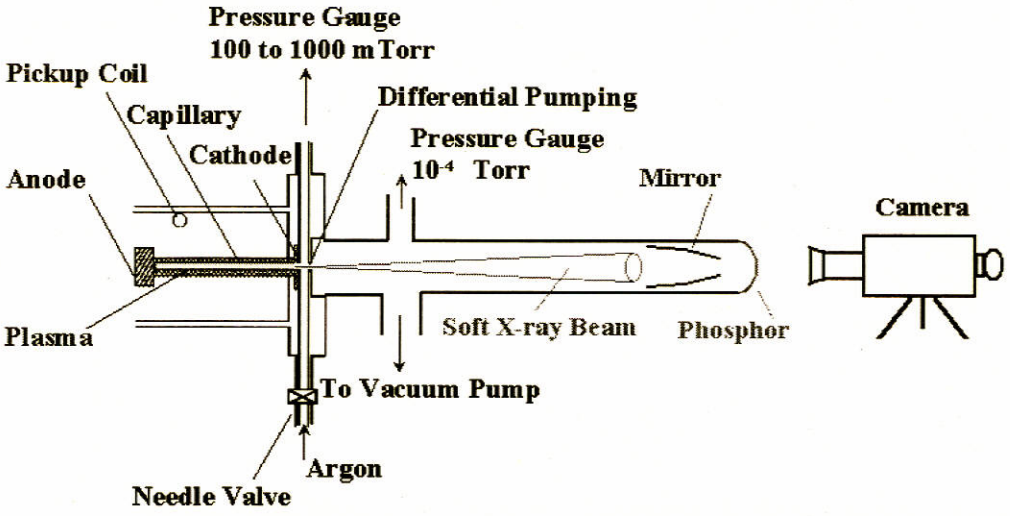

Fig.7 experimental apparatus for focusing the background soft x-ray

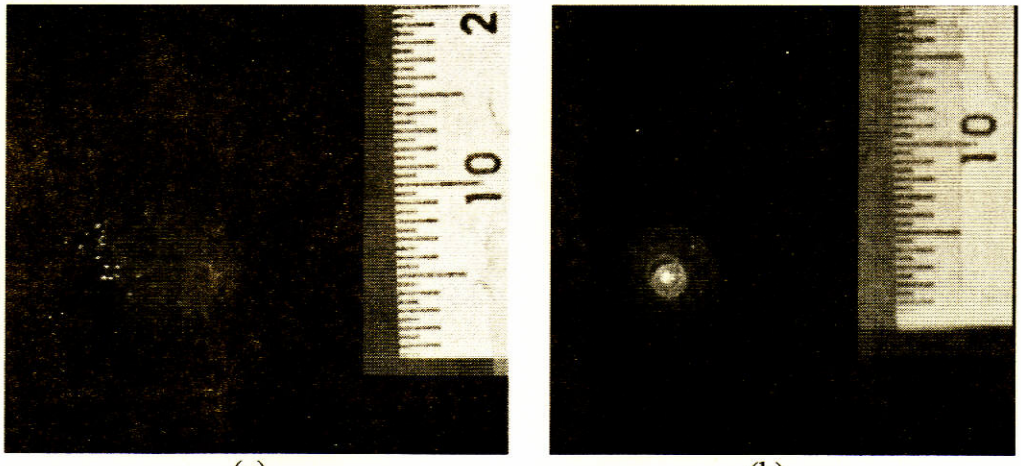

(a) (b)

Fig.8 Images observed with and without the Wolter mirror

Reference

[1] J. J. Rocca, V. Shlyaptsev, F. G. Tomasel, O. D. Cortazar, D. Hartshorn, and J. L. A. Chilla, Phys.Rev.Lett., **73**, (no. 8), p. 2192, 1994.

[2] G. Niimi, Y. Hayashi, M. Nakajima, M. Watanabe, A. Okino, K. Horioka and E. Hotta, J. Phys. D: Applied Physics, **30**, p.2123, 2001.

[3] G. Nimmi, Y. Hayashi, A. Okino, M. Watanabe and E. Hotta: J. Plasma and Fusion Research, **77**, p.1239, 2001.

[4] G. Nimmi, Y. Hayashi, N. Sakamoto, M. Nakajima, A. Okino, M. Watanabe, K, Horioka and E. Hotta: IEEE Trans. Plasma Sci., **30**, p.616, 2002.

[5] S. Aoki: J. Plasma and Fusion Research, **70**, p.843, 1994.

[6] B. R. Benware, A. Ozols, J. J. Rocca, I. A. Artioukov, V. V. Kondoratenko, A. V. Vinogradov: Optics Lett. **24**, p. 1714, 1999.

The Effect of Anode Shape on Plasmas Produced from Metal Powder

K. Takano, T.Yokoyama*, T. Amano, S. Ibuka, K.Yasuoka, and S.Ishii

Department of Electrical and Electronic Engineering
Tokyo Institute of Technology
2-12-1 O-okayama, Meguro-ku, Tokyo, Japan

ABSTRACT

Powder plasmas powered by a pulsed high current discharge are examined using high-speed cameras and laser schlieren technique. Pre-ionization systems are characterized to control the powder discharge. Since growing anode plasma hampers the vaporization process of the powder, influence of the effective anode area on the evaporation was examined by varying the anode shape to suppress the development of the anode plasma.

I. Introduction

Creation of plasma using metal powder injected between electrodes by a pulsed discharge in vacuum was proposed and verified experimentally [1]. The powder injection was controlled by electrostatic forces, which worked successfully to manipulate tiny particles in vacuum. The powder plasma is a new method to control the vacuum sparks that can produce short wave length light and to create dense microplasmas. To the author's knowledge, only one paper was published reporting that dense plasmas were produced using powder [2]. There are variety of applications of the powder plasma such as intense soft x-ray sources, formation of fine particles, and thin-film deposition in material science. Since the powder is solid, there are more kinds of material to become plasmas in comparison with gases. Consequently, peculiar fine particles and thin-films are accomplished that cannot be obtained with the gaseous plasmas.

We reported the experimental results on the powder discharges with plate-plate electrodes [3]. The early phase of the powder discharge was examined with optical measurements. Electrons created by a pre-ionization discharge collide with both an anode and powder particles, of which surfaces evaporate. However, the evaporation of the anode surface was remarkable that was usually observed in vacuum discharges [4]. Suppression of the anode plasma development [5] is required so that the electrical energy has to be delivered to the powder particles effectively . The reduction of the evaporating anode area by changing the anode shape from plane to conical was examined.

II. Experimental Apparatus

We employed copper powder with the diameter of about 100 μm that is shown as a micrograph in Fig. 1. The particles are spherical and their diameters are almost the same. The powder has to be precisely manipulated spatially and temporally between the discharge electrodes in order to produce the powder plasma with good reproducibility. The powder injection has to be accomplished with the fixed spatial distribution and to be synchronized with the discharge. Fig. 2 shows a conical anode used this experiments. The electrode material is tungsten. The separation between the cathode and the anode tip is 10mm. The tip angle of the conical anode is sixty degrees.

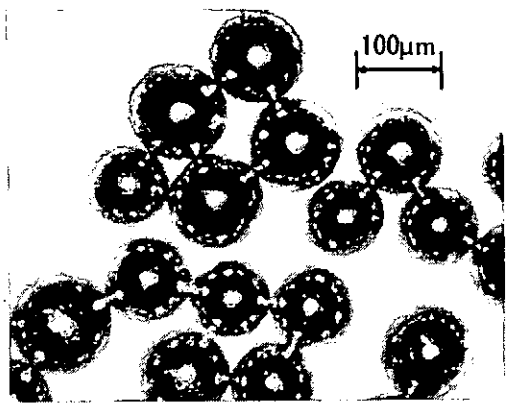

Fig. 1 Photomicrograph of powder

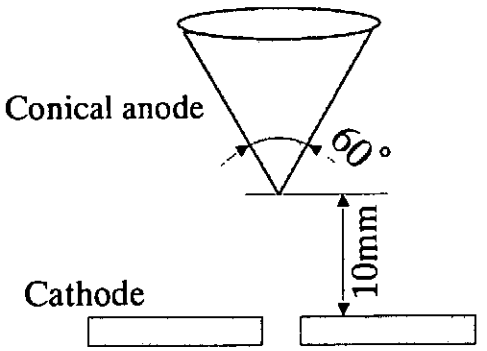

Fig. 2 Electrode configuration

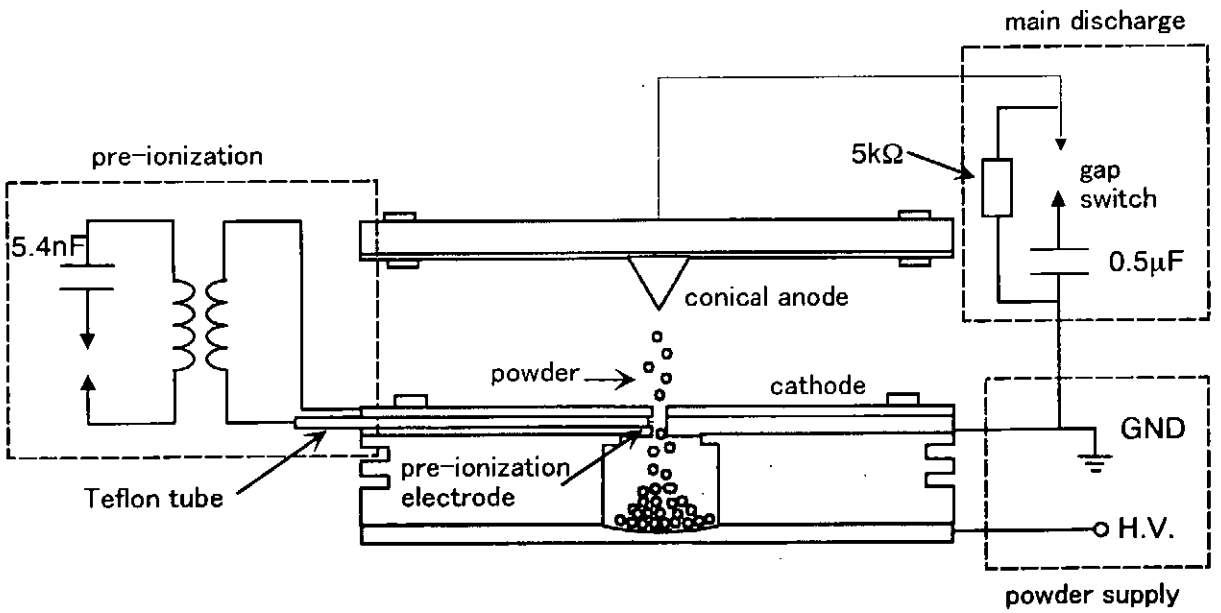

Fig. 3 Experimental setup of the pulsed discharge with an electrostatic powder supply system

The experimental setup is shown in Fig. 3. A powder injection system is placed under the main discharge electrodes. Two circular plate electrodes are separated by an acrylic insulating spacer with the thickness of 10 mm and the inner diameter of 16 mm. The lower electrode is used as the cathode of main discharges and has a hole of 2 mm in diameter at the center for the powder injection. The surface of the bottom electrode is shallowly cut conically so that the powder particles can always roll back to the central region of the electrode after each discharge. A rectangular pulsed voltage with a voltage of 10 kV and a pulse width of 100 ms was applied for the particles to be accelerated between the electrodes. When the electrostatic force acting on the particle with the charge of Q is greater than the gravitational force, the particle is lifted up and is accelerated toward the opposite electrode. Afterwards, the particle is ejected through the hole of the upper electrode to the discharge region.

The powder discharges were powered by a capacitor of 0.5 μF charged to 20 kV. Since we focused to study on the early stage of the powder discharges, the capacitor energy was kept as low as possible to avoid the unnecessary electrode erosion by high-current discharges. The electrode separation was 10mm for the main discharge. The discharge electrodes and the powder injection system were placed in a stainless vacuum chamber at a pressure of 10^{-5} Torr. The tungsten, which has a high boiling point (3680K), was used as the electrode material to reduce the electrode erosion.

Since the breakdown voltage is so high in vacuum and the injected particle distribution is spatially sparse, preionization is essential for the powder discharges. Fig. 4 shows the pre-ionization system that we used in the previous work [3]. The pre-ionization discharge was established automatically when the voltage was applied to the main electrode. However, the pre-ionization discharge was not able to be controlled temporally and had the excessive jitter in triggering. We have improved the pre-ionization system so that the discharge timing can be set independently from that of the main discharge. We placed a tungsten wire electrode in the cathode as shown in Fig. 5 for the preionization discharge that was powered by a capacitor of 5400pF.

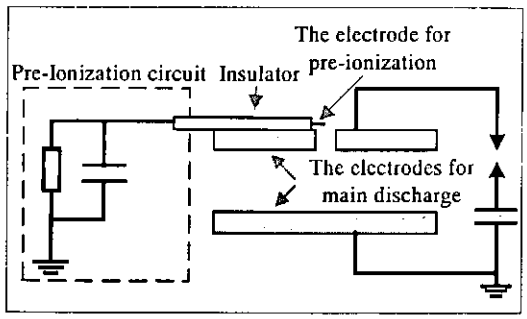

Fig. 4 Previous pre-ionization system

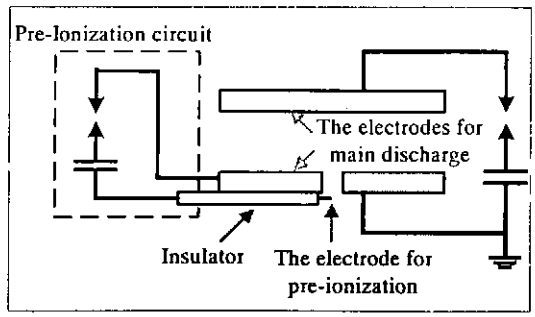

Fig. 5 Improved pre-ionization system

III. Results and Discussion

The influence of the anode shape on the anode plasma development was examined using high-speed cameras and laser schlieren technique. Framing photographs were taken by the Imacon 468 (Hadland Photonics) with an exposure time of 50 ns. Schlieren patterns were recorded with the film of FP-100B (Fuji-film). The second harmonic wavelength of 532nm of a pulsed Nd:YAG laser with a pulse-width of 8 ns was used. Discharge currents were measured using a Rogowskii coil. The temporal change of visible light intensity was measured by a photo-multiplier via an optical fiber.

The experiments were carried out for both the plate anode and the conical one with and without powder. Fig. 6 and Fig. 7 show the results with the plate anode. Fig. 8 and Fig. 9 show the results with the conical anode. Each of the figures contains framing photographs, schlieren patterns, and the waveforms of the current and the total light with the timing of observation. Although these photographs and schlieren patterns were not taken in the same discharge, they were selected as showing the typical profile at each time.

When the capacitor was fired, the electrons generated by the preionization discharge were accelerated to the anode and collided directly with it. The evaporated anode material formed the anode plasma that expanded toward the cathode. For the discharge with the plate anode, the anode plasma expands to larger volume in comparison with the conical anode discharge. The vaporization of the anode is observed as the dark region in the schlieren patterns. The peak of the light intensity waveform corresponds to the formation of anode plasma. At the beginning of the discharge, light emission from the powder is observed as shown in Fig. 7(a). The vaporization from the powder surface is confirmed by the schlieren pattern of Fig. 7(d). Two peaks appear in the temporal change of the light intensity. The first one, which is not observed in the discharge without powder, is caused by the emission from powder. The vaporization of the powder surface is suppressed at the current peak as shown in Fig. 7(f).

The anode plasma is formed at the tip of the conical anode only as shown in Fig. 8. The plasma stayed locally near the tip during the discharge and the volume is smaller in comparison with the plate anode discharge. The suppression of the anode plasma development is established with the conical anode. Changing the anode shape from the plate to the conical tip reduces the effective anode area. A bright plasma layer appears above the cathode as seen in Fig. 9(b). A plasma channel also bridges between the plasma layer and the anode plasma. The vaporization of the powder surface is remarkable in the schlieren pattern in Fig. 9(e). However, the vaporization of the powder ceases at the later phase shown in Fig. 9(c)(f), where the electric field between the electrodes is not so high that electrons cannot gain enough energy to vaporize the powder.

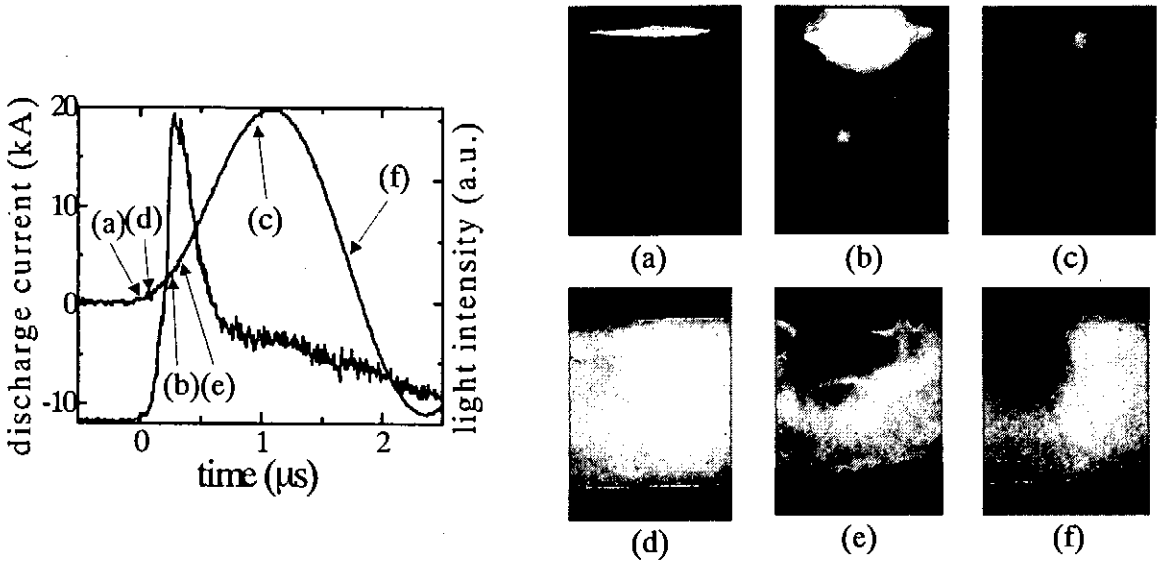

Fig. 6 Current and light intensity of the discharge without powder (plane-to-plane). : (a)-(c) are sequent frame photographs, (d)-(f) are sequent schlieren photographs of the discharge without powder.

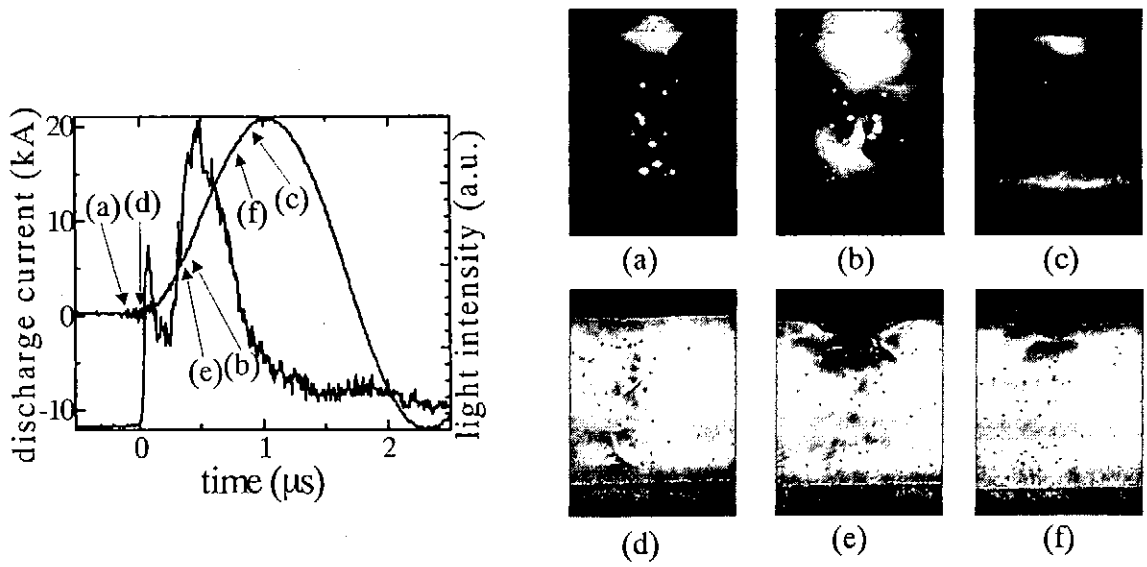

Fig. 7 Current and light intensity of the discharge with powder (plane-to-plane). : (a)-(c) are sequent frame photographs, (d)-(f) are sequent schlieren photographs of the discharge with powder.

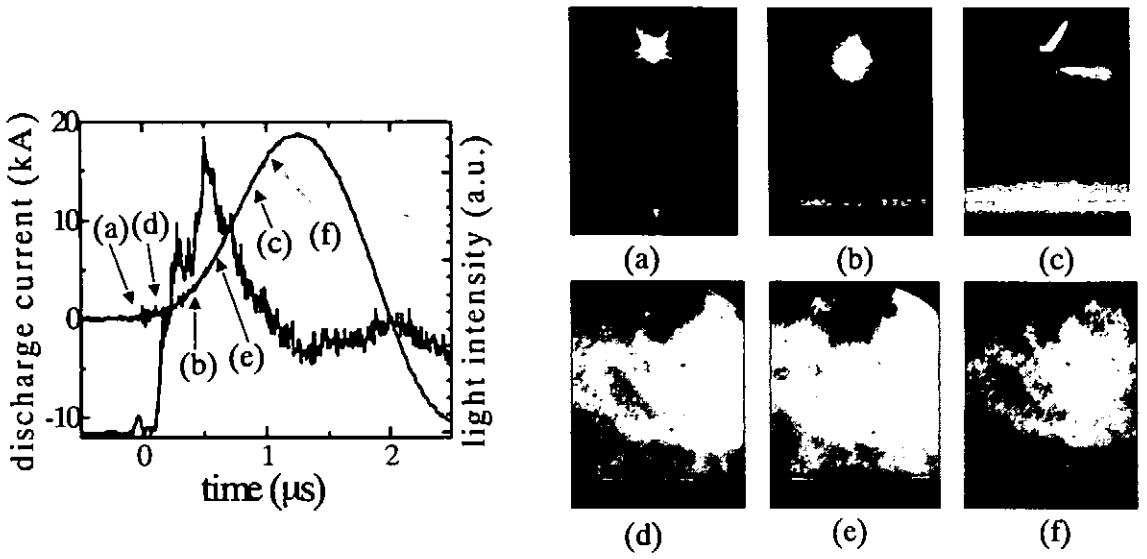

Fig. 8 Current and light intensity of the discharge without powder (conical-to-plane). : (a)-(c) are sequent frame photographs, (d)-(f) are sequent schlieren photographs of the discharge without powder.

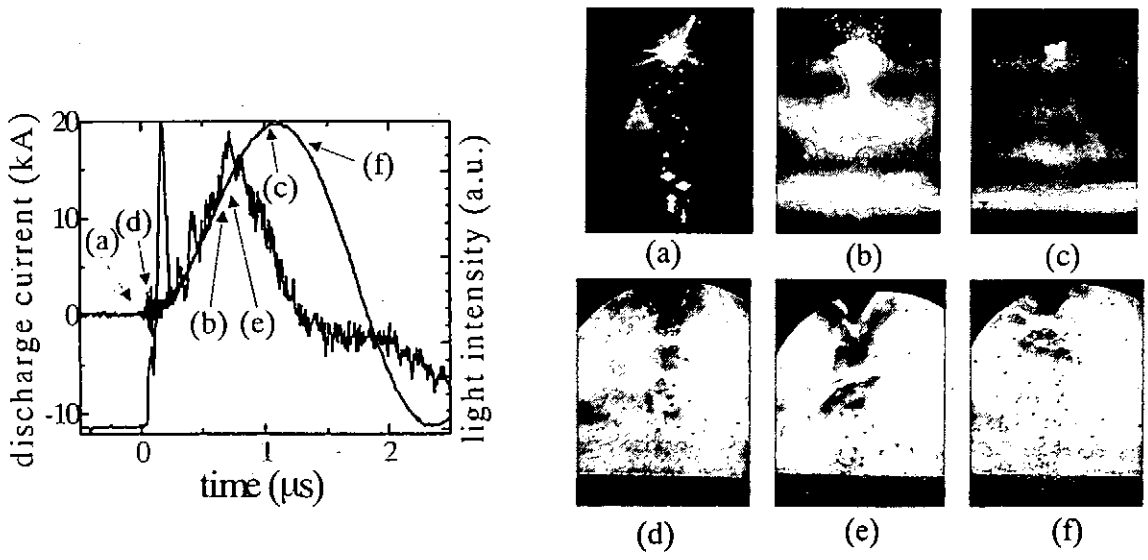

Fig. 9 Current and light intensity of the discharge with powder (conical-to-plane). : (a)-(c) are sequent frame photographs, (d)-(f) are sequent schlieren photographs of the discharge with powder.

IV. Conclusion

The anode plasma development is suppressed with the conical anode. The vaporization of the copper powder surface occurred as soon as the pulsed voltage is applied between the electrodes. The vaporization of the powder ceases at the current peak, because the electric field between the electrodes is not so high that electrons cannot gain enough energy to vaporize the powder.

References

[1] H.Nozawa et al.: Jpn.J.Appl.Phys. vol.40 (2001) p.1009

[2] Ch. Masonnier et al.: Plasma Physics and Controlled Fusion Research II (IAEA Vienna), (1996) p. 345

[3] T. Kuraoka et al.: NIFS-PROC-51, June(2002), p. 32

[4] Ch K Erber et al.: Plasmas Sources Sci. Technol. vol. 5 (1996) p. 436

[5] Hernan Chuqui et al.: IEEE Trans. Plasma Sci. vol. 26, no. 4 (1998) p.1162

OPERATION OF A PLASMA OPENING SWITCH ON THE SHOTGUN Z-PINCH DEVICE

T. Chiba, M. Hakuta and K. Takasugi

College of Science and Technology, Nihon University
1-8-14 Kanda-surugadai, Chiyoda-ku, Tokyo 101-8308, JAPAN

ABSTRACT

A plasma opening switch was tested to control the discharge current of the SHOTGUN z-pinch device. In order to realize an opening switch with long conduction time at large current, efficient plasma gun was developed. The opening operation with the conduction time about 1 μs at the current about 100 kA was attained.

I. Introduction

In z-pinch plasmas high density and high temperature parts called hot spots are formed with rapid contraction. From the observation result in the SHOTGUN z-pinch the space pattern of the hot spot was well correlated with that of the Rayleigh-Taylor instability generated in the contraction stage.[1)]

The growth rate of the Rayleigh-Taylor instability in consideration of finite Larmor radius effect takes the maximum value at the wave number[2, 3)]

$$k = \left(g / \omega_{ci}^{\,2} \rho_i^{\,4}\right)^{1/3}, \tag{1}$$

where g is the acceleration by the contraction, ω_{ci} is ion cyclotron frequency, and ρ_i is ion Larmor radius. The instability glows at the wave number k or corresponding wavelength $\lambda = 2\pi/k$. The wavelength of the instability was 3 - 5 mm which was well in agreement with this estimation.

Since the sign of the maximum growth rate is always positive, the instability is unavoidable. In order to obtain macroscopically uniform light source, it is necessary to generate the instability at large k. The wave number can be expressed with the magnetic field B and the ion temperature T_i as

$$k \propto B^{4/3} / T_i^{2/3}. \tag{2}$$

The application of high magnetic field without heating plasma will be able to generate macroscopically uniform z-pinch column. Therefore the power source with short rise time is necessary.

Plasma opening switch (POS) is a high power and high speed current switch using plasma. It has been used for pulse compression of pulsed power source. Although it is difficult to obtain long conduction time, the conduction time of 1 μs has been obtained in the ASO-X experiment.[4)] In this research, plasma gun with sufficient efficiency required for the long conduction time opening switch was developed. It was applied to the SHOTGUN z-pinch device, and the operating characteristic was investigated.

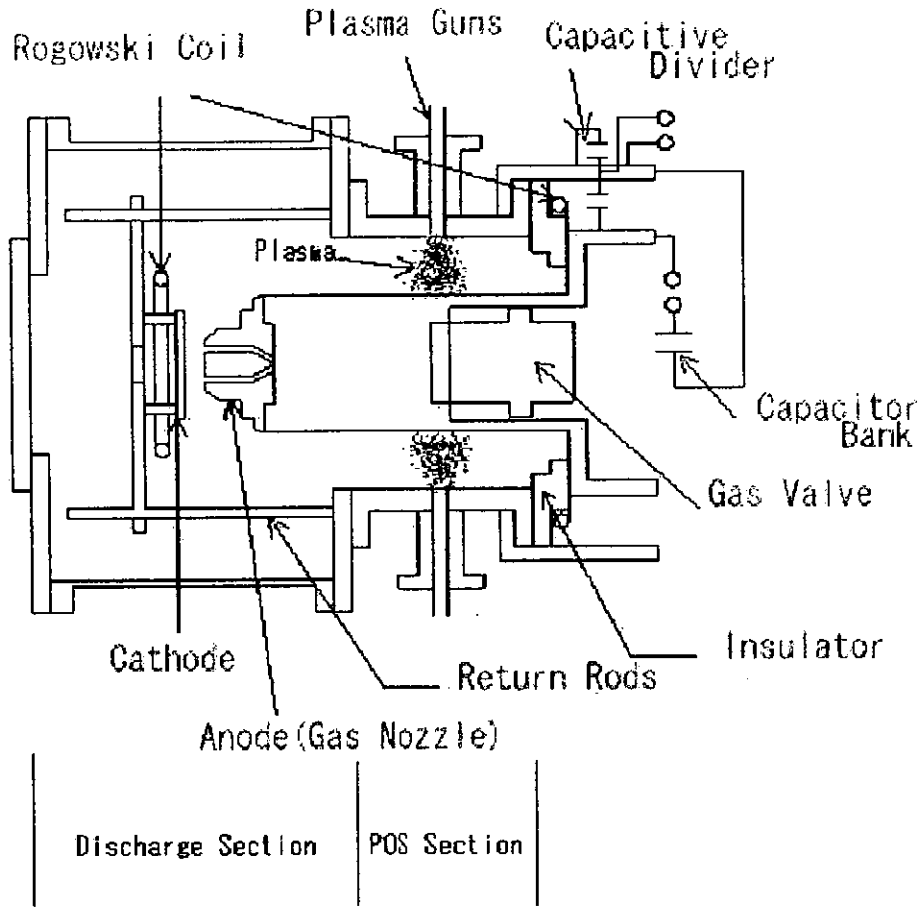

Fig. 1 The SHOTGUN z-pinch device with POS section.

II. Experimental Setup

Schematic view of the SHOTGUN z-pinch device is shown in Fig. 1. The capacitor bank consists of 24 μF high-speed capacitors, which is charged up to 23 kV (6.3 kJ). Gas is injected through a hollow nozzle mounted on the anode using a high-speed electromagnetic gas valve. The interval between the electrodes is 30 mm. The cathode has many holes in order not to prevent the gas flow. Rogowski coils are installed in both electrodes to measure discharge currents. The anode coil measures the input electric current into the discharge chamber, and the cathode coil measures the electric current through the z-pinch column. A discharge probe is installed in the point of the gas nozzle, which detects the emission of the gas from the gas valve. Trigger signal of main discharge refers to this signal, and this system ensures the reproducibility of discharge.

A chamber was newly added for the POS. Eight plasma guns can be installed in the chamber. A new plasma gun was constructed for the POS experiment. The plasma gun is required to generate high density plasma in order to make large conduction current. The plasma is produced by surface discharge of the polyethylene insulator when high voltage is applied between the center and the outer conductors of the gun. The diameter of the conductor is 28mm. The distance from the gun to the center conductor of the POS is 6.5 cm. The plasma parameters are measured by a Langmuir probe.

III. Plasma Gun

Plasma gun was operated at the charge voltage of $V = 24$ [kV], and the capacitance of $C = 0.15$ [μF]. Figure 2 shows the current which flows to the plasma gun, and the ion saturation current of the probe measured at 10 cm from the plasma gun. The period of oscillation of the current $T = 2.4$ [μs], and the time constant of attenuation $\tau = 3.9$ [μs]. The inductance $L = 1.0$ [μH] and the resistance $R = 0.26$ [Ω] of the circuit were calculated from them. The plasma density took the maximum value at about 6 μs after the discharge started.

Measurements of electron temperature and density of the plasma from plasma gun were performed by the probe. The voltage and current characteristic of the probe at 10 cm from the gun at 10 μs after the start of discharge were investigated, and the electron current is plotted logarithmic against the probe voltage (Fig. 3). The electron temperature obtained from this probe characteristic was $T_e = 8.7$ [eV], and electron density was $n_e = 2.7\times10^{17}$ [m^{-3}].

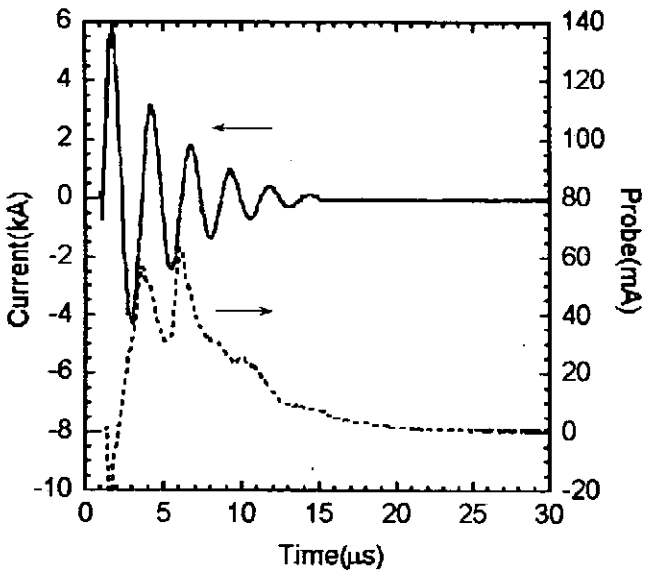

Fig. 2 Discharge current and probe signal

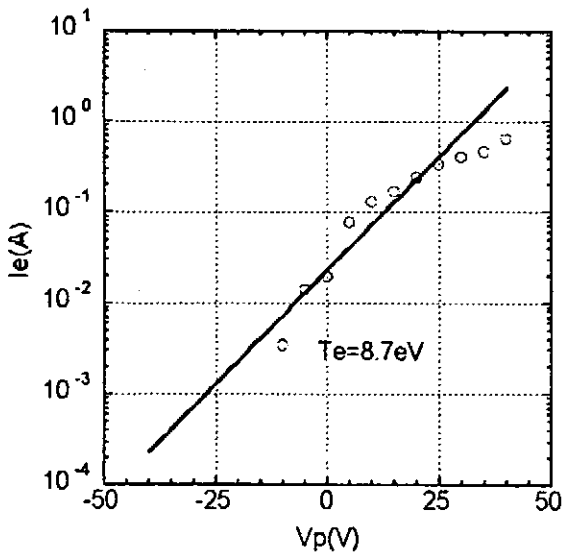

Fig. 3 Probe characteristic curve.

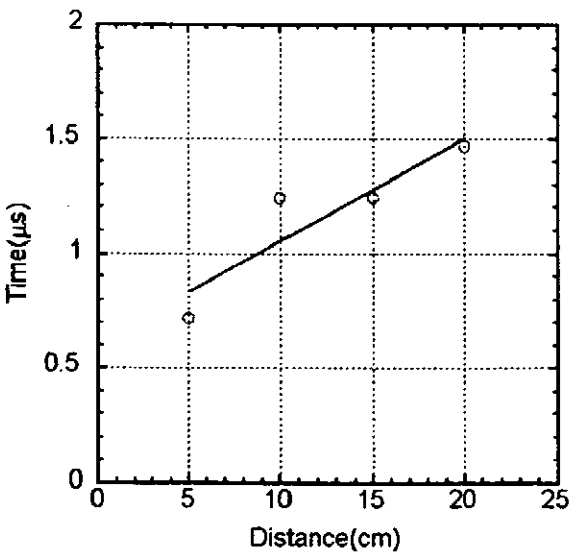

Fig. 4 Time of flight of the plasma.

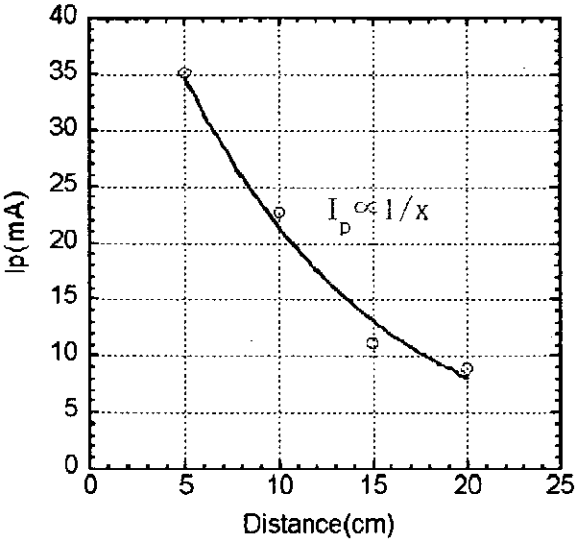

Fig. 5 Axial distribution of the plasma.

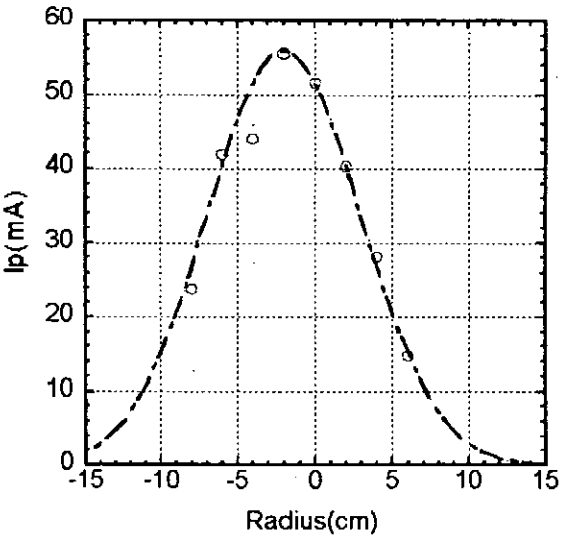

Fig. 6 Radial distribution of the plasma.

Next, the drift velocity of the plasma emitted from plasma gun was investigated. Figure 4 plots the time when the plasma reached the probe as a function of the distance from the gun. From the sloe of the graph, the drift velocity of the plasma was 22.2 cm/μs. Assuming H ion, the sound velocity is 2.9 cm/μs using the measured electronic temperature. The plasma was accelerated by the $J \times B$ force, and that is why the drift velocity was much faster than the sound velocity.

Figure 5 shows the distribution of the plasma along z-axis at 10 μs after the discharge. The horizontal axis is the distance from plasma gun, and the vertical axis is ion saturation current of the probe. Decrease of the plasma density along the axis is much more gently than $1/x^2$, and is close to $1/x$. This means that the plasma is emitted with directivity from the source of plasma of large area.

Figure 6 expresses the radial distribution of plasma at 10 cm away from the plasma gun and 10 μs after the start of discharge. The center was shifted in 2 cm, because the discharge was not uniform. The radial distribution of the plasma was well approximated by a Gauss function, and the radius when the density becomes 1/e was 6.8 cm. Integrating the radial density distribution over the area, the total number of particles per unit length is 1.0×10^{16} m^{-1}. Then the emission rate would be 2.2×10^{21} particles per second.

IV. Plasma Opening Switch

The plasma guns were applied to the opening switch experiment. Here a capacitor of 0.3 μF was used at the charged voltage of 24 kV.

At first symmetrically placed two plasma guns were used. Figure 7 expresses the anode current (solid line), the cathode current (chained line), and the difference of two currents (dotted line). The anode current shows the total input current into the system, the cathode current shows the current to the load, and the difference current shows the conduction through the gun plasma. The delay time from electric discharge of plasma gun to the main electric discharge is taken as a parameter.

When the delay time is 4 μs, conduction to the plasma from plasma gun is hardly seen. Opening is imperfect, although conduction to plasma is about 100 kA , when the delay time is

6 μs. When the delay time is 8 μs, conduction to plasma does not change but opening is also good. When the delay time is 10 μs, opening will become bad again. If the delay time is increased more than this, conduction to plasma will also fall. On this condition, it turns out that the best time of delay time is 8 μs for the POS operation. As the main discharge delays about 1 μs from trigger, It is mostly in agreement with the time when plasma density becomes the maximum in Fig. 2. The conduction current of about 100 kA and the conduction time for about 1 μs were obtained.

The result when using four plasma guns is shown in Fig. 8. When the delay time is 4 μs and 6 μs, conduction to plasma is hardly seen. When the delay time is 8 μs, although conduction to plasma comes out for a while, it is still inadequate. Even if delay time is set to 10 μs, conduction seldom improves. As a result of the number of plasma guns increasing, the energy of a capacitor will be distributed and it is possible that plasma was not fully generated.

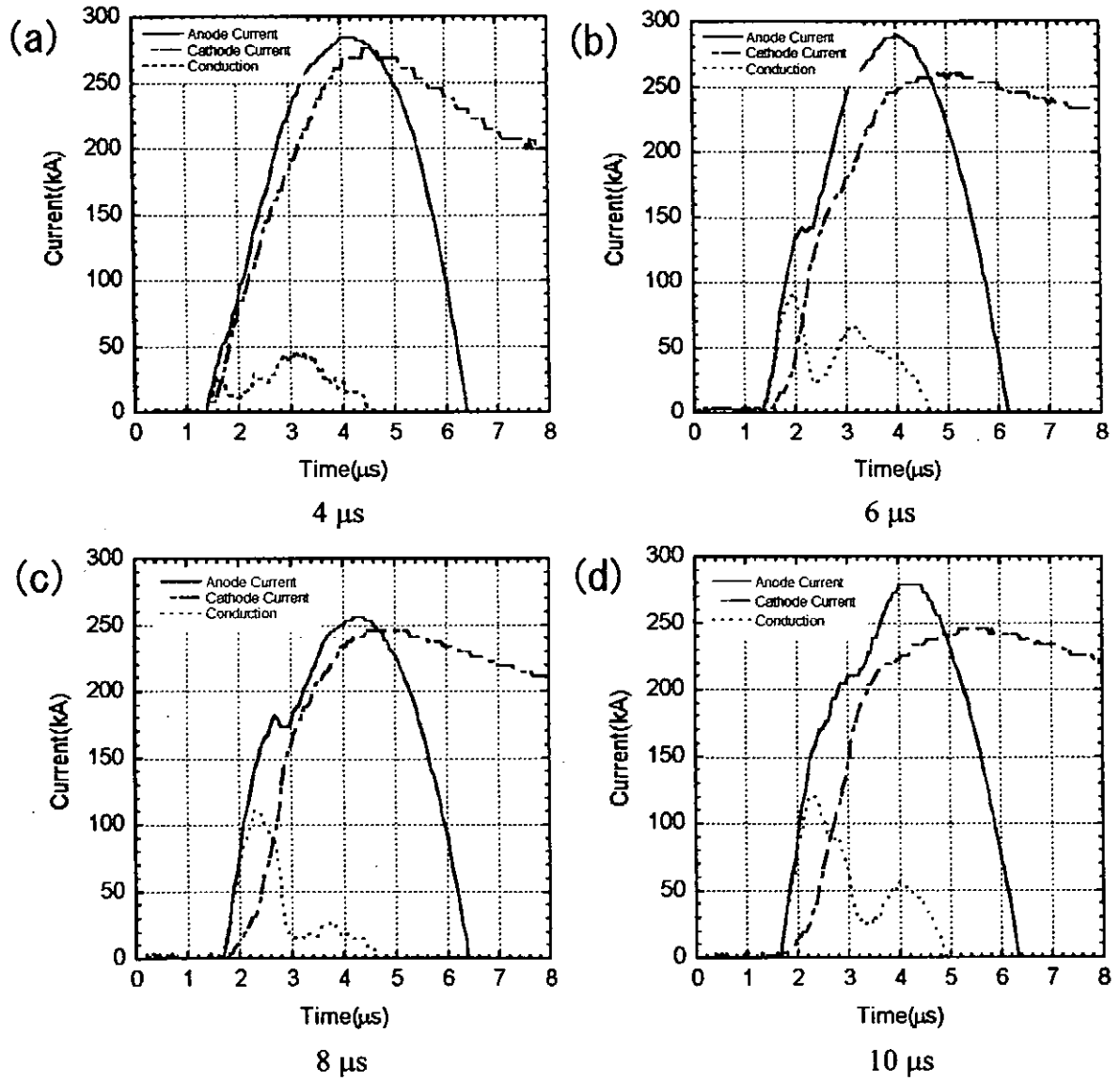

Fig. 7 POS experiment using two plasma guns. Delay time of main discharge from the plasma gun is taken as a parameter.

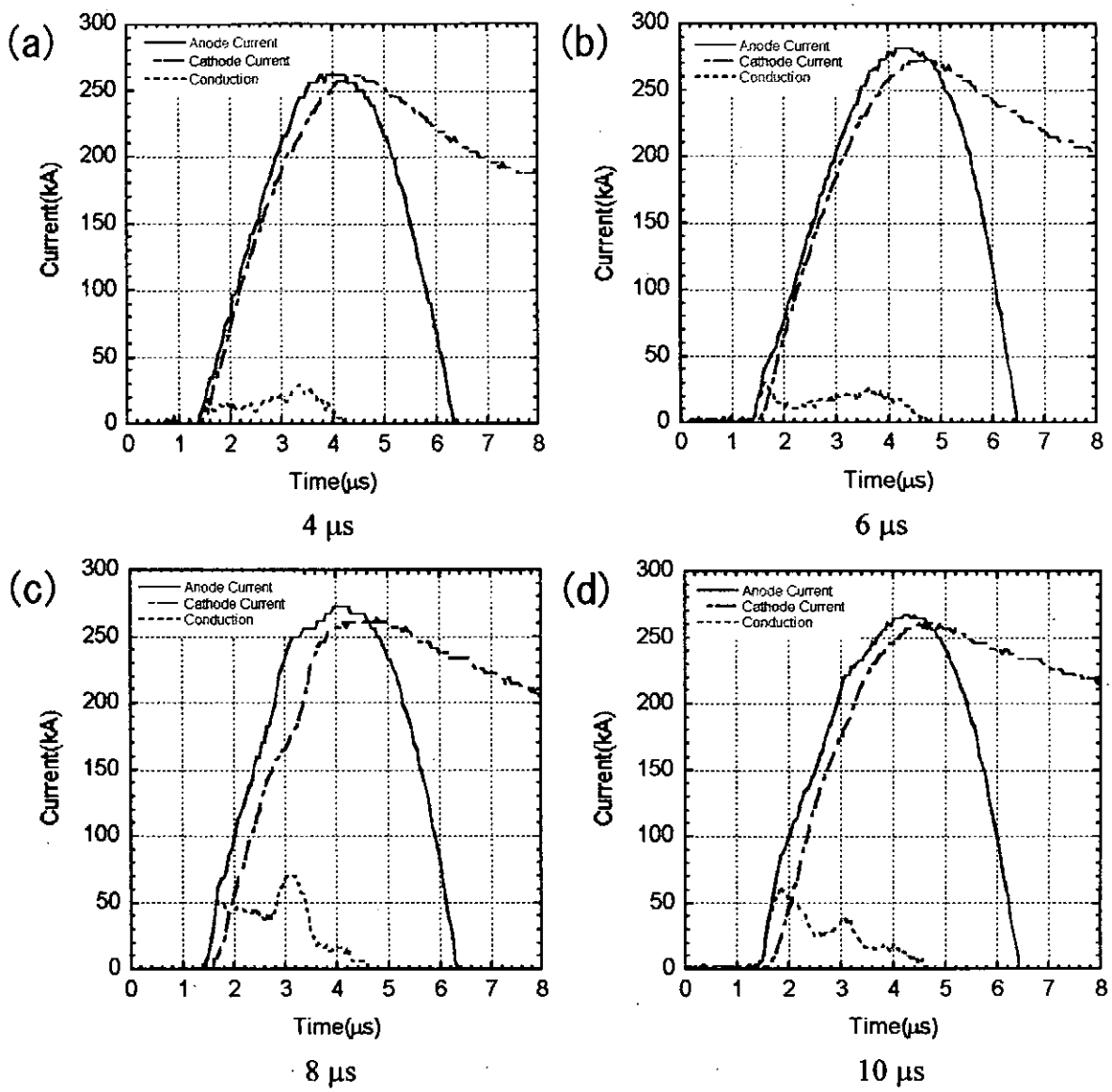

Fig. 8 POS experiment using four plasma guns.

V. Summary

Control of discharge current of the SHOTGUN z-pinch device was tried using plasma gun. Conduction for about 1 μs and opening operation were obtained at about 100 kA, when two plasma guns were used with the capacitor of 0.3 μF. Since conduction current falls when plasma gun is increased, it is thought that the energy of the capacitor is still insufficient. It is just going to prepare for adding capacitors in order to operate the POS at larger current with longer conduction time.

References

1) K. Takasugi, T. Miyamoto, K. Moriyama and H. Suzuki: AIP Conf. Proc. **299**, 251 (1994).
2) R. Muto, K. Takasugi and T. Miyamoto: NIFS-PROC-50, 139 (2001).
3) K. Moriyama, K. Takasugi, T. Miyamoto and K. Sato: NIFS-PROC-18, 90 (1994).
4) S. Kohno, Y. Teramoto, I.V. Lisitsyn, S. Katsuki and H. Akiyama: Jpn. J. Appl. Phys. **39**, 2829 (2000).

OBSERVATION WITH TIME-RESOLVED PIN HOLE CAMERA ON PLASMA FOCUS DEVICE

M. Sato and K. Shimoda

Department of Electronic Engineering, Gunma University,
1-5-1 Tenjin-cho, Kiryu, 376-8515, Japan

ABSTRACT

We modified a time-resolved X-ray pinhole camera, and were able to take the images by soft X-rays and ultraviolet rays at the same time. This camera was used in the experiment on a small plasma focus device. The images by ultraviolet rays and soft X-rays were taken and were compared in the focused phase of the plasma focus. The positions of the lighting regions in the image by ultraviolet rays were approximately agreed with that by soft X-rays.

I. Introduction

The plasma focus device is well known as an inexpensive and compact source of intense soft X-rays. It has been used for number of applications: soft X-ray microscopy[1], soft X-ray lithography[2], X-ray backlighting for high-density plasmas[3]. For these applications it is required that control for the size and the geometry of soft X-ray sources generated in the focused phase. It is well known that the geometries of soft X-ray sources are column shapes in the case of low Z gases, and are spot shapes (hot spot) in the case of high Z gases[3]. As the emission mechanisms of soft X-rays, a radiation-cooling model is well known but it cannot explain soft X-ray emission from the column shape source. In order to make clear about the emission mechanisms of soft X-rays, time-resolved measurement with higher resolution is required.

A time-resolved X-ray pinhole camera[4,5] usually consists of pinholes, a micro channel plate (MCP) with strip lines and a camera. In our time-resolved pinhole camera, circular MCP is used and has no strip line[6]. When a pulsed high voltage is supplied to the MCP, only one picture is obtained from one shot of discharge. The fact that multi-pictures are not obtained is disadvantage but use of a normal MCP gives advantages of low cost and easy manufacturing. We modified the camera in order to get a new advantage that one more image was simultaneously made on the MCP. The new image is constructed by ultraviolet rays and shows the geometry of a pinched plasma. As another advantage the two images are taken from the same direction, because the images are taken with one MCP. Moreover the time resolution of the camera is less than 1 ns. This value is better than the value obtained by an image converter camera (IMACON-700) in framing mode operation (10ns). In this paper modification of the time-resolved pinhole camera is presented in detail. For an example the experimental results obtained with the time-resolved pinhole camera are reported.

II. Experimental Setup

Figures 1 show the schematic drawings of the experimental setup. Configuration of a plasma focus device is shown in Fig. 1 (a). The plasma focus device consists of an inner

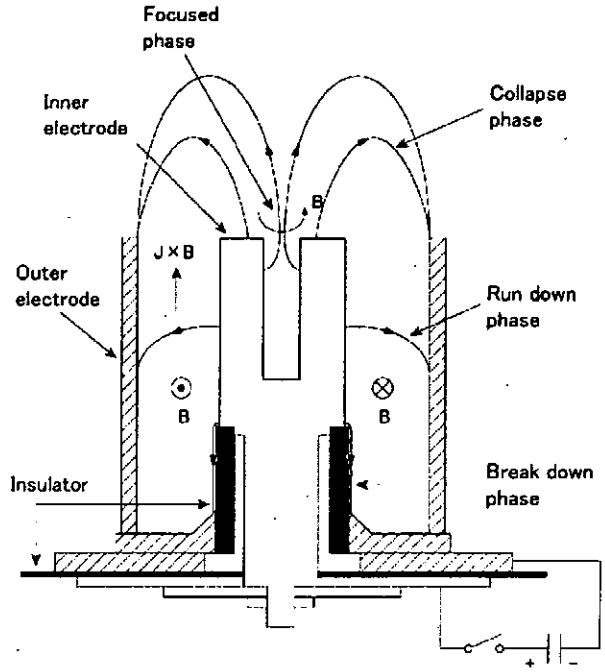

(a)

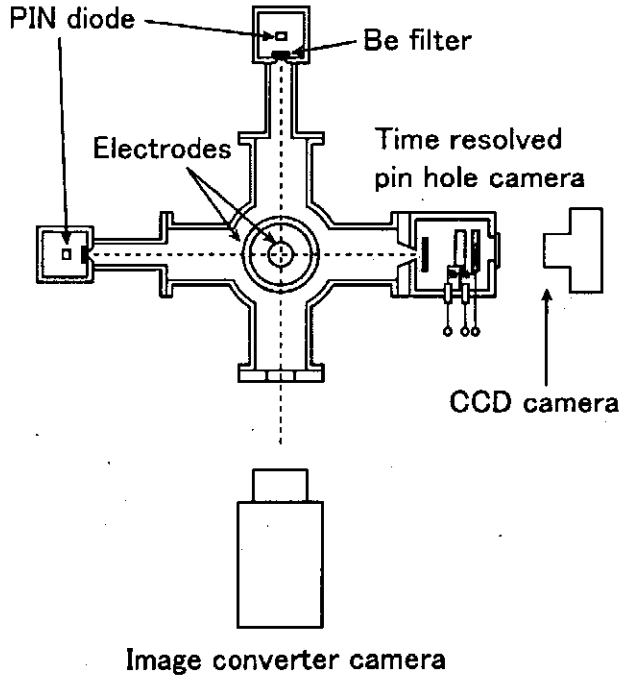

(b)

Fig. 1 Schematic drawings of experimental setup; configuration of plasma focus device (a), location of measurement tools (b).

electrode, an outer electrode and an insulator. The outer electrode is constructed from 24-copper rods of which diameters are 8 mm; the geometry of the plasma focus device is like a square cage. The inner diameter of the outer electrode is 100 mm. In order to prevent

erosion due to bombardment of the electron beams, a small hole was drilled on the axis of the inner electrode. The outer diameter of the inner electrode is 50 mm. The lengths of the electrodes are 155 mm. The insulator is made of a Pyrex glass, and the outer diameter and the length of it are 55 and 51 mm, respectively. The maximum voltage and the maximum stored energy of a condenser bank are 30 kV and 25 kJ, respectively. In all the experiments reported here, the condenser bank was used with the charged voltage of 14.5 kV. Hydrogen gas was used as a working gas, and a small amount of argon or neon gas was mixed to the working gas. In all the experiments reported here, the pressure of the working gas was set at 1.5 torrs, and about ten percents of it were the mixed gases.

In the experiments, PIN diodes, an image converter camera (IMACON-700) and a time-resolved pinhole camera were located as shown in Fig. 1 (b). In front of a PIN diode, the beryllium foil of which thickness was 20 micrometers was set as a filter. This PIN diode was used to detect the soft X-rays, and appearance of its signal also suggested pinching of the plasma. The time when the signal appears is usually used as the time origin in data arrangement. Another PIN diode was used to detect the visible light from the pinched plasma. Since separation of ultraviolet rays from PIN diode signal is very difficult, the PIN diode could not be used to detect ultraviolet rays. The image converter camera is usually used in a streak mode, and its measured result is used for estimation of a pinched velocity of the plasma. In this paper the measured result in a framing mode is used for comparison with the image taken with the time-resolved pinhole camera. In the framing mode the exposure time and the interval between framing pictures of IMACON-700 are 10 ns and 50 ns, respectively.

Figure 2 shows the schematic drawing of a time-resolved pinhole camera. This camera consists of a high voltage pulse generator, a micro channel plate and a charge couple device (CCD) camera. The high voltage pulse generator is self-made, and consists of several

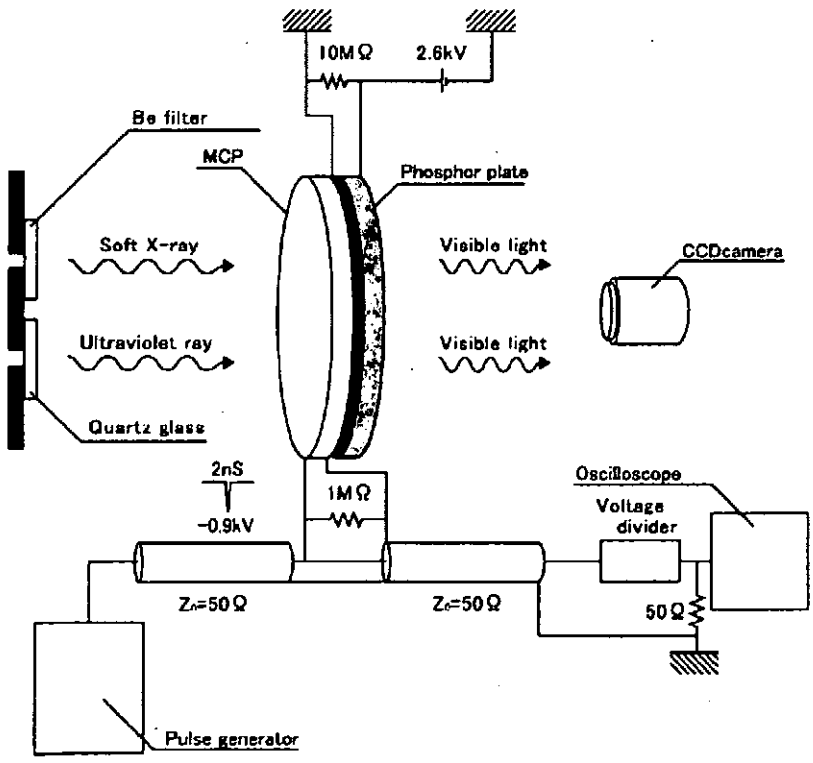

Fig. 2 Schematic drawing of time-resolved pinhole camera.

avalanche transistors connected with series. The maximum value and the pulse width of the output voltage generated by it are -900 V and 2 ns, respectively. The pulsed voltage is supplied to the MCP through a 50 Ω coaxial cable. Since the impedance of the MCP is very low, the network is mismatched and the pulsed voltage becomes low. However the voltage required to operate the MCP is supplied and its value is estimated by about -700 V. The exact time resolution is not made clear, but its value is less than 1ns because the pulsed voltage is triangular shape and the threshold voltage exists in operation of the MCP. The pulsed voltage passed through the MCP is observed with an oscilloscope and is used for estimation of time correlation with a diode current and the signals by the PIN diodes. The MCP is F2223-11P made by HAMAMATSU Photonics K. K. and its diameter is 27 mm. In front of the MCP, two pinholes are located. The diameters of the pinholes were 0.5 or 0.2 mm. At one pinhole the beryllium foil of which thickness was 20 micrometers was usually set as a filter. The image obtained through this pinhole is made by the soft X-rays of which wavelengths are shorter than about 2 nm. At another pinhole the thin quartz glass of which thickness was 1.5 mm was attached. Figure 3 shows the dependences of the detection efficiency of MCP and the transparency of the quartz glass as a function of the wavelength. From Fig. 3 the image obtained through this pinhole is made by ultraviolet rays of which wavelengths are approximately 160 nm. The electrons generated by soft X-rays and ultraviolet rays are amplified in the MCP and are accelerated towards the phosphor plate. The visible images on the phosphor plate generated by bombardment of the accelerated electrons are taken with the CCD camera. The advantages of our time-resolved pinhole camera are as follows.

1. By using this camera we can take the images by soft X-rays and ultraviolet rays at the same time.
2. Since the images are taken with one MCP, two images are taken from the same direction and the magnification factors of the images are same.
3. Time resolution of the camera is less than 1ns, and this is better than that obtained by the IMACON-700 in framing mode operation (10ns).

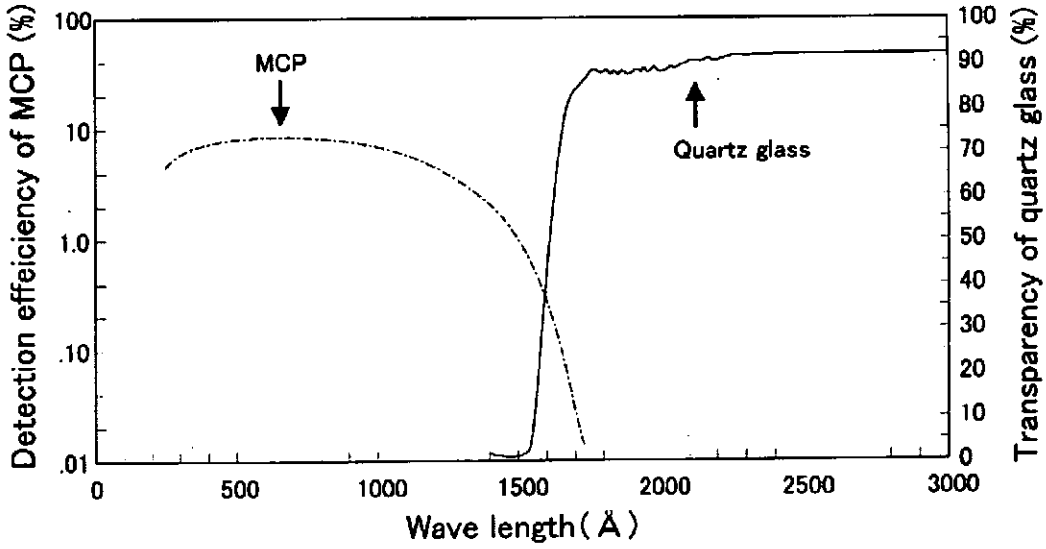

Fig. 3 Dependences of the detection efficiency of the MCP and the transparency of the quartz glass as a function of the wavelength.

III. Experimental Result

The typical waveforms of a discharge current and the signal of the PIN diode with the beryllium foil are shown in Fig. 4. In the figure, the upper and the lower trace correspond to the discharge current and the signal of the PIN diode, respectively. The discharge current reaches to about 500 kA by 1.4 microseconds from initiation of discharge, and the dip is seen at the tops of it. The difference by changing the admixture gas was not distinguished in the signals of the total currents. A sharp spike appears in the signal of the PIN diode, and appearance of this spike is coincident with the timing of the dip in the discharge current. After that two or three small spikes appear in the signal of the PIN diode.

Figures 5 show the framing pictures of a plasma focus in collapsed phase. In this figure a vertical line shows the centerlines of the inner electrode in the respect images. Since Fig. 5 (a) was taken with the image converter camera (IMACON-700), the image was constructed by visible light from the plasma. Figure 5 (b) was taken with the time-resolved pinhole camera. The time when this photograph was taken was displayed in Fig. 7. From the detection efficiency of MCP and the transparency of the quartz glass shown in Fig. 3, the image shown in Fig. 5 (b) was constructed by ultraviolet rays of which wavelengths were approximately 160 nm. Since the configurations of the images shown in Figs. 5 (a) and (b) are approximately same, it is considered that the image by the ultraviolet rays corresponds to the configuration of a plasma as like an image by visible light.

Figure 6 shows a pinhole photograph obtained with the time-resolved pinhole camera. In Fig. 6 the image shown in left side is constructed by ultraviolet rays, and that in right side is constructed by soft X-rays. In the figure I.E. shows the top surface of the inner electrode, and the vertical axis of Z shows the distance from the surface of the inner electrode. Two vertical lines show the centerlines of the inner electrode in the respect images. In this shot the argon gas was mixed to the hydrogen gas. The time when this photograph was taken was displayed in Fig. 8. From comparison with these two images, the emitting regions of the ultraviolet rays approximately agree with those of soft X-rays. It is suppose that this result supports the beam target model in which accelerated electrons are collide with the ions exist in the forward plasmas and emit soft X-rays. However soft X-rays are emitted from early time of focused phase as shown in Fig. 8. This fact means that soft X-rays are not emitted by the beam target model. If soft X-rays are generated by L-shell radiation, those might be generated from excitation by collision between thermal electrons and ions. Although the

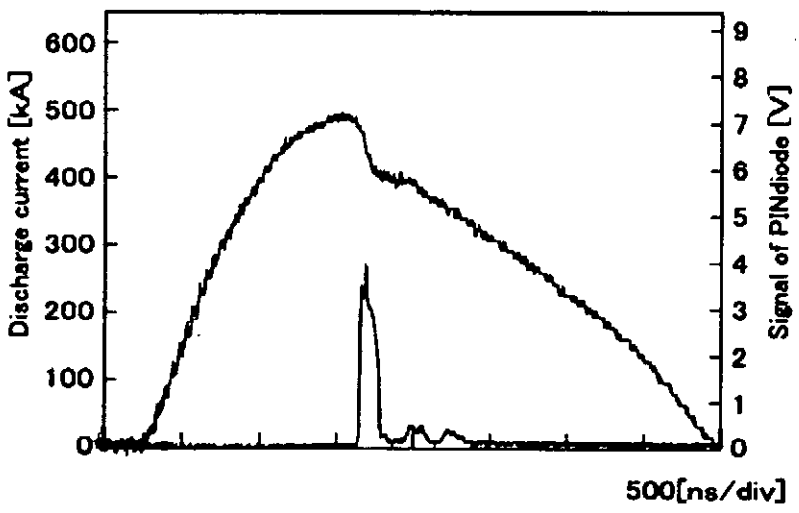

Fig. 4 Typical waveforms of discharge current and signal of PIN diode.

electron temperature of the pinched plasma in our device is not made clear, it is expected that the temperature is relatively low. Therefore it is considered that the radiation mechanism of soft X-rays is due to excitation by collision between thermal electrons and ions in the plasma.

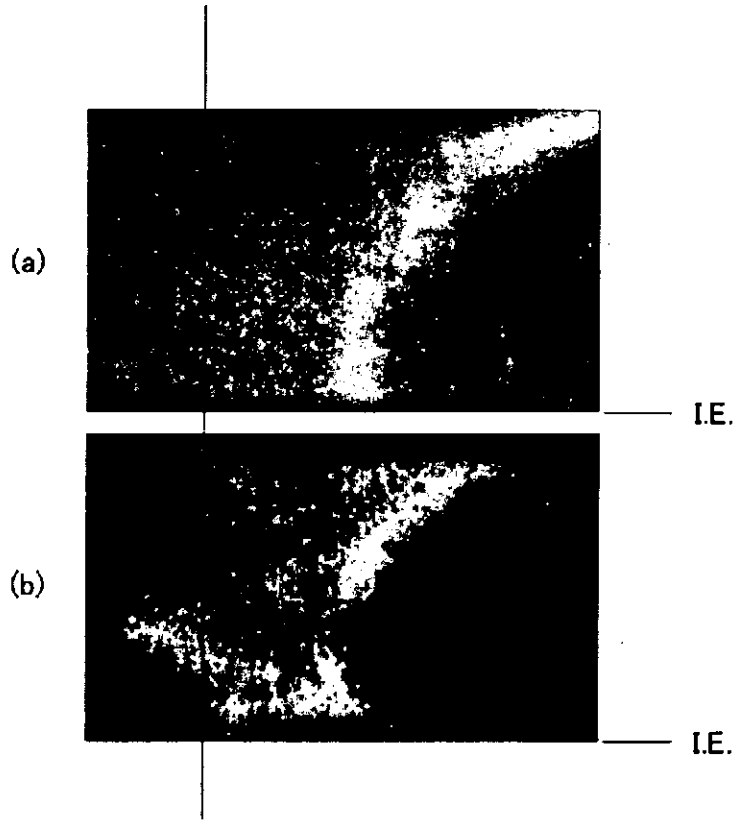

Fig. 5 Framing pictures of plasma focus in collapsed phase; taken with IMACON-700 (a) and taken with time-resolved pinhole camera (b).

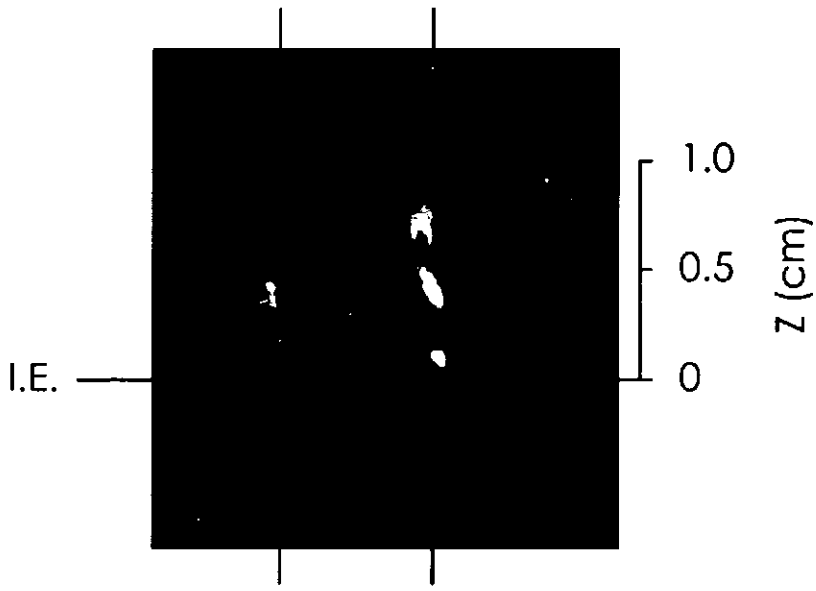

Fig. 6 Pinhole photographs obtained with time-resolved pinhole camera.

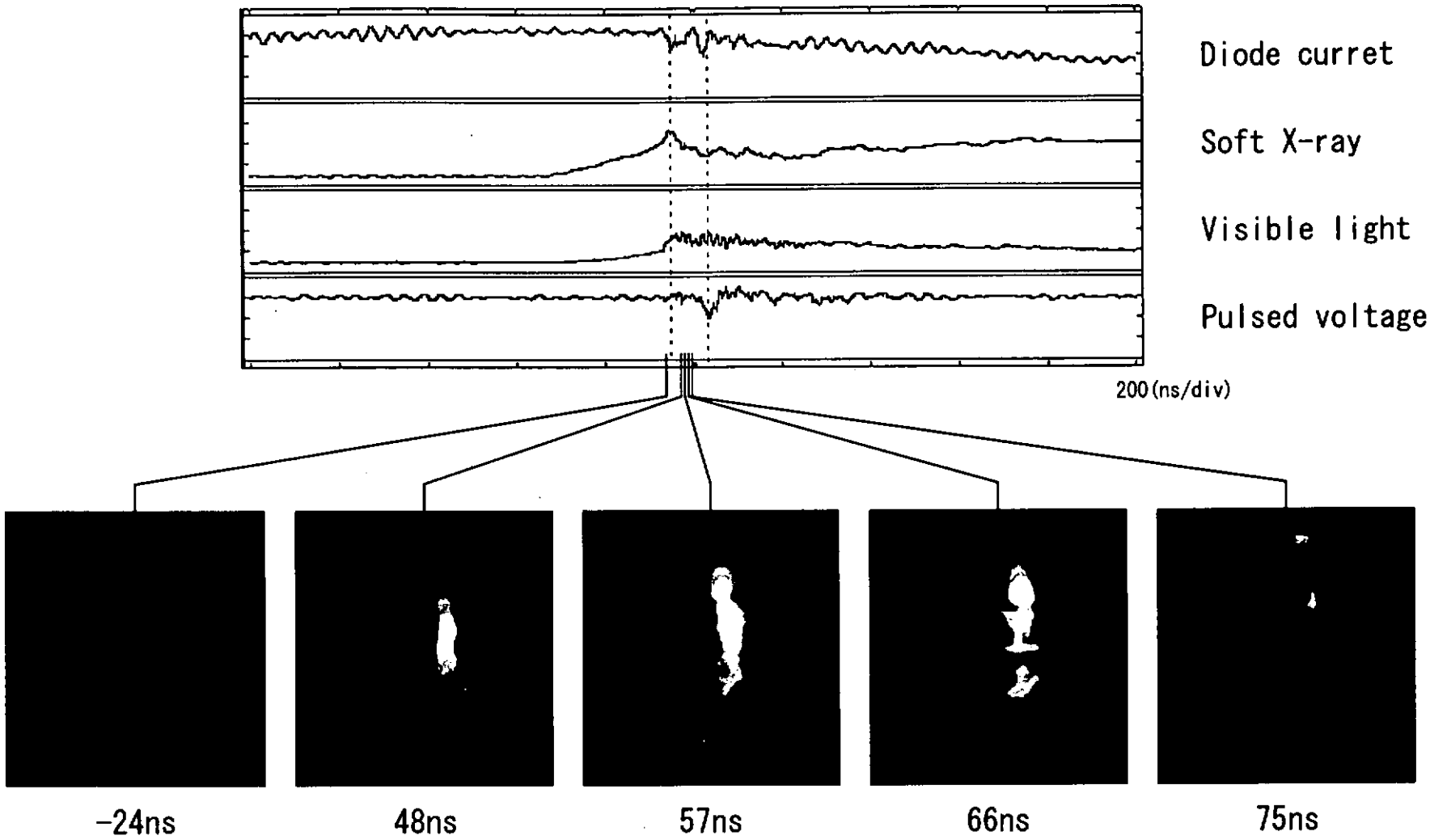

Fig. 7 Framing pictures that consist of the ultraviolet ray and the soft X-ray images in the case of neon gas.

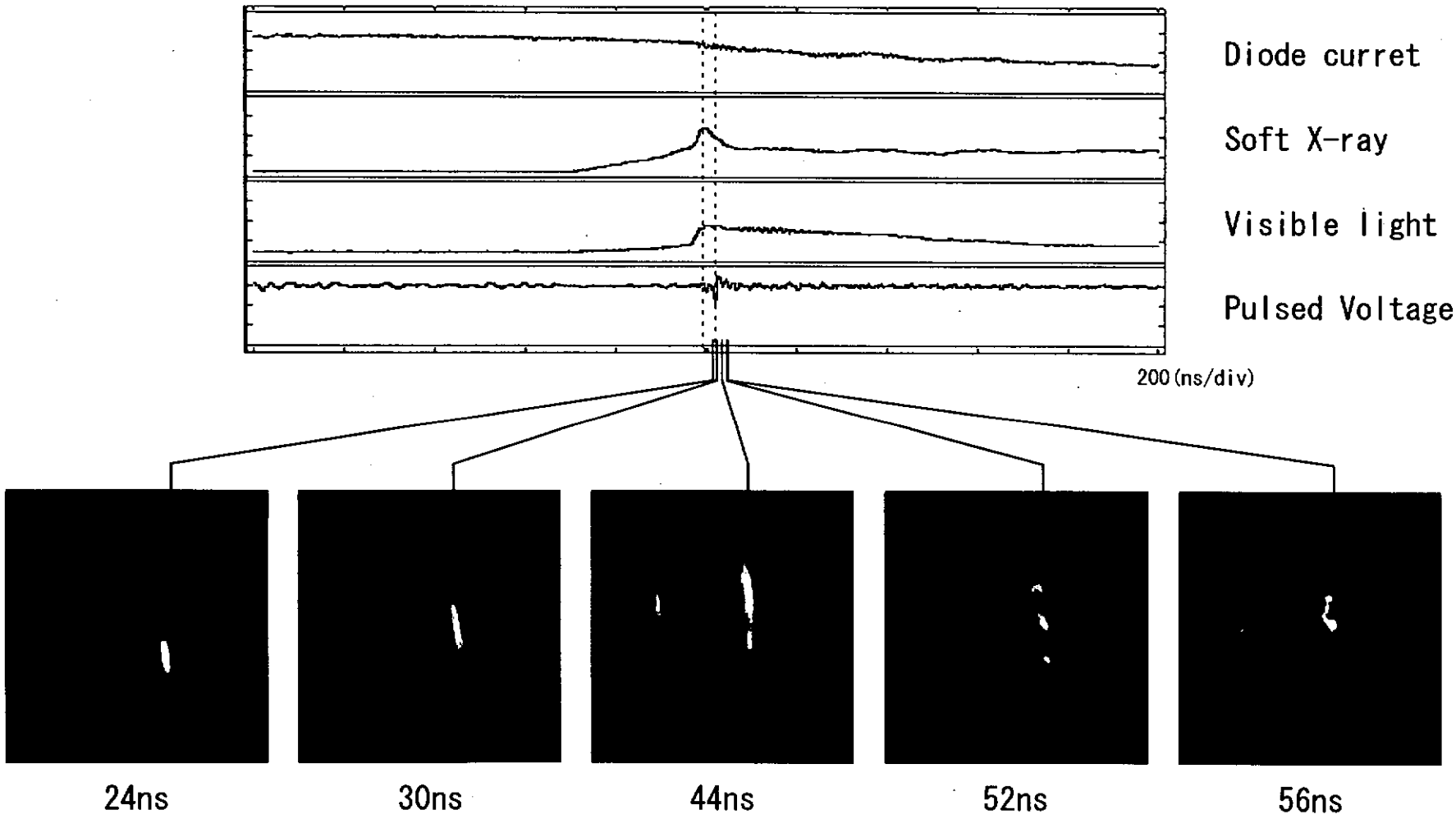

Fig. 8 Framing pictures that consist of the ultraviolet ray and the soft X-ray images in the case of argon gas.

The five framing pictures that consist of the ultraviolet ray and the soft X-ray images are shown in Figs. 7 and 8. Since only one framing picture is obtained from one shot, the five framing pictures are selected from several pictures. In all pictures the images shown in left side are constructed by ultraviolet rays, and those in right side are constructed by soft X-rays. The traces shown in upper side of the figures are the diode current, signals obtained with the PIN diodes and the pulsed high voltage. These traces are displayed as an example for showing the time correlation between the pictures and the diode current. As mentioned above the time origins were defined as the times when the spikes appeared in the soft X-ray signals obtained with the PIN diode.

The pictures shown in Fig. 7 were obtained by the working gas mixed with neon gas. In the first picture (t=-24ns), the outline of the plasma in collapsed phase is barely seen and the image by soft X-rays is not seen. From second picture (t=48ns) to fourth picture (t=57ns), the column shape images by ultraviolet rays are barely seen, and the images by soft X-rays vary from the column shape to the squashed shape due to the sausage instability. In the case of neon gas, it was reported in Ref. 3 that the images by soft X-rays are column shape, and the experimental results agree with these previous result. In the last picture (t=75 ns) the image by ultraviolet rays is not seen, and the image by soft X-rays becomes transparent and squashier.

The pictures shown in Fig. 8 were obtained by the working gas mixed with argon gas. From first picture (t=24ns) to third picture (t=44ns), the lighting region in the images by soft X-rays move towards the higher position, and are the column shape. The images by ultraviolet rays are not seen or barely seen. In fourth picture (t=52ns) and fifth picture (t=56ns), all the images become spot shape. The fourth picture is enlarged and is shown in Fig. 6. The all images by ultraviolet rays shown in Fig. 7 and Fig. 8 are transparent. This is caused by low detection efficiency of MCP and few ultraviolet rays passed through the quartz glass. One of the method to solve this problem is use of MCP with CsI coating. The data reported in Ref. 7 are displayed in Fig. 9. In this figure the detection efficiencies of MCP and MCP with CsI coating are plotted as a function of the wavelength. By coating of

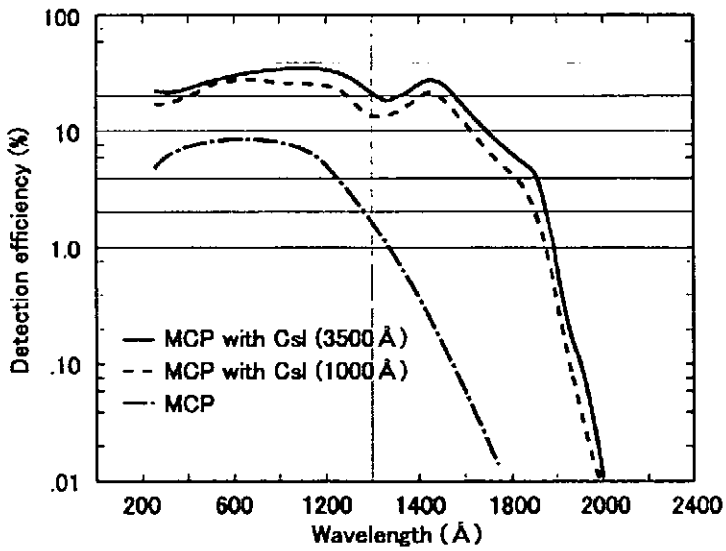

Fig. 9 Detection efficiency of MCP and MCP with CsI as a function of wavelength.

CsI the detection efficiency becomes high and the useable wavelength becomes long up to 200 nm.

IV. Summary

We modified a time-resolved X-ray pinhole camera, and were able to take the images by soft X-rays and ultraviolet rays at the same time. This camera was used in the experiment on the small plasma focus device. The images by ultraviolet rays and soft X-rays were taken and were compared in the focused phase of the plasma focus. The summaries are as follows.

1. The positions of the lighting regions by the ultraviolet rays were approximately agreed with that by the soft X-rays. If the soft X-rays are generated by L-shell radiation, those might be generated from excitation by collision between thermal electrons and ions.
2. From comparison between the images by ultraviolet rays and visible light, it is considered that the configuration of the image by the ultraviolet rays corresponds to the configuration of a plasma as like an image by visible light. The wavelengths of the detected ultraviolet rays are approximately 160 nm.

References

1) M. Howells, J. Kirz and D. Sayre, Sci. Am., **264** (1991) 42.
2) Y. Kato, I. Ochiai, Y. Watanabe and S. Murayama, J. Vac. Sci. Technol., **B6** (1988) 195.
3) F. Beg, I. Ross, A. Lorenz, J. Worley, A. Dangor and M. Haines, J. Appl. Phys., **88** (2000) 3225.
4) B. Shan, T. Yanagidaira, K. Shimoda and K. Hirano, Rev. Sci. Instrum., **70** (1999) 117.
5) P. Rowekamp, G. Decker, W. Kies, B. Lucas, F. Schmitz, G. Ziethen, D. Simanovskii and S. Bobashev, Proc. 11th Int. Conf. High Power Particle Beams, Prague, (1996) 174.
6) H. Itano, N. Iwami, K. Shimoda and M. Sato, NIFS-PROC-50 (2001) 131.
7) C. Martin and S. Bowyer, Appl. Opt., **21** (1982) 4206.

CHARACTERISTICS OF HIGH ENERGY IONS PRODUCED IN PLASMA FOCUS

T.Honda, I.Kitamura, T.Takahashi, and K.Masugata

Faculty of Engineering, Toyama University, 3190, Gofuku, Toyama, 930-8555, Japan

ABSTRACT

Characteristics of ion beams produced in the Mather type plasma focus (P.F) were studied experimentally to apply the beam to materials processing. The plasma focus was pre-filled with H_2 of 250 Pa, or mixture of H_2 (270 Pa) and Ne (30 Pa). At 213 mm downstream from the top of the anode on the electrode axis, ion beam of current density ≈ 4 kA/cm^2, pulse width ≈ 100 ns (FWHM) was observed when filling gas of H_2 was used. The ion species and energy spectra were evaluated by a Thomson parabola spectrometer (TPS). For protons of energy in the range of 0.1 – 1.5 MeV are observed when P.F was filled with H_2. From the X-ray measurement pinch plasma column of 3-4 mm in diam. and 40 mm in length is observed and line emission of He-like and H-like K shell X-ray emissions were observed when PF was filled with mixture gas. Measurement of pinhole image and an incident angle resolved proton energy spectrum ion production is found to be axial symmetry and the ion energy decreases with increasing incident angle.

I. Introduction

Strong emission of energetic ions, and x-ray are known to be emitted from the pinch plasma produced in plasma focus (P.F.). Especially, the energetic ions have following characteristics and expected to be applied to materials processing. [1-5)]

a) High energy ions of energy ranging from 100 keV to several MeV are produced with relatively low voltage pulsed power systems.[6)]

b) The power density and the brightness of the beams are very high. [1)]

To clarify the mechanism of the production of the ion beams and to apply them to materials processing we have evaluated the characteristic of the ion beam.

II. Experimental apparatus

Figure 1 shows a schematic of the Mather type P.F. was used in the experiment. The P.F. consists of an anode, a rod cathode, and a glass insulator. The anode is a cylindrical copper

electrode and the length and the diameter are 230 mm and 50 mm, respectively. To reduce the production of impurity ions and to reduce the damage of the electrode, the anode has a hollow shape top.

The cathode consists of 24 copper rods of diameter 10 mm, length 230 mm and the effective inner diameter of the cathode is 100 mm. The insulator is made of glass and the length and the outer diameter are 125 mm and 55 mm, respectively.

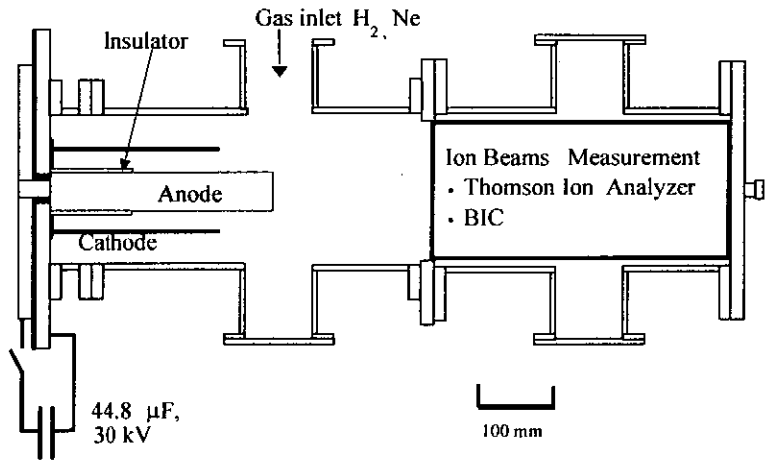

Fig. 1. Schematic of the experimental system.

To drive the P.F. a capacitor bank of capacitance 44.8 μF, maximum charging voltage 80 kV was used, which is connected to the P.F. through 224 of coaxial cables. In the experiment the charging voltage of the capacitor bank was fixed to 30 kV. The vacuum chamber was once evacuated to < 7×10^{-3} Pa and after that filling gas was introduced. In the experiment pure hydrogen (250 Pa), and mixture gas of hydrogen (270 Pa) and neon (30 Pa) were used as the filling gases. The experimental conditions are summarized in table I.

Table I. Experimental condition.

Capacitor	Charging voltage	Store energy	Base pressure	Gas	Pressure
44.8 μF	30 kV	20.2 kJ	< 7.0×10^{-3} Pa	H_2	250 Pa
				H_2 / Ne	270 / 30 Pa

Ⅲ. Experimental results

Figure 2 shows typical waveforms of the discharge current (I_{ch}) measured by a Rogowski coil, and an ion current density (J_i) measured at z = 218 mm downstream from the top of the anode on the electrodes axis. For the measurement of J_i, biased ion collector (BIC) was used. The BIC has a cup electrode inside the grounded body and the ions are injected into the cup electrode through an aperture of 0.3 mm in diameter. The electrode was biased to -300 V to remove commoving electrons. In the experiment the P.F. was pre-filled with pure hydrogen.

As seen in the figure, I_d has a peak of 750 kA at t = 1.6 μs and after that 150 kA of current dip is observed, which suggest the strong pinch of the plasma. In the figure, J_i rises sharply

at the end of the current dip (t = 1.7 μs) and has a peak 4.5 kA/cm^2 with pulse width of 80 ns (FWHM). Considering the TOF (time-of-flight) delay of J_i, ions are accelerated at the dip phase of I_{ch}.

Figure 3 shows the waveforms of J_i at different axial positions (z = 400 and 600 mm) for TOF evaluation of ion velocity. From the figure ion velocity is evaluated to be 5.7 x 10^6 m/s from the time deference of the peak of J_i. Since main component of the beam is considered to be proton, average proton energy is estimated to be 170 keV.

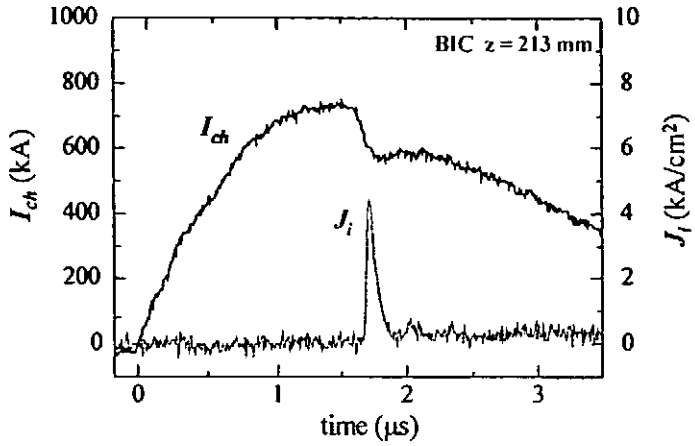

Fig. 2 Typical waveforms of I_d and J_i.

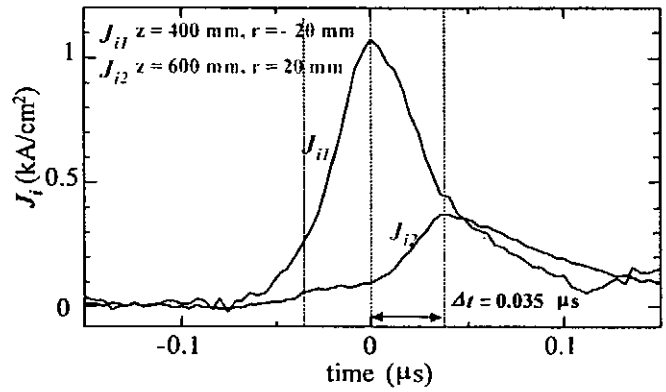

Fig. 3. Waveforms of J_i at different axial positions for TOF evaluation of ion energy.

For the measurement the species of ions and their energy spectra, Thomson parabola spectrometer (TPS) was used. The TPS is constructed of a pair of pinholes (1st and 2nd pinhole) to collimate a incident beam, a magnetic deflector, an electrostatic deflector, and a ion track detecting film of CR-39, the detail of the TPS is shown in the leterature[1]. Figure 4 shows the ion track pattern obtained by TPS. As seen in the figure, strong trace of protons is observed with weak trace of impurities. The energy of the protons is found to be in the range of 0.1 – 1.4 MeV.

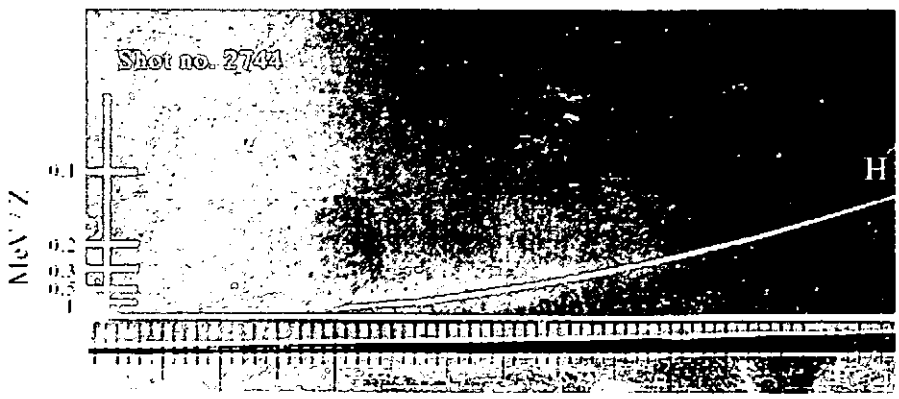

Fig. 4. The track pattern obtained by TPS. The filling gas was H_2 250 Pa.

To evaluate the spectral intensities (I_s) of protons of each beam energy[7] from Fig. 4, line

densities of the ion tracks (N_l, track number density along each parabola trace) of each energy was carefully evaluated. Here, I_s is evaluated by a following equation[7].

$$I_s \equiv \frac{1}{\Omega \cdot S} N_l \frac{dl}{dE}.$$

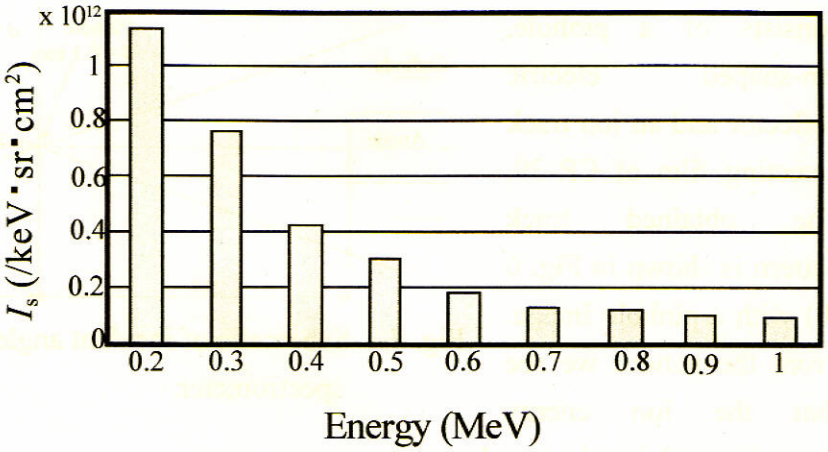

Fig. 5. Energy spectrum of protons evaluated from Fig. 4.

Here, l is the length of the parabola trace, E is the ion energy, S is the area of the 1st pinhole, Ω is the solid angle of the 2nd pinhole observed from 1st pinhole.

Figure 5 shows the result of the evaluation. As seen in the figure, I_s decreases with increasing energy. In addition the values of I_s are very large compared with that produced by a pulsed power ion diode[7].

Figure 6 (a) shows the particle pinhole image on CR-39 obtained by a particle pinhole camera. In the figure concentric circular patterns are observed, which suggest the axially-symmetric ion generation. Considering that ions passing off-axis are bended by a strong self-magnetic field of azimusal-direction, the ions seem to be produced on the axis.

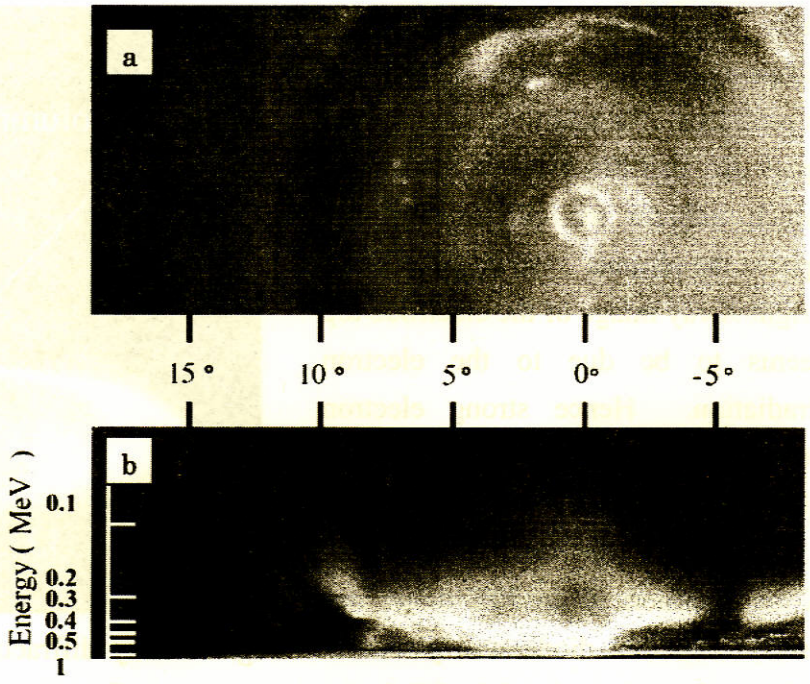

Fig. 6. Particle pinhole image (a) and an angular distribution of ion energy (b) obtained by a particle pinhole camera and an electric mass spectrometer, respectively. The incident pinholes for both measurement were placed at z = 213 mm on the electrode axis.

To evaluate the angular distribution of ion energy spectrum, electric ion energy spectrometer was used, which is shown in Fig. 7. The spectrometer

consists of a pinhole, fan-shaped electric deflector and an ion track detecting film of CR-39. The obtained track pattern is shown in Fig. 6 (b) with a pinhole image. From the pattern we see that the ion energy decreases with incident angle.

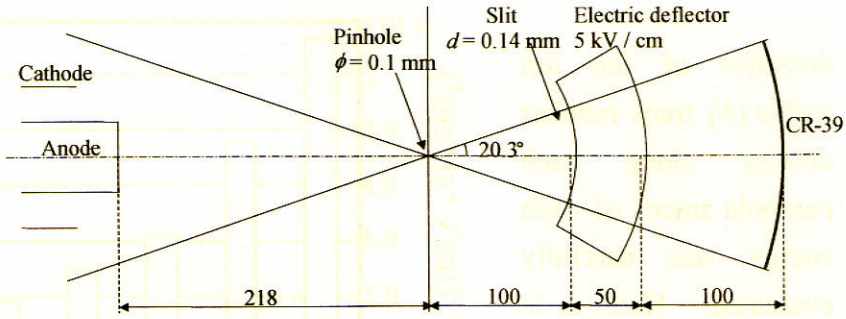

Fig. 7. Schematic of incident angle resolved electric ion energy spectrometer.

IV. X-ray measurement

To evaluate the characteristics of hydrogen pinch plasma by x-ray observations, 10 % of neon was added as a seed gas (H_2/Ne = 270/30 Pa). Figure 8 shows time integrated X-ray image of the P.F. obtained by an X-ray pinhole camera. Be filter of thickness 30 μm was used in the camera to remove visible light. As seen in the figure, X-ray images are observed from a pinch column of the plasma and from the top of hollow anode. The X-ray image from the pinch column has a size of 3-4 mm in diameter and 30 mm in length, hence we see that relatively uniform high temperature pinch column of that size is produced. In addition, some bright spots are also observed in the image, which indicate the existence of hot spot in the plasma. On the other hand, bright X-ray image of the electrode top seems to be due to the electron irradiation. Hence strong electron beam seems to be produced in the pinch plasma.

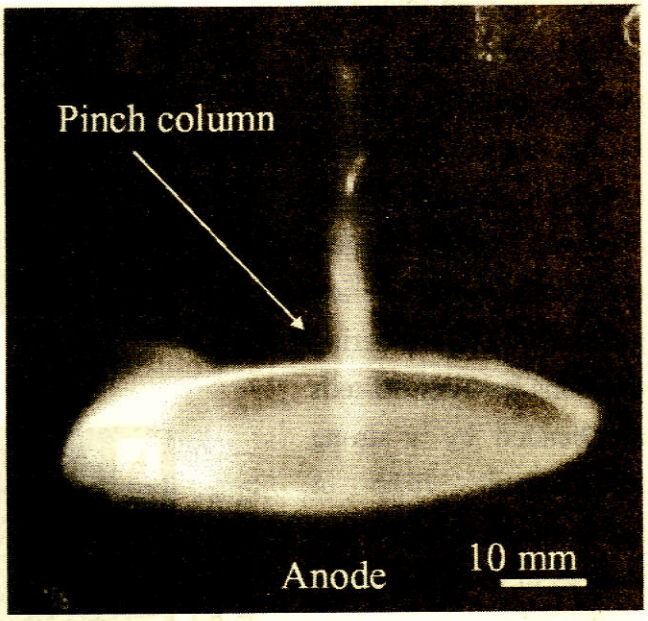

Fig. 8 X-ray diffraction patterns of amorphous Si thin films irradiated by pulsed proton beam.

To evaluate the time variation of X-ray emission, X-ray PIN diode was used. The PIN diode was placed at 110 mm from the axis of the P.F. in the vacuum chamber. Be filter of thickness 30 μm was used to remove light signal. Figure 9 shows the waveform of X-ray PIN diode output (V_{pin}). As seen in the figure, V_{pin} sharply rises with J_i and have a FWHM pulse width of less than 50 ns.

Figure 10 shows the X-ray spectrum obtained by a crystal spectrograph. In the spectrograph KAP crystal (2d = 2.664 nm) was used with an X-ray film of IP-21 (Kodak). Incident slit of width 0.1 mm was covered with Be foil. As seen from the figure K shell X-ray emission of H-like Ne and He-like Ne is observed, which indicate a existence of highly ionized Ne ions (Ne^{8+} and Ne^{9+}) in the pinch plasma.

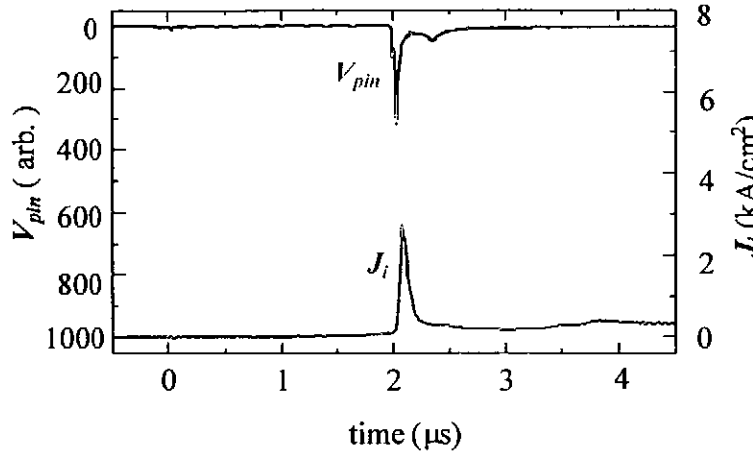

Fig. 9. Waveform of X-ray PIN diode output (V_{pin}) shown with J_i.

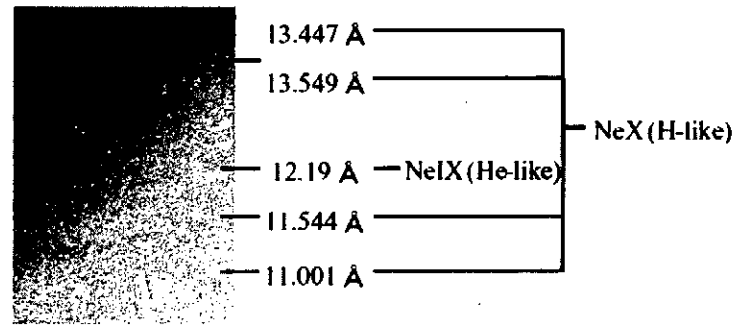

Fig. 10. The target positions in the irradiation experiment.

V. Conclusion

Characteristics of ion beams produced in the Mather type plasma focus (P.F) were studied experimentally to apply the beam to materials processing. The plasma focus was pre-filled with H_2 of 250 Pa, or mixture of H_2 (270 Pa) and Ne (30 Pa). At 218 mm downstream from the top of the anode on the electrode axis, ion beam of current density ≈ 4 kA/cm^2, pulse width ≈ 100 ns (FWHM) was observed when filling gas of H_2 was used. The ion species and energy spectra were evaluated by a Thomson parabola spectrometer (TPS). For protons of energy in the range of 0.1 – 1.4 MeV are observed when P.F was filled with H_2. From the X-ray measurement pinch plasma column of 3-4 mm in diam. and 30 mm in length is observed and line emission of He-like and H-like K shell X-ray emissions were observed when PF was filled with mixture gas. From the measurement of pinhole image and an incident angle resolved proton energy spectrum we see that ion production is axial symmetry and the ion energy decreases with increasing incident angle.

References

1) K. Takao, Y. Doi, S. Hirata, M. Shiotani, I. Kitamura, T. Takahashi and K. Masugata, Jpn. J.

Appl. Phys., **40**, Part 1 (2000) pp. 1013-1015

2) T. Takao, M. Shiotani, T. Honda, I. Kitamura, T. Takahashi, K. Masugata, Characteristics of the Nitrogen Ion Beam Produced in a Plasma Focus Device, Proc. 28th IEEE Int'l Conf. on Plasma Science and 13th IEEE Int'l Pulsed Power Conf., Las Vegas, Nevada, June 17-22, 2001, P1C01 (2001)

4) J. N. Feugeas, E. C. Llonch, C. O. de Gonzalez and G. Galambos, J. Appl. Phys., **64** (1988) 2648

5) H. Kelly, A. Lepone, A. Marquez, D. Lamas and C. Oviedo, Plasma Sources Sci. Technol. **5** (1996) 704

6) R.L. Gullickson and H.L. Sahlin, J. Appl. Phys., **49**, (1978) 1099

7) K. Masugata, H. Okuda, K. Yatsui and T. Tazima, "Evaluation of brightness of intense pulsed ion beam by a Thomson spectrometer" Laser and Particle Beams **15**(2) 325 (1997).

NOx REMOVAL FROM DIESEL ENGINE EXHAUST USING PULSE DRIVEN NON-THERMAL PLASMA REACTORS

Koichi Takaki, Takashi Sasaki, Shoji Kato, Seiji Mukaigawa and Tamiya Fujiwara

Department of Electrical and Electronic Engineering, Iwate University, Ueda 4-3-5, Morioka 020-8551, Japan

ABSTRACT

NOx removal from a diesel engine exhaust and its simulated gases was carried out using two different non-thermal plasma reactors. One is multipoints dielectric barrier discharge (DBD) reactor, the other is pulse streamer discharge (PSD) reactor. In the former reactor, the 2 mm thickness Pyrex glass plate is used as the dielectric barrier. The DBD reactor is driven by IGBT pulse modulator which can supply the 10 kV pulse voltage to the reactor with repetition rate of 2.5 kpps. The co-axial cylinder type discharge chamber is used as the PSD reactor which is driven by the pulse power generator with semiconductor opening switches (SOS). The SOS pulse generator can supply both polarity of 30 kV pulse with 300 pps repetition rate. The DBD reactor energy cost for NO removal from simulated gas (N_2:O_2=9:1, Initial NO concentration = 200 ppm) is obtained to 12 g/kWh at 65% removal in 5 *l*/min. gas flow rate. The energy cost of the PSD reactor is almost 12 g/kWh at 25% NO removal efficiency. The DBD reactor was applied to 20 kVA diesel engine generator exhaust gas treatment. The contained NOx ($NO+NO_2$) is abated from 70 to 40 ppm at no-load to the generator, and from 340 to 300 ppm at 50 A load. The energy cost for the NOx removal is obtained to 32 g/kWh.

I. Introduction

Huge amounts of air pollutants like carbon monoxide (CO), unburned hydrocarbons (HC), nitrogen oxides (NOx) and particulate matter (PM) have been released into the atmosphere over the last decades. These pollutants are the main cause of acid rain, urban smog, and respiratory organ disease.[1] An increasing portion of the pollutants is emitted from motor vehicles. The exhausts of gasoline engines are cleaned very efficiently with the three-way-catalyst. For diesel and lean burn engines the three-way-catalyst does not operate, because the high oxygen content in these exhaust gases prevents the reduction of nitrogen oxide (NO).[2]

Dry NOx removal technologies can solve such problems of the conventional processes. A non-thermal plasma process using a dielectric barrier discharge and/or a pulse streamer discharge is particularly attractive for this purpose because it can be operated stably at atmospheric pressure.[3)-5)] During the past decade, a lot of studies on this process have been conducted in small-scale systems.[5)-11)] Although encouraging results have been obtained in small-scale systems, the high flow rate test is necessary to prove the feasibility for practical application and improve this process further. Nevertheless, few studies have shown the possibility to realize this process in high flow rate up to 1 m^3/min.[12)]

Generally, the barrier discharge process requires a high voltage generator. Up to now, some types of sinusoidal waveform power supply have widely been used as high voltage

generator. One of these utilized the 110V-15 kV neon transformer because it can easily be made for a low price. [12), 13)] However, energy transfer efficiency of the neon transformer is not so high because it is a kind of leakage transformer. [14)] The energy transfer efficiency from the wall plug to the reactor load is an important requirement from the economical view-point.

We have designed and constructed a reactor and a pulse modulator for removal of NOx from the exhaust of a 20 kVA diesel-engine in which light oil is ignited by compression. The pulse modulator consists of two IGBT switching devices and a pulse transformer with magnetic-assist to generate repetitive high voltage pulse. A multipoint-to-plane geometry was used for the electrodes of the reactor to lower the operating voltage. [15)-17)] A dielectric barrier of glass with 2 mm thickness was put on the plane electrode. The reactor consists of six discharge cells, and each cell has five stacked multipoint-to-plane electrodes where an exhaust from the diesel-engine generator flows with a high flow rate. The ultimate goal of this study is to prove the possibility for realization of this process in a large scale. The detailed objectives are to induce dielectric barrier discharge successfully by applying repetitive pulsed voltage lower than 10 kV, reduce power consumption required for NOx removal, and develop a reliable pulsed voltage generator. Moreover, we also constructed a cylindrical plasma reactor driven by a compact pulsed power generator using semiconductor-opening switches (SOS). The NO removal efficiency of the pulse streamer reactor was obtained using a simulated gas and was compared with the efficiency of the pulse driven multipoint DBD reactor.

II. Performance of multipoint DBD reactor

A. IGBT pulse modulator

Fig. 1 shows a circuit of the pulse modulator used to drive the DBD reactor. The diode bridge (D_1,...D_4) is a full-wave rectifier circuit. The full-wave rectified current charges the capacitors C_3 and C_4 up to 283 V through the capacitors C_1 and C_2 which supplies DC bias voltage. Energies stored in C_3 and C_4 are released to the reactor through a pulse transformer PT and magnetic switch Ls by two IGBT switches. The timing of the switching of IGBT was controlled by the gate pulse. When IGBT1 switch is turned on, the electric charge of C_3 is discharged and a negative high-voltage pulse is applied to the reactor. If only one IGBT switch is used, the magnetic switch Ls cannot be reset and cannot work. When IGBT2 switch is turned on, C_4 is discharged and a positive high-voltage is applied to the reactor.

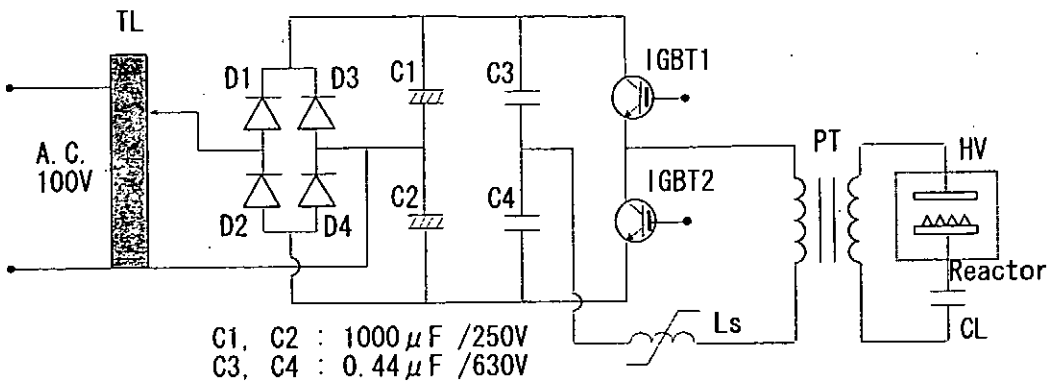

Fig. 1 Pulse modulator for DBD reactor.

The specifications of the pulse modulator used are as follows; the available peak voltage is 10 kV, the pulse repetition rate is variable from 0.1 to 2.5 kHz. Typical waveforms of applied voltage and dielectric barrier discharge current are shown in Fig. 2. The voltage rises to 10 kV with rise time of 4 μs.

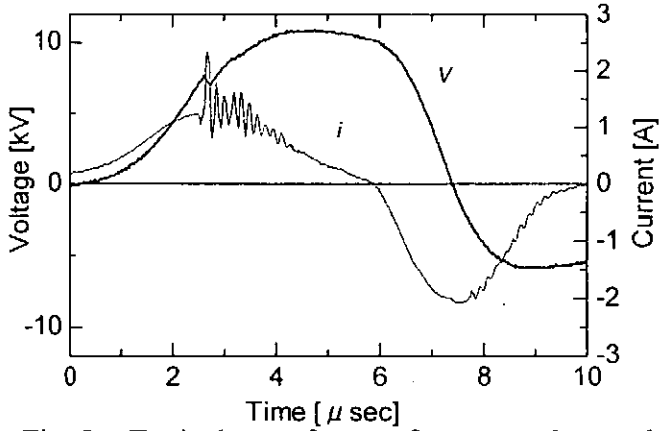

Fig. 2 Typical waveforms of output voltage of the pulse modulator and dielectric barrier discharge current.

B. Multipoint DBD reactor and experimental procedure

The configuration of the DBD reactor is shown in Fig. 3. We used the multipoint type electrode to decrease the DBD operating voltage and to increase the gas flow conductivity. The electrode has 528 pyramids with a height of 5 mm and an angle of 45° in an area of 132 cm^2 (220 mm×60 mm). The reactor chamber is a rectangular prism with dimension of 335 × 600 × 405 mm (width × length × height). The 2 mm thickness pyrex glass plates are used as dielectric barrier. The points-to-barrier distance is 2.0 mm. In the experiment, we used one unit as shown in Fig. 3 for simulated gas remediation and 6 units (shown in Fig. 4) for Denyo DCA-25 diesel engine exhaust. The rated values of this engine are 2,369 cc displacement, 200 V output voltage with three phase and 20 kVA output power. The flow rate of the exhaust gas is 1.2 m^3/min. The remedied exhaust gas was analyzed using Hodaka testo 350 combustion exhaust gas analyzer. The voltage was measured by a Tektronix P6015 probe, and current was measured by Pearson 2878F current transformer. The power consumed in the reactor was obtained by integrating the voltage-charge curve (V-Q Lissajous figure) measured using 0.2 or 1.1μF capacitors.

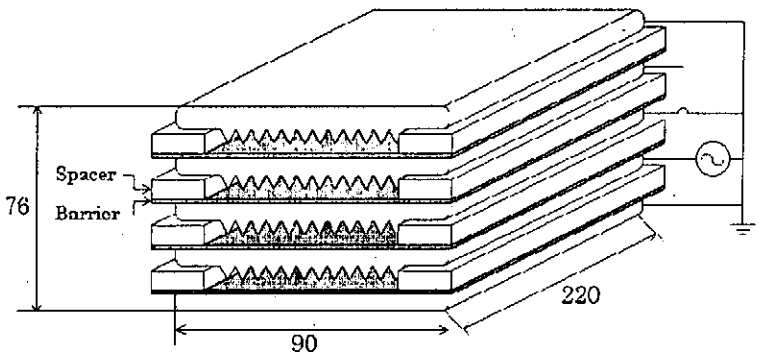

Fig. 3 Configuration of the multipoint DBD reactor.

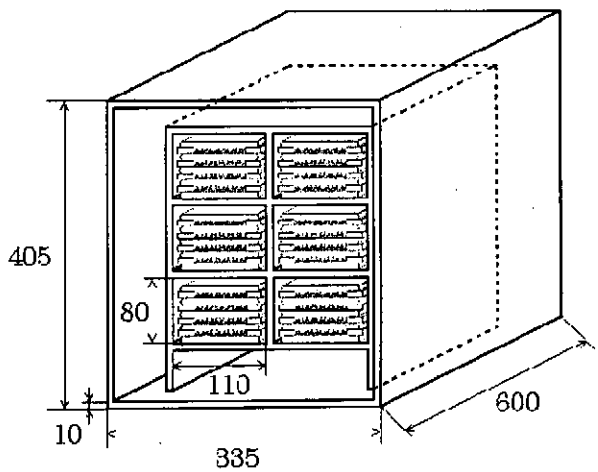

Fig. 4 DBD reactor for high-flow rate gas treatment.

C. Reactor performance for low flow rate simulated gas

NO and NOx (=NO+NO_2) removal from the simulated gas using multipoint DBD reactor is shown in Fig. 5. The gas flow rate is 5 *l*/min. In this case, a rf power source was used as DBD driver. The waveform of the output voltage was sinusoidal and the frequency of applied voltage was changed from 10 to 50 kHz. The 200 ppm NO is oxidized to NO_2 at 100 J/*l* input energy and 200 ppm NO+NO_2 is almost removed at 250 J/*l* input energy. The energy efficiency for NO removal is calculated to 11.7 g/kWh (389 μmol/Wh) at 65% NO removal rate.

D. Reactor performance for diesel engine exhaust gas

Fig. 6 relates the removals of NO and NOx as a function of electrical energy density in the diesel exhaust gas stream. The load current of the diesel engine generator is 0 A, that is no load condition. In this case the concentrations of O_2, NO and NO_2 contained in the engine exhaust gas are 18%, 70 and 17 ppm, respectively. The removals of NO and NOx linearly increased with energy density. This is caused by the fact that the production of radicals such O, OH, HO_2, and O_3 for removal of NO and NO_2 is proportional to the energy density. Higher concentrations of radicals result in faster removal of NO and NO_2. In our experimental condition, about 30% (26 ppm) of NOx on the basis of initial concentration of 87 ppm was removed at energy density of 11 J/*l* (3.06 Wh/m^3). The energy efficiency of NO removal is 11.9 g/kWh (398 μmol/Wh) at 40 % NO removal.

Fig. 7 shows the removals of NO

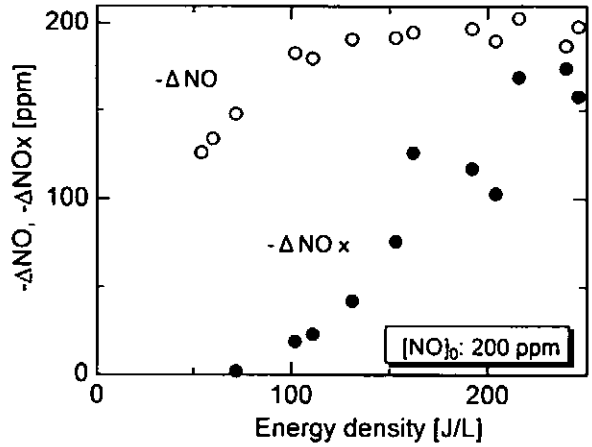

Fig. 5 NO and NOx (NO+NO_2) removals from simulated gas as a function of electrical energy density in DBD reactor.

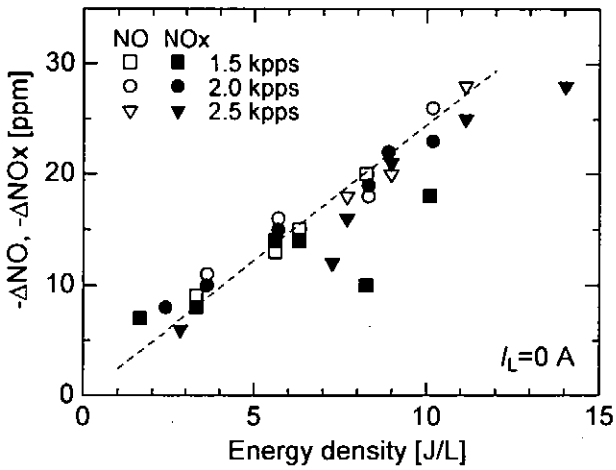

Fig. 6 Removals of NO and NOx (NO+NO_2) as a function of input energy density in case of no-load.

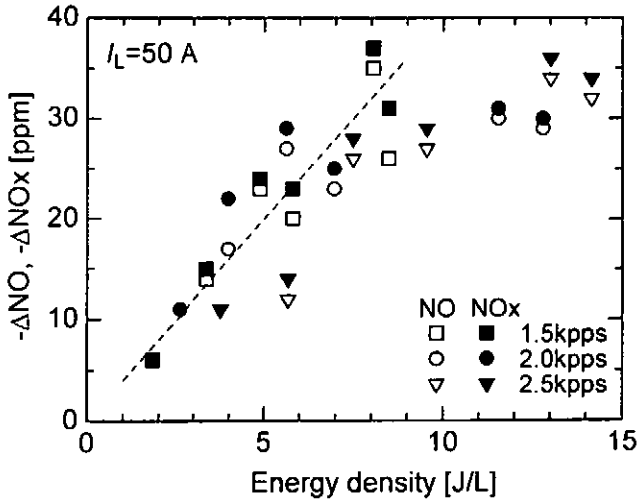

Fig. 7 Removals of NO and NOx as a function of input density in the case of 50 A load current.

and NOx at the engine load current of 50 A, that is 85% of the full load. Under this condition, the concentrations of O_2, NO and NO_2 contained in the engine exhaust gas are 7%, 340 and 54 ppm, respectively. In this case, a flow rate of the exhaust gas was controlled to 1.2 m^3/min. by a leak valve which was inserted between the engine and the dust filter. The removals of NO and NOx increased with energy density. In this case, about 35 ppm (9%) of NOx on the basis of initial concentration of 394 ppm was removed at energy density of 8 J/*l* (2.2 Wh/m^3). The NOx removal of 35 ppm with energy density of 8 J/*l* corresponds to the efficiency of 32 gNOx $kW^{-1}h^{-1}$ (53 eV in specific energy cost for NOx removal). The energy efficiency of NO removal is 21.1 g/kWh (703 μmol/Wh) at 10 % NO removal.

III. Performance of PSD reactor driven by SOS pulse generator

A. SOS pulse generator

The pulse generator for pulse streamer discharge reactor consists of a capacitor, a energy storage inductor and SOS diode as shown in Fig. 8. The capacitance of the capacitor *C* and the inductance of the inductor *L* were chosen to interrupt the circuit current by SOS diode at peak current, and these values were 1.3 nF and 13 μH, respectively. The twenty SOS diodes (VMI K25UF) were connected in series and were used as opening switches. The applied voltage and the circuit current were measured by a Tektronix P6015 probe and Pearson

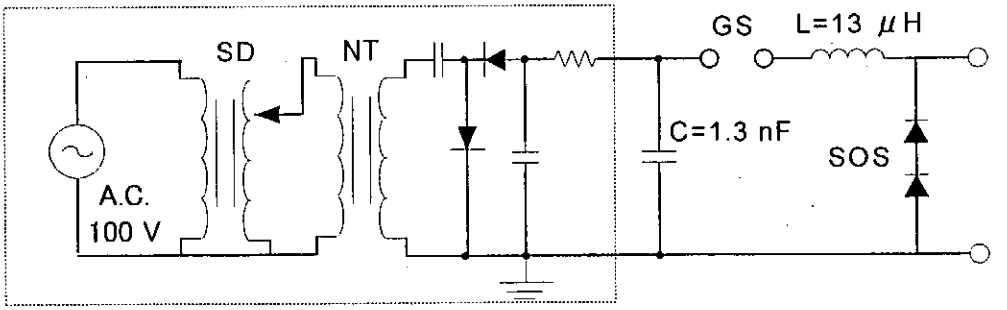

Fig. 8 SOS pulse generator for the pulse streamer reactor.

2878F current transformer, respectively. The energy consumed in the reactor was calculated in the computer.

Figure 9 shows the waveforms of the positive output voltage and the circuit current. The charged voltage in the capacitor C is –7.5 kV. The current starts to flow after the switch GS closing and reaches to peak value –90 A. The SOS diode starts to open almost 100 ns after reversal of current polarity. The output voltage has 35 ns pulse width (full-width half-maximum) and has 23 kV peak voltage.

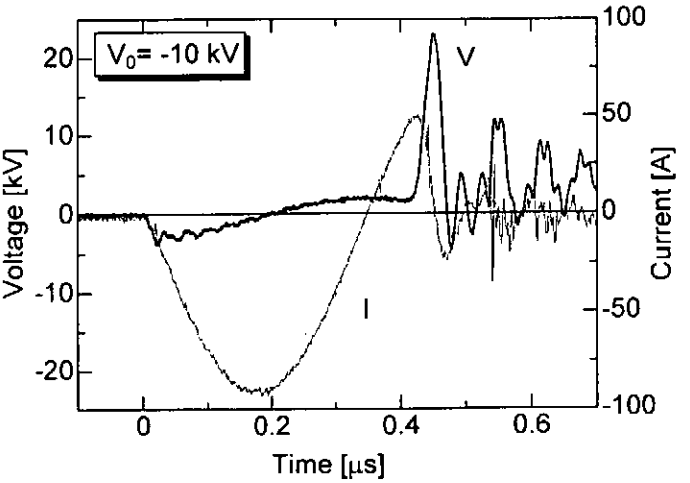

Fig. 9 Waveforms of a voltage and a current of the pulse generator at no-load condition.

B. Experimental setup

Figure 10 shows a schematic of the experimental setup using the pulse streamer discharge reactor. The simulated gas was diluted NO with nitrogen and oxygen mixed gas with rate 9:1. The co-axial PSD reactor consists of 1mm$^{\phi}$ tungsten wire and a copper cylinder of 20 mm in inner diameter. The length of the reactor is 300 mm, which corresponds to 94 cc in volume. The initial concentration of NO gas was controlled to 200 ppm using mass flow controller. The flow rate of the simulated gas was changed from 2 to 5 *l*/min. The remedied gas was analyzed using Best Sokki BCL-511 gas analyzer for NO and NO_2.

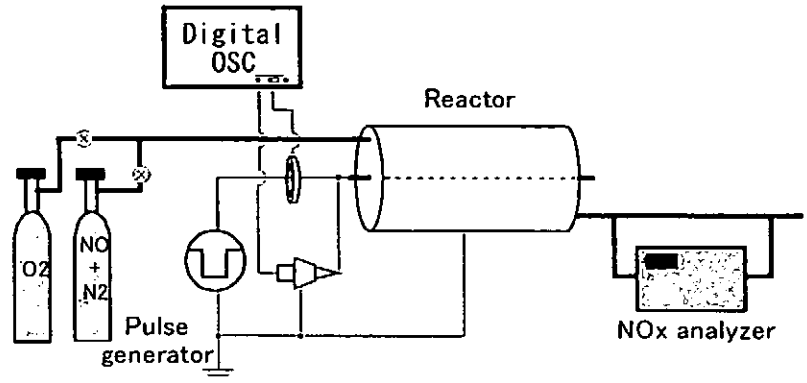

Fig. 10 Experimental setup for NOx removal using pulse streamer discharge.

C. PSD reactor performance for low flow rate simulated gas

The performance of the pulse streamer reactor driven by the pulse generator with SOS switch was tested for NO removal from the simulated gas. Figure 11 shows the applied voltage and discharge current of the reactor. The capacitor *C* was charged up to 7.5 kV. The peak current of the discharge is 29 A at peak voltage 18.7 kV. The energy consumption is calculated to 14 mJ per one pulse.

Figure 12 shows the NO removal efficiency as function of input energy density for various gas flow rates. The polarity of the applied voltage is negative. The energy input was controlled with frequency (from 5 to 50 Hz) of applied voltage. NO removal efficiency increases with increasing input energy density. The energy

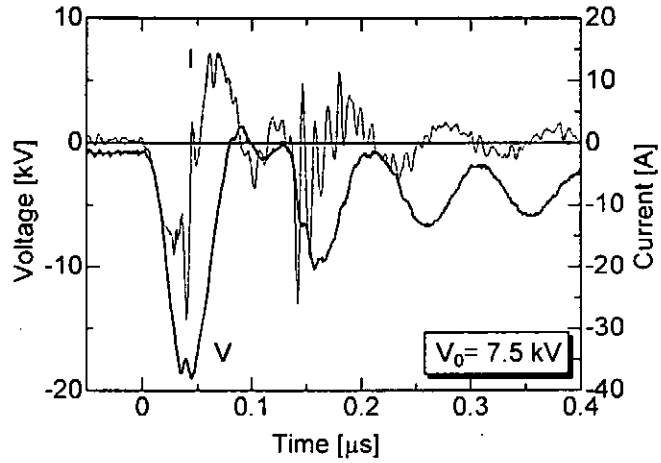

Fig. 11 Waveforms of a negative applied voltage and discharge current of the PSD reactor.

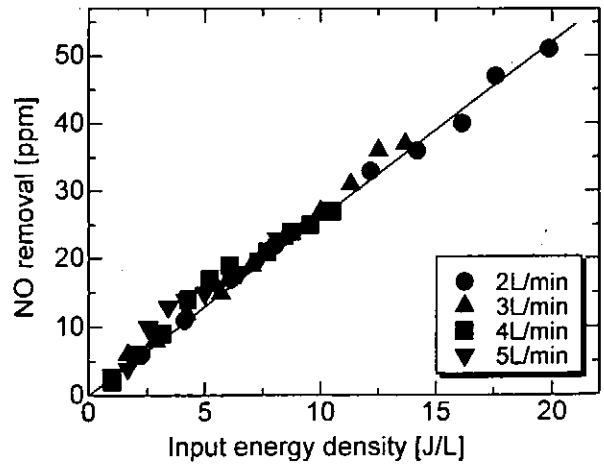

Fig. 12 NO removal from simulated gas as a function of electrical energy density at negative applied voltage.

efficiency of NO removal is calculated to 12.3 g/kWh (410 μmol/Wh) at 25 % NO removal.

Figure 13 shows the NO removal efficiency at positive applied voltage. NO removal efficiency increases with increasing input energy density. The energy efficiency of NO removal is calculated to 8.3 g/kWh (275 μmol/Wh) at 41 % NO removal. It is necessary to optimize the reactor configuration and dimensions to the present pulse generator.

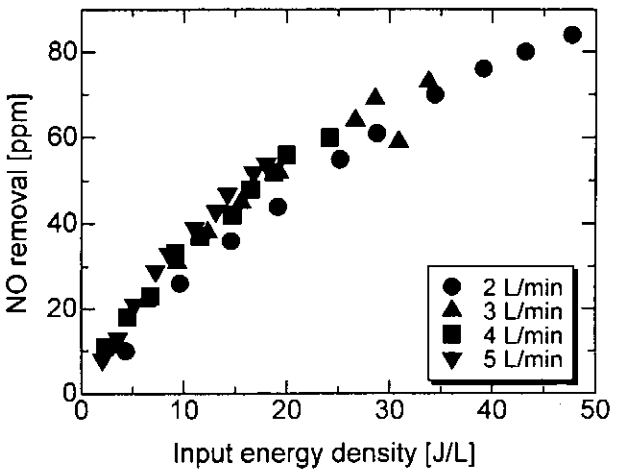

Fig. 13 NO removal from simulated gas as a function of electrical energy density at positive applied voltage.

IV. Conclusion

NOx removal from a diesel engine exhaust and simulated gases was carried out using two different non-thermal plasma reactors. The DBD reactor energy cost for NO removal from simulated gas (N_2:O_2=9:1, Initial NO concentration = 200 ppm) is obtained to 11.7 g/kWh at 65% removal in 5 *l*/min. gas flow rate. The energy cost of the PSD reactor is almost 12.3 g/kWh and 8.3 g/kWh at 25% and 41% NO removal efficiency. The DBD reactor was applied to 20 kVA diesel engine generator exhaust gas treatment. The contained NOx (NO+NO_2) is abated from 70 to 40 ppm at no-load to the generator, and from 340 to 300 ppm at 50 A load. The energy cost for the NOx removal is obtained to 32 g/kWh. NOx removal from gasoline engine exhaust was also carried out using these reactors.

Acknowledgments

The authors would like to thanks Drs.. H. Akiyama of Kumamoto University and J. S. Chang of McMaster University in Canada for their valuable discussions and comments.

References

1) Y.S. Mok and I. Nam, "Positive Pulsed Corona Discharge Process for Simultaneous Removal of SO2 and NOx from Iron-Ore Sintering Flue Gas", IEEE Trans. Plasma Sci., vol.27, no.4, pp. 1188-1196, 1999.
2) S. Broer, T. Hammer and T. Kishimato, "NO-Removal in Hydrocarbon Containing Gas Mixtures Induced by Dielectric Barrier Discharges", Proc. of 12th Int. Conf. Gas Discharge & Their Applications, I, pp.188-191, 1997.
3) B. Eliasson, and U. Kogelschatz, "Nonequilibrium Volume Plasma Chemical Processing", IEEE Trans. Plasma Sci., vol.19, no.6, pp. 1063-1077, 1991.
4) J. S. Chang, P. A. Lawless, and T. Yamamoto, "Corona Discharge Processes", IEEE Trans. Plasma Sci., vol.19, no.6, pp. 1152-1166, 1991.
5) M. B. Chang, M. J. Kushner, and M. J. Rood, "Removal of SO2 and the Simultaneous Removal of SO2 and NO from Simulated Flue Gas Streams Using Dielectric Barrier Discharge Plasmas", Plasma Chemistry and Plasma Processing, vol.12, no.4, pp. 565-580, 1992.

6) G. Lepperhoff, K. Hentschel, P. Wolters, W. Neff, K. Pochner and F. Trompeter, "Lean-Combustion Spark-Ignition Engine Exhaust Aftertreatment Using Non Thermal Plasma", SAE Paper 982512, pp.79-85, 1998.
7) W. Sun, B. Pashaie, S. K. Dhali, F. I. Honea, "Non-thermal plasma remediation of SO2/NO using a dielectric-barrier discharge", J. Appl. Phys., vol.79, pp.3438-3444, 1996.
8) A. Gal, M. Kurahashi, and M. Kuzumoto, "An energy-cinsumption and byproduct-generation analysis of the discharge nonthermal plasma-chemical NO-reduction process", J. Phys. D: Appl. Phys. vol.32, pp.1163-1168, 1999.
9) T. Nomura, Y. Ehara, T. Ito, and M. Matsuyama, "Effect of applied voltage frequency on NOx removal rate for a superimposing discharge reactor", J. Electrostatics, vol.49, pp.83-93, 2000.
10) C.R. McLarnon and B.M. Penetrante, "Effect of gas composition on the NOx conversion chemistry in a plasma", SAE Paper 982433, pp.37-48, 1998.
11) K. Takaki, M.A. Jani, and T. Fujiwara, "Removal of Nitric Oxide in Flue Gas by Multipoint-to-Plane Dielectric Barrier Discharge", IEEE Trans. on Plasma Sci., vol.27, no.4, pp.1137-1145, 1999.
12) M. Higashi, S. Uchida, N. Suzuki, and K. Fujii, "Soot Elimination and NOx and Sox Reduction in Diesel-Engine Exhaust by a Combination of Discharge Plasma and Oil Dynamics", IEEE Trans. Plasma Sci., vol.20, no.1, pp. 1-12, 1992.
13) S.K. Dhali and I. Sardja, "Dielectric-barrier discharge for processing of SO2/NOx", J. Appl. Phys., vol.69, no.9, pp.6319-6324, 1991.
14) T. Suzuki, M.A. Jani, S. Kudo, K. Takaki, S. Kato and T. Fujiwara, "Energy Transfer Efficiency of NOx Reduction System Using Neon Transfer by Dielectric Barrier Discharge", T. IEE Japan, vol.119-A, no.1, pp. 13-18, 1999 [in Japanese].
15) T. Suzuki, H. Murakami, K. Takaki, and T. Fujiwara, "Reduction of NO2 in simulated gas using dielectric barrier discharge", T. IEE Japan, Vol.117-A, no.11, pp.1084-1089, 1997 [in Japanese].
16) M. A. Jani, K. Takaki, and T. Fujiwara, "Low-Voltage Operation of a Plasma Reactor for Exhaust Gas Treatment by Dielectric Barrier Discharge", Rev. Sci. Instrum., vol.69, no.4, pp. 1847-1849, 1998.
17) M. A. Jani, K. Takaki, and T. Fujiwara, "Streamer polarity dependence on NOx removal by dielectric barrier discharge with a multipoint-to-plane geometry", J. Phys. D: Appl. Phys., vol.32, pp.2560-2567, 1999.

BREAKDOWN CHARACTERISTICS WITH POROUS METALS

S.Furuya, H.Toi, S.Takano and J.Irisawa

Nagaoka University of Technology, Niigata, 940-2188, JAPAN

ABSTRACT

We have investigated the breakdown characteristics with porous metals as a discharge electrode. The gap we investigated is needle-plain electrode. First, we examine the DC flashover voltage of the gap when we use a mirror finished brass plate and a porous metal as a plain electrode. Second, we investigate the breakdown characteristics of the statistical time-lag and formative time-lag of flashover when a flat-top nanosecond pulse is applied to the gap. Lastly, we predict the formative time-lags using streamer theory and compare them with the experimental results.

1. Introduction

Mirror finished electrodes are usually used as an electrode of discharge gap. By the way porous metals can be made recently. Porous metals have a lot of pores as shown in Fig.1. Then we have investigated the breakdown characteristics with porous metals as a discharge electrode. The gap we investigated is needle-plain electrode. First, we examine the DC flashover voltage of the gap when we use a mirror finished brass plate and a porous metal as a plain electrode. Second, we investigate the breakdown characteristics of the statistical time-lag and formative time-lag of flashover when a flat-top nanosecond pulse is applied to the gap. Lastly, we predict the formative time-lags using streamer theory and compare them with the experimental results.

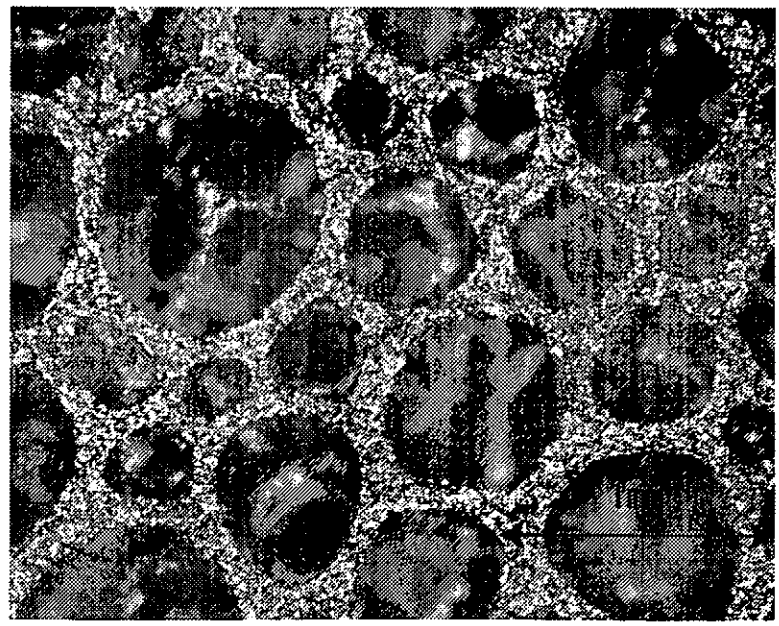

Fig.1 surface micrograph of porous metal

2. Experimental Setup

The gap we investigate is needle-plain electrode shown in Fig.2. The needle electrode is a steel needle for sewing and the curvature radius of its tip is approximately 35 μm. The plain electrode is a circular brass plate of 80 mm in diameter and its surface is mirror finished. When the plain electrode is the porous metal, we put the porous metal on the brass plate shown in Fig.2(b). The porous metal we use is made of copper and its average diameter of pores is 600 μm. Its size is 40×40mm and thickness is 2mm. The experiments are carried out in an atmosphere of air of 1 atm. The plain electrode is grounded and positive or negative voltages are applied to the needle electrode. UV irradiation is not done in our experiments.

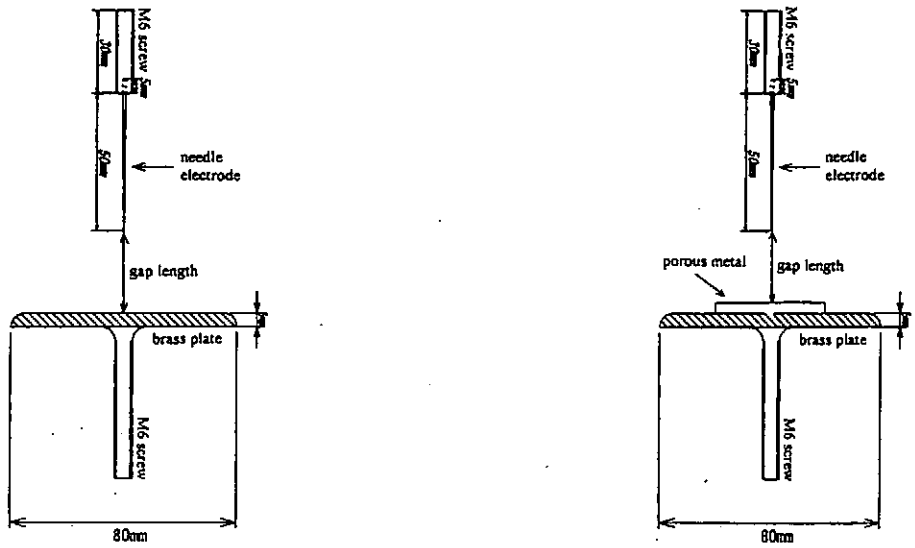

(a) mirror finished electrode (b) porous metal

Fig.2 geometry of gap

The voltage pulses applied to the gap have the rise times of 5-10 ns and pulse duration of 180 ns, and the rise times depend on the charging voltage of a capacitor. The pulses are generated by a 100 cm long coaxial type ferrite sharpener.[1] Fig.3 shows the examples of voltage pulse waveforms applied to the gap. The voltage values become approximately twice as the charging voltage of the capacitor. Voltages are detected by high voltage probe Tektronix P6015A and digital oscilloscope HP54542A.

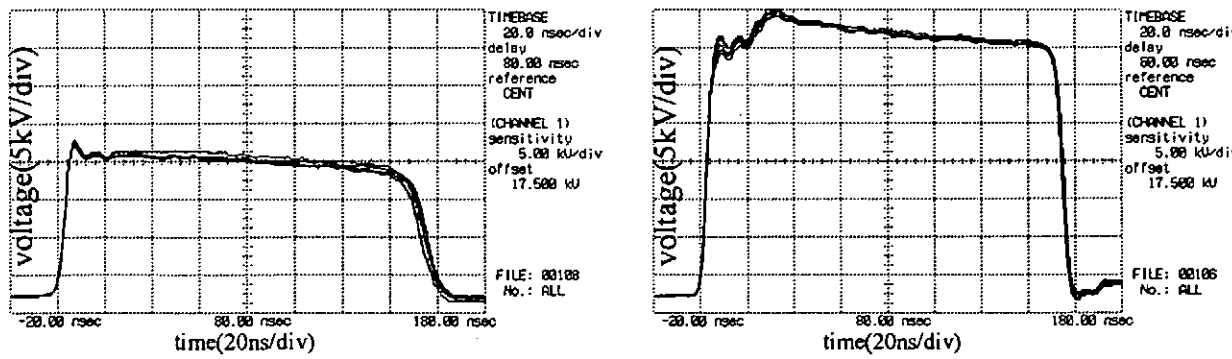

(a) charging voltage is +10kV (b) charging voltage is +20kV

Fig.3 voltage pulses applied to the gap

3. Experimental Results

3.1 DC flashover voltage

First, we examine the DC flashover voltage of the gap when we use a mirror finished brass plate and a porous metal as a plain electrode. Fig.4 shows the DC flashover voltages when the gap lengths are 1, 3 and 5 mm. As shown in the figure, the DC flashover voltages under all the conditions are almost same when the gap lengths are 1 and 3 mm. For the gap length of 5mm, the effect of polarity is seen and the flashover voltage of negative needle is higher than that of positive needle. For the positive needle, the flashover voltage of porous metal is higher than that of mirror finished. On the contrary, the flashover voltage of porous metal is lower than that of mirror finished for the negative needle.

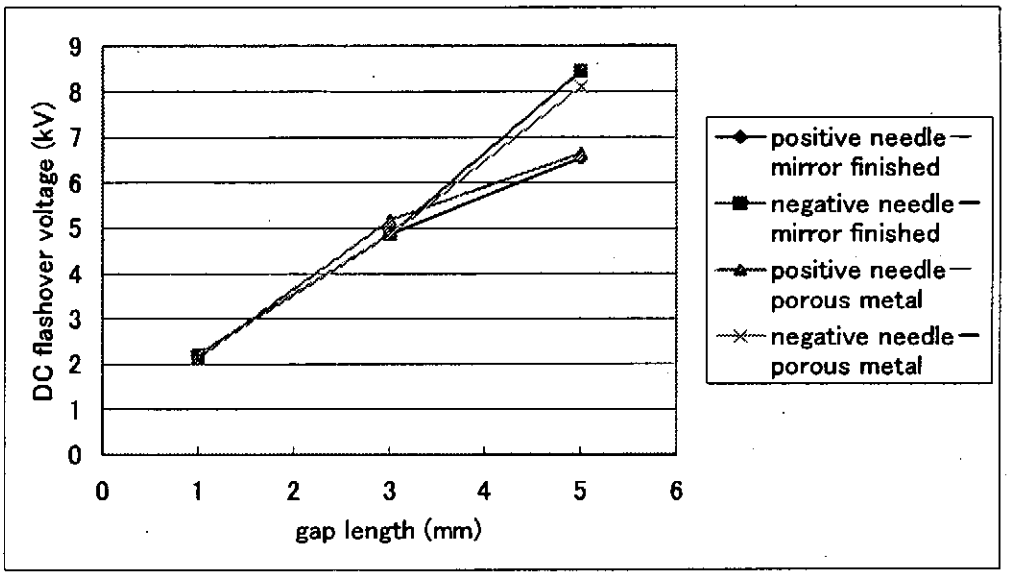

Fig.4 DC flashover voltage

3.2 breakdown characteristics of voltage pulse

Second, we investigate the breakdown characteristics of the statistical time-lag and formative time-lag of flashover when a flat-top nanosecond pulse is applied to the gap. Fig.5 shows the examples of voltage waveforms when the pulses are applied to the gap of 5 mm length. Fifty shots under each experimental condition are performed, so 50 shots are superimposed in the figure. Fig.5 also shows the UV radiation waveforms measured by a photomultiplier.

From the time-lags of spark obtained in the voltage waveforms, we draw Laue plots. Fig.6 shows the examples of Laue plots for the experimental conditions same as that of Fig.5.

From Laue plots, the formative and statistical time-lags are obtained. Based on all the data, Fig.7 and 8 show the formative and statistical time-lags respectively. The formative time-lag decreases as the charging voltage increases. Both formative and statistical time-lags increase with the gap length.

4. Calculation of Formative Time-lag

Along with streamer theory in Ref.2, we calculate the formative time-lags and compare them with the experimental results. Fig.9 shows the calculated and measured formative time-lags of needle-mirror finished plain electrodes when the gap length is 1mm. The calculated time-lags have the same tendency as the measured ones.

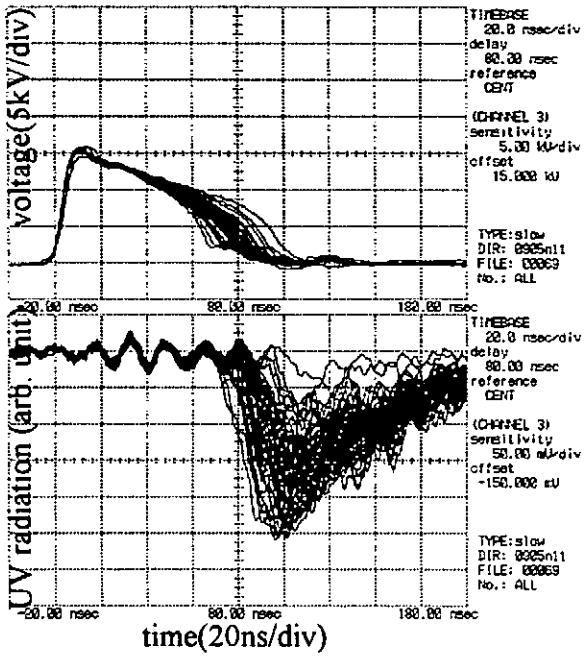

(a) positive needle - mirror finished

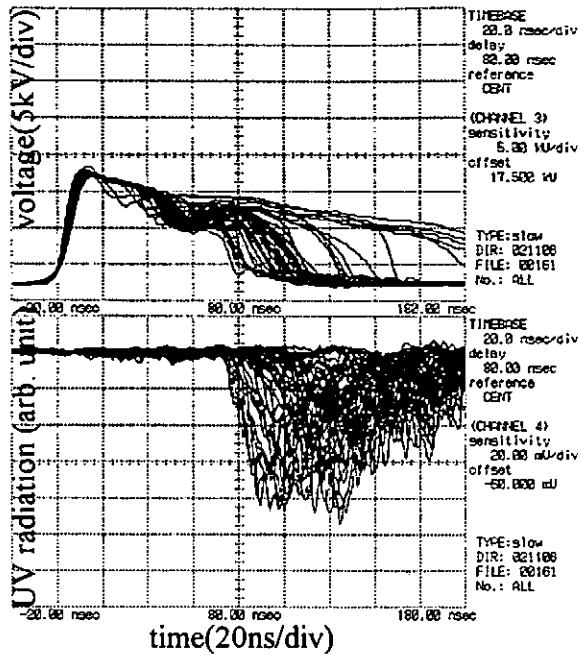

(b) positive needle – porous metal

Fig.5 voltage and UV radiation waveforms with breakdown

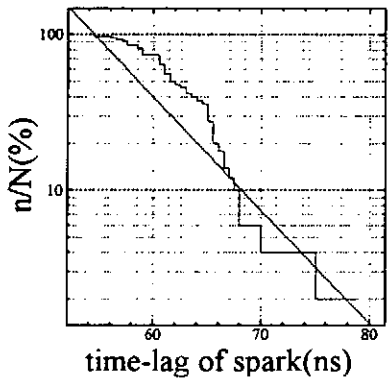

(a) positive needle - mirror finished

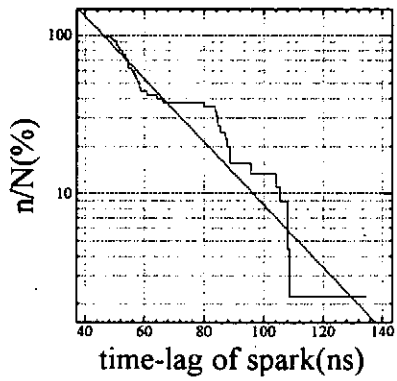

(b) positive needle – porous metal

Fig.6 Laue plots correspond to Fig.5

5. Conclusion

We have investigated the breakdown characteristics with porous metals as a discharge electrode. The gap we investigated is needle-plain electrode. First, we examine the DC flashover voltage of the gap when we use a mirror finished brass plate and a porous metal as a plain electrode. Second, we investigate the breakdown characteristics of the statistical time-lag and formative time-lag of flashover when a flat-top nanosecond pulse is applied to the gap. Contrary to our expectations, a significant difference was not seen. In the future we are going to examine the sphere-plain electrodes as a uniform electric field gap.

References

1) S.Furuya, H.Matsumoto, H.Fukuda, T.Ohboshi, S.Takano and J.Irisawa, "Simulation of Nonlinear Coaxial Line Using Ferrite Beads", Jpn. J. Appl. Phys., **41**, 6536-6540 (2002).

2) R.C.Fletcher, "Impulse Breakdown in the 10^{-9}-Sec. Range of Air at Atmospheric Pressure",

Phys. Rev., **76**, 1501-1511 (1949).

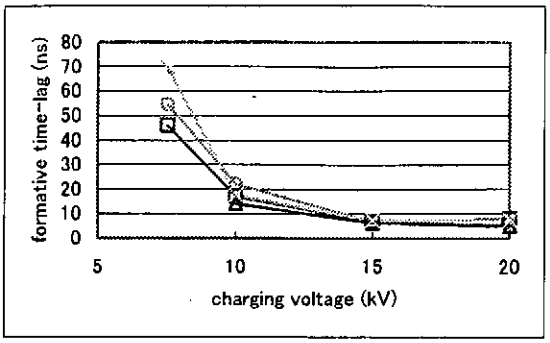

(a) gap length is 5mm

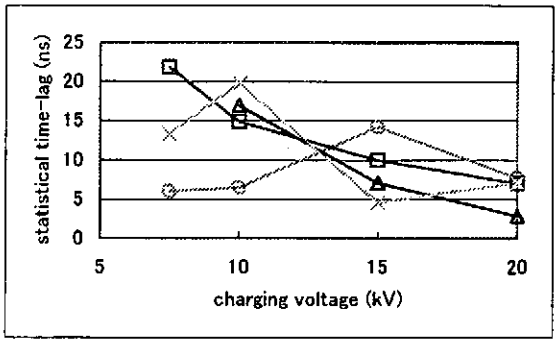

(a) gap length is 5mm

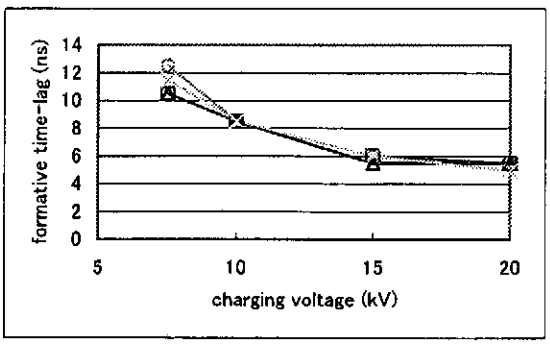

(b) gap length is 3mm

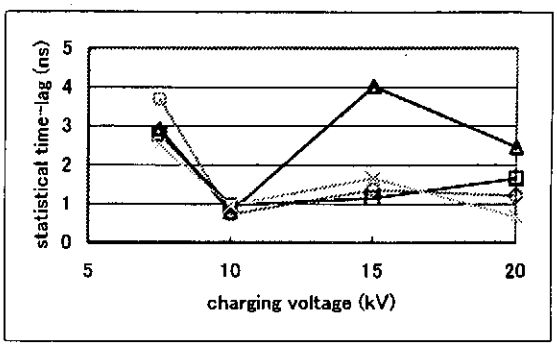

(b) gap length is 3mm

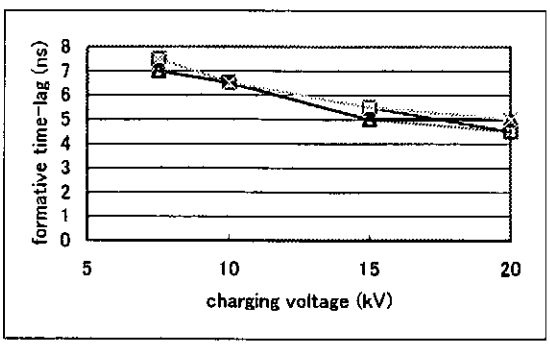

(c) gap length is 1mm

Fig.7 formative time-lag

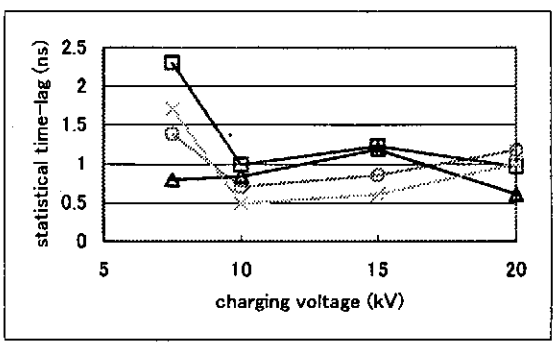

(c) gap length is 1mm

Fig.8 statistical time-lag

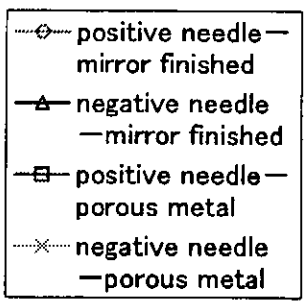

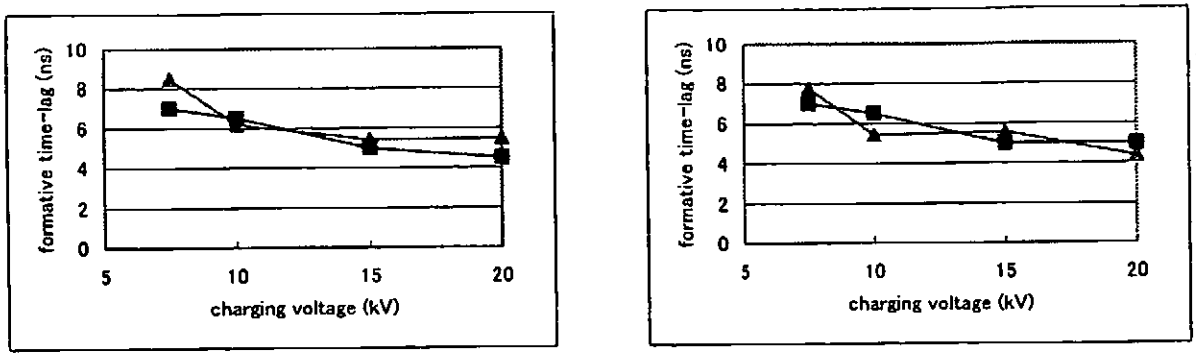

(a) positive needle-mirror finished plain (b) negative needle-mirror finished plain

Fig.9 calculated and measured formative time-lags

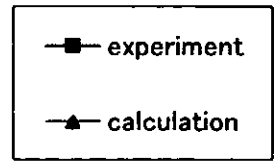

Future of Self-Magnetic Confinement Fusion Approaches

Tetsu MIYAMOTO

Atomic Science Research Institute,
2-13-19 Higasi-Kokubu, Ichikawa, Chiba, Japan

The classification of fusion approaches was reexamined. The approaches should be classified not into two categories, i.e., the magnetic and inertia confinement fusion, but three categories, i.e., the external magnetic, self-magnetic and inertia confinement fusion. The guiding principle of fusion approach based on z-pinches is discussed.

1. Introduction

In the early days of fusion research, z-pinches were intensively investigated. They emitted neutrons that showed occurrence of nuclear reactions, but were strongly unstable. The emitted neutrons resulted not necessarily from thermonuclear reactions but from deuterons accelerated by instabilities [1]. After the simple or classical z-pinches failed to demonstrate a prospect of fusion reactor, they are not considered to be fusion-oriented methods for long years until the laser-initiated, gas-embedded z-pinch that was investigated by Hammel et al. at the middle of 1970's [2]. The aim of the restarted z-pinch research is to produce and sustain a quasi-steady state of dense pinch plasma column that can satisfy the fusion condition for short confinement time limited by instabilities. However, the gas-embedded z-pinch failed to produce the fusion plasma due to accretion of surrounding gas. After that, fiber and other types of z-pinches have carried out by many researchers. However, they seem not to have given the prospect for producing the fusion plasma so far. The main reason results from the stability problem that expected stabilizing effects, such as finite Larmor radius effect, were not effective. It seems that the intrinsic stabilizing effects are insufficient for the purpose. The instabilities of z-pinches result from the cylindrical symmetric geometry. Hence, it was proposed to stabilize z-pinches due to deform their cross-section [3].

On the other hand, a multi-wire array z-pinch succeeded to emit intensive X-ray radiation recently, and has been proposed to be a candidate of driver for the inertia confinement fusion. In this pinch, tungsten was used as wire material, and uniform pinch plasma column with

temperature of a few hundred electron volts was produced. The growth time of sausage instability is about acoustic transit time, i.e., inversely proportional to the thermal speed. The mass ratio of tungsten to the deuteron is about a hundred and the temperature of tungsten plasma is also about a hundredth of the fusion's one. Hence, the growth time of instabilities is prolonged by about a hundred times than that of the fusion plasma, because the thermal speed is proportional to the square root of the mass and temperature. This is one of reasons that the relatively uniform plasma column was produced in the wire array z-pinch. This application of z-pinch is of interest, but will it be the best choice in the fusion approach using z-pinches? The purpose of this paper is to examine this problem from a historical and philosophical view.

2. Short History of Fusion Researches

So far, many fusion devices have been investigate so for since 1950's. They are classified into three categories – "magnetic bottle", "discharge" and "inertia" types, as shown in Fig.1. In "the magnetic bottle type" the plasma is confined in the magnetic bottle composed by a strong magnetic field such as cusp, mirror and stellarator field. When the plasma is heated, discharges are often applied, but are independent of the confinement in principle. In "the discharge type" the plasma is produced and heated by discharges, and at the same time the discharge current plays an important role for confining the plasma. Z-pinches, stabilized pinches and theta pinches are belong to this type. The tokamak will belong to this type or be z-pinch ancestry at least. These two types have investigated intensively from the early days of fusion research. On the other hand, the inertia type appeared at the end of 1960's. While about fifty years, a lot of devices have been shut down -- simple z-pinch, stabilized z-pinch, Zeta, stellarator, Astron, theta pinch, cusp and mirror machines, electron beam fusion, light ion beam fusion etc. It is not clear whether the decisions of shutdown are definite for some ones. For example, some devices were reactivated, for example, z-pinches in 1970's and stellarator after it was once shut down at Princeton University in the end of 1960's.

In the Geneva conference Dr. Baba manifests that the fusion research will succeed within thirty years. The thirty years already passed through in many years ago. There will be no special meaning in "thirty years" itself, because it will be only mean a period permitted for some projects. In the plan of recent ITER project, a fusion reactor is supposed to be constructed in the end of this century, that is, after several decades or nearly a hundred years. Whether is this period permitted for any engineering project in historical or empirical view? Is the fusion research

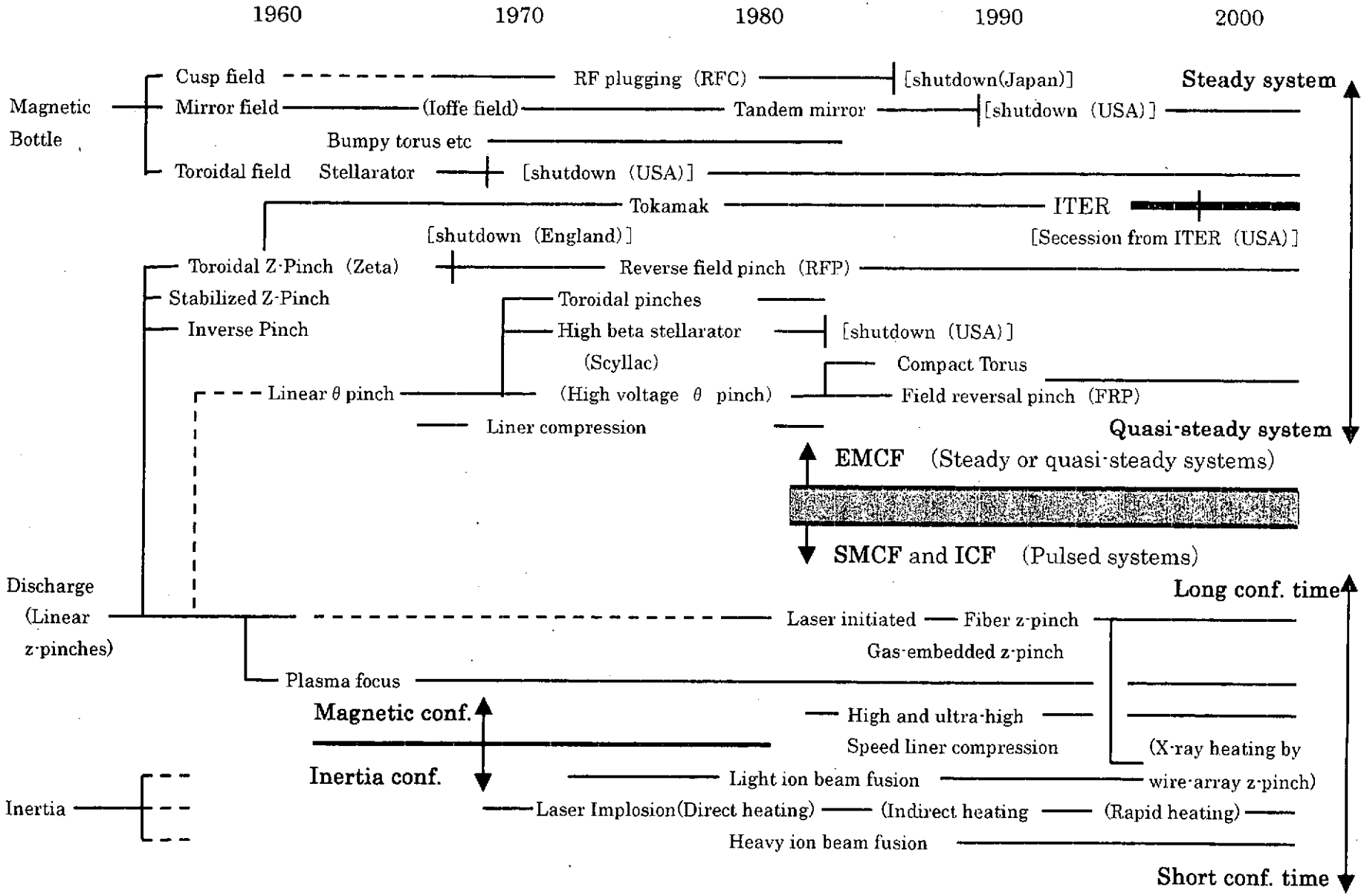

Fig.1 Classification of plasma production methods and devices for fusion

special? If the fusion is quite different from the other engineering projects existed so far, it is another problem, but if it is not so, we have to consider that the fusion research is in deadlock. If we are in deadlock, it will be important to reexamine all of approaches appeared in the fusion research.

3. Three Fusion Approaches

The classification of Sec.2 (the right hand column of Fig.1) is based on the plasma production and confinement. In the view of the approaches to realize the fusion conditions, the fusion researches are classified into three categories. So far, fusion approaches have often been classified into the magnetic (MCF) and inertia confinement fusions (ICF). However, the magnetic confinement should be divided into two different types – "external magnetic confinement fusion (EMCF)" and "self-magnetic confinement fusion (SMCF)", depending on whether solenoid coils are used or not. There is not deep crevasse between the whole magnetic confinement including z-pinches and the inertia confinement (ICF), but between the EMCF and the SMCF (see Fig.2). The coils introduce two difficulties – heat generation and mechanical strength. Super-conducting coils remove the former difficulty, but the latter puts a limitation for available field strength that limits the plasma density. The plasma density is also limited by the energy flow through the first wall of reactor. Hence, the plasma density will not be able to exceed $\sim 10^{22}$ m^{-3}, and the confinement time must be long enough for satisfying the fusion condition for the nt value. The energy density is limited to be less than several tens joule/cm^{-3} (practically less than a few joule/cm^{-3}).

On the other hand, the limitation on available field strength (i.e., density) is removed in the SMCF, as the solenoid coil is unnecessary. Unfortunately, z-pinch plasmas, which are a typical method of the SMCF, are strongly unstable, and the confinement time is limited. Hence, the plasma density must be high enough to satisfy the fusion condition, corresponding to this confinement time. The SMCF results in a kind of the ICF, when it gives up the magnetic confinement. In this case, the pinch effect is to heat plasma and to compress it to a tiny region. It is clear that there is no crevasse between the SMCF and ICF. They belong to a group of pulsed systems, while the EMCF is a steady or quasi-steady system. In the present definition, the pulsed systems have an upper limit on the confinement time (i.e., the lower limit on density) and on the reacting plasma size, as it should not be explosive. On the other hand, the steady or quasi-steady systems have an upper limit on the density and a lower limit on the size. Their devices have to be

scaled up for obtaining better plasma parameters, and as a result, have a tendency to be large and expensive. There is the difference of more than 10^6 on the target density or confinement time between the pulsed and steady systems. Therefore, the reactor concept between the pulsed and steady systems is completely different.

The ICF limit of z-pinches needs electrodes, but the plasma is directly heated and compressed. On the other hand, the conventional ICF needs no electrode, but the plasma must be imploded indirectly using drivers such as laser, X-ray and so on. It is well known that a steady system has an advantage in the EMCF. Generally speaking, the pulsed system will also have advantages when the confinement time is longer. Hence, the stability problem is also essentially important for the SMCF. There are other requirements for the SMCF. Because of necessity of extremely high field and existence of electrodes, the SMCF should be a compact system with extremely narrow plasma and with as low current as possible. These facts mean that the device is economical and need only a short period for developing to the reactor, if the fusion plasma is successfully created. In spite of unstable characteristics of z-pinches and the long history of unsuccessful z-pinch researches, the above-mentioned features that differ from other approaches inspires us to the SMCF research.

4. Self-Magnetic Confinement Fusion Approach

4.1 Basic Relations of Z-Pinches

First we survey the basic relations of a cylindrical z-pinch column. In the pressure equilibrium state the plasma column satisfies the Bennett condition [5]

$$\mu_0 (I^{(c)})^2 = 16\pi N^{(c)} kT \quad , \tag{1}$$

where $I^{(c)}$, $N^{(c)}$, T and k are the total current, the line density, the temperature and the Boltzmann constant. When the thermal conduction is fast enough, the temperature is nearly uniform in the plasma, and the current density is also nearly uniform, and the density distribution is approximately inversely parabolic on radius. Hence, the line density is given by $N^{(c)} = \pi r_0^2 n_0^{(c)} / 2$, where r_0 and $n_0^{(c)}$ are the plasma radius and the peak density at the axis. Then, the steady state of isolated cylindrical z-pinches is achieved at the Pease-Braginskii current (PB current) I_{PB} [6], which is obtained putting as the Joule heating $\int P_J dS = \int \bar{\eta} T^{-3/2} dS$ equals to the a Bremsstralung radiation loss $\int P_b dS = \int \bar{P}_b n^2 T^{-3/2} dS$,

$$I_{PB} \equiv \frac{8\pi k}{\mu_0}\sqrt{\frac{3\bar{\eta}}{P_b}} = 4.33\times10^5\sqrt{\ln\Lambda}\ \ (\mathrm{A}) \quad , \tag{2}$$

and at the line energy density w_{PB} corresponding to I_{PB},

$$w_{PB} \equiv (3NkT)_{PB} = \frac{3\mu_0 I_{PB}^{\ 2}}{16\pi} \approx 1.41\times10^4 \ln\Lambda \ \ (\mathrm{J/m}), \tag{3}$$

where $\ln\Lambda$ is the Coulomb logarithm. We express the confinement time of this pinched plasma column as

$$t = \alpha\frac{r_0}{v_{th}} = \alpha r_0\sqrt{\frac{m}{2kT}} \quad . \tag{4}$$

When $\alpha = 1$, t corresponds to the theoretical growth time of m = 0 instability. Many experiments have shown that $\alpha \geq 1$ due to several stabilizing effects, but at the same time, that the coefficient α was not so large for extremely hot, dense z-pinch plasma. We should consider as $\alpha \sim 1$. The case of $\alpha = 1$ corresponds to a kind of inertia confinement, where the current plays only the role of heating and gathering the plasma in a tiny volume, that is, the role of a driver in the ICF.

We can suppose a quasi-equilibrium state, where the pressure equilibrium almost holds but the current I can differ from the Pease-Braginskii current. The radiation collapse is an example. Then, the line plasma energy density is rewritten as

$$w_p = 3NkT = w_{PB}(I/I_{PB})^2 = w_{PB}\varsigma^2. \tag{5}$$

The magnetic energy per unit length (i.e., the line magnetic energy density) is given as

$$w_m = \int_{r_0}^{r_w}\frac{B^2}{2\mu_0}2\pi r dr = \frac{\mu_0 I^2}{4\pi}\left[\frac{1}{4}+\ln\frac{r_w}{r_0}\right] = \frac{w_{PB}\varsigma^2}{3}\left[1+4\ln\frac{r_w}{r_0}\right] \quad . \tag{6}$$

Hence, the total line energy density is expressed as

$$w \equiv w_p + w_m = \frac{4}{3}w_{PB}\varsigma^2\left[1+\ln\frac{r_w}{r_0}\right] \equiv \frac{w_p}{\chi} \quad , \quad \text{where } \frac{1}{\chi} = \frac{4}{3}\left[1+\ln\frac{r_w}{r_0}\right] \tag{7}$$

4.2 Fusion Conditions

The ratio of the released energy to the input one must satisfy

$$Q = \frac{\int P_r dSdt}{w + \int P_B dSdt} \geq \frac{1-\eta_{ec}}{\eta_{ec}} \quad , \tag{8}$$

where $w = w_p + w_m = w_p / \chi$. When the plasma is kept at a temperature T and a density n during the period t and the efficiency η_{ec} is 1/3, this ratio must satisfy $Q > 2$ (the Lawson criterion). We introduce the function

$$F(T,Q) = Q \Big/ \left[\frac{\bar{P}_r(T)}{3kT} - Q \frac{\bar{P}_B}{3kT^{1/2}} \right]$$

The Lawson condition is expressed as

$$n_0 t = \frac{F(T,Q)}{f\chi} \geq \frac{F(T,2)}{f\chi} \quad , \tag{9}$$

where $f = \int_S n^2 dS / n_0 \int_S n dS$ is a correction factor on the density distribution. The function $F(T,2)$ gives the optimum temperature of about 2×10^8 (K) and $F(2\times10^8,2) \approx 0.7\times10^{20}$ (for simplicity, we use the value $F(2\times10^8,2)=10^{20}$ hereafter). Using Eq.(4), condition (9) is rewritten for cylindrical z-pinches as

$$n_0 r_0 = \sqrt{\frac{2kT}{m}} \frac{F(T,Q)}{\alpha f\chi} > \sqrt{\frac{2kT}{m}} \frac{F(T,2)}{\alpha f\chi} \quad . \tag{10}$$

Considering Eqs.(5), we can rewrite Eq.(10) as conditions for the radius and density as function of the current as

$$r_0 = \frac{\mu_0 {I_{PB}}^2 m^{1/2}}{4\pi^2 (2kT)^{3/2}} \frac{\alpha f\chi}{F(T,Q)} \varsigma^2 < 2.39\times10^{24} \ln\Lambda \frac{\alpha f\chi}{F(T,2)} \frac{\varsigma^2}{T^{3/2}} \tag{11}$$

$$n_0 = \frac{4\pi^2 (2kT)^2}{\mu_0 {I_{PB}}^2 m} \left(\frac{F(T,Q)}{\alpha f\chi\varsigma} \right)^2 > \frac{3.82\times10^{-23}}{\ln\Lambda} \left(\frac{F(T,2)}{\alpha f\chi} \right)^2 \left(\frac{T}{\varsigma} \right)^2 . \tag{12}$$

In the cylindrical z-pinches, the density correction factor is $f = 1/3$. We suppose $\ln\Lambda = 10$ and $\chi = 0.1$. In the optimum condition ($T = 2\times10^8$ (K) and $F(2\times10^7,2) = 10^{20}$) for $Q = 2$, the line energy and density are given as

$$w = 1.41\times10^6 \varsigma^2 \quad \text{and} \quad N = 1.7\times10^{19} \varsigma^2 \quad , \tag{13}$$

and the condition for the radius and the density result in

$$r_0 < 6.04\times10^{-9}\alpha\varsigma^2 \quad \text{and} \quad n_0 > 2.99\times10^{35}(\alpha\varsigma)^{-2} \ . \tag{14}$$

4.3 Inertia Confinement Limit of Cylindrical Z-Pinches

The inertia confinement limit is obtained putting as $\alpha = 1$. At $\varsigma = 1$ (i.e., the steady state) the radius must be about 6 nm and extremely high density is required. Relating to the inertia confinement limit, we are interested in the radiation collapse [7] that creates an extremely narrow, dense plasma column. However, it had been pointed out that the radiation collapse will be limited by several reasons, i.e., radiation opacity, energy feeding and so on [8]. It will be difficult to achieve such a narrow radius and high density. When $\varsigma \simeq 31.6$ (i.e., $I \approx 44$ MA), Eq.(14) gives the moderate value $r_0 < 6.04$ μm and $n_0 > 2.99\times10^{33}$ m^{-3}. However, it will be also difficult to flow such a high current in a small region. Hence, it will be important to increase the stability factor α.

5. Concluding Remarks

The SMCF essentially differs from the EMCF, and is the same pulsed system with the ICF. In comparison with the ICF, the SMCF has drawbacks due to necessity of electrodes, but merits due to long confinement time that makes the SMCF attractive in pulsed systems. For achieving long confinement the plasma column must be stabilize, but the intrinsic stabilizing effects will not be enough for the purpose. It will be the most important subject in the SMCF to find the other stabilizing methods. One of example will be to deform the cross section of plasma column.

References

1. O. A. Anderson, W. R. Baker, S. A. Colgate, H. P. Furth, J. Ise Jr and R. V. Pyle, Phys. Rev., **110**, 1375 (1958).
2. J. Hammel, D. W. Scudder and J. S. Schlachter, Nucl. Instrum. Meth. **207**, 161 (1983).
3. T. Miyamoto, J Phys. Soc. Japan **68**, 1238 (1999) ; AIP Conf. Proc. **651**, 295 (2002).
4. M. K. Matzen, Phys. of Plasma, **4** (Pt.2), 1519 (1997).
5. W. H. Bennett, Phys. Rev. **45**, 890 (1934).
6. R. S. Pease, Proc. Phys. Soc. London **B70**, 11 (1957) ; S. I. Braginskii, Sov. Phys. JETP **6**, 494 (1958).
7. J. W. Shearer, Phys. Fluids, **19**, 1426(1976).
8. P. Choi and C. Dumitrescu-Zoita, AIP Conf. Proceeding **409**, 51(1997).

Recent Issues of NIFS-PROC Series

NIFS-PROC-34 プラズマ対向機器・PSI・熱・粒子制御合同研究会報告
平成 9 年 6 月 27 日（金）9:00 ～16:20 核融合科学研究所・管理棟 4 F 第 1 会議室
1997年 10月
T. Yamashina (Hokkaido University)
Plasma Facing Components, PSI and Heat/Particle Control June 27, 1997, National Institute for Fusion Science T. Yamashina (Hokkaido University) : Oct. 1997 (in Japanese)

NIFS-PROC-35 T. Watari,
Plasma Heating and Current Drive: Oct. 1997

NIFS-PROC-36 T. Miyamoto and K. Takasugi (Eds.)
Production and Physics of High Energy Density Plasma: Production and Physics of High Energy Density Plasma: Oct. 1997

NIFS-PROC-37 (Eds.)T. Fujimoto, P. Beiersdorfer,
Proceedings of the Japan-US Workshop on Plasma Polarization Spectroscopy and The International Seminar on Plasma Polarization Spectroscopy January 26-28, 1998, Kyoto: June 1998

NIFS-PROC-38 (Eds.) Y. Tomita, Y. Nakamura and T. Hayashi,
Proceedings of the Second Asian Pacific Plasma Theory Conference APPTC '97, January 26-28, 1998, Kyoto: Aug. 1998

NIFS-PROC-39 (Ed.) K. Hirano,
Production, Diagnostics and Application of High Energy Density Plasmas: Dec. 1998

NIFS-PROC-40 研究代表者 加古 孝（電気通信大学）
所内世話人 渡辺 二太
平成 10 年度核融合科学研究所共同研究 研究会「プラズマ閉じ込めに関連する数値計算手法の研究」
Ed. by T. Kako and T. Watanabe
Proceeding of 1998-Workshop on MHD Computations "Study on Numerical Methods Related to Plasma Confinement Apr. 1999

NIFS-PROC-41 (Eds.) S. Goto and S. Yoshimura,
Proceedings of The US-Japan Workshop and The Satellite Meeting of ITC-9 on Physics of High Beta Plasma Confinement in Innovative Fusion System, Dec. 14-15, 1998, NIFS, Toki: Apr. 1999

NIFS-PROC-42 (Eds.) H. Akiyama and S. Katsuki,
Physics and Applications of High Temperature and Dense Plasmas Produced by Pulsed Power: Aug. 1999

NIFS-PROC-43 (Ed.) M. Tanaka,
Structure Formation and Function of Gaseous, Biological and Strongly Coupled Plasmas: Sep. 1999

NIFS-PROC-44 (Ed.) T. Kato and I. Murakami,
Proceedings of the International Seminar on Atomic Processes in Plasmas, July 29-30, 1999, Toki, Japan: Jan. 2000

NIFS-PROC-45 (Eds.) K. Yatsui and W. Jiang,
Physics and Applications of Extreme Energy-Density State, Nov. 25-26, 1999, NIFS: Mar. 2000

NIFS-PROC-46 研究代表者 加古 孝（電気通信大学）
所内世話人 渡辺 二太
平成 11年度核融合科学研究所共同研究 研究会「プラズマ閉じ込めに関連する数値計算手法の研究」
Ed. by T. Kako and T. Watanabe
Proceeding of 1999-Workshop on MHD Computations "Study on Numerical Methods Related to Plasma Confinement June. 2000

NIFS-PROC-47 岡本正雄、村上定義、中島徳嘉、汪衛生
プラズマ物理におけるモンテカルロシミュレーション
WatanabeM. Okamoto, S. Murakami, N. Nakajima, W.X. Wang,
Monte Carlo Simulations for Plasma Physics: July 2000

NIFS-PROC-48 K. Miyamoto,
Fundamentals of Plasma Physics and Controlled Fusion: Oct. 2000

NIFS-PROC-49 (Ed.) K. Kawahata,
Proceeding of the 5th International Workshop on Reflectometry, 5-7 march, 2001: May 2001

NIFS-PROC-50 (Ed.) S. Ishii
Workshop on Extremely High Energy Density Plasmas and Their Diagnostics, Mar. 8-9, 2001, National Institute for Fusion Science, Toki, Japan: Sep. 2001

NIFS-PROC-51 (Ed.) K. Horioka,
Physics and Applications of High Energy Density Plasmas -Extreme state driven by pulsed electromagnetic energy, Dec.20-21, 2001, National Institute for Fusion Science; June 2002

NIFS-PROC-52 第６回「シミュレーション・サイエンス・シンポジウム」及び核融合科学研究所共同研究「大型シミュレーション研究」合同研究会 集録
Proceedings of Joint Meeting of the 6th Simulation Science Symposium and the NIFS Collaboration Research "Large Scale Computer Simulation": Mar. 2003

NIFS-PROC-53 研究代表者 渡邉二太
LHD型磁場配位を用いたICRF支援 水素・硼素核融合炉の理論的研究ー平成14年度核融合科学研究所共同研究ー
(Ed.) T. Watanabe
Theoretical Study for ICRF Sustained LHD Type p-^{11}B Reactor: Apr. 2003

NIFS-PROC-54 (Ed.) K. Masugata
Physics and Applications of Micro and Fast Z-Pinch Plasmas (Dec. 5-6, 2002, NIFS): July 2003